# Spin-orbit torques and photocurrents in 2D materials

Jan Hidding

**Book cover:** By flipping the book you switch between day and night, representing the transition between "0" and "1" in binary computer memory. The waves represent the first- and second-harmonic Hall voltages observed in spin-orbit torque measurement, while the lighthouse serves as a nod to the optical measurements conducted in this thesis. Designed by me, Jan Hidding.

university of groningen / faculty of science and engineering


NANO LABNL

Zernike Institue PhD thesis series: 2024-04
ISSN: 1570-1530

The work described in this thesis was performed in the research group Optospintronics of Quantum Materials of the Zernike Institute for Advanced Materials at the University of Groningen, the Netherlands. This work supported by NanoLab NL and the Zernike Institute for Advanced Materials. This work was in large part financed by the EU Graphene Flagship (Core 2 and 3 - Grant Agreement No. 696656 and 785219) and the Dutch Research Council (NWO).

An electronic version of this dissertation is available at:
https://research.rug.nl/en/publications.

Printed by: Ipskamp printing, Enschede.

rijksuniversiteit
groningen

# Spin-orbit torques and photocurrents in 2D materials

**Proefschrift**

ter verkrijging van de graad van doctor aan de
Rijksuniversiteit Groningen
op gezag van de
rector magnificus prof. dr. ir. J.M.A. Scherpen
en volgens besluit van het College voor Promoties.

De openbare verdediging zal plaatsvinden op

dinsdag 16 januari 2024 om 16:15 uur

door

**Jan Hidding**

geboren op 20 augustus 1994
te Groningen, Nederland

**Promotores**
Prof. dr. M.H.D. Guimarães
Prof. dr. B.J. van Wees

**Beoordelingscommissie**
Prof. dr. P. Gambardella
Prof. dr. R.A. Duine
Prof. dr. L.J.A. Koster

# Contents

# chapter 1

## Introduction

*This chapter serves as a general introduction to the field of spintronics and two-dimensional materials and highlights the motivation behind the research presented in this thesis. To put this line of research in context, first a short description of the historical development of computer memory throughout the last few decades is presented, after which the current dilemmas in the further development of these technologies are described. Next, the spintronic effects called the spin-transfer torque and spin-orbit torque are introduced as promising candidates to further improve computer memory storage. However, before these can be used and flourish to their full potential, a number of open questions on the exact mechanisms involved in these effects need to be answered. In this context, the promise of more fundamental research on two-dimensional van der Waals materials to shed light on these unknowns is discussed, and the use case of two-dimensional van der Waals materials as convenient platform in this line of research is argued. Finally, a concise summary of each of the up coming chapters in this thesis is given, highlighting the results and their implications from a fundamental point of view.*

# 1

The invention of the transistor in 1947 by Bardeen, Brattain, and Shockley accelerated the beginning of the information age [1]. Ever since, the semiconductor industry has had a major impact on society with the development of multiple technologies, such as the internet, personal computers, smartphones, a variety of sensors, etc. Especially during the recent COVID-19 pandemic, it has become apparent how dependent our society has become on the semiconducting industry and the continuous ability to produce high quality chips for applications such as personal computers, medical equipment, and the automotive industry. With new and emerging technologies around the corner holding great promise for future advances of the semiconducting industry, such as artificial intelligence, quantum and neuromorphic computing, big data, 5G and the internet-of-things, etc., semiconducting materials might become even more embedded in our society in the near future, than they are at the time of writing.

Multiple challenges, however, lie ahead before these promises can be fulfilled. One prime example is meeting the exponential growth of our memory demand. By 2040, the world wide stored information is expected to be between $10^{24}$ and $10^{28}$ bits [2]. Currently, a single bit of NAND FLASH memory uses about 1 picogram ($10^{-12}$ g) of silicon. Performing a back-on-the-envelop calculation allows us to estimate that the total mass of silicon needed to store this information would be in the order of $10^{9}$ to $10^{13}$ kg. With only a linear increase of silicon wafer production each year, the total mass of silicon wafers required to store this information would far exceed the world's total available silicon supply (estimated at $\sim 2.3 \times 10^{7}$ kg in 2040) [2].

Furthermore, with the fast increase of data centers for cloud storage and cloud computing, the energy consumption of information technologies rises exponentially while the energy production worldwide only increases approximately linearly. At the time of writing, data centers worldwide use an estimated 200 terawatt hours (TWh) each year, which corresponds to about 1% of the total worldwide electricity demand [3]. In 2030, it is predict that the entire information and communication technology sector is estimate to demand 8% to 51% of the total electricity production [4]. The alarming increase in energy consumption, together with the challenge of reducing $CO_2$ emission to fight global warming, demands for more energy efficient techniques and the use of more sustainable materials in information technologies.

Looking back at the development of information technologies in the last few decades, the continuous improvement of integrated circuits and the ever decreasing transistor size has shown an astounding increase in computations per joule and reduction in size already. The first general computer is considered to be the ENIAC (Electronic Numerical Integrator and Computer), build between 1943 and 1946 [5]. As it was constructed before the invention of the solid-state transistor, this computer relied on 17,468 vacuum tubes, 1500 relays, 70,000 resistors and 10,000 capacitors, all soldered by hand, consumed almost 200 kilowatts of electrical power, weighted 30 tons, and occupied a room of $9 \times 15$ m$^2$ [6]. It was designed to calculate ballistic equations for World War II and could perform 5,000 calculations per second [7]. The first big leap in miniaturization and increased energy efficiency began with the invention of the bipolar solid-state transistor, only one year later in 1947 [1]. Other big steps were made with the invention of the integrated circuit (ICs) by Jack Kilby

and Robert Noyce [8] in 1958, and more recently, the invention of complementary metal oxide semiconductor (CMOS) devices in the early 1990s [9]. Already in 1965, Gordon Moore predicted the miniaturization that started with the solid-state transistor to continue for the decades to come, stating that the number of components on a chip would continue to double every two years [10] Ever since his prediction, this has continued to be a self-fulfilling prophecy, now famously referred to as "Moore's law". As example, the Intel 4004 chip from 1971 had 2,300 transistors [11], while the more recent Apple M1 Ultra chip, launched in 2022, has nearly 114,000,000,000 transistors [12], still in line with Moore's prediction.

However, with a gate pitch (minimum distance between two transistor gates) reaching approximately 40 nm [13] (200 silicon atoms), the limit to further transistor miniaturization is inevitably getting closer [14]. The continuation of Moore's law in the last two decades is not solely due to simple miniaturization of existing planar transistor designs. Rather, clever transistor designs, such as fin field-effect transistors (FinFET) or gate-all-around field-effect transistors (GAAFET), has helped manufacturers to abide to Moore's law [15].

In addition, while Moore's law has continued to be true due to clever new IC designs, another prediction related to transistor scaling, referred to as Dennard's law (1974), already seized to continue since the early 2000s. Robert H. Dennard predicted in 1974 that the power consumption of chips upon simple transistor miniaturization would remain constant, as the power usage of transistors would be proportional to their area [16]. Nevertheless, with the microscopic transistor sizes of today, current leakage poses a greater challenge causing the chip to heat up, which in turn, results in more leakage. This increases the energy loss, and therefore, resulted in the end of Dennard's law [17].

Now that the physical limits of conventional CMOS chips are approaching, the quest for new methods and techniques intensifies to keep increasing computing speed, capacity and efficiency [18]. Although the transistor technology has been refined to exquisite levels, the basic physical working principle has not changed drastically since its invention in 1947. This has inspired researchers to explore new fields of physics to reinvent information processing and storage technologies, such as neuromorphic computing, analog computing and quantum computing. One of these new fields of research is called *spintronics*. While in classical electronics, the charge of the electron is used to process, communicate and store information using electric fields, with spintronics, information is carried by the electron spin rather than the electron charge. One of the advantages of spintronics compared to conventional electronics, is that it allows one to imprint and manipulate information in nanoscopic magnetic layers using electric fields. The research presented in this thesis focuses on the electron spin and the relevant effects and is thus considered as part of the field of spintronics. Before we discuss the field of spintronics, and how it could potentially make memory storage more efficient and faster, a brief description of the development of computer memory in the last few decades is presented.

1

## 1.1. Short history of magnetic memory

Storing information in magnetic materials (i.e. magnetic storage or magnetic recording) is not new. Already at the end of the 19th century, the first reports on storing an electrical audio signal in a magnetic wire, referred to wire recording, were published. To store the signal, the magnetic wire is pulled through a so-called "write head" which magnetizes each point along the wire in accordance with the intensity and polarity of an electrical audio signal. Vice versa, the electrical signal could be regenerated by passing the wire through a so-called "read head" producing an electrical signal in accordance with the magnetization of the wire. This wire recording was later superseded by magnetic tape which offered a better signal to noise ratio.

The first commercial magnetic random access memory (MRAM), a type of memory with no moving parts for use in computers, dates back to the 1950s where digital information was stored in arrays of magnetic donut shaped rings, as shown in Fig. 1.1(a). Each magnetic ring, also referred to as a core, has its magnetization rotated either clockwise or counter clockwise, representing the "0" and "1" bit, respectively. Four wires were woven through these closely packet rings to allow for reading and writing the magnetization and thus the information. The writing process is schematically depicted in the simplified schematic of 1.1(b). Note that only two of the four wires are drawn for clarity. By passing half of the switching current through one horizontal wire (red), and the other half through one vertical wire (blue), only the ring where these horizontal and vertical wires intersect is switched, as only here the Oersted field from the combined currents is strong enough to change the state. By controlling the direction of the switching current, the magnetization state of the ring can be set either clockwise or counter clockwise. In this way, the magnetization state of each individual ring can be selectively written by selecting the corresponding horizontal and vertical wires. The reading process involves one of the other two wires, not shown in Fig. 1.1.

Starting 1968, this type of magnetic memory was superseded by so called dynamical random access memory (DRAM) where information is stored electrically by charging a capacitor rather then using the magnetization direction of a magnet (see Fig. 1.2(b)). As only one transistor and capacitor are needed for one bit, it allowed for more facile scalability, mass-production, and better integration with integrated circuits at that time. Throughout the years DRAM has been greatly miniaturized to transistor channel lengths of about 28 nm, allowing for a low cost, high capacity memory, which is still widely used as main memory of personal computers currently. On the other hand, the miniaturization causes a major drawback of DRAM, as the charge on the capacitor can more easily leak away through the 28 nm channel. DRAM thus gradually loses its stored information when the power is removed, making it a volatile memory (vs. non-volatile memory). To counter act this problem, DRAM needs to be regularly refreshed, which in turn demands complicated refresh circuitry and timing. In addition, the writing speeds for DRAM is typically in the order of $\approx$ 100 ns [19]. Although this is significantly faster compared to hard-disk drives and magnetic tapes (used for high capacity purpuses) with a writing speeds of only $\approx$ 10 ms, there is faster memory on the market.

In this regards, another type of electronic memory, called static random access

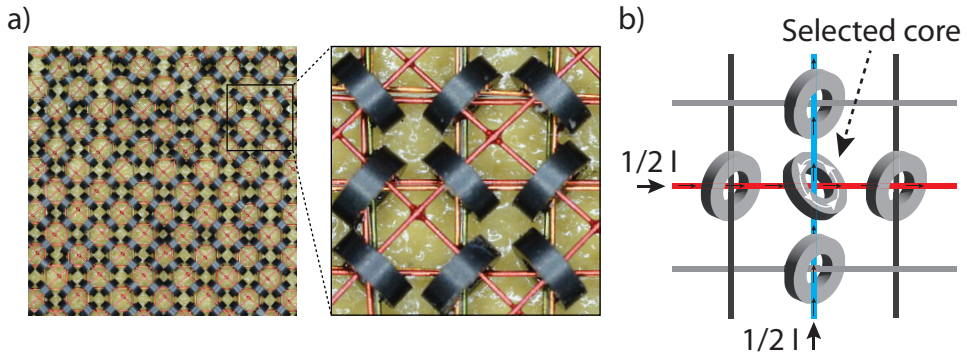


Figure 1.1: (a) A photo, and a zoomed in region, of the first type of commercial magnetic random access memory used in the 1950s consisting of an array of magnetic donut shaped rings (cores) with four wires woven through each rings. The "0" and "1" are stored in the clockwise or counter clockwise magnetization of each rings. For referrence, these magnetic rings had a diameter of around 2.5 mm. (b) Schematic of the core memory depicted in (a) where only two wires are depicted for clarity. By passing half of the switching current through the horizontal (red) and the other half of the switching current through the vertical (blue) wire, the magnetization of the ring (white arrows) where both wires intersect is switched by the Oersted field of the combined currents. By changing the current direction, the magnetization state of the ring can be controlled. Each individual ring can be switched by selecting the corresponding horizontal and vertical wire.

memory (SRAM), exhibits faster performance compared to DRAM memory with write speeds of $\approx$ 1 ns [20]. SRAM was invented in 1963 by Robert Norman at Fairchild Semiconductors and uses so called latching circuitry, schematically depicted in Fig. 1.2(b). A major benefit of SRAM compared to DRAM is that this type of memory does not need to be refreshed. On the other hand, more transistors (typically six) per bit are needed, making it less dense and more expensive compared to DRAM, and read and write operations typically require more energy. Therefore, SRAM is mainly used in the fastest memory parts of the computer, such as cache memory and registers, while DRAM is used as main memory where speed is less important and higher capacity is needed.

Recently, however, a new type of random access memory based on spintronic effects has been created, offering the fast speeds (or even faster speeds) of SRAM memory, capacity of DRAM memory, and non-volatility of FLASH memory, all in a more energy efficient way. But before this is discussed, a more general introduction in the field of spintronics is given in the section below.

## 1.2. Spintronics

In classical electronics, the charge of the electron is used to process, communicate and store information using electric fields. on the other hand, For magnetic recordings, information is stored in the alignment of the magnetization of magnetic materials. Spintronics offers a convenient way of inter-converting these two technologies by exploiting another property of the electron, namely its intrinsic magnetic moment, called spin [22]. Using and manipulating the electron spin to intertwine

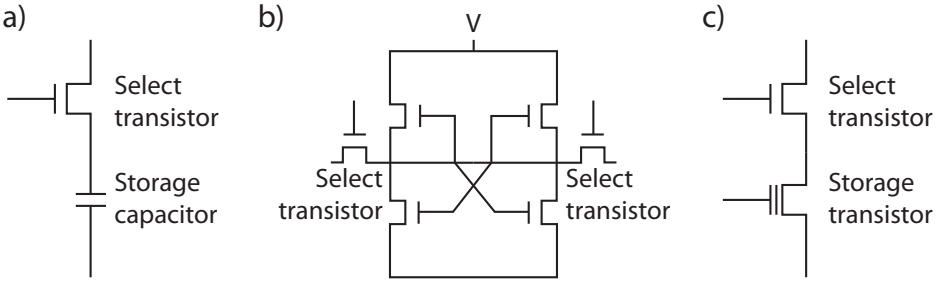


Figure 1.2: Schematic electrical diagram of different types of electronics memory, namely (a) DRAM, (b) SRAM, and (c) FLASH memory. (a) The relatively simple DRAM uses only one transistor and one capacitor per bit and stores the information by charging the capacitor. It is considered as volatile memory, as the charges on the capacitor leak away with time. To counter act this problem, DRAM needs special refreshing circuitry which refreshes the capacitor approximately 16 times per second [21]. (b) SRAM, on the other hand, is considered volatile memory as it stores the information in so called latching circuitry. This type of circuitry need six transistors per bit, making it more expensive. (c) FLASH memory, used in solid-state drives and USB-drives, needs two transistors, and stores the information by charging a so-called "floating gate" in the storage transistor.

these technologies allow to design new, faster, and more efficient logic devices and memory storage, surpassing current semiconductor technologies. Nonetheless, before spintronics can fully flourish, gaining more control of the generation, transport, manipulation, and detection of spin-currents is necessary [23].

The independent discovery of the giant magnetoresistance (GMR) effect by the groups of Albert Fert and Peter Grunberg in 1988 is often coined as the start of the field of spintronics [24, 25]. They observed that the resistance between two ferromagnetic materials, spaced with a normal metal, depends on the relative alignment of the magnetization of the ferromagnetic layers. This allows for a convenient way to electrically read-out the magnetic order in these devices. That the resistance of a material can depend on its magnetization, called anisotropic magnetoresistance (AMR), was not new. Already in 1856 this was observed by William Thomson (also known as Lord Kelvin) [26]. He noticed that the resistance of an iron or nickel wire changed when the magnetic force was aligned parallel to the current compared to a perpendicular alignment. The particular geometry of the devices of Albert Fert and Peter Grunberg, however, allowed for a much larger change in resistance. The device, consisting of two ferromagnetic layers spaced with a normal metal, showed a change in resistance of 50% at 4.2 K, and 3% at room temperature, when the relative alignment of the magnetization of the ferromagnets were changed from parallel to an antiparallel configuration. It was later realized that this magnetoresistive effect can be increased further by replacing the normal metal with a thin insulating layer, called the tunnel magnetoresistance (TMR) effect, in a so called magnetic tunnel junction, or MTJ in short, depicted in Fig. 1.3. The tunnel magnetoresistive effect as actually already observed in 1975 at 4.2 K but did not attract much attention then as the poor quality of the tunnel barriers limited the change in resistance to approximately 14% [27]. But with the development of high-quality crystalline mag-

nesium oxide tunnel barriers, TMR ratios of greater than 180% were achieved at room temperature [28, 29].

These spintronic effects caused a revival in magnetic storage media and were successfully implemented as MTJs in the "read" heads of hard-disk drives. Here, the MTJ inside the "read" head is placed is close proximity to the magnetic domains on the hard drive. The stray field of the magnetic domain on the hard-disk drive directly under the read head causes the magnetization of the free layer to switch, allowing one to read the magnetization direction of the domains on the hard-disk drive electrically. Contrarily, to write information on the hard-disk drive, the magnetic domains on the hard drive are switched using an external magnetic field. This poses a problem, however, as this method does not allow for high-density memory. In addition, reading the domains of the hard drive requires multiple moving parts, such as the spinning hard drive and the movement of the read head across the hard drive, which is energy consuming and prone to failure. New ways of controlling the magnetization direction of the free layer in MTJs by electrical means without moving parts are therefore sought after. One of these ways is by means of another spintronic effect, namely the so called spin-transfer torque (STT). This effect holds great promise for improving current computer memory and will be discussed below.

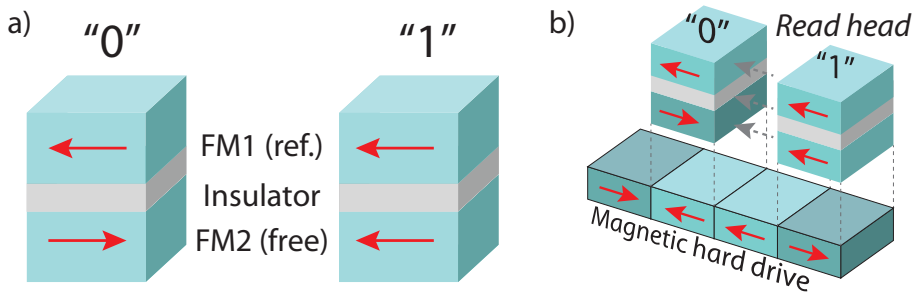


Figure 1.3: (a) A schematic illustration of a magnetic tunnel junction (MTJ) consisting of two ferromagnetic layer layer (FM1 and FM2) spaced by an insulating layer. The "0" and "1" are stored in the relative alignment of the magnetization of the ferromagnetic layers, indicated with the red arrows. Due to the tunnel magneto-resistance (TMR), the resistance through the stack changes from high to low for anti-parallel to parallel configuration, respectively, allowing one to distinguish between these two configurations. The magnetization of one of the ferromagnetic layers is pinned, usually due to the presence of an antiferromagnetic layer in its proximity, while the other ferromagnetic layer is free to switch. (b) The read head used in hard-disk drives uses this MTJ to sense the magnetization state of the domains on the magetic disk. The bottom free FM layer closest the the magnetic hard-disk drive switches its magnetization according to the magnetization of the domains on the hard drive, while the reference FM layer keeps its magnetization fixed.

### 1.2.1. Spin-transfer torques

Recently, a lot of research has been performed to incorporate another spintronic effect together with the MTJ, namely the current induced spin-transfer torque (STT) [30]. In this case, rather than using the MTJ as a read head to sense the information stored on a hard-disk drive, the MTJ itself is used to store one bit of information. Recall that with HDDs, the magnetization of the free layer was switched by the

stray fields of the magnetic domains on the magnetic disk. With the STT, on the other hand, a spin-polarized current is injected into the free ferromagnetic layer, where it can subsequently interact with the magnetization and exert a torque. If the torque is strong enough, it can be used to switch the magnetization of the free layer from parallel to anti-parallel or vise versa [31] This effect is briefly description below.

The ability to exert a torque on the magnetization of a ferromagnet using a spin-current dates back to the late 1970s and 1980s [32, 33]. This effect did not attract much attention, mainly because of the huge currents needed to excite magnetization dynamics ( 45 A!) for the wide samples at that time [34]. It was not until the theoretical work of Slonczewski and Berger in 1996 [35, 36] that this phenomenon got more attention. Ever since, there has been a lot of further theoretical and experimental developments [34]. The principle of the STT in a MTJ is illustrated in Fig. 1.4, where we see two ferromagnetic layers, a reference layer and a free layer, spaced by an insulating layer. Note that in Fig. 1.4, the magnetization of the two layers (M1, M2) are not aligned. When an unpolarized charge current is applied through the MTJ (going from bottom to top), the charge current is first spin-polarized in the reference layer, i.e. the spins of the electrons are aligned with the magnetization of the reference layer (M1). Subsequently, the electrons tunnels through the insulator into the free layer. If the spin-polarization direction of the electrons is not aligned with the magnetization of the free layer (M1), the spins will start to precess around the magnetization of the free layer and dephase. Here, due to the strong exchange field from the ferromagnet, the spins will start to precess around the magnetization. The electrons from different electronic states precess incoherently, causing the transverse component of spin-angular momentum to be lost. Due to the conservation of angular momentum, the lost angular momentum is transferred to the magnetization of the ferromagnet causing it to move away from its equilibrium position. As a change of angular momentum with respect to time is the definition of a torque, $\vec{\tau} \equiv \frac{d\vec{L}}{dt}$, this effect, where the conduction electrons exert a torque on the magnetization of a magnetic layer, is called a spin-transfer torque (indicated by the yellow arrow in Fig. 1.4). If a large enough charge current is passed through the stack, and the torque exerted on the magnetization overcomes the magnetic anisotropy energy, the spin-current causes the magnetization of the free layer to align with the magnetization of the reference layer. By controlling the spin-polarization direction of the spin-current, the magnetization direction of the free layer can thus be switched at will.

As the magnetization direction can be controlled electrically, rather than relying on an external magnetic field, it allows for higher density, faster and more energy efficient writing and reading compared to HDDs. In addition, while currently used SRAM and DRAM lose their information when no power is supplied (volatile memory), this type of MRAM is considered non-volatile as it retains its information even when the power is lost. Lastly, by fabricating a matrix of multiple MTJs as illustrated in Fig. 1.5, high-density memory chips can be made. By selecting the correct contacts, each bit of information is easily accessible without any moving parts. The fabrication of MRAM with magnetic materials possessing in-plane magnetic

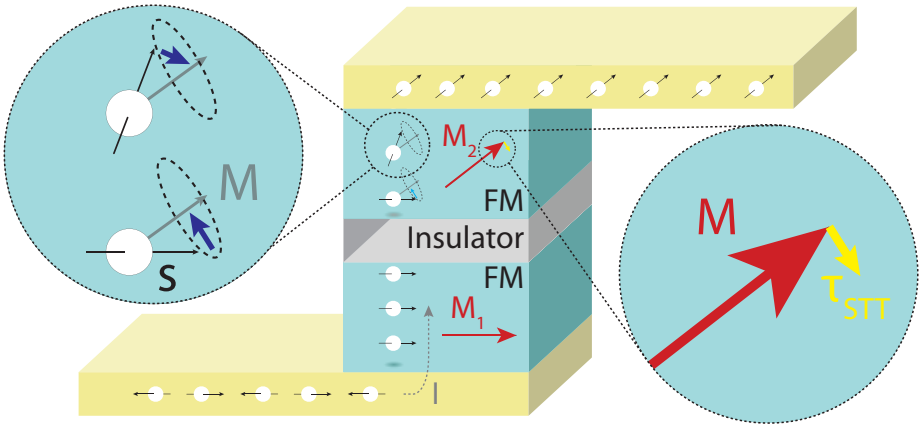


Figure 1.4: A schematic of the spin transfer torque (STT) in a device consisting of two ferromagnetic (FM) layers spaced by an insulator. A charge current is applied through the stack causing the electrons to move from bottom to top. In the first FM layer, the reference layer, the charge current is spin-filtered and all spins are aligned with the magnetization (red arrow) of this first FM layer. Subsequently, the spins tunnel through the insulating layer into the other free ferromagnetic layer. As the entering spins are not aligned with the magnetization of the free layer (red arrow), they will start to precess around the effective field inside the FM, and dephase. In this process they lose their component of angular momentum transverse to the magnetization, which is transfered to the magnetization of the top FM. This results in a torque (yellow arrow) on to the magnetization, causing the magnetization to align with the spin direction.

anisotropy (materials where the magnetization preferably lies in-plane as illustrated in Fig. 1.5), such as Fe, Co, CoFe, and NiFe, has already started around 2012. At the time of writing, the first STT-MRAM chips with a storage capacity of 1 Gb are already commercially manufactured. However, the thermal stability of the magnetization of in-plane anisotropy materials becomes a problem when the lateral size of the MTJ is reduced below approximately 60 nm due to the increase of the magnetostatic field. To continue miniaturization of these memory cells, researchers now study alternatives that allow for smaller devices based on perpendicular anisotropy materials (PMA) (magnetic materials where the magnetization preferably points out of the plane).

Still, there are some drawbacks to STT-MTJs that need to be overcome to improve its performance. First, the read and write paths are the same which means that to write information into the MTJ, one needs to pass large charge currents through the tunnel barrier. This leads to accelerated aging of the tunnel barrier and decreases its energy efficieny. It highly limits the endurance of these type of memories, making them unreliable and unpractical for high-performance applications [19]. In addition, at rest, the magnetization of the magnetic layers are either parallel or anti-parallel, resulting in a zero STT [37]. The switching of STT-memory therefore needs thermal activation which limit switching speed to $\approx$ 1 ns and induces a broad switching time distribution [38]. For these reasons, there has been a lot of focus of research on alternatives to STT. One of the alternatives uses another spintronic effect called the spin-orbit torque, which has the potential to decrease the

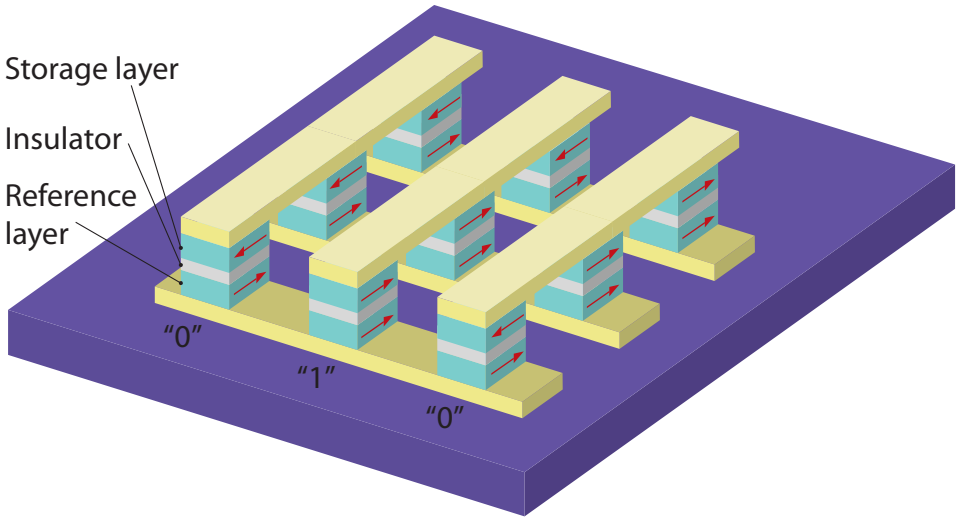


Figure 1.5: A schematic of a MRAM chip based on the spin-transfer torque (STT). Similarly, to the core memory depicted in Fig. 1.1, the chip consists of a matrix of bits, where each bit is now an MTJ rather than a donut shaped magnet. Also here, each stack can be addressed by selecting the corresponding contacts.

switching speeds to sub-ns levels and while exhibiting higher endurance [39].

### 1.2.2. Spin-orbit torques

Very recently, research has focused on controlling the magnetization of a ferromagnet using a heavy-metal (HM) material as spin source rather than a ferromagnetic layer [40]. This effect is known as the spin-orbit torque (SOT) as the charge current that exerts the torque on the magnetization of the magnet is spin-polarized due to the spin-orbit coupling in the HM material. In Fig. 1.6 one can see an MTJ-based memory on using SOTs. An additional heavy-metal layer is introduced under the MTJ which allows to separate the read and write paths for the MTJ. Reading the state of the MTJ is done in the same way as with the STT-MTJ, by measuring the resistance through the MTJ as illustrated in Fig. 1.6(b). For writing, on the other hand, a charge current is applied through the heavy metal layer. Here, due to charge-to-spin conversion effects from the strong spin-orbit interaction of the heavy metal, the charge current can become spin-polarized or give rise to a spin-accumulation at the HM/FM interface. Similar as with the STT, this spin current or spin accumulation can in turn interact with the magnetization of the ferromagnet and exert a torque, allowing one to switch the magnetization. As the write current does not need to go through the tunnel barrier, a smaller switching current is needed, making the device more energy efficient and durable.

Before SOTs can be used to its full potential, a better understanding of the exact mechanisms involved in creating these current induced spin-orbit torques is needed. This thesis presents work on the SOT generation in HM/FM bilayers to better un-

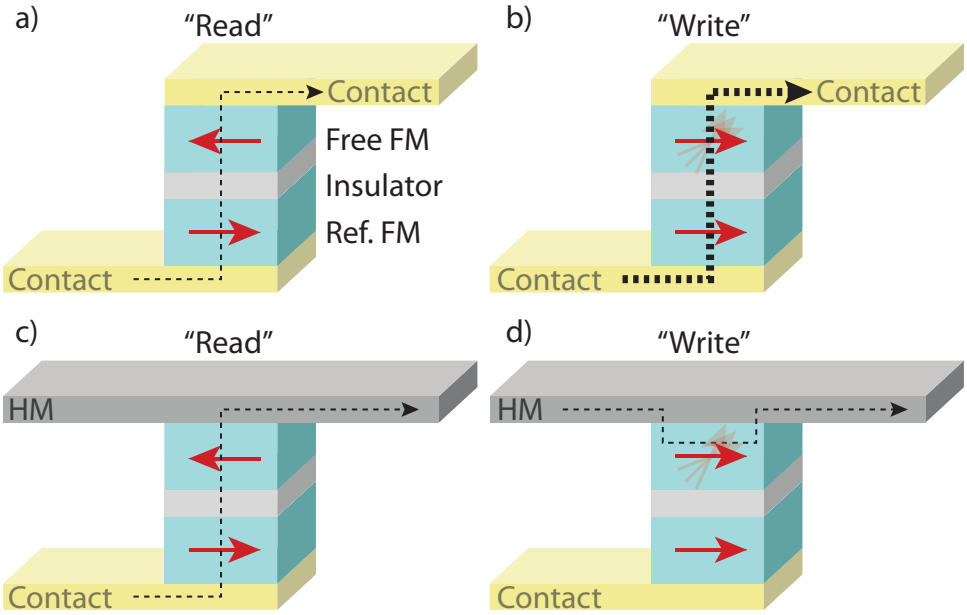


Figure 1.6: A schematic depicting a comparison between the "read" and "write" processes in MTJs used for STTs, (a) and (b), and SOTs, (c) and (d). (a) For STT-MTJs, the MTJ is "read" by passing a small current (black dashed arrow) through the stack. The parallel and anti-parallel configurations of the magnetizations (red arrows) can be distinguished by measuring the resistance through the stack due to the TMR. (b) To write the bit and change the state from anti-parallel to a parallel configuration, a larger charge current is passed through the stack. The charge current is first spin-polarized in the bottom FM layer, then tunnels through the insulator, and exerts a torque on the magnetization of the top FM layer, causing the magnetization of the top layer to switch, resulting in a parallel configuration. (c) For the MTJ based on SOTs, one of the normal contacts is replaced by a heavy metal (HM) material. The state of the MTJ is still read by passing a small charge current through the stack, similar to the STT-MTJ. d) The writing process is different however. Now, a charge current is passed through the HM layer where, due to to the large SOC of the HM material, the charge current is converted into a spin-current or spin-polarization, which in turn exerts a torque on the free FM layer. By changing the current direction, the magnetization direction of the free layer can be controlled at will. As the charge current does not need to pass through the insulating layer, a smaller charge current is needed for switching, increasing the energy efficiency and durability of the MTJ.

derstand the origins of the SOTs. In Chapter 5, thickness dependent measurements of the HM layer are performed to distinguish the strength of interfacial effects from those of bulk effects in these HM/FM bilayers. In addition, Chapter 6 shows that the observed SOTs do not necessarily originate from the HM layer, as sizable SOTs can also be observed in single layer FM devices.

Fabricating an efficient MTJ needs careful consideration of the anisotropy strength of the magnetic layer. It is a balancing act between strong enough anisotropy to have stable memory cells, and low enough anisotropy to still allow switching of the free layer. Furthermore, for high density MRAM memory, magnetic layers with PMA are necessary, as the thermal stability of the magnetization of in-plane anisotropy mate-

rials becomes a problem when the lateral size of the MTJ is reduced below approximately 60 nm due to the increase of the magneto-static field. To effectively switch PMA magnetic layers, specific torques, called out-of-plane damping-like torques, are needed. Unfortunately, the most well known charge-to-spin conversion effects in the most well known materials do not produce these type of torques. Therefore, focus has shifted to other type of charge-to-spin conversion effects and other materials to understand better, how the out-of-plane damping-like torque can be produced strongly and reliably. One of these materials are the so-called two-dimensional van der Waals materials which will be discussed in the next section.

## 1.3. The promise of two-dimensional van der Waals materials

The type of materials referred to as two-dimensional (2D) van der Waals materials are a special group of materials where the bulk is made up of stacked sheets of atomically thin layers. The layers are only weakly held together by van der Waals forces, hence the name, while the atoms in one layer are strongly bond by covalent bonds. This allows us to readily study these materials down to the ultimate thickness of only one atom by simply thinning down the bulk crystal using, for instance, the famous scotch tape method [41]. The platform of 2D van der Waals materials offers a huge library of different materials with a vast variety of diverse properties, such as spin-orbit coupling strengths, crystal symmetries, electrical, magnetic, mechanical, and optical properties [42]. Due to this diverse list, 2D van der Waals materials are considered as potential building blocks for a wide range of different applications, including spintronics. In this regard, particularly the 2D van der Waals material graphene has received much attention due to its long spin diffusion length of several micrometers at room temperature and extremely high carrier mobility, lending itself ideal as spin-transport material [43]. On the other hand, the family of 2D van der Waals materials called "transition-metal dichalcogenides" (TMDs) and topological insulators possess strong spin-orbit coupling, allowing for electrical manipulation and generation of spin [44]. In addition, the recent discovery of 2D magnets brings the capability of spin-filtering and non-volatile memory storage [45].

Lastly, the semiconducting TMDs possess a layer dependent band gap with strong spin-photon coupling that enables the generation of spin by optical methods. The band structure of the most popular monolayer TMDs have a direct band gap at the K and K' valley, discussed in Chapter 2. Using circularly polarized light, we can selectively excite one of the two valleys, as the valley can be considered a pseudo-spin [46]. If the inversion symmetry of the TMD is broken, these valleys are spin-split due to the large SOC of the transition metal, coupling the valley degree of freedom to the spin degree of freedom. This effect is often referred to as spin-valley coupling and allows one to excite not only a specific valley, but also a specific spin. This opens up a new field of *opto*-spintronics, where apart from electronics and magnetism, also light is considered as an additional knob to obtain full control of the electron spin.

While these individual 2D materials possess compelling properties for spintronic research, a combination of the different functionalities is mostly necessary for spintronic applications. With their atomically flat surfaces, the 2D materials allow for

pristine interfaces when stacking them together in so called heterostructures [47, 48] Due to their close proximity, resulting in a strong orbital overlap between the materials, the 2D materials can inherent properties from their neighboring 2D materials, referred to as the proximity effect. This causes a synergistic effect as the properties of the entire stack becomes a combination of the best of both materials. As example, the strong spin-orbit coupling from TMDs can be induced in the graphene by stacking them together, allowing for the manipulation of spin in graphene [49–52]. Similarly, stacking graphene on a 2D magnet causes the graphene itself to become magnetic [53, 54]. Lastly, a heterostructure of graphene and a monolayer TMD allows for optical generation of spins in the TMD using circularly polarized light which can subsequently be transported through the graphene channel for several micrometers [55, 56].

Apart from simply creating heterostructures of different 2D materials, there is another degree of freedom upon stacking of these materials which has huge consequences for the resulting properties of the stack. The concept of creating heterostructures of different 2D materials is often explained with the analogy of stacking lego blocks. However, while lego blocks need to be stacked together in predefined ways, such that the pieces line up properly, this is not the case for 2D materials. For stacking 2D materials, there is another degree of freedom, namely twisting. In 2018 it was experimentally shown for the first time that graphene becomes superconductive when it is stacked on to itself with a relatively aligned at the very specific "magic-angle" of 1.1° [57]. Since this astounding discovery, the importance of the relative alignment of 2D materials upon stacking has been recognized and research on the different physical phenomena arising while twisting has boomed, starting the field of *twisttronics*. As example, by changing the charge carrier density in "magic-angle" twisted bilayer graphene devices, it was found that in between the superconductive regimes, there are insulating and semimetallic phases [58]. Also the strength of the induced SOC in graphene due to its proximity to neighboring heavy metal materials, such as TMDs, turns out to be heavily dependent on the relative twist angle between the two layers [59, 60]. Not only for graphene, but also other 2D van der Waals materials have been shown to exhibit twist-dependent properties. The interlayer and intralayer excitonic properites of TMDs, for instance, are heavily dependent on the relative twist angle [61–63].

With all these different 2D materials with different properties to choose from, and all these different parameters to control at hand, such as layer thickness, stacking sequence, twist angle, etc., the possibilities to study fundamental physics in these materials is endless. With the start of this field only in 2004, there still remains a lot to be explored today.

In this thesis, 2D van der Waals materials are used to study the SOTs in TMD/ferromagnet bilayers. To elucidate to which extend interfacial and bulk effect in these bilayers contribute, we perform TMD thickness dependent SOT measurements. Here, 2D van der Waals materials are key, as they allow us to fabricate devices with very well defined crystal thicknesses, up to the monolayer limit. In addition, the atomically flat interfaces and high quality crystals of 2D van der Waals materials allow for pristine interfaces, which reduced the effects of contaminants

at the TMD/ferromagnet interface on the SOTs. Lastly, we take advantage of the unique optoelectronic properties of TMDs to study the dependence of the optoelectronic reponse on the polarization of the light and the crystallographic phase of the TMD.

## 1.4. This thesis

As described before, increasing our understanding of the generation of SOTs allows us to increase energy efficiency, speed, and reduce the dimensions of computer memory. Furthermore, using the spin-dependent optical properties of TMDs will allow for integration of optics with future spintronic devices. This dissertation presents results on SOTs in HM/FM bilayers using 2D van der Waals materials to get a better understanding of the underlying mechanisms involved. In addition, work is presented on the optoelectronic properties of $MoSe_2$, showing the effect of Schottky barriers on the helicity dependent response allowing for a better understanding of spin-current generation using circularly polarized light.

This thesis is organized as follows:

- **Chapter 2** presents a theoretical discussion on the different materials and spintronic effects needed to understand this dissertation. First, the family of materials playing a central role in this thesis, the transition metal dichalcogenides, and their variety of crystal structures and corresponding electrical and optical properties are discussed. Next, the magnetic interactions and resulting dynamics are described needed to understand the different types of spin-orbit torques. Then, the different charge-to-spin conversion effects stemming from the large spin-orbit coupling and other microscopic mechanisms involved in the generation of the spin-orbit torques are discussed. Lastly, the optical properties of TMDs and the most relevant effects in photocurrent measurements (e.g. the photoconductive, photothermal, circular photogalvanic, and spin galvanic effect) are touched upon.

- **Chapter 3** presents a description of the experimental methods used to fabricate the devices used in this thesis. Furthermore, the electrical and optical setups used to perform the experiments presented in the other chapters are carefully described.

- **Chapter 4** presents a literature review of the current spin-orbit torques research in TMD/permalloy heterostructures. In order to shed light on the differences and similarities among the works in literature, in this literature review we compare the results for various TMD/ferromagnetic devices. We highlight the experimental techniques used to fabricate the devices and quantify the SOTs, and discusses the ascribed mechanisms underlying the observed SOTs. This enables us to both identify the impact of particular fabrication steps on the observed SOTs, and give suggestions for their underlying microscopic mechanisms

- **Chapter 5** presents our experimental results on SOTs and magnetic anisotropy in $WSe_2$/permalloy heterostructures. In this chapter, we perform thickness de-

pendent SOT measurements to elucidate the contribution from interfacial and bulk effects on the observed SOT. We find a strong field-like torque compared to the damping-like torque in our $WSe_2$/permalloy bilayers, with no clear thickness dependence. This experimental work indicates that the dominant field-like torque in our devices arises from interfacial effects, which is inline with previous theoretical predictions. Furthermore, we observe a strong induce uniaxial magnetic anisotropy in the planar Hall measurements, which is aligned to a specific crystallographic direction of the underlying $WSe_2$. This serves as another indication that the polymer-free fabrication method used in our devices facilitates a strong interaction between the $WSe_2$ and permalloy layer.

- **Chapter 6** presents experimental results on the role of self-torques in MOCVD $MoS_2$/permalloy bilayers. We show that the torques measured in a single-layer permalloy device has a significant magnitude compared to the torques measured in our MOCVD grown $MoS_2$/permalloy bilayers. This indicates that the self-torque of the ferromagnetic layer can play a dominant role in SOT measurements on TMD/ferromagnet bilayers. Previous contrasting reports on the spin-orbit torques observed in similar TMD/ferromagnet bilayers can thus be ascribed to differences in the material quality or deposition method of the ferromagnetic layer.

- **Chapter 7** presents experimental results on photocurrents in a locally phase-transformed n-type 2H-1T $MoTe_2$ photodetector. We perform scanning photocurrent measurements to spatially resolve the areas involved in the photocurrent generation and find that the photocurrent originates from the 2H-1T' junction rather than from the Ti/Au electrodes. This observation, together with the non-linear IV-curve, indicates that the underlying mechanisms for the photocurrent is the photovoltaic effect due to a local electric field between the 1T and 2H-$MoTe_2$ region. Subsequently, we compare the optoelectronic performance of a device with and without a phase-changed region, and find that the 2H-1T $MoTe_2$ device exhibits a fast optoelectronic response over a wavelength range of 700 nm to 1100 nm, with a rise and fall time of 113 µs and 110 µs, two order of magnitude faster compared to a directly contacted 2H-$MoTe_2$ device.

- **Chapter 8** presents experimental results on polarization-dependent photocurrents in $MoSe_2$. In this chapter, we show the effect of Schottky contacts on the polarization-dependent photocurrents by characterizing the helicity-dependent photoresponse of a monolayer $MoSe_2$ photodiode with, and without, hBN tunnel barriers at the contacts. From out comparison, we find that the device with Schottky barrier contacts has additional contributions to the polarization-dependent photocurrents. In addition, the polarization-dependent photocurrents is observed at normal incidence, which by symmetry should not be allowed. The non-trivial modulation of the polarization-dependent photocurrents for devices with Schottky barrier contacts indicates

that spatially resolved experiments should be used in combination with angle-resolved measurements to obtain a complete microscopic understanding of the helicity-dependent optoelectronic response of 2D-TMD devices.

- **Chapter 9** presents an outlook. This chapter summarizes the main conclusions drawn in the earlier chapters. In addition, it identifies some of the pertinent open questions in the field and provides suggestions for experiments that would be useful to carry out in the near future.

# Bibliography


[1] J. Bardeen and W. Brattain, "The Transistor, A Semiconductor Triode", Proceedings of the IEEE **86**, 29–30 (1998).

[2] S. R. Corporation, *Decadal Plan for Semiconductors Decadal Plan Executive Committee*, tech. rep. (2022), pp. 1–20.

[3] N. Jones, "How to stop data centres from gobbling up the world's electricity", Nature **561**, 163–166 (2018).

[4] A. Andrae and T. Edler, "On Global Electricity Usage of Communication Technology: Trends to 2030", Challenges **6**, 117–157 (2015).

[5] J. J. P. Eckert and J. W. Mauchly, *Electronic numerical integrator and computer*, 1964.

[6] H. D. Huskey, "ENIAC", in *Encyclopedia of computer science* (John Wiley and Sons Ltd., 2003), pp. 649–651.

[7] M. H. Weik, "The ENIAC Story", Ordnance **45**, 571–575 (1961).

[8] J. Kilby, "Invention of the integrated circuit", IEEE Transactions on Electron Devices **23**, 648–654 (1976).

[9] P. Ball, "Computer engineering: Feeling the heat", Nature **492**, 174–176 (2012).

[10] G. E. Moore, "Cramming more components onto integrated circuits", IEEE Solid-State Circuits Society Newsletter **11**, 33–35 (2006).

[11] F. Faggin, M. Hoff, S. Mazor, and M. Shima, "The history of the 4004", IEEE Micro **16**, 10–20 (1996).

[12] S. Shankland, *M1 Ultra: Apple Just Unveiled Its Most Powerful Mac Chip Yet*, 2022.

[13] IRDS, "International Roadmap for Devices and Systems 2017 Edition More Moore", IEEE Advancing Technology for Humanity, 1–36 (2016).

[14] S. Moore, "There are better ways to measure progress than the old Moore's law metric", IEEE Spectrum **43**, 01–01 (2006).

[15] K. Y. Kamal, "The Silicon Age: Trends in Semiconductor Devices Industry", Journal of Engineering Science and Technology Review **15**, 110–115 (2022).

[16] R. Dennard, F. Gaensslen, H.-N. Yu, V. Rideout, E. Bassous, and A. LeBlanc, "Design of ion-implanted MOSFET's with very small physical dimensions", IEEE Journal of Solid-State Circuits **9**, 256–268 (1974).

[17] M. Bohr, "A 30 Year Retrospective on Dennard's MOSFET Scaling Paper", IEEE Solid-State Circuits Newsletter **12**, 11–13 (2007).

[18] B. Dieny, I. L. Prejbeanu, K. Garello, P. Gambardella, P. Freitas, R. Lehndorff, W. Raberg, U. Ebels, S. O. Demokritov, J. Akerman, A. Deac, P. Pirro, C. Adelmann, A. Anane, A. V. Chumak, A. Hirohata, S. Mangin, S. O. Valenzuela, M. C. Onbal, M. D'Aquino, G. Prenat, G. Finocchio, L. Lopez-Diaz, R. Chantrell, O. Chubykalo-Fesenko, and P. Bortolotti, "Opportunities and challenges for spintronics in the microelectronics industry", Nature Electronics **3**, 446–459 (2020).

[19] Q. Shao, P. Li, L. Liu, H. Yang, S. Fukami, A. Razavi, H. Wu, K. Wang, F. Freimuth, Y. Mokrousov, M. D. Stiles, S. Emori, A. Hoffmann, J. Akerman, K. Roy, J.-P. Wang, S.-H. Yang, K. Garello, and W. Zhang, "Roadmap of SpinOrbit Torques", IEEE Transactions on Magnetics **57**, 1–39 (2021).

[20] A. D. Kent and D. C. Worledge, "A new spin on magnetic memories", Nature Nanotechnology **10**, 187–191 (2015).

[21] JEDEC, *DDR2 SDRAM SPECIFICATION*, tech. rep. January (2005), pp. 1–104.

[22] C. Chappert, A. Fert, and F. N. Van Dau, "The emergence of spin electronics in data storage", Nature Materials **6**, 813–823 (2007).

[23] J. Fabian, A. Matos-Abiague, C. Ertler, P. Stano, and I. uti, "Semiconductor spintronics", Acta Physica Slovaca. Reviews and Tutorials **57**, 1–343 (2007).

[24] M. N. Baibich, J. M. Broto, A. Fert, F. N. Van Dau, F. Petroff, P. Etienne, G. Creuzet, A. Friederich, and J. Chazelas, "Giant Magnetoresistance of (001)Fe/(001)Cr Magnetic Superlattices", Physical Review Letters **61**, 2472–2475 (1988).

[25] G. Binasch, P. Grünberg, F. Saurenbach, and W. Zinn, "Enhanced magnetoresistance in layered magnetic structures with antiferromagnetic interlayer exchange", Physical Review B **39**, 4828–4830 (1989).

[26] W. Thomson, "XIX. On the electro-dynamic qualities of metals:Effects of magnetization on the electric conductivity of nickel and of iron", Proceedings of the Royal Society of London **8**, 546–550 (1857).

[27] M. Julliere, "Tunneling between ferromagnetic films", Physics Letters A **54**, 225–226 (1975).

[28] S. S. P. Parkin, C. Kaiser, A. Panchula, P. M. Rice, B. Hughes, M. Samant, and S.-H. Yang, "Giant tunnelling magnetoresistance at room temperature with MgO (100) tunnel barriers", Nature Materials **3**, 862–867 (2004).

[29] S. Yuasa, T. Nagahama, A. Fukushima, Y. Suzuki, and K. Ando, "Giant room-temperature magnetoresistance in single-crystal Fe/MgO/Fe magnetic tunnel junctions", Nature Materials **3**, 868–871 (2004).

[30] S. Bhatti, R. Sbiaa, A. Hirohata, H. Ohno, S. Fukami, and S. Piramanayagam, "Spintronics based random access memory: a review", Materials Today **20**, 530–548 (2017).

[31] E. B. Myers, D. C. Ralph, J. A. Katine, R. N. Louie, and R. A. Buhrman, "Current-Induced Switching of Domains in Magnetic Multilayer Devices", Science **285**, 867–870 (1999).

[32] L. Berger, "Low-field magnetoresistance and domain drag in ferromagnets", Journal of Applied Physics **49**, 2156–2161 (1978).

[33] L. Berger, "Domain drag effect in the presence of variable magnetic field or variable transport current", Journal of Applied Physics **50**, 2137–2139 (1979).

[34] D. Ralph and M. Stiles, "Spin transfer torques", Journal of Magnetism and Magnetic Materials **320**, 1190–1216 (2008).

[35] J. Slonczewski, "Current-driven excitation of magnetic multilayers", Journal of Magnetism and Magnetic Materials **159**, L1–L7 (1996).

[36] L. Berger, "Emission of spin waves by a magnetic multilayer traversed by a current", Physical Review B **54**, 9353–9358 (1996).

[37] K. Garello, C. O. Avci, I. M. Miron, M. Baumgartner, A. Ghosh, S. Auffret, O. Boulle, G. Gaudin, and P. Gambardella, "Ultrafast magnetization switching by spin-orbit torques", Applied Physics Letters **105**, 212402 (2014).

[38] T. Devolder, C. Chappert, J. A. Katine, M. J. Carey, and K. Ito, "Distribution of the magnetization reversal duration in subnanosecond spin-transfer switching", Physical Review B **75**, 064402 (2007).

[39] V. Krizakova, M. Perumkunnil, S. Couet, P. Gambardella, and K. Garello, "Spin-orbit torque switching of magnetic tunnel junctions for memory applications", Journal of Magnetism and Magnetic Materials **562**, 169692 (2022).

[40] P. Gambardella and I. M. Miron, "Current-induced spinorbit torques", Philosophical Transactions of the Royal Society A: Mathematical, Physical and Engineering Sciences **369**, 3175–3197 (2011).

[41] K. S. Novoselov, D. Jiang, F. Schedin, T. J. Booth, V. V. Khotkevich, S. V. Morozov, and A. K. Geim, "Two-dimensional atomic crystals", Proceedings of the National Academy of Sciences **102**, 10451–10453 (2005).

[42] K. S. Novoselov, "Nobel Lecture: Graphene: Materials in the Flatland", Reviews of Modern Physics **83**, 837–849 (2011).

[43] S. Roche, J. Åkerman, B. Beschoten, J.-C. Charlier, M. Chshiev, S. Prasad Dash, B. Dlubak, J. Fabian, A. Fert, M. Guimarães, F. Guinea, I. Grigorieva, C. Schönenberger, P. Seneor, C. Stampfer, S. O. Valenzuela, X. Waintal, and B. van Wees, "Graphene spintronics: the European Flagship perspective", 2D Materials **2**, 030202 (2015).

[44] A. Avsar, H. Ochoa, F. Guinea, B. Özyilmaz, B. J. van Wees, and I. J. Vera-Marun, "Colloquium: Spintronics in graphene and other two-dimensional materials", Reviews of Modern Physics **92**, 021003 (2020).

[45] M. Gibertini, M. Koperski, A. F. Morpurgo, and K. S. Novoselov, "Magnetic 2D materials and heterostructures", Nature Nanotechnology **14**, 408–419 (2019).

[46] X. Xu, W. Yao, D. Xiao, and T. F. Heinz, "Spin and pseudospins in layered transition metal dichalcogenides", Nature Physics **10**, 343–350 (2014).

[47] A. K. Geim and I. V. Grigorieva, "Van der Waals heterostructures", Nature **499**, 419–425 (2013).

[48] Y. Liu, N. O. Weiss, X. Duan, H.-C. Cheng, Y. Huang, and X. Duan, "Van der Waals heterostructures and devices", Nature Reviews Materials **1**, 16042 (2016).

[49] A. Avsar, J. Y. Tan, T. Taychatanapat, J. Balakrishnan, G. Koon, Y. Yeo, J. Lahiri, A. Carvalho, A. S. Rodin, E. O'Farrell, G. Eda, A. H. Castro Neto, and B. Özyilmaz, "Spinorbit proximity effect in graphene", Nature Communications **5**, 4875 (2014).

[50] T. S. Ghiasi, J. Ingla-Aynés, A. A. Kaverzin, and B. J. van Wees, "Large Proximity-Induced Spin Lifetime Anisotropy in Transition-Metal Dichalcogenide/Graphene Heterostructures", Nano Letters **17**, 7528–7532 (2017).

[51] T. S. Ghiasi, A. A. Kaverzin, P. J. Blah, and B. J. van Wees, "Charge-to-Spin Conversion by the RashbaEdelstein Effect in Two-Dimensional van der Waals Heterostructures up to Room Temperature", Nano Letters **19**, 5959–5966 (2019).

[52] C. K. Safeer, J. Ingla-Aynés, F. Herling, J. H. Garcia, M. Vila, N. Ontoso, M. R. Calvo, S. Roche, L. E. Hueso, and F. Casanova, "Room-Temperature Spin Hall Effect in Graphene/MoS2 van der Waals Heterostructures", Nano Letters **19**, 1074–1082 (2019).

[53] B. Karpiak, A. W. Cummings, K. Zollner, M. Vila, D. Khokhriakov, A. M. Hoque, A. Dankert, P. Svedlindh, J. Fabian, S. Roche, and S. P. Dash, "Magnetic proximity in a van der Waals heterostructure of magnetic insulator and graphene", 2D Materials **7**, 015026 (2020).

[54] T. S. Ghiasi, A. A. Kaverzin, A. H. Dismukes, D. K. de Wal, X. Roy, and B. J. van Wees, "Electrical and thermal generation of spin currents by magnetic bilayer graphene", Nature Nanotechnology **16**, 788–794 (2021).

[55] Y. K. Luo, J. Xu, T. Zhu, G. Wu, E. J. McCormick, W. Zhan, M. R. Neupane, and R. K. Kawakami, "Opto-Valleytronic Spin Injection in Monolayer MoS2/Few-Layer Graphene Hybrid Spin Valves", Nano Letters **17**, 3877–3883 (2017).

[56] A. Avsar, D. Unuchek, J. Liu, O. L. Sanchez, K. Watanabe, T. Taniguchi, B. Özyilmaz, and A. Kis, "Optospintronics in Graphene via Proximity Coupling", ACS Nano **11**, 11678–11686 (2017).

[57] Y. Cao, V. Fatemi, S. Fang, K. Watanabe, T. Taniguchi, E. Kaxiras, and P. Jarillo-Herrero, "Unconventional superconductivity in magic-angle graphene superlattices", Nature **556**, 43–50 (2018).

[58] X. Lu, P. Stepanov, W. Yang, M. Xie, M. A. Aamir, I. Das, C. Urgell, K. Watanabe, T. Taniguchi, G. Zhang, A. Bachtold, A. H. MacDonald, and D. K. Efetov, "Superconductors, orbital magnets and correlated states in magic-angle bilayer graphene", Nature **574**, 653–657 (2019).

[59] Y. Li and M. Koshino, "Twist-angle dependence of the proximity spin-orbit coupling in graphene on transition-metal dichalcogenides", Physical Review B **99**, 075438 (2019).

[60] T. Naimer, K. Zollner, M. Gmitra, and J. Fabian, "Twist-angle dependent proximity induced spin-orbit coupling in graphene/transition metal dichalcogenide heterostructures", Physical Review B **104**, 195156 (2021).

[61] F. He, Y. Zhou, Z. Ye, S.-H. Cho, J. Jeong, X. Meng, and Y. Wang, "Moiré Patterns in 2D Materials: A Review", ACS Nano **15**, 5944–5958 (2021).

[62] K. Tran, J. Choi, and A. Singh, "Moiré and beyond in transition metal dichalcogenide twisted bilayers", 2D Materials **8**, 022002 (2021).

[63] A. Ciarrocchi, F. Tagarelli, A. Avsar, and A. Kis, "Excitonic devices with van der Waals heterostructures: valleytronics meets twistronics", Nature Reviews Materials **7**, 449–464 (2022).

# chapter 2

## Theoretical background

*In this chapter, the theoretical background required to appreciate and understand the experimental work presented in the upcoming chapter is described. We will touch upon a broad range of topics, as the experimental work presented in this thesis ranges from electrical detection of spin-orbit torques to photocurrents in two-dimensional materials. A central role is played by the family of two-dimensional materials called transition metal dichalcogenides, which is therefore discussed first. The available crystal phases, and the corresponding electrical and optical properties are described, together with the methods used to transform the crystal phase. Next, the mathematical description of the magnetization dynamics are presented. Subsequently, the mechanisms involved in the generation of spin-orbit torques are discussed, which entail the charge-to-spin conversion effects, such as the spin-Hall effect, Rashba-Edelstein effect, and other interfacial effect, such as spin-orbit filtering and spin-orbit precession. The chapter ends with a discussion on the photocurrents in two-dimensional materials, introducing the photoconductive, photothermal and photogalvanic effects.*

## 2.1. Transistion metal dichalcogenides

In this thesis, one family of materials plays a central role: the so-called transition metal dichalcogenides, or TMDs in short. They belong to a larger group of materials, called the two-dimensional (2D) van der Waals materials. For van der Waals materials, the bulk crystal is made up of atomically thin layers, which are bonded weakly by van der Waals forces, while the atoms within each layer are bonded covalently (also mentioned in Chapter 1). Other examples van der Waals materials are graphene, hexagonal boron nitride (hBN), black phosphorus, and many more. In this section, we will briefly touch upon the different crystal structures, or crystal phases, the TMD can reside in, and describe how the different crystal phases affect the electrical and optical properties (relevant for Chapter 7). Next, we will discuss the field of phase-engineering, where one seeks for methods to transform the phase of the TMD on demand, to take advantage of the different properties of each phase. Lastly, the remarkable optical properties of TMDs, allowing optics to be incorporated with spintronics, are discussed (relevant for Chapter 8). But first, a short introduction on TMDs is presented below.

TMDs have a long history with the structure of $MoS_2$ already determined in 1923 by Linus Pauling [1], ultrathin $MoS_2$ layers produced using adhesive tapes in 1963 [2], and single-layer $MoS_2$ already obtained in 1986 by Joensen et al. [3] using lithium intercalation with n-butyllithium. The rapid growth of graphene-related research in 2004 also stimulated the further characterization of other 2D materials such as TMDs. Due to its higher mobility, graphene took the center of attention for the first few years. But in 2009, with the theoretical prediction of a direct band gap of monolayer $MoS_2$, TMD related research started to boom [4].

At the time of writing, TMDs are one of the most famous and extensively studied family of 2D van der Waals materials. A single layer of TMD is 3 atoms thick, where the transition metal atom (M) is sandwiched between two planes of chalcogen atoms (X) in a X-M-X fashion [5]. With the general chemical formula $MX_2$, where M is a transition metal atom (e.g. Mo, W, Nb, Zr, etc.) and X is a chalcogen atom (e.g. S, Se, Te, etc.), there is a plethora of different combinations of elements, which lead to a large diversity in electrical and optical properties. They offer insulating, semiconducting and semi-metallic properties, direct and indirect band gaps of different energies, and come in a wide range of different crystal symmetries. All these different properties open the door for an abundance of research possibilities, relating the crystal structure, symmetry, layer thickness, and elemental composition to the electrical and optical properties in these two-dimensional materials.

### 2.1.1. Crystal phases

As mentioned before, TMDs can reside in several crystal phases (1H/2H, 3R, 1T, 1T', $1T_d$, 1T", etc.) of which the hexagonal (1H/2H), rhombohedral(3R), and tetragonal (1T and 1T') phases are discussed here. Only the bulk crystals of $MoS_2$ and $WS_2$ are naturally occurring in nature as the minerals molybdenite and tungstenite. The naturally occuring $MoS_2$ resides in either of the two phases 2H-$MoS_2$ or 3R-$MoS_2$. The two phases 2H and 3R only differ in their stacking of subsequent layers, and thus have an identical structure for each individual layer. In each layer,

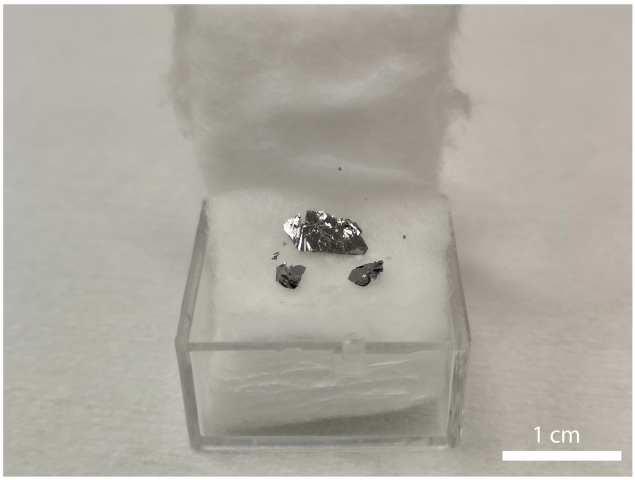


Figure 2.1: A photograph of a bulk $WSe_2$ crystal which is used for exfoliation as described in Chapter 3. The layered structure of the material is easily identified by the naked eye.

the chalcogen atoms in the top and bottom atomic plane are in the same position, corresponding to an ABA atomic stacking sequence [6]. The molybdenum atom resides at the center of a trigonal-prismatic coordination sphere and convalently bonds with six sulfur atoms, as depicted for the 2H phase in Fig. 2.2. In addition, monolayer TMDs in the H-phase have a direct band gap at the K and K' point, where the states are strongly related to the d-orbitals of the transition metal atom. When increasing the layer thickness of the TMD, it remains semiconducting but the band gap becomes indirect, causing a strong decrease in photoluminescence (PL) efficiency [7, 8].

By gliding one plane of chalcogen atoms, the 2H phase transforms into the octahedral metallic 1T-phase, shown in Fig. 2.2. In this case, the chalcogen atoms in the top and bottom layer are not aligned anymore, corresponding to an ABC stacking sequence and a octahedral coordination of the transition metal atom with the chalcogen atoms. Compared to the 2H phase (space group $P\bar{6}m2$ or $P6_3/mmc$), the 1T phase has a lower symmetry (space group $Pmn2_1$). When the 1T-TMD is interfaced with another material, the symmetry is reduced even further as the screw-axis and glide-plane symmetries are broken, leaving only a single mirror symmetry [9]. This reduced symmetry has large consequences for the type of spin-orbit torques that are allowed, as will be discussed in a later section.

Both experimental and theoretical work suggests, however, that the 1T-phase of TMDs is unstable and spontaneously distorts into another phase denoted as 1T' (also depicted in Fig. 2.2). Here, the transition metal atoms cluster in pairs resulting in transition metal zigzag chains when seen from the top. At the Γ-point, the Fermi level crosses both the Mo d- and S p-orbitals [6]. With the distorted zigzag chain structure of the 1T' phase, on the other hand, the transition metal d-orbitals are lowered below the chalcogen p-orbitals. In turn, this leads to a band inversion

resulting in a small band gap at the Γ-point.

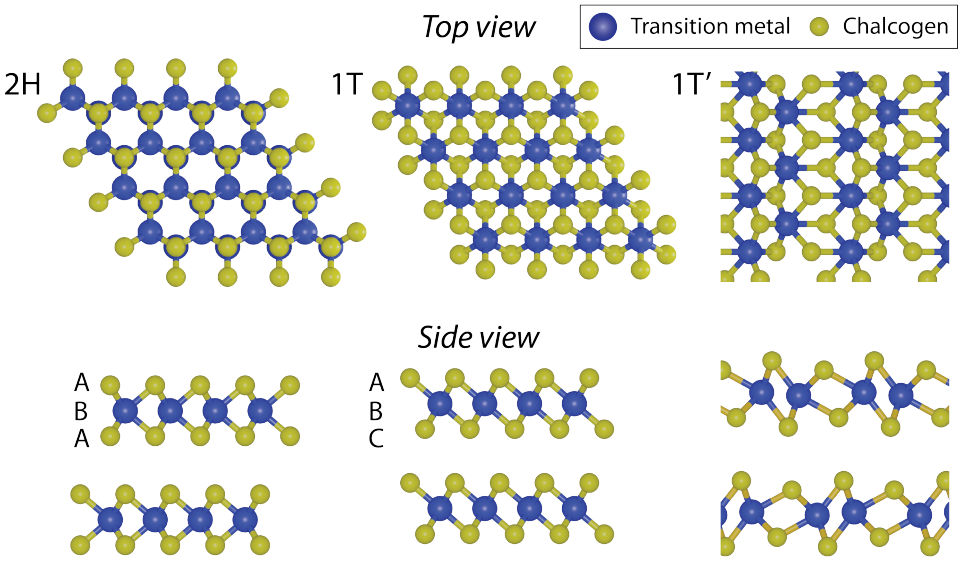


Figure 2.2: A top- and side-view of the crystal structure of the TMD residing in the hexagonal 2H, and trigonal 1T and (distorted) 1T' phase. The transition metal and chalcogen atoms are indicated by in blue and yellow, respectively.

As the structural phase of the TMD has large consequences for both the electrical and optical properties, it is important to know in which of these phases the TMD resides. Furthermore, gaining control of the phase of the TMD allows one to investigate the unique properties of each crystallographic phase and use the different electrical and optical properties to once advantage. Therefore, recent research, referred to as phase engineering, has focused on new techniques to alter the phase of different TMDs locally by inducing a phase transition, which will be the topic of the next section.

### 2.1.2. Phase transition

The different crystallographic phases have different advantages and drawbacks regarding the electrical and optical properties. Local phase engineering of the same TMD crystal allows one to use the advantages of the different phases concurrently in a single phase-change device, creating high-quality heterophase structures. Because the 2H-phase TMDs are semiconducting, contacting the TMD is problematic using direct metal contacts. The metal-semiconductor contacts result in a large Schottky barrier and a van der Waals gap, giving highly resistive contacts. By transforming the TMD to the metallic 1T-phase locally underneath the contacts, Ohmic contacts are obtained, as evidenced from a linear dependence of the drain-source current ($I_{ds}$) on the drain-source voltage ($V_{ds}$). It was shown that, in this way, the 2-probe mobility of a 2H-$WSe_2$ field-effect transistors (FETs) was improved from 2 $cm^2/(V\cdot$

s) to 67 $cm^2/(V\cdot s)$ [10]. Similar results are obtained for other TMDs such as $MoTe_2$ (1 to 50 $cm^2/(V\cdot s)$) [11] and $MoS_2$ (19 to 46 $cm^2/(V\cdot s)$ [12].

The different TMDs have to overcome different energy barriers to change its crystallographic phase from the 2H to the 1T'-phase. As example, $MoTe_2$ has one of the smallest energy barriers of 40 meV [13] , while $WSe_2$ has 270 meV [13], and $MoS_2$ has the largest of the group IV TMDs of 550 meV [14]. Therefore, multiple techniques have been investigated to perform a phase transformation. Although there is no clear consensus in literature about the exact mechanisms which drive the phase transformation, in general, the available techniques can be subdivided in to two methods: charge doping or crystal deformation.



### Charge doping

There is a myriad of techniques that allow for charge doping to initiate a phase transformation. One important method is by intercalation the TMD with alkali metals (typically lithium). As already mentioned before, n-butyllithium (n-BuLi) was used to chemically exfoliate TMDs in 1986. However, when the Li ions intercalate the TMD layers they donate electrons to the TMD, favoring the 1T-phase [15–18]. By tuning the concentration of lithium ions and immersion time, a phase transformation can occur. This technique was shown to work in exfoliated $MoS_2$ [12] and later in $WSe_2$ grown by chemical vapor deposition (CVD) [10]. For the latter case, the transformation was shown to be reversible by heating the 1T-$WSe_2$ to 180°C for 72 hours. A recent study on $MoS_2$ showed that the phase transition by Li-intercalation occurs faster with increase layer thickness, suggesting that the energetic barrier between the H-phase and the 1T-phase reduces with layer thickness [19].

Also ionic liquid gating can be used to change the phase of the TMD by means of electrostatic doping. After the first theoretical predictions [20] [21], it was soon experimentally confirmed in $MoTe_2$ [22]. Using Raman and second-harmonic generation (SHG) spectroscopy they showed that the phase of a monolayer $MoTe_2$ could reversibly be transformed from the H- to the 1T'-phase by increasing the doping level to $2.2 \times 10^{14}$ $cm^{-2}$.

Lastly, changing the doping level can also be performed by creating vacancies and defects in the TMD crystal. In 2015 it was shown that Te vacancies can be locally created in $MoTe_2$ by laser irradiation using a high intensity focused laser beam. The local Te vacancies trigger a local phase transition from 2H to 1T' in $MoTe_2$, stable up to 300°C. This technique is used in Chapter 7 to locally change the phase of a $MoTe_2$ flake allowing to study the effect of the different properties of 2H- and 1T'-$MoTe_2$ on the observed photocurrents.

### Crystal deformation

Another method to induce a phase transformation for TMDs is by crystal deformation. This can be achieved by applying high pressure onto the TMD crystal, by using for instance a high-pressure diamond anvil cell. Already in 2004, it was reported that the resistance of single crystals of $MoSe_2$ and $MoS_2$ decreases with an increasing pressure [23]. At pressures of >6.5 GPa, the TMD samples became increasingly more metallic which was attributed to the overlapping conduction and

valence bands as the interlayer spacing decreases [6]. Note that this semiconductor-to-metal transition is thus different from the a phase transition of the TMD.

While the pressure is applied in the out-of-plane direction, also strain applied in the in-plane direction (compressive or tensile) can cause a structural phase transformation due to a distortion of the transition metal sublattice, as theoretically predicted in 2014 [13]. It was experimentally shown that in $MoTe_2$ a 0.2% tensile strain causes a phase transition from 2H to 1T' at room temperature [24]. Also, strain induced by a lattice mismatch was shown to cause a phase transformation in $MoS_2$ by bonding of to an cobalt array or Au/Pd [25, 26].

The successful transformation can be identified using multiple techniques. For $MoTe_2$, $MoS_2$, and $WSe_2$ the Raman spectra of the H and 1T-phase are significantly different, which allows to monitor the phase transformation process and identify possible mixtures of different phases [10–12]. Furthermore, monolayer TMDs in a 2H-phase have a direct band gap, resulting in strong PL. The 1T-phase, on the other hand, has no band gap and therefore shows significantly weaker PL. In addition, a strong decrease in resistivity is an indication of the phase transformation, as the H-phase is semiconducting, while the 1T-phase is metallic. Lastly, SHG can be used to indicate the phase transformation. As inversion symmetry is present in the 1T'-phase (resulting in no SHG), but absent in the 2H-phase, the SHG is a sensitive probe for distinguishing between these two phases [22].

### 2.1.3. Optical properties

The direct band gap for monolayer TMDs in the 2H-phase, make them possible candidates for a plethora of optoelectronic applications, such as phototransistors, solar cells, light-emmiting diodes, etc. Current photodetectors predominantly use silicon as photosensitive material. Silicon, with its indirect band gap of 1.1 eV ($\lambda \approx 1127$ nm) and brittle structure, is not an ideal material as the indirect band gap reduces its sensitivity, light of a longer wavelength than 1127 nm is not easily detectable, and it brittle structure does not allow for incorporation into flexible electronics. TMDs, on the other hand, have a band gap that is layer dependent and direct for monolayers, strong absorption, and strong mechanical properties suited for flexible electronics. In addition, TMDs possess strong photoluminescence, fast optoelectronic response, and high power conversion efficiency making them highly promising for optoelectronics applications.

The astounding optical properties of TMDs can only be fully appreciated, however, when understanding its potential in the field of opto-spintronics. Apart from exciting charge carriers, one can excite spins in TMDs using circularly polarized light. This opens up the possibility to use TMDs in the field of opto-spintronics where light is considered as an additional knob to obtain full control of the electron spin. In this section, I will briefly discuss some of the interesting opto-spintronic properties related to spins in TMDs. For a discussion on photocurrents in 2D materials, I refer to Sec. 2.4.

The band structure of monolayer 2H-$MoSe_2$, with its direct band gap, is schematically depicted in Fig. 2.3(a). The position of the valence band maximum and conduction band minimum is located at the two non-equivalent high symmetry points

K and K', at the corners of the hexagonal Brillioun zone, and are referred to as the K- and K'-valley [27].

In monolayer 2H-TMDs, in-plane inversion symmetry is broken giving rise to interesting valley-dependent optoelectronic properties due to an opposite Berry curvature for these two valleys [28, 29]. For a system which is inversion symmetric, symmetry requires that the Berry curvature $\mathbf{\Omega}(k)$ obeys:

$$\mathbf{\Omega}(k) = \mathbf{\Omega}(-k). \tag{2.1}$$

If the system has time-reversal symmetry too, then:

$$\mathbf{\Omega}(k) = -\mathbf{\Omega}(-k). \tag{2.2}$$

From Eqs. 2.1 and 2.2, we can conclude that the Berry curvature vanishes for systems which possess both time-reversal symmetry and spatial inversion symmetry [28].

For monolayer TMDs, spatial inversion symmetry is broken allowing for a non-zero Berry curvature. As the K and K' valleys are related to each other by time reversal symmetry, the Berry curvature is opposite for both valleys [28, 29]. The Berry curvature yields an effective magnetic field with an equal magnitude but opposite sign for the K and K' valley, making the valleys non-equivalent [29]. This leads to the so-called valley-Hall effect, where the carriers in the K and K' valleys are deflected to opposite sides due to the opposite sign of the Berry curvature [30, 31].

In addition, due to the inversion symmetry breaking and remaining time-reversal symmetry, the K and K' valleys couple to light of opposite helicities (right-handed and left-handed circularly polarized light): i.e. the K and K' valley's absorb left- and right-handed circularly polarized light differently (referred to as circular dichroism) [32–34]. It is therefore possible to selectively excite carriers into one specific valley, K or K', using circularly polarized light [29, 35], as depicted with the black dashed arrow in Figs. 2.3(b) and (c).

Furthermore, TMDs possess strong spin-orbit coupling (SOC) originating from the d-orbitals of the heavy transition metal atoms [36], causing the spin degeneracy of the bands to lift, as shown in Fig. 2.3. This is experimentally observed in absorption spectra of monolayer TMDs as two distinct excitonic peaks [8, 37]. As the K and K' valleys are related by time-reversal symmetry, the spin-splitting in these valleys is opposite, which causes the valley and spin degree of freedom to be coupled (referred to as spin-valley locking) [29, 37]. In other words, by exciting one specific valley with circularly polarized light of a specific wavelength, one does not only create valley polarized carriers, but also spin polarized carriers [30]. Monolayer 2H-TMDs can thus be used as spin source using circularly polarized light. This was already shown in TMD/graphene bilayers, where the spins are excited in the TMD using circularly polarized light and are subsequently transported through the graphene and detected using ferromagnetic contacts [38, 39]. Note that the spin splitting of the conduction band is opposite for Mo-based and W-based TMDs (Figs. 2.3(b) versus (c)) [40, 41].

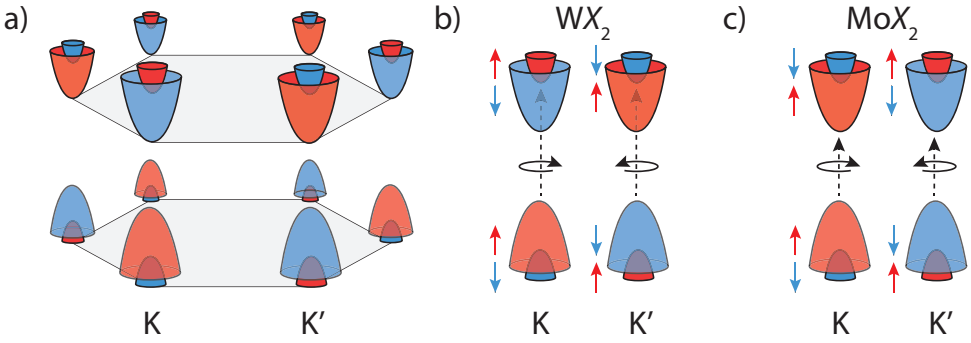


Figure 2.3: (a) A simplified schematic of the band structure of monolayer 2H-$MoSe_2$ showing K- and K'-valley at the corners of the hexagonal Brillouin zone. The spin splitting of the bands for spin up and spin down are indicated by the red and blue color, respectively. The band structure near the K and K' point for the TMDs (b) $WX_2$ and (c) $MoX_2$, where X represent a chalcogen atom. Note that the spin-splitting of the conduction band is opposite, depending on the transition metal atom.

In Chapter 8, the TMD $MoSe_2$ is excited using circularly polarized light, which allows us to study its relation with the induced photocurrent in $MoSe_2$ phototransistors.

## 2.2. Magnetic interactions and dynamics

We have seen that the optical generation of spins in TMDs allow us to incorporate light into the field of spintronics. This might provides us a way to merge the fields of photonics and spintronics in the future for new information technology applications. Light, however, is only one of the knobs that can be tuned to obtain control of the electron spin.

Another already more established knob is magnetism. The exchange interaction between the electron spin and the magnetization of magnetic materials allows us to manipulate the electron spin using magnetic materials, and vice versa, manipulate the magnetization of magnetic materials using the electron spin. As discussed in Chapter 1, the spintronic applications already on the market today, such as the MTJ, uses magnetic materials as spin-filter of electrical currents. In addition, the spin-transfer torque (STT) and spin-orbit torque (SOT) have great potential for non-volatile memory applications using magnetic materials. The research topic of Chapters 4, 5, and 6 involves the interaction of the electron spin with the magnetization of magnetic materials via SOTs. Therefore these interactions and the resulting magnetization dynamics are discussed below.

### 2.2.1. Magnet moments and angular momentum

In magnetism, the fundamental object is the magnetic dipole moment, $\vec{m}$. In classical electromagnetism, this magnetic dipole moment is equated with a simple current loop, created by a charged particle moving in a circular orbit. Here, we only consider

charged particles with a certain mass, and therefore, the orbiting charged particle also has angular momentum associated with it. This links the magnetic dipole moment to the angular momentum [42]. The intimate relation between magnetization and angular momentum was already revealed in 1915 by Barnett and, separately, by Einstein and de Haas [43] [44]. Barnett found that a rod of demagnetized material attained a magnetization when spun, which is now called the Barnett effect. On the other hand, Einstein and de Haas observed the opposite: a change in magnetization causes a free body to rotate, now referred to as the Einstein-de Haas effect.

The electrons that carry charge currents in electronic circuits also possess intrinsic angular momentum called spin. The spin angular momentum $\vec{S}$ results in a small magnetic moment $\vec{m}$ according to:

$$\vec{m} = \gamma \vec{S} \tag{2.3}$$

were $\gamma$ is a constant called the gyromagnetic ratio. If the magnetic moment is placed inside an external magnetic field B, the energy $E$ of the magnetic moment is given by:

$$E = -\vec{m} \cdot \vec{B} \tag{2.4}$$

so that the energy is minimized when the magnetic dipole moment is aligned with the magnetic field. The field exerts a torque on the magnetic dipole moment according to:

$$\vec{\tau} = -\vec{m} \times \vec{B} \tag{2.5}$$

which causes the magnetic moment to precess around the applied magnetic field.

Similarly, the magnetic dipole moment of the electron can exert a torque onto the magnetization of a ferromagnet, which by definition, involves the transfer of angular momentum ($\vec{\tau} = d\vec{L}/dt$). From a general perspective, the Hamiltonian for the electron in a crystal lattice can be described by [45]:

$$H = \frac{\hbar^2 \nabla^2}{2m_e} + V_0(\vec{r}) + \Delta(\vec{r})(\hat{m} \cdot \vec{s}) + V_{SO}(\vec{L} \cdot \vec{S}). \tag{2.6}$$

Here, the first term is the kinetic energy of the electron, and $V_0(r)$ is the crystal field potential. The third term is the exchange interaction between the electron spin ($\vec{s}$) and the magnetization $\hat{m}$ with strength $\Delta(\vec{r})$, which can be position dependent. The last term represents the SOC, where only the contribution from the atomic-like $\vec{L} \cdot \vec{s}$ is included with a strength of $V_{SO}$. In most materials this is the dominant source of SOC due to the strong E-fields from the charged nucleus and the rapid orbital motion (relative to the linear one) of the electrons [45]. At interfaces and low-symmetric materials, however, other forms of SOC may dominate, which are discussed in Sec. 2.3.3.

The degrees of freedom in Eq. 2.6 represent the different reservoirs of angular momentum, which are coupled by the different interactions, as illustrated in Fig. 2.4 [45]. Recall that for the STT, the charge current is spin-polarized in the ferromagnetic reference layer, which subsequently enters the ferromagnetic free layer. In

this layer, there is a transfer of angular momentum from the mobile carriers to the magnetization of the free layer mediated via exchange interaction. This effectively allows one to exert a torque on the free layer as discussed in Chapter 1.

In the case of SOTs, the transfer of angular momentum is more complicated. In heavy metals, the large SOC mediates angular momentum transfer between spin and orbital degrees of freedom of the electron. In addition, the crystal field potential allows for orbital angular momentum transfer between the electron and the lattice. Therefore, these SOTs can be understood as an angular momentum transfer from the lattice to the magnetic moments mediated via the electrons [46, 47], which is convenient as the crystal lattice provides a large reservoir of angular momentum that can be tapped into [48]. This transfer of angular momentum is schematically depicted in Fig. 2.4.

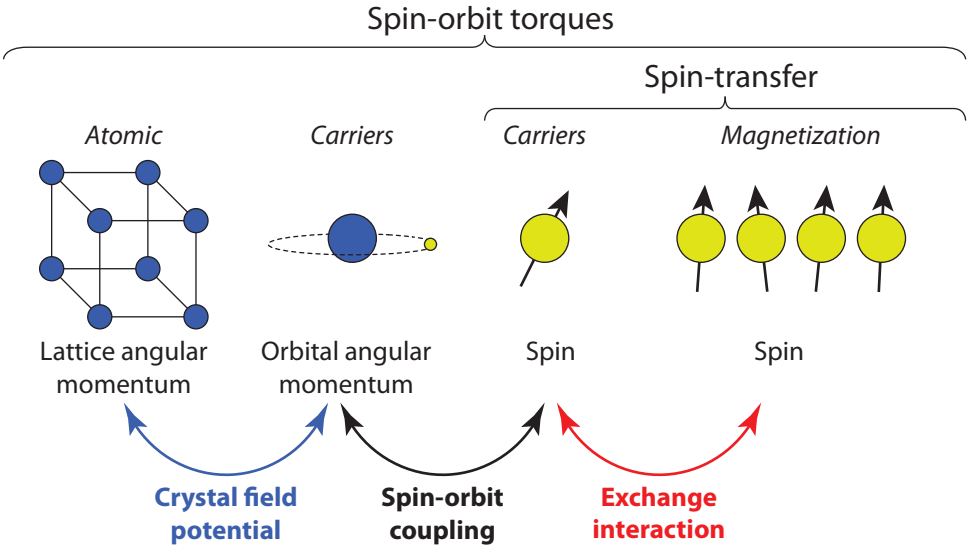


Figure 2.4: A schematic of the different reservoirs of angular momentum involved with STTs and SOTs. For the STT, there is an exchange of angular momentum between the spin angular momentum of the mobile carriers and the magnetization via the exchange interaction. For SOTs, on the other hand, the picture is more complicated, as the crystal field potential and spin-orbit coupling allow for a flow of angular momentum from the lattice to the mobile carriers, which in turn interact with the magnetization of the material via the exchange interaction.

As a side note, the opposite is also possible, where a change in magnetization causes a mechanical torque. As previously mentioned, the Einstein-de Haas effect was already observed in 1915, but more recently, it was shown that this effect is also present at the nanoscale, in literature referred to as a spin-flip transfer torque [49].

One advantage of the SOTs, is that the spins can interact multiple times with the magnetization. For the STT, the spin can only transfer one unit of angular momentum ($\hbar/2$) from the reference layer to the free layer, as the writing current is applied in the out-of-plane direction through the MTJ. In the case of SOTs, however, the writing current is applied in-plane. Now, the electron can interact multiple times

with the magnetic and heavy metal layer as it diffuses back and forth across the interface [50].

In general, one can distinguish between two types of SOTs, namely the field-like and the damping-like torque (see Sec. 2.2.3). But before we discuss the effect of these different torques on the magnetization of a magnet, first, a general discussion on magnetization dynamics is presented.



### 2.2.2. Landau-Lifshitz-Gilbert equation

The magnetization dynamics of a magnetization ($\vec{M}$) are mathematically described by the famous Landau-Lifshitz-Gilbert (LLG) equation [51–53]:

$$\frac{d\hat{m}}{dt} = -\gamma \hat{m} \times \mu_0 \vec{H}_{eff} + \alpha_G \hat{m} \times \frac{d\hat{m}}{dt} \tag{2.7}$$

where $\hat{m}$ is the magnetization unit vector ($\hat{m} = \vec{M}/\vec{M}_s$), $\vec{M}_s$ is the saturation magnetization, $\gamma$ is the gyromagnetic ratio, $H_{eff}$ is the effective magnetic field (including the external field $H_{ext}$, anisotropy field $H_{ani}$ and dipole field $H_{dip}$), $\mu_0$ is the permeability of free space, $\alpha_G$ is the Gilbert damping. The first term on the right describes the precession of the magnetization around the effective field, as depicted in Fig. 2.5(a). The second term describes the damping of the magnetization towards its equilibrium direction, illustrated in Fig. 2.5(b). This term encompasses all dissipation channels through which the magnetization can lose energy and relax to its ground state. This damping can be caused by internal and external mechanisms. An example of an internal process is Gilbert damping of the magnetization due to the SOC [54]. An example of an external process is, for instance, spin-pumping. Both terms together result in a spiraling motion of the magnetization around $H_{eff}$ until the magnetization is fully aligned with $H_{eff}$, illustrated in Fig. 2.5(c).

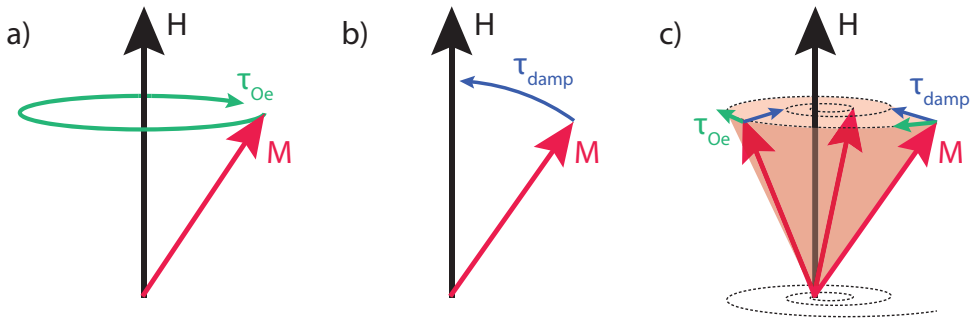


Figure 2.5: An illustration of the dynamic of the magnetization $M$ in an external magnetic field $H$. (a) Depicts the precession of the magnetization around the $H$, described by the first term on the right of Eq. 2.8. (b) Illustrated the damping of $M$ towards $H$, described by the second term on the right of Eq. 2.8. (c) illustrated the combined effect of both, resulting in a spiraling motion of the magnetization around $H$.

### 2.2.3. Spin-orbit torque driven magnetization dynamics

In 1996, Slonczewski expanded this model and added an additional term to account for the STT, now known as the Landau-Lifshitz-Gilbert-Slonczewski (LLGS) equation:

$$\frac{d\hat{m}}{dt} = -\gamma \hat{m} \times \mu_0 \vec{H}_{eff} + \alpha_G \hat{m} \times \frac{d\hat{m}}{dt} + \frac{\gamma}{M_s}\vec{\tau} \tag{2.8}$$

where $\vec{\tau}$ represent the torques exerted on the magnetization by a spin-polarized current. These torques adopt the general form of:

$$\vec{\tau} = \tau_{FL}\left(\hat{m} \times \hat{\sigma}\right) + \tau_{DL}\left(\hat{m} \times (\hat{\sigma} \times \hat{m})\right) \tag{2.9}$$

where $\tau_{FL}$ and $\tau_{DL}$ are the so-called *field-like* and *damping-like* torque, and $\hat{\sigma}$ ($\hat{\sigma} = \hat{x}, \hat{y}, \hat{z}$) is the spin-polarization direction. The spin-polarization direction depends on the origin of the spin-current. For the STT, depicted in Fig. 1.4 of Chapter 1, the current is spin-polarized by the first ferromagnetic reference layer, and $\hat{\sigma}$ thus corresponds to the magnetization direction of the reference layer. For SOTs, on the other hand, the spin-current originates from the charge-to-spin conversion effects induced by the large SOC of the heavy metal. As there are multiple effects that cause charge-to-spin conversion, the direction of $\hat{\sigma}$ highly depends on the specific microscopic mechanism, and may differ from material to material.

In general, the torques are distinguished based on their symmetry with respect to the magnetization [55]. The field-like torque is described by:

$$\vec{\tau}_{FL} \propto \hat{m} \times \hat{\sigma} \tag{2.10}$$

which is anti-symmetric with respect to the magnetization. The effect of this torque on the magnetization dynamics is similar to the torque applied by an external field, hence it is referred to as a *field-like* torque. In literature, this type of torque is often ascribed to an effective field similar to the first part of Eq. 2.8. The *damping-like* torque, as the name suggests, acts like effective magnetic damping, and is described by:

$$\vec{\tau}_{DL} \propto \hat{m} \times (\hat{\sigma} \times \hat{m}) \tag{2.11}$$

which is symmetric with respect to the magnetization. Note however, that the damping-like torque can also act as an antidamping-like torque depending on its sign, and the details of the magnetization and the current direction [56] [55].

With many techniques, including the harmonic Hall measurements in this thesis, the torques are measured indirectly and modeled as effective fields. This is achieved by replacing $\tau_{DL}\left(\hat{\sigma} \times \hat{m}\right)$ by $\vec{H}_{DL}$ and $\tau_{FL}\hat{\sigma}$ by $\vec{H}_{FL}$ [57]. As both the direct torques and the effective fields are used interchangeably to describe the magnetization dynamics in literature, it might cause confusion to people outside the field. Especially, because the torque and its related effective field are perpendicular to each other by definition. It should be noted, that in case of a exerted torque, the initial reaction of the magnetization will be in the direction of the torque: ($\frac{d\vec{m}}{dt} \sim \gamma \frac{d\vec{L}}{dt}$). However,

given enough time ($\sim$ picoseconds in most materials), the magnetization will precess around the effective field, which is the cross product between the magnetization and the torque direction, and eventually align along the effective field (finding an equilibrium position between all the effective fields acting on the magnetization, e.g. demagnetizing field, anisotropy, SOT effective fields). As the measurements in this thesis are performed in a quasi-static regime (10s to 100s Hz AC-current frequency), we are sensitive to the effective fields related to the SOTs, and not to the intial ultrafast reaction of the magnetization. In other words, the out-of-plane effective field from $\vec{\tau}_{DL}$ gives rise to a deflection of the magnetization in the out-of-plane direction, while the in-plane effective field related to $\vec{\tau}_{FL}$ causes a deflection in the in-plane direction.

## 2.3. Spin-orbit effects

So far, we have discussed how the electron spin and magnetization interact, but we have neglected the mechanisms behind the generation of the spin-current or spin-polarization. For the STT, the charge current is filtered by the ferromagnetic reference layer, resulting in a spin-polarized current which can interact with the ferromagnetic free layer. SOTs, on the other hand, rely on the large SOC of the heavy metal layer to convert a charge current into a spin-current or spin-accumulation at the heavy metal/ferromagnet interface. In this section, these charge-to-spin conversion effects and other effects related to the large SOC are discussed, and a brief description of the resulting SOTs is given. In addition, the symmetry considerations for the generation of SOTs are presented.

### 2.3.1. Spin-Hall effect

The most well-studied effect for converting a *charge* current into a *spin* current is the spin-Hall effect (SHE) [58]. Already predicted in 1971 [59], it remained relatively unexplored until a similar prediction was published in 1999 [60, 61]. Its first observation soon followed in 2004 by optical means [62–64] and electrically in 2006 [65] in aluminum.

With the SHE, a charge current passing through a material with high SOC generates a transverse spin current, polarized perpendicular to both the charge current and spin current:

$$\hat{s} = \hat{j}_c \times \hat{j}_s \tag{2.12}$$

Here, $\hat{s}$ is the spin polarization direction, and $\hat{j}_c$ and $\hat{j}_s$ represent the charge and spin current density unit vectors, respectively. Figure 2.6 shows an illustration of the effect, where a charge current applied in the $\hat{x}$-direction is converted in a transverse spin current in the $\hat{z}$-direction with its spin polarization in the $\hat{y}$-direction. The inverse effect, where a spin-current is generating a transverse charge current is also possible and is referred to as the inverse spin-Hall effect (ISHE). The efficiency with which the charge current density is converted into a spin current density is phenomenologically described by the spin-Hall angle $\theta_{SH}$:

$$\theta_{SH} = \frac{j_s}{j_c} \tag{2.13}$$

As both $j_s$ and $j_c$ are expressed in A/m$^2$, $\theta_{SH}$ is a dimensionless number. The spin current density $j_s$ can be converted to a flux of angular momentum by multiplying with $\hbar/2e$, where $e$ is the electron charge, and $\hbar$ is the reduced Planck's constant ($1.0546 \times 10^{-34}$ J·s) [66].

The SHE originates from spin-orbit interactions, which results in a different momentum for spin up and spin down electrons. Three distinct microscopic mechanisms underlie the SHE: the side-jump, skew-scattering, and intrinsic mechanism. Of these, the side-jump and skew-scattering mechanisms are both considered and referred to as extrinsic mechanisms in literature, and therefore, the SHE is sometimes differentiated into the extrinsic SHE and the intrinsic SHE.

Only the extrinsic mechanisms were considered for the intial prediction of the SHE in 1971 by D'yakanov and Perel. D'yakanov and Perel referred to the phenomena of Mott scattering [67], where electrons with opposite spins scatter differently from heavy nuclei in a vacuum environment. They argued that the same effect can happen in a solid-state environment of a non-magnetic material, causing spin up and spin down to deflect and accumulate on opposite transverse sides of the channel. For the extrinsic mechanisms, two different mechanisms are distinguished: spin skew scattering and side-jump events. For spin skew scattering, the spin orbit coupling gives rise to spin dependent scattering with a different momentum direction for spin up and spin down [68]. In this case, the spin Hall conductivity $\sigma_{xy}^{s_z}$ depends on the momentum relaxation time $t_s$: $\sigma_{xy}^{s_z} \propto t$ (as $\tau$ is already used to denote the torques in this thesis, the momentum relaxation time is denoted by $t_s$). For side jump events, the spin-dependent displacement originates from a different acceleration and deceleration for spin up and spin down during scattering events.

In 2010, however, it was observed that even in the ballistic regime, with no scattering, the SHE persisted [69]. This observation lead to the discovery of an intrinsic mechanism contributing to the SHE, now referred to as the intrinsic SHE. For this mechanism, spin up and spin down electrons obtain an opposite transverse velocity in between scattering event due to the band structure, such that it is independent of $t_s$.

In a bilayer of a heavy metal (HM) and ferromagnet (FM), the spin current arising from the spin Hall effect can interact with the magnetization of the ferromagnet and exert a torque. This will be discussed below.

### Spin-orbit torques due to the spin Hall effect

In a HM/FM bilayer, where the HM is generating a spin current due to the SHE, the spins propagate towards the FM as illustrated in Fig. 2.6. Neglecting any spin-memory loss and a perfect transmission across the HM/FM interface, the spin current is injected in to the FM layer. Similar as described earlier for the STT, the spins transfer their angular momentum to the magnetization, effectively exerting a damping-like torque, analogous to the STT. As the spin-polarization direction for the SHE is in the $\hat{y}$-direction, the expected torque from the SHE is a damping-like torque of the form:

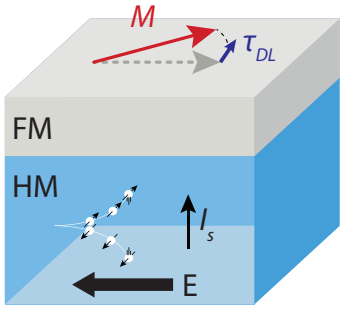


Figure 2.6: A schematic illustration of the spin-Hall effect (SHE). A charge current is applied through the heavy metal (HM) layer, indicated in blue, which is subsequently converted into a perpendicular spin-current ($\vec{I}_s$) due to the large SOC of the HM. The spin-current and -polarization are both perpendicular to each other and perpendicular to the charge current, according to Eq. 2.12. Subsequently, the spin-current propagates towards the ferromagnetic layer on top, indicated in grey. If the magnetization of the ferromagnet ($M$, red arrow) is not parallel to the spin-polarization of the spin-current, the spin-current exerts a damping-like torque ($\vec{\tau}_{DL}$, blue arrow) on the magnetization, similar to the STT, causing $M$ to move away from its equilibrium direction (dashed grey arrow).

.

$$\vec{\tau}_{DL} \propto \hat{m} \times (\hat{y} \times \hat{m}) \tag{2.14}$$

In many experiments on conductive HM/FM bilayers, the observed damping-like torque is therefore ascribed to originate from the SHE and is used to determine the effective spin Hall angle $\theta_{SH}$, assuming that no other effects contribute to the damping-like torque. However, as this is generally not the case, the extracted $\theta_{SH}$ should be taken as an effective phenomenological parameter for the SOT efficiency [53].

In addition, the spin current in the HM, eminent from the SHE, can also lead to a spin accumulation at the edges of the HM [53]. This spin accumulation in turn can interact with the magnetization of the adjacent magnet via magnetic exchange and exert a field-like torque. Therefore, the SHE does not necessarily produce a damping-like torque but can also exert a field-like torque of the form:

$$\vec{\tau}_{FL} \propto \hat{m} \times \hat{y} \tag{2.15}$$

as the spin accumulation at the HM/FM interface is polarized in the $\hat{y}$-direction. As both a field-like and a damping-like torque can be produced by the SHE, the decomposition of the these torques does not allow one to easily disentangle the contribution of the SHE from other microscopic mechanisms [53].

As a large $\theta_{SH}$ amounts to strong charge-to-spin conversion, which in turn leads to a large SOT efficiency, a lot of SOT research is based on finding materials with a high $\theta_{SH}$. Already in 2007, it was found that the spin Hall angle of platinum (Pt) was four orders of magnitude larger when compared to other materials used at the time [70]. Ever since, Pt has been a popular material for bilayer HM/FM SOT

devices with a $\theta_{SH} \approx 0.10$ [71–74]. For other 4d and 5d transition metals, such as tantalum (Ta) and Tungsten (W), similar values for $\theta_{SH}$ were found, and likewise became popular HM materials for SOT devices.

Apart from the spin Hall effect, a more recent and related effect might play a role in these systems, called the orbital Hall effect (OHE) [75–79]. In this case, the flow of angular momentum does not come from the spin of the electron, but rather from its orbital angular momentum. Similar to the spin Hall effect, the direction of angular momentum is perpendicular to both the applied electric field and the angular momentum flow, and is injected from the HM to the FM where it can exert a torque on the magnetization. Distinguishing the SHE from the OHE is both experimentally and theoretically challenging [47, 79]. Combining theory that incorporates the flow of both spin and orbital angular momentum with experiments may shine light on the contributions of each of these mechanisms by appropriate material selection.

In addition, Pt and W doped with oxygen were shown to increase $\theta_{SH}$ to values of $\approx 0.9$ and $\approx -0.49$, respectively [80–82]. These increases, however, were ascribed not to the SHE, but to effects eminent from the interface. This shows that also the HM/FM interface can significantly contribute to an efficient generation of SOTs. Therefore, SOTs originating from interfacial effects will be the topic of the next sections.

### 2.3.2. Rashba-Edelstein effect

When electrons move in an perpendicular electric field ($\vec{E}$), they experience an effective magnetic field $\vec{B}_{eff} \sim \vec{E} \times \vec{p}/(mc^2)$ in their own reference frame, even in the absence of an external magnetic field [83]. This field, referred to as the spin-orbit (SO) field, couples to the electron's magnetic moment. In crystals, the electric field comes from the gradient of the crystal potential $\vec{E} = -\vec{\nabla}V$. In addition, in structures where the inversion symmetry is broken, for instance at an interface of two different materials, the SO field becomes odd in the electron momentum and a non-equilibrium spin accumulation confined at the interface becomes allowed by symmetry [84]. This result of SOC can be described by the Hamiltonian [84]:

$$H_R = (\alpha_R/\hbar)(\hat{z} \times \vec{k}) \cdot \vec{\sigma} \tag{2.16}$$

which was first described for an two-dimensional electron gas by Bychkov and Rashba in 1984 and is now referred to as Rashba SOC [84]. Here, $\alpha_R$ is the Rashba parameter, $\hat{z}$ is a unit vector pointing in the symmetry breaking direction, $\hat{k}$ is the electron wave vector, and $\vec{\sigma}$ are the Pauli spin matrices. The momentum-dependent SO field, causes a k-space spin texture as illustrated in Fig. 2.7(a). The spin direction of the electrons are locked to their momentum, which is referred to as spin-momentum locking, and results in this characteristic winding spin texture around the Fermi surface, as depicted in Fig. 2.7(). This is called the Rashba effect.

In equilibrium, there is no net spin polarization, as all states with opposite spin directions are equally populated. However, when an external E-field is applied the Fermi surface shifts. As illustrated in Fig. 2.7 for an applied E-field in the

x-direction, the states with momentum in the +x-direction are populated more compared to states with momentum in the -x-direction, resulting in a net charge current in the x-direction. The states with momentum in the +x-direction feel an effective SO field in the +y-direction, and therefore, have their spins aligned in the +y-direction. As the electronic states with their spins aligned in the +y-direction are more populated compared to the states with spins pointing in the -y-direction, this results in a net spin polarization in the +y-direction. The generation of a spin polarization by means of a charge current in a system with Rahsba SOC was first described by Edelstein in 1990 [85], and is now referred to as the Rashba-Edelstein effect (REE). The REE thus allows one to create a spin polarization, or spin imbalance called a spin accumulation, at the FM/HM interface as illustrated in Fig. 2.7(c). This spin polarization in turn can interact with the magnetization of the FM layer by means of exhange interaction, exerting a torque [55, 86]. As the spin polarization originates from the SOC of the HM, this torque is also considered a SOT. The type of torque it exerts is heavily debated in literature. At the time of writing, there is no clear consensus on whether the REE leads to a field-like torque, damping-like torque, or a mixture of both. This will briefly discussed below.

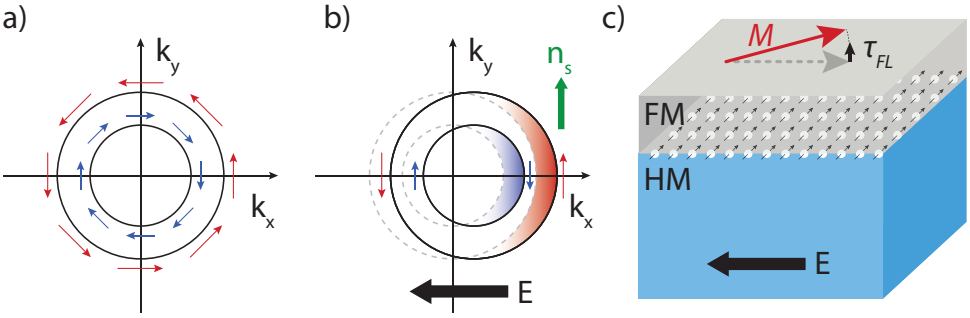


Figure 2.7: (a) Schematic of the Fermi surface at equilibrium of a 2D free electon gas with Rashba SOC. The spin angular momentum, indicated with the red and blue arrows, is locked to the linear momentum resulting in the winding spin-texture. In equilibrium, the states with opposite spin are equally populated, resulting in no net spin-polarization. (b) When an external electric field is applied, the Fermi contours shift away from their equilibrium position (dashed circles). The redistribution of the states (filled contours) result in a non-zero spin density ($n_s$) with a polarization perpendicular to $\vec{E}$ (green arrow). (c) When an electric field ($\vec{E}$) is applied to a FM/HM bilayer, the broken inversion symmetry at the interface allows for Rashba SOC, resulting in a spin-accumulation at the interface. The spin-accumulation can interact with the magnetization (red arrow) of the top FM layer, exerting a field-like torque $\vec{\tau}_{FL}$ (black arrow).

### Spin-orbit torques due to the Rashba-Edelstein effect

Machon and Zhang were the first to theoretically study SOTs due to the Rashba-Edelstein effect in 2008 for a ferromagnetic layer sandwiched in between two dissimilar insulating layers [87, 88]. They argued that this Rashba torque arises from the intrinsic SOC and does not involve the transfer of the conduction-electron spin to the magnetization, as is the case for the STT and SHE-SOT, but instead acts as an effective magnetic field, resulting in a field-like torque. Ever since, many reports

have been published where the observed SOTs are ascribed to the Rashba-Edelstein effect [53, 86, 89–91]. However, ascribing the exact mechanisms underlying the observed SOTs is difficult, as different mechanisms may result in similar SOTs, making it difficult to distinguish them from one another. To illustrate this problem, some examples from literature from recent years will be presented below.

The first observation of SOT switching of a magnet with perpendicular magnetic anisotropy in Co/Pt bilayers was attributed to the Rashba-Edelstein effect [86]. Here, the authors observe both a field-like and damping-like torque which they ascribed to the REE as they had reported before [92, 93]. In contrast, other researchers observed dominant damping-like torques in a similar bilayers, which were ascribed to the SHE rather than the REE [72, 94, 95]. Another example is the dissimilar torques observed in FM/$MoS_2$ bilayers [89, 96]. Although both reports ascribe the torques to interfacial effect (such as the REE), Zhang et al. observe a large damping-like torque and smaller field-like torque, while Shao et al. only observe a large field-like torque. This illustrates that it is difficult to exactly pin point what the exact mechanisms which are underlying the observed SOTs in these FM/HM bilayers. Also, multiple reports observe a gigantic damping-like torque which can not be explained by the SHE alone. As example, Lee et al. observe an effective spin Hall angle $\theta_{SH}^{eff} \approx 0.12$ in Pd/FePd bilayers, while Pd has a $\theta_{SH}^{eff}$ of $0.006 - 0.012$ [97], Jamali et al. report $\theta_{SH}^{eff} \approx 4.4$ in Pd/Co multiplayers [98], and Mellnik et al. obverse a gigantic $\theta_{SH}^{eff} \approx 2.2 - 3.5$ in conductive $Bi_2Se_3$ [99].

To get a better understanding on which torques arise from the REE, multiple theoretical models have been studied. A theoretical model based on the Boltzmann equation, that incorporates both the REE and SHE in HM/FM bilayers, shows that both the SHE and REE can produce both damping-like and field-like torques [55]. They find that the field-like torque is predominant for the REE, while for the SHE, the damping-like torque is dominant, but argue that the dominating torque depends heavily on the specific parameters of the particular system [55]. Similarly, another model based on the equilibrium Green's function find a dominant field-like torque for the REE effect [100]. This model, however, assumes a system in the ballistic regime. More recently, multiple theoretical reports using different methods (computational quantum transport and analytical) arrive at the same conclusion that increased scattering off impurities leads to an enhanced damping-like torque for Rashba systems [101, 102].

### 2.3.3. Other interfacial effects

Apart from the REE, there are myriad of other interfacial effects discussed in literature that may play a role in these bilayer devices. In this section, I will present two other recently proposed ones, namely spin-orbit filtering and spin-orbit precession, to illustrate that the resulting torque of different effect might be similar, making it hard to disentangle which effects dominate in the generation of SOTs.

#### Spin-orbit filtering

In the case of an Rashba field in the $\vec{k} \times \hat{z}$ direction at the interface of the HM/FM bilayer, another interfacial effect was proposed by Amin et al. that could lead to

the generation of a spin current and thus a torque on the magnetization. The effect is called spin-orbit filtering (SOF) and is depicted in Fig. 2.8(a).

An unpolarized charge current that is incident on the interface with Rashba SOC undergoes spin-dependent scattering at the interface. The interfacial Rashba field creates a spin-dependent potential barrier and preferentially transmits and reflects electrons based on their spin, effectively acting as a spin filter. Without applying an electric field, the net spin-current is zero when integrated over all k-states, which is analogous to the REE where there is no spin accumulation without applying a bias. However, with an applied electric field, the k-states become anisotropically occupied, resulting in a non-zero out-of-plane spin current ($\vec{j}_s$) with a polarization in the $\vec{E} \times \hat{z}$ direction.

The resulting spin current and spin polarization directions generated by the SOF are similar to the ones created by the SHE. Using a three-dimensional model, Amin et al. showed that SOF generates the same type of SOT as the SHE: $\vec{\tau}_{DL} \propto \hat{m} \times (\hat{y} \times \hat{m})$, which makes is difficult to distinguish between the two effects [45]. The SHE is a bulk effect which mainly depends on the material properties of the HM layer. The SOF, on the other hand, is an interfacial effect and depends on the momentum relaxation times and electronic structure of both layers [45, 103]. This effect could explain experimental observations of interfacial damping-like torques [72, 92, 104–106] rather than field-like torques as expected from the REE.

### Spin-orbit precession

Another interfacial effect, referred to as spin-orbit precession, is depicted in Fig. 2.8(b) [45]. Again, we consider a bilayer of a FM on top of a HM with a Rashba spin-orbit field $\vec{B}_{SO}$ at the interface. We assume a charge current in the ferromagnet that is spin-polarized along the direction of the magnetization $\hat{m}$. If the incoming spins are polarized perpendicular to $\vec{B}_{SO}$, they will briefly precess around $\vec{B}_{SO}$ and become misaligned with $\hat{m}$ prior to scattering off the interface [107, 108]. In this process the spins attain a component of angular momentum in the $\hat{\sigma} \times \hat{m}$ direction. The reflected and rotated spins propagate back into the ferromagnet where they dephase and exert a torque on the magnetization in the $\vec{\tau} \propto \hat{m} \times (\hat{\sigma} \times \hat{m})$ direction.

### Spin memory loss

In the presence of SOC, for instance at the HM/FM interface, the total spin is not conserved [109]. Similar as the angular momentum can be transferred from the lattice to the electrons, the electrons can lose their angular momentum back to the lattice when they traverse an interface due to interfacial SOC. Here, the lattice thus acts as a sink for angular momentum. Without interfacial SOC, when spins cross the HM/FM interface, they retain their spin polarization aligned with the magnetization, but lose their transverse component of spin due to dephasing within the ferromagnet. With interfacial SOC, the spins can transfer their angular momentum (in all directions) back to the lattice [107, 108]. This effect is called spin-memory loss and is considered a parasitic effect because it obstructs the efficient transfer of angular momentum to the magnetization [110]. Spin memory loss not only interferes with SOTs but affects multiple spin transport phenomena such as magnetoresistance, STTs in spin-valves and Josephson currents [111].

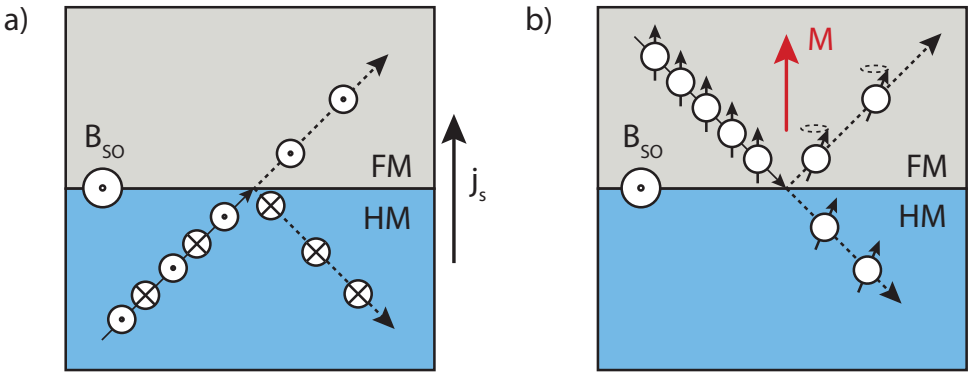


Figure 2.8: (a) Schematic of the effect referred to as spin-orbit filtering. For an unpolarized charge current propogating towards the HM/FM interface, the spins aligned parallel to the spin-orbit field ($\vec{B}_{SO}$) are preferentially transmitted while the spins aligned antiparallel to $\vec{B}_{SO}$ are reflected. This results in an out-of-plane spin-current $\vec{J}_s$ which can exert a torque on the magnetization of the top ferromagnetic layer. (b) Schematic of the effect referred to as spin-orbit precession. Here, a spin-current is flowing through the ferromagnet which its polarized parallel to the magnetization ($M$, red arrow). Upon reaching the HM/FM interface, the spins shortly precess around $\vec{B}_{SO}$, resulting in a misaligned with the magnetization. The reflected spins, precess around the magnetization, dephase, and transfer their transverse component of angular momentum to the magnetization, exerting a torque ($\hat{m} \times (\hat{\sigma} \times \hat{m})$).

### 2.3.4. Self-torques

Although the majority of the SOT measurements are performed in a bilayer configuration of a HM and FM, there have been reports of SOTs in systems consisting only of a single FM layer [112–115]. For some reports, the torques emerging in the single ferromagnetic layer could even switch its own magnetization [116, 117]. In literature, these torques are referred to as *anomalous* torques or *self*-torques, and the exact mechanisms involved are under debate.

In a inversion symmetric single layer device, no torques are allowed by symmetry as the torques at opposite interfaces will cancel perfectly (see Sec. 2.3.6 for more details). However, if inversion symmetry is broken, this may lead to the generation of self-torques in single layer FM devices. The inversion symmetry can be broken in multiple ways: (i) The FM layer is interfaced between two different materials (e.g. NM1/FM/NM2), (ii) In a system of NM1/FM/NM1, where the interfaces are different, (iii) The FM layer lacks inversion symmetry in its bulk form [118].

If the FM has different opposite interfaces (case i or ii), the spin transparency, spin memory loss, and SOC at these interfaces may differ. The spin currents generated in the bulk of the FM which flow to the opposite sides of the FM, due to e.g. the SHE, could transmit and reflect differently from the different interfaces due to a difference in spin transparency, spin memory loss, or different interfacial SOC. This causes the net flow of angular momentum to be non-zero which results in a torque on the magnetization. Also if the origin of the spin polarization is interfacial, such as the REE, a self-torque could be generated due to the different interfaces. A difference in interfacial SOC could lead to the generation of different spin accu-

mulations at the interfaces, resulting in a net non-zero spin accumulation. In turn, this spin polarization can exert a torque on the magnetization when the it is not parallel with the magnetization.

In Chapter 6, we compare the SOTs in our $MoS_2$/permalloy devices to the SOTs in a single-layer permalloy device to determine the role of the self-torque in permalloy in these bilayers. We find that the field-like self-torque in permalloy are of significant magnitude compared to the torques in our $MoS_2$/permalloy devices. In addition, we observe a weak damping-like torque in our devices, with a strong device-to-device variation. These observations indicates that the self-torques in the FM layer may dominate the SOTs observed in TMD/FM bilayers.



### 2.3.5. Electron-magnon scattering

In HM/FM bilayers multiple magnetoresistance effects may be present, such as the anisotropic magnetoresistance (AMR), spin Hall magnetoresistance (SMR), and Rashba-Edelstein magnetoresistance (EMR) effects [119]. These magnetoresistance effects are invariant on inversion of either the current ($j$) or magnetization direction ($M$): $R(j, M) = R(-j, M) = R(j, -M)$. However, recent studies have shown that there may be an additional non-linear effect in these systems referred to as the unidirection (spin) magnetoresistance (UMR), which is odd under reversing either the current or magnetization direction : $R(j, M) = -R(-j, M) = -R(j, -M)$ [120]. This effect is analogous to the in-plane giant magnetoresistance effect (GMR), where the resistance of two adjacent FMs, spaced by a NM, depends on their relative orientation. Here, charge-to-spin conversion effects, such as the SHE and REE, replace one of the FM layers.

The origins of the UMR are still under debate, but so far, two mechanisms have been proposed [119, 121, 122]. The first mechanism consists of two parts: the interfacial and bulk spin-dependent scattering. For the interfacial mechanism, the scattering rate or the probability of transmission of an electron depends on the orientation of its spin $\vec{\sigma}$ relative the magnetization $\vec{M}$, which results in a magnetoresistance. For the bulk spin-dependent scattering, we consider that the FM layer has a spin-dependent conductivity. By injecting spins from the HM layer due to charge-to-spin conversion effects, the electron spin density in the FM is modulated which generates a non-linear resistivity [123]. The second mechanism, referred to as spin-flip UMR, invokes the annihilation or creation of magnons due to electron-magnon scattering by the current generated spin polarization [56, 119]. The annihilation and creation of the magnons changes both the longitudinal and transverse resistance [124, 125]. As the UMR causes current-induced changes to the resistivity and scales proportionally to the current the signal corresponding to the UMR is expected in the second-harmonic Hall measurements performed for measuring SOTs in Chapters 5 and 6. It was shown that the second-harmonic Hall voltage has a $\cos(\phi)$ dependence when rotating the magnetic field in-plane [125]. Furthermore, the second-harmonic Hall voltage from to UMR decreases with increasing magnetic field, due to a decrease in magnon population at high magnetic fields. Therefore, UMR can result in an inaccurate determination of $\tau_{DL}$ and should therefore be characterized using second-harmonic longitudinal measurements.

### 2.3.6. Symmetry considerations

The symmetry of the system is crucial for understanding which SOTs can exist [126]. The link between the allowed SOTs and the symmetry of the system can be made through the *Neumann's principe* which states that any macroscopic physical property must have at least the symmetry of the system [127]. For SOTs, it is important to know which current-induced spin polarizations are allowed by symmetry as the current induced spin polarization $\hat{\sigma}$ is directly related to the allowed torques by $\vec{\tau}_{DL} \propto \hat{m} \times (\hat{\sigma} \times \hat{m})$ and $\vec{\tau}_{FL} \propto \hat{m} \times \hat{\sigma}$ [128].

The spin polarization induced by an electric field $\vec{E}$ can be described by:

$$\vec{\sigma} = \chi \cdot \vec{E} \tag{2.17}$$

where $\chi$ is a 3-dimensional pseudotensor which relates the obtained spin polarization $\vec{\sigma}$ to the applied electric field $\vec{E}$ ($\chi$ is generally referred to as the magnetoelectric pseudotensor). The spin is a pseudovector which transforms under a symmetry operation, $S$, as $\vec{\sigma'} = \det(R)R\vec{\sigma}$, where $R$ is a matrix representation of the symmetry operation $S$, and $\det(R)$ is its determinant [50]. This holds for the whole set of symmetry operations $\{R\}$ in the space group of the crystal. The electric field, however, is a normal vector and transforms under $S$ as $\vec{E'} = R\vec{E}$. Using these two transformations and Eq. 2.17, one can derive the relation:

$$\chi = \det(R)R\chi R^{-1}. \tag{2.18}$$

Using Eq. 2.18 and the matrix representation for the inversion symmetry operation:

$$i = \begin{pmatrix} -1 & 0 & 0 \\ 0 & -1 & 0 \\ 0 & 0 & -1 \end{pmatrix} \tag{2.19}$$

one finds that Eq. 2.18 results in $\chi = -\chi = 0$ [128]. This shows that the inversion symmetry needs to be broken as otherwise no spin polarization, and thus no SOTs, can be obtained by an applied electric field.

The structural inversion symmetry can be broken in a variety of ways. As discussed above, the interface between two dissimilar materials provides the inversion symmetry breaking for polycrystalline materials such as Pt, W, Ta, etc. With this type of inversion symmetry breaking for polycrystalline materials, however, a lot of other symmetry operations remain, such as a rotation axis along the $\hat{z}$-axis and multiple mirror planes dissecting the $xy$-plane. Due to the high symmetry of these systems, the only allowed spin-polarization is a Rashba-like symmetry depicted in Fig. 2.7 [50, 129]. Here, an applied electric field in the $\hat{x}$-direction generates a in a spin polarization in the $\hat{y}$-direction, and thus to torques of the form $\hat{m} \times (\hat{y} \times \hat{m})$ and $\hat{m} \times \hat{y}$.

For high density memory applications, on the other hand, magnets with a perpendicular magnetic anisotropy (PMA) are necessary, which are most efficiently switched using a damping-like torque in the $\hat{z}$-direction. The damping torque $\vec{\tau}_{DL} \propto \hat{m} \times (\hat{z} \times \hat{m})$ is, therefore, considered the holy grail of SOTs. From symmetry analysis, we know that this torque is not allowed in the case that there is

a rotation axis along the $\hat{z}$-axis or more than 2 mirror planes dissecting the $xy$-plane [128]. To allow for deterministic switching of PMA materials, reducing the symmetry of the SOT device was studied in recent years using multiple methods. Here, I will briefly discuss three different methods: (i) applying a magnetic field in the x-direction, (ii) asymmetric device geometry, and (iii) low-symmetry single crystalline material.

The first method is by applying a static external in-plane magnetic field ($\vec{B}_{app}$) along the current direction ($J$), as illustrated in Fig. 2.9(b). After applying a mirror transformation on the system in the xz-plane, the current direction, being a normal vector, does not change. The magnetization and the applied magnetic field, on the other hand, are pseudovectors and thus do flip their direction. The applied magnetic field breaks the symmetry between the two configurations of the magnetization (up and down), allowing for a unique magnetic state. In Fig. 2.9(b), this is illustrated as the magnetization is up when the applied magnetic field is parallel to the current direction, while the magnetization is down when the applied magnetic field is anti-parallel to the current direction. Using this method on SOT devices consisting of conventional polycrystalline materials, such as Pt, Ta, and W, researchers were able to deterministically switch PMA magnets by means of the REE and SHE effects [72, 86, 95]. However, as the application of an in-plane magnetic field is not considered scalable, other means of breaking the symmetry have been sought after.

The second method is fabricating devices with a asymmetric geometry, which breaks the mirror symmetry in the xz-plane. Yu et al. fabricated trilayer Ta/CoFeB/TaOx devices with a wedges shaped Ta layer, as illustrated in Fig. 2.9(c), reducing the symmetry of the device to one single mirror plane in the $xz$-plane [130]. They observed a $\vec{\tau}_{FL} \propto \hat{m} \times \hat{z}$ when they applied the current perpendicular to the single mirror. Although the thickness gradient was rather small, the results did show a $\vec{\tau}_{FL} \propto \hat{m} \times \hat{z}$, later studies were able to reproduce the effect [131].

The last method for a creating a low-symmetry SOT device discussed here is using a low-symmetry single crystalline material. Multiple studies were performed on grown materials, such as Ga(Mn)As [132], GaAs/Fe [133], NiMnSb [129]. Here, Dresselhaus-like spin polarizations were observed which are consistent with their symmetries. For out-of-plane spin polarizations, materials with lower crystal symmetries are needed which are difficult to grow epitaxially. Therefore, studies are performed by thinning down a low-symmetry bulk crystal. In this respect, van der Waals materials are a popular choice as the layers of these crystals are weakly bonded by van der Waals interactions, and can therefore be thinned down by means of mechanical exfoliation (discussed in Chapter 3). One prime example of a low-symmetry van der Waals material which is heavily studied in recent years is tungsten ditelluride ($WTe_2$), which only possesses one mirror plane. [9, 134–137]. An out-of-plane damping-like torque was observed in $WTe_2$/Py devices when the current was applied perpendicular to the mirror plane, while the torque was absent when the current was applied along the mirror plane. Ever since, $WTe_2$ and other low-symmetry 2D van der Waals materials have been studied to get a better understanding on the relation between the observed torque and the crystal symmetry ($WTe_2$[9, 134–137], $MoTe_2$ [138], $TaTe_2$ [139], $NbSe_2$ [91]). In Chapter 7, we change the crystallographic phase

of the TMD $MoTe_2$ locally, from a high-symmetry 2H phase to a low-symmetry 1T' phase, which could be used in future studies to more accurately determine the relation between the allowed SOTs and the crystal symmetry.

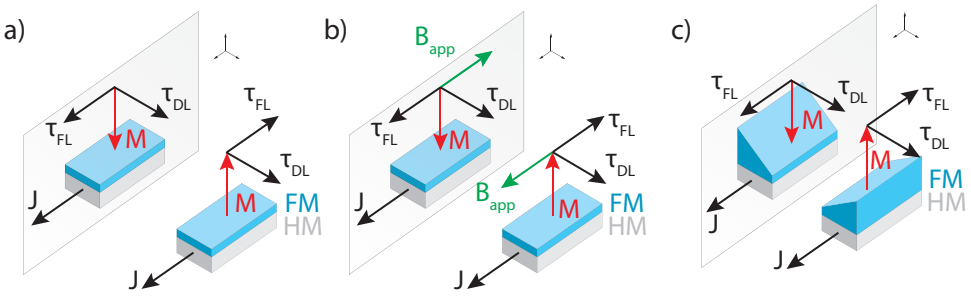


Figure 2.9: (a) Illustration of a HM (grey)/FM (blue) bilayer, together with its mirror image. The $\vec{\tau}_{FL}$ and $\vec{\tau}_{DL}$ are allowed due to the breaking of inversion symmetry in the out-of-plane direction. The pseudo-vectors $M$ is reflected upon a mirror transformation, while the current direction ($J$) remain the same. As the same direction of current allows for the magnetization to point up as well as down, there is no prefered state for the magnetization, and thus no deterministic switching. (b) This changes however, when an external magnetic field is applied ($\vec{B}_{app}$) in the x-direction which breaks the symmetry in the xz-plane. Now, the state with its magnetization up is preferred when the current and applied field are in the same direction, while the state with its magnetization down is preferred when these are antiparallel. (c) The symmetry in the xz-plane is similarly broken when fabricating a wedged shaped device as illustrated here. Without applying an external magnetic field, this allows for field-free deterministic switching.

## 2.4. Photocurrents in 2D materials

In this section, I will shed light on the mechanisms involved in the electronic response of 2D materials to light illumination. A device in which this response can be measured consists of a channel of the material in question, contacted by a source and drain contact and a gate which allows one to control the carrier density via the field-effect.

The electronic response is measured by optoelectronic measurements, referred to as photocurrent measurements, where the induced or modulated current flowing through a device by illumination of light is measured with the source and drain contacts. The total photocurrent ($I_{pc}$) is defined as the difference between the current under illumination and the current in dark conditions: $I_{pc} = I_{light} - I_{dark}$ These type of measurements are performed and discussed in Chapters 7 and 8 for $MoTe_2$ and $MoSe_2$, respectively.

There are different light-matter interactions that induce or modulate the photocurrent in a device. Here, I will describe the photogating/photodoping, photoconductive effect, photothermal electric effect and the polarization-dependent photocurrents.

### 2.4.1. Photoconductive effect

In general, when light is absorbed by a semiconducting material, it excites an electron to the conduction band, leaving a hole in the valence band. This is only possible when the energy of the photon is the same or larger than the band gap of the material, i.e. $E_{ph} \geq E_{bg}$. The excited free electrons increase the carrier density $n$ which increases the electrical conductivity of the semiconductor $\sigma = q\mu n$, where $q$ is the carrier charge, $\mu$ is the mobility and $n$ is the carrier density. This effect can be measured by measuring the drain source current ($I_{ds}$) while sweeping the drain source voltage ($V_{ds}$). As $I_{ds} \propto \sigma V_{ds}$ for a simple resistor, the slope of the IV-curve is altered by the illumination of light, as illustrated in Fig. 2.10. Note, however, that without applying a $V_{ds}$ there is no current in both cases.

#### Photogating

With a related effect, referred to as photogating or photodoping, the absorbed photons generates free electrons and holes as before, but now one of the carriers is trapped in localized states at the band edge. The trapped charged shift the Fermi level of the semiconductor, acting as an effective gate. This therefore leads to a shift of the $I_{ds}$ curve when sweeping the gate voltage ($V_g$), as illustrated in Fig. 2.10. These trapped states are usually located at defects or at the surface of the material. In particular, the material hexagonal boron nitride (hBN), has shown to result in significant photogating in graphene/hBN devices. The optical excitation excites electrons from defects in hBN that are subsequently transferred to the graphene and leave behind trapped holes [140].

### 2.4.2. Photothermal effects

The absorption of the laser light used for excitation can cause the device to heat, which can modulate the electrical resistance of the device via the so called photobolometric effect (PBE) [141, 142]. This effect is proportional to the conductance variation of the material with temperature: $dG/dT$.

In addition, for optical measurements where the laser light is focused and only small parts of the sample are illuminated, the local heating results in temperature gradients, which in turn, can generate photocurrents of photo voltages via the photothermoelectric effect (PTE). The difference in temperature ($\Delta T$) for the two sides of the device causes a difference in voltage ($\Delta V$) due to the Seebeck effect:

$$\Delta V = S \cdot \Delta T \tag{2.20}$$

where $S$ is referred to as the Seebeck coefficient. The Seebeck coefficient can be obtained from the Mott relation as [143–145]:

$$S = \frac{\pi^3 k_B^2 T}{3e} \frac{1}{G} \frac{dG}{dE}\Big|_{E=E_f} \tag{2.21}$$

where $k_B$ is the Boltzmann constant, $e$ is the electron charge, $G$ is the conductance, and its derivative with respect to energy is evaluated at the Fermi energy $E_f$.

In a short circuit configuration, the photocurrent ($I_{pc}$) generated by the PTE can be described as:

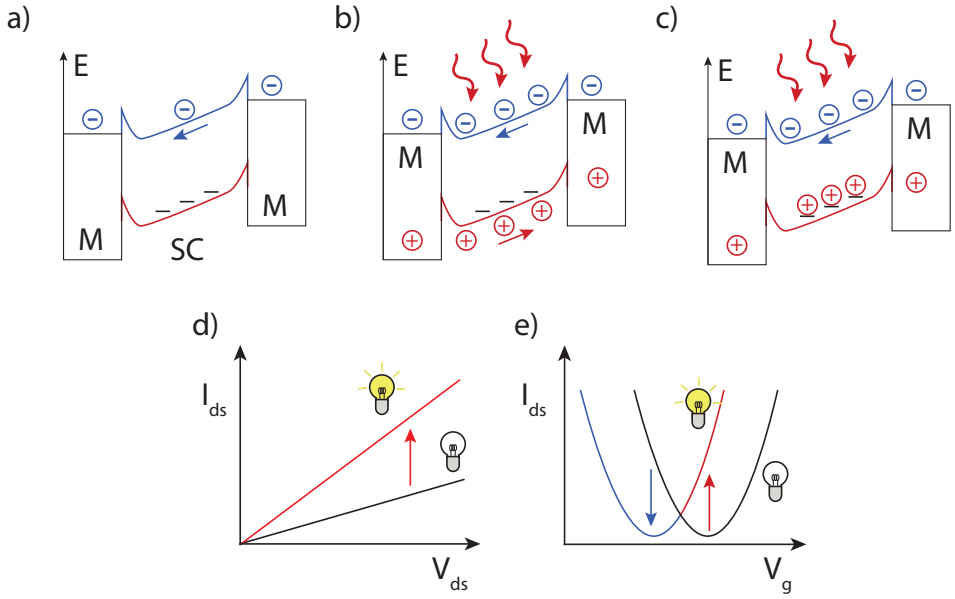


Figure 2.10: A schematic illustration of the photoconductive effect in a semiconducting material (SC) contacted with two metal contacts (M). (a) A representation of the band alignment in dark conditions, with the valence and conduction band indicated in red and blue, respectively. Under these conditions a small current flows through the semiconducting channel. (b) Upon illumination, photons with $E_p \geq E_{bg}$ excite electron-hole pairs which are separated by the external bias, causing an increase in carrier density. (d) A schematic of an IV-measurement in dark (black) and under illumination (red). The increase in carrier density results in an increase of the conductivity which is easily observed as a change in the slope of the IV-measurement. (c) Representation of the photogating effect. Here, localized states near the band edge (valence band) trap holes which effectively gate the SC channel. (e) This lead to a shift in the $I_{ds}$ versus $V_g$ measurement. The illumination can either cause an increase of the current, indicated in red, or decrease in the current, indicated in blue, compared to the measurement in dark conditions (black line), depending on where the Fermi energy of the SC material is positioned.

$$I_{pc} = \frac{(S_2 - S_1)\,\Delta T}{R} \tag{2.22}$$

where $R$ is the resistance, and $S_1$ and $S_2$ represent the Seebeck coefficients of the contact and channel material, respectively. As the Seebeck coefficient for metal contacts are low ($\sim 1$ µV K$^{-1}$) compared to most semiconductors, this equation can be simplified: $S_2 - S_1 \approx S_2$. For the PTE to generate a current as zero applied drain source voltage, however, the $\Delta V_{PTE}$ should be larger than the Schottky barrier height at the metal-semiconductor interface.

### 2.4.3. Polarization-dependent photocurrents

So far, the discussion is based on light-electric conversion. However, the striking properties of TMDs can be appreciated more when the direct band gap and its large SOC properties are combined in opto-spintronic applications. The coupling

between the spin and valley degree of freedom in TMDs, discussed in Sec. 2.3.6, gives rise to unique phenomena such as the circular photogalvanic effect and spin galvanic effect, where light creates spin polarized currents. This will be discussed in this section.



As mentioned in Sec. 2.3.6, a spin polarization can be generated in TMDs by optical excitation with circularly polarized light, originating from its large and opposite spin-orbit interaction in the K and K'-valley. The optical generation of the spin polarization, analogous to charge transport, leads to an increase of the spin conductivity, which in turn, results in a spin-polarized current when an external bias ($V_{ds}$) is applied.

On the other hand, it was shown that by illuminating TMDs with circular polarized light, photocurrents can also occur without applying an external bias in TMDs. There are several mechanisms underlying these spontaneous photocurrents, such as the circular photogalvanic effect (CPGE) and the spin-galvanic effect (SGE).

### 2.4.4. Circular photogalvanic effect

The circularly polarized photogalvanic effect (CPGE) can be considered as a transfer of the angular momentum of the photon into linear momentum of the charge carrier [146]. A very simple analogy would be the conversion of the rotary motion of a propeller into linear motion of the plane. The microscopic origin of the photocurrent can be explained in a Rashba system where the spin sub-bands are spit, illustrated in Fig. 2.11(a). Right handed circularly polarized light induces a spin-flip transitions from $s = +1/2$ to $s = -1/2$, as indicated by the vertical red arrow, which leads to the asymmetric filling of the bands. The non-equilibrium distribution in the upper band relaxes more rapidly by emitting phonons, resulting in a current in the x-direction [147].

The circular photogalvanic effect was predicted in 1978 by Ivchenko and Pikus [148] and Belinicher [149] independently. The effect was first observed in tellurium where it arises due to spin splitting of the valence band [150]. In TMDs the bands are spin-split too as discussed before, and likewise, circular photogalvanic effects have been reported. The CPGE in TMDs was first demonstrated by Yuan *et al.* in bilayer $WSe_2$ in 2014 [151]. They showed generation of spin and valley polarized photocurrents and its control with the helicity of the excitation light. Furthermore, they were able to control the photocurrent by increasing the magnitude of the broken inversion symmetry with a gate voltage. Since then, the CPGE has been reported in $MoS_2$ and $MoSe_2$ [152, 153].

The dependence of the photocurrent on the circular polarization can be characterized experimentally using a rotatable $\lambda/4$ plate. The $\lambda/4$ plate changes the helicity ($P_c$) of the light depending on the angle $\phi$ between the optical axis of the plate and the polarization plane of the laser, according to $P_c = sin(2\phi)$. In this case, the photocurrent may be given by the phenomenological equation:

$$I_{pc} = I_0 + C\sin(2\phi) + L\sin(4\phi + \phi_0) \tag{2.23}$$

Here, the first term on the right represents the polarization independent contribution to the photocurrent, while the second and third term are the photocurrents which

are dependent on the circular and linear polarization, respectively. This equation is used in Chapter 8 to extract the circular and linear components of the photocurrent observed in a $MoSe_2$ phototransistor.

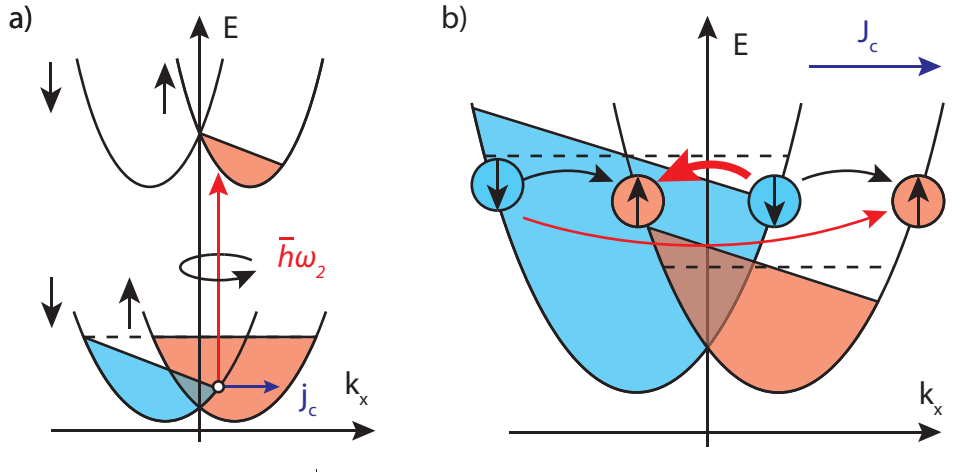


Figure 2.11: (a) A schematic of the spin-split band diagram for the circular photogalvanic effect. A spin-flip transition is induced by right handed circularly polarized light (straight red arrow), creating an asymmetric filling of the bands indicated with the tilted filled bands. This results in a charge current in the x-direction. (b) A schematic of the spin-split band diagram similar to (a). By injecting spins, either electrically or optically, an imbalance in the filling of the spin up and spin down bands is obtained, indicated with the black dashed line. Due to the k-dependent rates of the spin-flip events, indicated with the black and red arrows, an asymmetric filling is obtained, resulting in a charge current in the x-direction.

### 2.4.5. Spin galvanic effect

Another mechanism which creates spin photocurrent when exciting a system possessing non-degenerate spin bands with circularly polarized light is the spin-galvanic effect (SGE). It was predicted by Ivchenko et al. in 1989 [154] and experimentally confirmed by Ganichev et al. in 2002 [155].

The microscopic mechanism behind the SGE can be explained using Fig. 2.11(b). As before, we consider a system where the spin bands are split in k-space. If spins are injected into the system, either electrically with magnetic contacts or optically by means of circularly polarized light, an imbalance in the filling of the spin up and spin down bands is initially created, illustrated with the black dashed line in Fig. 2.11(b). This non-equilibrium distribution will relax due to spin-flip scattering events, of which there are multiple path ways, indicated by the solid red and black arrows in Fig. 2.11(b). The rates of these events is dependent on the value of the wave vectors of the initial and final state [147]. The scattering events indicated by solid black arrows have the same rates and therefore preserve the symmetric filling of the band. However, the rates of the events indicated by the red arrows are different. This results in an asymmetric filling of the bands, indicated by the tilted filled blue

and red bands, and thus results in a current flow ($J_c$) in the x-direction [147].

If the spin injection is done by optical means, the SGE can be regarded as another mechanism of the CPGE effect. In experiments the SGE and CPGE are often measured simultaneously. Time-resolved measurements poses a way to separate both contributions, as the SGE current decays with $t_s$ (spin relaxation time) while the CPGE current decays with the $t_p$ (momentum relaxation time).

# Bibliography


[1] R. G. Dickinson and L. Pauling, "The Crystal Structure of Molybdenite", Journal of the American Chemical Society **45**, 1466–1471 (1923).

[2] R. F. Frindt and A. D. Yoffe, "Physical properties of layer structures : optical properties and photoconductivity of thin crystals of molybdenum disulphide", Proceedings of the Royal Society of London. Series A. Mathematical and Physical Sciences **273**, 69–83 (1963).

[3] P. Joensen, R. Frindt, and S. Morrison, "Single-layer MoS2", Materials Research Bulletin **21**, 457–461 (1986).

[4] S. Lebègue and O. Eriksson, "Electronic structure of two-dimensional crystals from ab initio theory", Physical Review B **79**, 115409 (2009).

[5] Q. H. Wang, K. Kalantar-Zadeh, A. Kis, J. N. Coleman, and M. S. Strano, "Electronics and optoelectronics of two-dimensional transition metal dichalcogenides", Nature Nanotechnology **7**, 699–712 (2012).

[6] X. Yin, C. S. Tang, Y. Zheng, J. Gao, J. Wu, H. Zhang, M. Chhowalla, W. Chen, and A. T. S. Wee, "Recent developments in 2D transition metal dichalcogenides: phase transition and applications of the (quasi-)metallic phases", Chemical Society Reviews **50**, 10087–10115 (2021).

[7] A. Splendiani, L. Sun, Y. Zhang, T. Li, J. Kim, C.-Y. Chim, G. Galli, and F. Wang, "Emerging Photoluminescence in Monolayer MoS2", Nano Letters **10**, 1271–1275 (2010).

[8] K. F. Mak, C. Lee, J. Hone, J. Shan, and T. F. Heinz, "Atomically Thin MoS2: A New Direct-Gap Semiconductor", Physical Review Letters **105**, 136805 (2010).

[9] D. MacNeill, G. M. Stiehl, M. H. D. Guimaraes, R. A. Buhrman, J. Park, and D. C. Ralph, "Control of spinorbit torques through crystal symmetry in WTe2/ferromagnet bilayers", Nature Physics **13**, 300–305 (2017).

[10] Y. Ma, B. Liu, A. Zhang, L. Chen, M. Fathi, C. Shen, A. N. Abbas, M. Ge, M. Mecklenburg, and C. Zhou, "Reversible Semiconducting-to-Metallic Phase Transition in Chemical Vapor Deposition Grown Monolayer WSe2 and Applications for Devices", ACS Nano **9**, 7383–7391 (2015).

[11] S. Cho, S. Kim, J. H. Kim, J. Zhao, J. Seok, D. H. Keum, J. Baik, D.-h. Choe, K. J. Chang, K. Suenaga, S. W. Kim, Y. H. Lee, and H. Yang, "Phase patterning for ohmic homojunction contact in MoTe2", Science **349**, 625–628 (2015).

[12] R. Kappera, D. Voiry, S. E. Yalcin, B. Branch, G. Gupta, A. D. Mohite, and M. Chhowalla, "Phase-engineered low-resistance contacts for ultrathin MoS2 transistors", Nature Materials **13**, 1128–1134 (2014).

[13] K.-A. N. Duerloo, Y. Li, and E. J. Reed, "Structural phase transitions in two-dimensional Mo- and W-dichalcogenide monolayers", Nature Communications **5**, 4214 (2014).

[14] D. H. Keum, S. Cho, J. H. Kim, D.-H. Choe, H.-J. Sung, M. Kan, H. Kang, J.-Y. Hwang, S. W. Kim, H. Yang, K. J. Chang, and Y. H. Lee, "Bandgap opening in few-layered monoclinic MoTe2", Nature Physics **11**, 482–486 (2015).

[15] M. A. Py and R. R. Haering, "Structural destabilization induced by lithium intercalation in MoS2 and related compounds", Canadian Journal of Physics **61**, 76–84 (1983).

[16] M. Kertesz and R. Hoffmann, "Octahedral vs. trigonal-prismatic coordination and clustering in transition-metal dichalcogenides", Journal of the American Chemical Society **106**, 3453–3460 (1984).

[17] A. N. Enyashin, L. Yadgarov, L. Houben, I. Popov, M. Weidenbach, R. Tenne, M. Bar-Sadan, and G. Seifert, "New Route for Stabilization of 1T-WS2 and MoS2 Phases", The Journal of Physical Chemistry C **115**, 24586–24591 (2011).

[18] M. Chhowalla, H. S. Shin, G. Eda, L.-J. Li, K. P. Loh, and H. Zhang, "The chemistry of two-dimensional layered transition metal dichalcogenide nanosheets", Nature Chemistry **5**, 263–275 (2013).

[19] L. Sun, X. Yan, J. Zheng, H. Yu, Z. Lu, S.-p. Gao, L. Liu, X. Pan, D. Wang, Z. Wang, P. Wang, and L. Jiao, "Layer-Dependent Chemically Induced Phase Transition of Two-Dimensional MoS2", Nano Letters **18**, 3435–3440 (2018).

[20] Y. Li, K.-A. N. Duerloo, K. Wauson, and E. J. Reed, "Structural semiconductor-to-semimetal phase transition in two-dimensional materials induced by electrostatic gating", Nature Communications **7**, 10671 (2016).

[21] C. Zhang, S. KC, Y. Nie, C. Liang, W. G. Vandenberghe, R. C. Longo, Y. Zheng, F. Kong, S. Hong, R. M. Wallace, and K. Cho, "Charge Mediated Reversible MetalInsulator Transition in Monolayer MoTe2 and WxMo1xTe2 Alloy", ACS Nano **10**, 7370–7375 (2016).

[22] Y. Wang, J. Xiao, H. Zhu, Y. Li, Y. Alsaid, K. Y. Fong, Y. Zhou, S. Wang, W. Shi, Y. Wang, A. Zettl, E. J. Reed, and X. Zhang, "Structural phase transition in monolayer MoTe2 driven by electrostatic doping", Nature **550**, 487–491 (2017).

[23] M. Dave, R. Vaidya, S. G. Patel, and A. R. Jani, "High pressure effect on MoS2 and MoSe2 single crystals grown by CVT method", Bulletin of Materials Science **27**, 213–216 (2004).

[24] S. Song, D. H. Keum, S. Cho, D. Perello, Y. Kim, and Y. H. Lee, "Room Temperature SemiconductorMetal Transition of MoTe2 Thin Films Engineered by Strain", Nano Letters **16**, 188–193 (2016).

[25] Y.-c. Lin, D. O. Dumcenco, Y.-s. Huang, and K. Suenaga, "Atomic mechanism of the semiconducting-to-metallic phase transition in single-layered MoS2", Nature Nanotechnology **9**, 391–396 (2014).

[26] B. Shang, X. Cui, L. Jiao, K. Qi, Y. Wang, J. Fan, Y. Yue, H. Wang, Q. Bao, X. Fan, S. Wei, W. Song, Z. Cheng, S. Guo, and W. Zheng, "Lattice -Mismatch-Induced Ultrastable 1T-Phase MoS2Pd/Au for Plasmon-Enhanced Hydrogen Evolution", Nano Letters **19**, 2758–2764 (2019).

[27] S. Manzeli, D. Ovchinnikov, D. Pasquier, O. V. Yazyev, and A. Kis, "2D transition metal dichalcogenides", Nature Reviews Materials **2**, 17033 (2017).

[28] D. Xiao, M.-C. Chang, and Q. Niu, "Berry phase effects on electronic properties", Reviews of Modern Physics **82**, 1959–2007 (2010).

[29] D. Xiao, G.-B. Liu, W. Feng, X. Xu, and W. Yao, "Coupled Spin and Valley Physics in Monolayers of MoS2 and Other Group-VI Dichalcogenides", Physical Review Letters **108**, 196802 (2012).

[30] K. F. Mak, K. L. McGill, J. Park, and P. L. McEuen, "The valley Hall effect in MoS2 transistors", Science **344**, 1489–1492 (2014).

[31] N. Ubrig, S. Jo, M. Philippi, D. Costanzo, H. Berger, A. B. Kuzmenko, and A. F. Morpurgo, "Microscopic Origin of the Valley Hall Effect in Transition Metal Dichalcogenides Revealed by Wavelength-Dependent Mapping", Nano Letters **17**, 5719–5725 (2017).

[32] K. F. Mak, K. He, J. Shan, and T. F. Heinz, "Control of valley polarization in monolayer MoS2 by optical helicity", Nature Nanotechnology **7**, 494–498 (2012).

[33] H. Zeng, J. Dai, W. Yao, D. Xiao, and X. Cui, "Valley polarization in MoS2 monolayers by optical pumping", Nature Nanotechnology **7**, 490–493 (2012).

[34] T. Cao, G. Wang, W. Han, H. Ye, C. Zhu, J. Shi, Q. Niu, P. Tan, E. Wang, B. Liu, and J. Feng, "Valley-selective circular dichroism of monolayer molybdenum disulphide", Nature Communications **3**, 887 (2012).

[35] W. Yao, D. Xiao, and Q. Niu, "Valley-dependent optoelectronics from inversion symmetry breaking", Physical Review B **77**, 235406 (2008).

[36] Z. Y. Zhu, Y. C. Cheng, and U. Schwingenschlögl, "Giant spin-orbit-induced spin splitting in two-dimensional transition-metal dichalcogenide semiconductors", Physical Review B **84**, 153402 (2011).

[37] X. Xu, W. Yao, D. Xiao, and T. F. Heinz, "Spin and pseudospins in layered transition metal dichalcogenides", Nature Physics **10**, 343–350 (2014).

[38] Y. K. Luo, J. Xu, T. Zhu, G. Wu, E. J. McCormick, W. Zhan, M. R. Neupane, and R. K. Kawakami, "Opto-Valleytronic Spin Injection in Monolayer MoS2/Few-Layer Graphene Hybrid Spin Valves", Nano Letters **17**, 3877–3883 (2017).

[39] A. Avsar, D. Unuchek, J. Liu, O. L. Sanchez, K. Watanabe, T. Taniguchi, B. Özyilmaz, and A. Kis, "Optospintronics in Graphene via Proximity Coupling", ACS Nano **11**, 11678–11686 (2017).

[40] Z. Wang, L. Zhao, K. F. Mak, and J. Shan, "Probing the Spin-Polarized Electronic Band Structure in Monolayer Transition Metal Dichalcogenides by Optical Spectroscopy", Nano Letters **17**, 740–746 (2017).

[41] K. F. Mak, D. Xiao, and J. Shan, "Lightvalley interactions in 2D semiconductors", Nature Photonics **12**, 451–460 (2018).

[42] Stephen Blundell, "Magnetism in Condensed Matter", Oxford University Press, 80–81 (2001).

[43] S. J. Barnett, "Magnetization by Rotation", Physical Review **6**, 239–270 (1915).

[44] A. Einstein and W. J. de Haas, "Experimental proof of the existence of Ampère's molecular currents", Koninklijke Akademie van Wetenschappen te Amsterdam, Proceedings **18**, 696–711 (1915).

[45] V. P. Amin, P. M. Haney, and M. D. Stiles, "Interfacial spinorbit torques", Journal of Applied Physics **128**, 151101 (2020).

[46] P. M. Haney and M. D. Stiles, "Current-Induced Torques in the Presence of Spin-Orbit Coupling", Physical Review Letters **105**, 126602 (2010).

[47] D. Go, F. Freimuth, J.-P. Hanke, F. Xue, O. Gomonay, K.-J. Lee, S. Blügel, P. M. Haney, H.-W. Lee, and Y. Mokrousov, "Theory of current-induced angular momentum transfer dynamics in spin-orbit coupled systems", Physical Review Research **2**, 033401 (2020).

[48] M. B. Jungfleisch and A. Hoffmann, "A new twist on phonons", Nature Physics **14**, 433–434 (2018).

[49] G. Zolfagharkhani, A. Gaidarzhy, P. Degiovanni, S. Kettemann, P. Fulde, and P. Mohanty, "Nanomechanical detection of itinerant electron spin flip", Nature Nanotechnology **3**, 720–723 (2008).

[50] G. Stiehl, "Crystal Symmetry and Spin-Orbit Torques", PhD thesis (Cornell University, 2018), pp. 1–203.

[51] M. Hayashi, J. Kim, M. Yamanouchi, and H. Ohno, "Quantitative characterization of the spin-orbit torque using harmonic Hall voltage measurements", Physical Review B **89**, 144425 (2014).

[52] X. Zhang and W. Butler, "Theory of Giant Magnetoresistance and Tunneling Magnetoresistance", in *Handbook of spintronics* (Springer Netherlands, Dordrecht, 2016), pp. 3–69.

[53] A. Manchon, J. elezný, I. M. Miron, T. Jungwirth, J. Sinova, A. Thiaville, K. Garello, and P. Gambardella, "Current-induced spin-orbit torques in ferromagnetic and antiferromagnetic systems", Reviews of Modern Physics **91**, 035004 (2019).

[54] M. C. Hickey and J. S. Moodera, "Origin of Intrinsic Gilbert Damping", Physical Review Letters **102**, 137601 (2009).

[55] P. M. Haney, H.-W. Lee, K.-J. Lee, A. Manchon, and M. D. Stiles, "Current induced torques and interfacial spin-orbit coupling: Semiclassical modeling", Physical Review B **87**, 174411 (2013).

[56] V. E. Demidov, S. Urazhdin, E. R. J. Edwards, M. D. Stiles, R. D. McMichael, and S. O. Demokritov, "Control of Magnetic Fluctuations by Spin Current", Physical Review Letters **107**, 107204 (2011).

[57] M.-H. Nguyen and C.-F. Pai, "Spinorbit torque characterization in a nutshell", APL Materials **9**, 1–15 (2021).

[58] J. Sinova, S. O. Valenzuela, J. Wunderlich, C. H. Back, and T. Jungwirth, "Spin Hall effects", Reviews of Modern Physics **87**, 1213–1260 (2015).

[59] M. Dyakonov and V. Perel, "Current-induced spin orientation of electrons in semiconductors", Physics Letters A **35**, 459–460 (1971).

[60] J. E. Hirsch, "Spin Hall Effect", Physical Review Letters **83**, 1834–1837 (1999).

[61] S. Zhang, "Spin Hall Effect in the Presence of Spin Diffusion", Physical Review Letters **85**, 393–396 (2000).

[62] Y. K. Kato, R. C. Myers, A. C. Gossard, and D. D. Awschalom, "Current-Induced Spin Polarization in Strained Semiconductors", Physical Review Letters **93**, 176601 (2004).

[63] C. Day, "Two Groups Observe the Spin Hall Effect in Semiconductors", Physics Today **58**, 17–19 (2005).

[64] J. Wunderlich, B. Kaestner, J. Sinova, and T. Jungwirth, "Experimental Observation of the Spin-Hall Effect in a Two-Dimensional Spin-Orbit Coupled Semiconductor System", Physical Review Letters **94**, 047204 (2005).

[65] S. O. Valenzuela and M. Tinkham, "Direct electronic measurement of the spin Hall effect", Nature **442**, 176–179 (2006).

[66] National Institute of Standards and Technology, *Reduced Planck Constant*, 2023.

[67] N. F. Mott, "The scattering of fast electrons by atomic nuclei", Proceedings of the Royal Society of London. Series A, Containing Papers of a Mathematical and Physical Character **124**, 425–442 (1929).

[68] A. Hoffmann, "Spin Hall Effects in Metals", IEEE Transactions on Magnetics **49**, 5172–5193 (2013).

[69] C. Brüne, A. Roth, E. G. Novik, M. König, H. Buhmann, E. M. Hankiewicz, W. Hanke, J. Sinova, and L. W. Molenkamp, "Evidence for the ballistic intrinsic spin Hall effect in HgTe nanostructures", Nature Physics **6**, 448–454 (2010).

[70] T. Kimura, Y. Otani, T. Sato, S. Takahashi, and S. Maekawa, "Room-Temperature Reversible Spin Hall Effect", Physical Review Letters **98**, 156601 (2007).

[71] K. Ando, S. Takahashi, K. Harii, K. Sasage, J. Ieda, S. Maekawa, and E. Saitoh, "Electric Manipulation of Spin Relaxation Using the Spin Hall Effect", Physical Review Letters **101**, 036601 (2008).

[72] L. Liu, O. J. Lee, T. J. Gudmundsen, D. C. Ralph, and R. A. Buhrman, "Current-Induced Switching of Perpendicularly Magnetized Magnetic Layers Using Spin Torque from the Spin Hall Effect", Physical Review Letters **109**, 096602 (2012).

[73] H. Kurebayashi, J. Sinova, D. Fang, A. C. Irvine, J. Wunderlich, V. Novak, R. P. Campion, B. L. Gallagher, E. K. Vehstedt, L. P. Zarbo, K. Vyborny, A. J. Ferguson, and T. Jungwirth, "Observation of a Berry phase anti-damping spin-orbit torque", arXiv preprint, 1–23 (2013).

[74] M.-h. Nguyen, D. C. Ralph, and R. A. Buhrman, "Spin Torque Study of the Spin Hall Conductivity and Spin Diffusion Length in Platinum Thin Films with Varying Resistivity", Physical Review Letters **116**, 126601 (2016).

[75] B. A. Bernevig, T. L. Hughes, and S.-C. Zhang, "Orbitronics: The Intrinsic Orbital Current in p-Doped Silicon", Physical Review Letters **95**, 066601 (2005).

[76] T. Tanaka, H. Kontani, M. Naito, T. Naito, D. S. Hirashima, K. Yamada, and J. Inoue, "Intrinsic spin Hall effect and orbital Hall effect in 4d and 5d transition metals", Physical Review B **77**, 165117 (2008).

[77] H. Kontani, T. Tanaka, D. S. Hirashima, K. Yamada, and J. Inoue, "Giant Orbital Hall Effect in Transition Metals: Origin of Large Spin and Anomalous Hall Effects", Physical Review Letters **102**, 016601 (2009).

[78] D. Go, D. Jo, C. Kim, and H.-W. Lee, "Intrinsic Spin and Orbital Hall Effects from Orbital Texture", Physical Review Letters **121**, 086602 (2018).

[79] D. Go and H.-W. Lee, "Orbital torque: Torque generation by orbital current injection", Physical Review Research **2**, 013177 (2020).

[80] K.-u. Demasius, T. Phung, W. Zhang, B. P. Hughes, S.-H. Yang, A. Kellock, W. Han, A. Pushp, and S. S. P. Parkin, "Enhanced spinorbit torques by oxygen incorporation in tungsten films", Nature Communications **7**, 10644 (2016).

[81] H. An, Y. Kanno, A. Asami, and K. Ando, "Giant spin-torque generation by heavily oxidized Pt", Physical Review B **98**, 014401 (2018).

[82] H. An, T. Ohno, Y. Kanno, Y. Kageyama, Y. Monnai, H. Maki, J. Shi, and K. Ando, "Current-induced magnetization switching using an electrically insulating spin-torque generator", Science Advances **4**, 1–8 (2018).

[83] A. Manchon, H. C. Koo, J. Nitta, S. M. Frolov, and R. A. Duine, "New perspectives for Rashba spinorbit coupling", Nature Materials **14**, 871–882 (2015).

[84] Y. A. Bychkov and E. I. Rashba, "Properties of a 2D electron gas with lifted spectral degeneracy", JETP Letters **39**, 78–81 (1984).

[85] V. Edelstein, "Spin polarization of conduction electrons induced by electric current in two-dimensional asymmetric electron systems", Solid State Communications **73**, 233–235 (1990).

[86] I. M. Miron, K. Garello, G. Gaudin, P.-J. Zermatten, M. V. Costache, S. Auffret, S. Bandiera, B. Rodmacq, A. Schuhl, and P. Gambardella, "Perpendicular switching of a single ferromagnetic layer induced by in-plane current injection", Nature **476**, 189–193 (2011).

[87] A. Manchon and S. Zhang, "Theory of nonequilibrium intrinsic spin torque in a single nanomagnet", Physical Review B **78**, 212405 (2008).

[88] A. Manchon and S. Zhang, "Theory of spin torque due to spin-orbit coupling", Physical Review B **79**, 094422 (2009).

[89] Q. Shao, G. Yu, Y.-W. Lan, Y. Shi, M.-Y. Li, C. Zheng, X. Zhu, L.-J. Li, P. K. Amiri, and K. L. Wang, "Strong Rashba-Edelstein Effect-Induced SpinOrbit Torques in Monolayer Transition Metal Dichalcogenide/Ferromagnet Bilayers", Nano Letters **16**, 7514–7520 (2016).

[90] W. Lv, Z. Jia, B. Wang, Y. Lu, X. Luo, B. Zhang, Z. Zeng, and Z. Liu, "Electric-Field Control of SpinOrbit Torques in WS2/Permalloy Bilayers", ACS Applied Materials & Interfaces **10**, 2843–2849 (2018).

[91] M. H. D. Guimarães, G. M. Stiehl, D. MacNeill, N. D. Reynolds, and D. C. Ralph, "SpinOrbit Torques in NbSe2/Permalloy Bilayers", Nano Letters **18**, 1311–1316 (2018).

[92] I. Mihai Miron, G. Gaudin, S. Auffret, B. Rodmacq, A. Schuhl, S. Pizzini, J. Vogel, and P. Gambardella, "Current-driven spin torque induced by the Rashba effect in a ferromagnetic metal layer", Nature Materials **9**, 230–234 (2010).

[93] I. M. Miron, T. Moore, H. Szambolics, L. D. Buda-Prejbeanu, S. Auffret, B. Rodmacq, S. Pizzini, J. Vogel, M. Bonfim, A. Schuhl, and G. Gaudin, "Fast current-induced domain-wall motion controlled by the Rashba effect", Nature Materials **10**, 419–423 (2011).

[94] L. Liu, T. Moriyama, D. C. Ralph, and R. A. Buhrman, "Spin-Torque Ferromagnetic Resonance Induced by the Spin Hall Effect", Physical Review Letters **106**, 036601 (2011).

[95] L. Liu, C.-F. Pai, Y. Li, H. W. Tseng, D. C. Ralph, and R. a. Buhrman, "Spin-Torque Switching with the Giant Spin Hall Effect of Tantalum", Science **336**, 555–558 (2012).

[96] W. Zhang, J. Sklenar, B. Hsu, W. Jiang, M. B. Jungfleisch, J. Xiao, F. Y. Fradin, Y. Liu, J. E. Pearson, J. B. Ketterson, Z. Yang, and A. Hoffmann, "Research Update: Spin transfer torques in permalloy on monolayer MoS2", APL Materials **4**, 1–9 (2016).

[97] H.-R. Lee, K. Lee, J. Cho, Y.-H. Choi, C.-Y. You, M.-H. Jung, F. Bonell, Y. Shiota, S. Miwa, and Y. Suzuki, "Spin-orbit torque in a bulk perpendicular magnetic anisotropy Pd/FePd/MgO system", Scientific Reports **4**, 6548 (2014).

[98] M. Jamali, K. Narayanapillai, X. Qiu, L. M. Loong, A. Manchon, and H. Yang, "Spin-Orbit Torques in Co/Pd Multilayer Nanowires", Physical Review Letters **111**, 246602 (2013).

[99] A. R. Mellnik, J. S. Lee, A. Richardella, J. L. Grab, P. J. Mintun, M. H. Fischer, A. Vaezi, A. Manchon, E.-A. Kim, N. Samarth, and D. C. Ralph, "Spin-transfer torque generated by a topological insulator", Nature **511**, 449–451 (2014).

[100] A. Kalitsov, S. A. Nikolaev, J. Velev, M. Chshiev, and O. Mryasov, "Intrinsic spin-orbit torque in a single-domain nanomagnet", Physical Review B **96**, 214430 (2017).

[101] K. Zollner, M. D. Petrovi, K. Dolui, P. Plechá, B. K. Nikoli, and J. Fabian, "Scattering-induced and highly tunable by gate damping-like spin-orbit torque in graphene doubly proximitized by two-dimensional magnet Cr2Ge2Te6 and monolayer WS2", Physical Review Research **2**, 043057 (2020).

[102] F. Sousa, G. Tatara, and A. Ferreira, "Skew-scattering-induced giant antidamping spin-orbit torques: Collinear and out-of-plane Edelstein effects at two-dimensional material/ferromagnet interfaces", Physical Review Research **2**, 043401 (2020).

[103] V. P. Amin, J. Zemen, and M. D. Stiles, "Interface-Generated Spin Currents", Physical Review Letters **121**, 136805 (2018).

[104] X. Fan, H. Celik, J. Wu, C. Ni, K.-J. Lee, V. O. Lorenz, and J. Q. Xiao, "Quantifying interface and bulk contributions to spinorbit torque in magnetic bilayers", Nature Communications **5**, 3042 (2014).

[105] Y. Fan, P. Upadhyaya, X. Kou, M. Lang, S. Takei, Z. Wang, J. Tang, L. He, L.-t. Chang, M. Montazeri, G. Yu, W. Jiang, T. Nie, R. N. Schwartz, Y. Tserkovnyak, and K. L. Wang, "Magnetization switching through giant spinorbit torque in a magnetically doped topological insulator heterostructure", Nature Materials **13**, 699–704 (2014).

[106] T. Gao, A. Qaiumzadeh, H. An, A. Musha, Y. Kageyama, J. Shi, and K. Ando, "Intrinsic Spin-Orbit Torque Arising from the Berry Curvature in a Metallic-Magnet/Cu-Oxide Interface", Physical Review Letters **121**, 017202 (2018).

[107] V. P. Amin and M. D. Stiles, "Spin transport at interfaces with spin-orbit coupling: Phenomenology", Physical Review B **94**, 104420 (2016).

[108] V. P. Amin and M. D. Stiles, "Spin transport at interfaces with spin-orbit coupling: Formalism", Physical Review B **94**, 104419 (2016).

[109] K. D. Belashchenko, A. A. Kovalev, and M. van Schilfgaarde, "Theory of Spin Loss at Metallic Interfaces", Physical Review Letters **117**, 207204 (2016).

[110] L. Zhu, D. C. Ralph, and R. A. Buhrman, "Spin-Orbit Torques in Heavy-MetalFerromagnet Bilayers with Varying Strengths of Interfacial Spin-Orbit Coupling", Physical Review Letters **122**, 077201 (2019).

[111] K. Dolui and B. K. Nikoli, "Spin-memory loss due to spin-orbit coupling at ferromagnet/heavy-metal interfaces: Ab initio spin-density matrix approach", Physical Review B **96**, 220403 (2017).

[112] C. Safranski, E. A. Montoya, and I. N. Krivorotov, "Spinorbit torque driven by a planar Hall current", Nature Nanotechnology **14**, 27–30 (2019).

[113] M. Haidar, A. A. Awad, M. Dvornik, R. Khymyn, A. Houshang, and J. Åkerman, "A single layer spin-orbit torque nano-oscillator", Nature Communications **10**, 2362 (2019).

[114] W. Wang, T. Wang, V. P. Amin, Y. Wang, A. Radhakrishnan, A. Davidson, S. R. Allen, T. J. Silva, H. Ohldag, D. Balzar, B. L. Zink, P. M. Haney, J. Q. Xiao, D. G. Cahill, V. O. Lorenz, and X. Fan, "Anomalous spinorbit torques in magnetic single-layer films", Nature Nanotechnology **14**, 819–824 (2019).

[115] R. W. Greening, D. A. Smith, Y. Lim, Z. Jiang, J. Barber, S. Dail, J. J. Heremans, and S. Emori, "Current-induced spinorbit field in permalloy interfaced with ultrathin Ti and Cu", Applied Physics Letters **116**, 052402 (2020).

[116] L. Liu, J. Yu, R. González-Hernández, C. Li, J. Deng, W. Lin, C. Zhou, T. Zhou, J. Zhou, H. Wang, R. Guo, H. Y. Yoong, G. M. Chow, X. Han, B. Dupé, J. elezný, J. Sinova, and J. Chen, "Electrical switching of perpendicular magnetization in a single ferromagnetic layer", Physical Review B **101**, 220402 (2020).

[117] M. Tang, K. Shen, S. Xu, H. Yang, S. Hu, W. Lü, C. Li, M. Li, Z. Yuan, S. J. Pennycook, K. Xia, A. Manchon, S. Zhou, and X. Qiu, "Bulk Spin TorqueDriven Perpendicular Magnetization Switching in L10 FePt Single Layer", Advanced Materials **32**, 2002607 (2020).

[118] H. Kurebayashi, J. Sinova, D. Fang, A. C. Irvine, T. D. Skinner, J. Wunderlich, V. Novák, R. P. Campion, B. L. Gallagher, E. K. Vehstedt, L. P. Zârbo, K. Výborný, A. J. Ferguson, and T. Jungwirth, "An antidamping spinorbit torque originating from the Berry curvature", Nature Nanotechnology **9**, 211–217 (2014).

[119] C. O. Avci, J. Mendil, G. S. Beach, and P. Gambardella, "Origins of the Unidirectional Spin Hall Magnetoresistance in Metallic Bilayers", Physical Review Letters **121**, 087207 (2018).

[120] C. O. Avci, K. Garello, A. Ghosh, M. Gabureac, S. F. Alvarado, and P. Gambardella, "Unidirectional spin Hall magnetoresistance in ferromagnet/normal metal bilayers", Nature Physics **11**, 570–575 (2015).

[121] G. Liu, X.-g. Wang, Z. Z. Luan, L. F. Zhou, S. Y. Xia, B. Yang, Y. Z. Tian, G.-h. Guo, J. Du, and D. Wu, "Magnonic Unidirectional Spin Hall Magnetoresistance in a Heavy-MetalFerromagnetic-Insulator Bilayer", Physical Review Letters **127**, 207206 (2021).

[122] Y. Cheng, J. Tang, J. J. Michel, S. K. Chong, F. Yang, R. Cheng, and K. L. Wang, "Unidirectional Spin Hall Magnetoresistance in Antiferromagnetic Heterostructures", Physical Review Letters **130**, 086703 (2023).

[123] S. S. Zhang and G. Vignale, "Theory of unidirectional spin Hall magnetoresistance in heavy-metal/ferromagnetic-metal bilayers", Physical Review B **94**, 140411 (2016).

[124] K. Yasuda, A. Tsukazaki, R. Yoshimi, K. S. Takahashi, M. Kawasaki, and Y. Tokura, "Large Unidirectional Magnetoresistance in a Magnetic Topological Insulator", Physical Review Letters **117**, 127202 (2016).

[125] K. Yasuda, A. Tsukazaki, R. Yoshimi, K. Kondou, K. S. Takahashi, Y. Otani, M. Kawasaki, and Y. Tokura, "Current-Nonlinear Hall Effect and Spin-Orbit Torque Magnetization Switching in a Magnetic Topological Insulator", Physical Review Letters **119**, 137204 (2017).

[126] J. elezný, H. Gao, A. Manchon, F. Freimuth, Y. Mokrousov, J. Zemen, J. Maek, J. Sinova, and T. Jungwirth, "Spin-orbit torques in locally and globally noncentrosymmetric crystals: Antiferromagnets and ferromagnets", Physical Review B **95**, 014403 (2017).

[127] M. Fox, *Optical Properties of Solids*, second edi (CRC Press, Oxford, United Kingdom, Apr. 2010) Chap. 1, pp. 1–396.

[128] Y. Liu and Q. Shao, "Two-Dimensional Materials for Energy-Efficient Spin-Orbit Torque Devices", ACS Nano **14**, 9389–9407 (2020).

[129] C. Ciccarelli, L. Anderson, V. Tshitoyan, A. J. Ferguson, F. Gerhard, C. Gould, L. W. Molenkamp, J. Gayles, J. elezný, L. mejkal, Z. Yuan, J. Sinova, F. Freimuth, and T. Jungwirth, "Room-temperature spinorbit torque in NiMnSb", Nature Physics **12**, 855–860 (2016).

[130] G. Yu, P. Upadhyaya, Y. Fan, J. G. Alzate, W. Jiang, K. L. Wong, S. Takei, S. A. Bender, L.-T. Chang, Y. Jiang, M. Lang, J. Tang, Y. Wang, Y. Tserkovnyak, P. K. Amiri, and K. L. Wang, "Switching of perpendicular magnetization by spinorbit torques in the absence of external magnetic fields", Nature Nanotechnology **9**, 548–554 (2014).

[131] C.-F. Pai, M. Mann, A. J. Tan, and G. S. D. Beach, "Determination of spin torque efficiencies in heterostructures with perpendicular magnetic anisotropy", Physical Review B **93**, 144409 (2016).

[132] D. Fang, H. Kurebayashi, J. Wunderlich, K. Výborný, L. P. Zârbo, R. P. Campion, A. Casiraghi, B. L. Gallagher, T. Jungwirth, and A. J. Ferguson, "Spinorbit-driven ferromagnetic resonance", Nature Nanotechnology **6**, 413–417 (2011).

[133] T. D. Skinner, K. Olejník, L. K. Cunningham, H. Kurebayashi, R. P. Campion, B. L. Gallagher, T. Jungwirth, and A. J. Ferguson, "Complementary spin-Hall and inverse spin-galvanic effect torques in a ferromagnet/semiconductor bilayer", Nature Communications **6**, 6730 (2015).

[134] D. MacNeill, G. M. Stiehl, M. H. D. Guimarães, N. D. Reynolds, R. A. Buhrman, and D. C. Ralph, "Thickness dependence of spin-orbit torques generated by WTe2", Physical Review B **96**, 054450 (2017).

[135] P. Li, W. Wu, Y. Wen, C. Zhang, J. Zhang, S. Zhang, Z. Yu, S. A. Yang, A. Manchon, and X.-x. Zhang, "Spin-momentum locking and spin-orbit torques in magnetic nano-heterojunctions composed of Weyl semimetal WTe2", Nature Communications **9**, 3990 (2018).

[136] S. Shi, S. Liang, Z. Zhu, K. Cai, S. D. Pollard, Y. Wang, J. Wang, Q. Wang, P. He, J. Yu, G. Eda, G. Liang, and H. Yang, "All-electric magnetization switching and DzyaloshinskiiMoriya interaction in WTe2/ferromagnet heterostructures", Nature Nanotechnology **14**, 945–949 (2019).

[137] B. Zhao, D. Khokhriakov, Y. Zhang, H. Fu, B. Karpiak, A. M. Hoque, X. Xu, Y. Jiang, B. Yan, and S. P. Dash, "Observation of charge to spin conversion in Weyl semimetal WTe2 at room temperature", Physical Review Research **2**, 013286 (2020).

[138] G. M. Stiehl, R. Li, V. Gupta, I. E. Baggari, S. Jiang, H. Xie, L. F. Kourkoutis, K. F. Mak, J. Shan, R. A. Buhrman, and D. C. Ralph, "Layer-dependent spin-orbit torques generated by the centrosymmetric transition metal dichalcogenide $\beta$-MoTe2", Physical Review B **100**, 184402 (2019).

[139] G. M. Stiehl, D. MacNeill, N. Sivadas, I. El Baggari, M. H. D. Guimarães, N. D. Reynolds, L. F. Kourkoutis, C. J. Fennie, R. A. Buhrman, and D. C. Ralph, "Current-Induced Torques with Dresselhaus Symmetry Due to Resistance Anisotropy in 2D Materials", ACS Nano **13**, 2599–2605 (2019).

[140] L. Ju, J. Velasco, E. Huang, S. Kahn, C. Nosiglia, H.-Z. Tsai, W. Yang, T. Taniguchi, K. Watanabe, Y. Zhang, G. Zhang, M. Crommie, A. Zettl, and F. Wang, "Photoinduced doping in heterostructures of graphene and boron nitride", Nature Nanotechnology **9**, 348–352 (2014).

[141] L. Vicarelli, M. S. Vitiello, D. Coquillat, A. Lombardo, A. C. Ferrari, W. Knap, M. Polini, V. Pellegrini, and A. Tredicucci, "Graphene field-effect transistors as room-temperature terahertz detectors", Nature Materials **11**, 865–871 (2012).

[142] M. Freitag, T. Low, F. Xia, and P. Avouris, "Photoconductivity of biased graphene", Nature Photonics **7**, 53–59 (2013).

[143] M. Cutler and N. F. Mott, "Observation of Anderson Localization in an Electron Gas", Physical Review **181**, 1336–1340 (1969).

[144] P. Wei, W. Bao, Y. Pu, C. N. Lau, and J. Shi, "Anomalous Thermoelectric Transport of Dirac Particles in Graphene", Physical Review Letters **102**, 166808 (2009).

[145] Y. M. Zuev, W. Chang, and P. Kim, "Thermoelectric and Magnetothermoelectric Transport Measurements of Graphene", Physical Review Letters **102**, 096807 (2009).

[146] S. D. Ganichev and W. Prettl, "Spin photocurrents in quantum wells", Journal of Physics: Condensed Matter **15**, R935–R983 (2003).

[147] M. I. Dyakonov, *Spin Physics in Semiconductors*, edited by M. I. Dyakonov, Vol. 157, Springer Series in Solid-State Sciences (Springer Berlin Heidelberg, Berlin, Heidelberg, 2008), p. 532.

[148] E. Ivchenko and G. Pikus, "New photogalvanic effect in gyrotropic crystals", JETP Letters **27**, 604–608 (1978).

[149] V. Belinicher, "Space-oscillating photocurrent in crystals without symmetry center", Physics Letters A **66**, 213–214 (1978).

[150] V. M. Asnin, A. A. Bakun, A. M. Danishevskii, E. L. Ivchenko, G. E. Pikus, and A. A. Rogachev, "Observation of a photo-emf that depends on the sign of the circular polarization of the light", ZhETF Pisma Redaktsiiu **28**, 80–84 (1978).

[151] H. Yuan, X. Wang, B. Lian, H. Zhang, X. Fang, B. Shen, G. Xu, Y. Xu, S.-C. Zhang, H. Y. Hwang, and Y. Cui, "Generation and electric control of spinvalley-coupled circular photogalvanic current in WSe2", Nature Nanotechnology **9**, 851–857 (2014).

[152] M. Eginligil, B. Cao, Z. Wang, X. Shen, C. Cong, J. Shang, C. Soci, and T. Yu, "Dichroic spinvalley photocurrent in monolayer molybdenum disulphide", Nature Communications **6**, 7636 (2015).

[153] J. Quereda, T. S. Ghiasi, J.-S. You, J. van den Brink, B. J. van Wees, and C. H. van der Wal, "Symmetry regimes for circular photocurrents in monolayer MoSe2", Nature Communications **9**, 3346 (2018).

[154] E. Ivchenko, Y. Lyanda-Geller, and G. Pikus, "Circular magnetophotocurrent and spin splitting of band states in optically-inactive crystals", Solid State Communications **69**, 663–665 (1989).

[155] S. D. Ganichev, E. L. Ivchenko, V. V. Bel'kov, S. A. Tarasenko, M. Sollinger, D. Weiss, W. Wegscheider, and W. Prettl, "Spin-galvanic effect", Nature **417**, 153–156 (2002).

# chapter 3

## Experimental Methods

*In this chapter, the experimental methods used to both fabricate the devices and perform the subsequent electrical and optical measurements are described. The chapter starts with a description of the device fabrication for spin-orbit torque devices and photodiodes, which includes the exfoliation and identification of two-dimensional van der Waals materials, the polymer-free PMMA mask preparation and the subsequent transfer on top of the substrate, electron-beam lithography, electron-beam evaporation, and plasma etching. Next, the electrical characterization using 2-probe, 3-probe, and 4-probe measurements are outlined. The electrical setup used to measure the spin-orbit torques by means of the harmonic Hall technique is described, and the relevant effects involved in these measurements are discussed. Lastly, the setup used for the optoelectronic measurements are described, which include both the scanning photocurrent measurement and polarization-dependent photocurrent measurement setup.*

## 3.1. Device fabrication

In this section, I will describe the methods used for fabricating the devices discussed in this thesis from start to finish. It starts with the exfoliation of bulk 2D materials using the famous "Scotch tape method", and the subsequent characterization using optical contrast, atomic force microscopy and Raman spectroscopy. In addition, I will describe a polymer-free technique used to reduce the polymer contamination on the interface of 2D materials during device fabrication. Lastly, the final contact fabrication methods are described covering the steps of electron beam lithography, electron beam evaporation, and plasma etching.



### 3.1.1. Exfoliation an characterization of 2D materials

A variety of techniques can be used to obtain 2D van der Waals materials in different thicknesses. These can be subdivided in bottom-up approaches, where the atomic layers are grown atom-by-atom, or top-down approaches, where you start with a bulk crystal and thin it down. A prominent example of a bottom-up approach is chemical vapor deposition (CVD) [1, 2], while common top-down approaches are liquid phase exfoliation [3], and mechanical exfoliation [4, 5]. With mechanical exfoliation, one starts with a bulk crystal (few millimeters in size) of the desired 2D material (e.g. graphite, $WSe_2$, $WS_2$, $MoSe_2$, etc.), which is subsequently thinned down using sticky tape. The method of using adhesive tape to obtain thin layers of 2D van der Waals materials was already used in 1963 [6] and was further developed by Novoselov et al. [7] where they showed that it was possible to obtain monolayer flakes of graphene using this seemingly simple technique. The advantage of mechanical exfoliation, is that it is a relatively easy and cheap method to obtain 2D van der Waals materials in a range of different thicknesses. The disadvantage, however, is that the yield of 2D material flakes and their position on the substrate are unpredictable, and their size relatively small (∼µm). Therefore, mechanical exfoliation is primarily used for fundamental research, like the research presented in Chapters 5, 7, and 8 of this thesis. The steps are described below.

First, using regular Scotch tape (3M), a layer of the material is cleaved from the bulk crystal, as shown in Fig. 3.1. Subsequently, this piece of scotch tape is fixed on to a table with the sticky side facing up. This piece of scotch tape is now used as a source to cover a new piece of a different tape, called Nitto tape, which reduces the amount of residual glue on to the final silicon/silicon-oxide ($Si/SiO_2$) substrate. The Nitto tape is repeatedly pressed on to the source scotch tape in an array-like fashion to increases the area on the Nitto tape which is covered by the 2D material. This increased area is useful as a larger substrate can be covered with the 2D material in the final step, which in turn increases the chances of finding a suitable flake. Next, to reduce the layer thickness of the 2D material on the tape further, a new piece of clean Nitto tape is put onto the covered Nitto tape and subsequently exfoliated. This last step is repeated 3 to 4 times, after which the covered Nitto tape is placed onto the final $Si/SiO_2$ substrate to transfer the thin flakes onto the substrate.

This technique can be used for multiple van der Waals materials, e.g. graphene, hBN, $MoS_2$, $MoSe_2$, $WSe_2$, $Fe_{3\text{-}5}GeTe_2$, $MoTe_2$, etc. However, these different materials possess different strengths of interlayer van der Waals interactions and in-

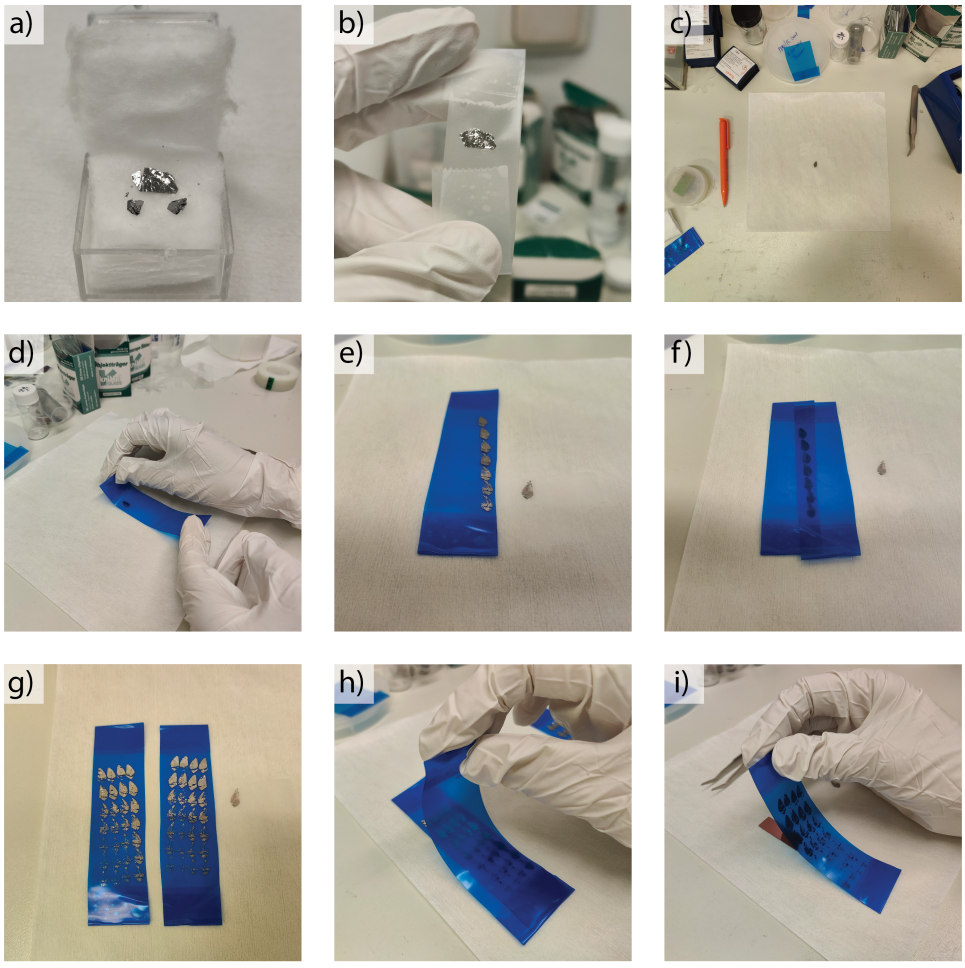


Figure 3.1: Photos of the exfoliation process. (a) A bulk crystal of $WSe_2$ is put on a piece of scotch tape (b), and subsequently cleaved to obtain a thin layer of the bulk crystal on the tape. (c) The piece of scotch tape is taped on to a cleanroom tissue with the $WSe_2$ crystal facing up. (d) This will be used as a source for the coverage of a piece of Nitto tape (blue tape). (e) The Nitto tape is repeatedly pressed on the cleaved $WSe_2$ on the scotch tape to cover a larger area with the TMD. (f) Using another piece of Nitto tape, the area covered with $WSe_2$ is further increase, until both pieces of Nitto tape are fully covered, as in (g). (h) To further thin down the layers of $WSe_2$ on these pieces of Nitto tape, multiple new exfoliation steps can be performed until the desired thickness is obtained. (i) As a final step, the piece of Nitto tape is placed onto the final $Si/SiO_2$ substrate to transfer the thin flakes onto the substrate.

tralayer covalent bonding, which results in different exfoliation characteristics for each material. Likewise, the coverage and yield of the material on the final $Si/SiO_2$ differs significantly for the different 2D van der Waals materials. Other techniques can be used to enhance the interaction between the 2D van der Waals material and $Si/SiO_2$ to enhance the coverage and yield of usable flakes [8]. Treating the $Si/SiO_2$

substrate by $O_2$-plasma causes dangling bonds of the $SiO_2$ resulting in a stronger interaction between the 2D material and substrate, and consequently, in a larger density of transferred flakes. Another technique to increase the interaction between the 2D van der Waals material and the substrate is to anneal the $Si/SiO_2$ with the Nitto tape on top, prior to removing the Nitto tape. Here, the interaction increases as gas bubbles which are trapped between the material and substrate are removed, effectively increasing the interaction area between the flake and the substrate. Note, however, that the increased interaction between the flake and the $Si/SiO_2$ makes it more difficult to pick up the flake from the substrate. The increased interaction can be useful for 2D van der Waals materials which interact only weakly with the substrate, making it easier to exfoliate them and increasing their yield. Also for the fabrication of twisted bilayer graphene (tBLG) samples it can be useful to increase the interaction between the substrate and graphene, as for this particular case, the monolayer graphene flake is cut into two using an AFM tip [9]. With only a weak interaction, the flake will more easily fold and crumble while making a cut.

After transfering the exfoliated flakes on to the $Si/SiO_2$, an optical microscope is used to scan the substrate for desirable flakes, e.g. large enough size ($\sim 5 \times 10$ $\mu m^2$), thickness, shape, surrounding, roughness, etc. The position of each flake on the substrate that fits these criteria is tracked by making a mark on the edge of the substrate with a sharpy or by outlining the substrate on the computer and indicate the position there. The thickness of the flake can initially be estimated using optical contrast, which depends on the thickness of both the flake and the $SiO_2$ [10, 11]. A $SiO_2$ of 285 nm is used as this was shown to enhance the contrast of monolayer graphene and TMD flakes, making them easier to find during scanning [12–14].

Atomic force microscopy, AFM, can be used in conjunction to verify the thickness of the flake and measure the flake roughness [15, 16]. Especially for Chapter 5, where the thickness dependence of the observed spin-orbit torques is measured, it is important to have an accurate measurement on the thickness. Furthermore, AFM allows us to measure the surface roughness of the flakes, which is an important parameter for a pristine interface between the ferromagnet deposited on top of the TMD flake. For the spin-orbit torque devices in this thesis, only flakes with a surface roughness of $< 400$ pm are selected for further device fabrication.

When some usable flakes are found, one can continue to the next step, which for spin-orbit torque devices is the deposition of a ferromagnet on top of the selected flakes using a polymer-free technique. This is discussed in the next section.

### 3.1.2. Permalloy Hall bar deposition using a PMMA mask

For the SOT devices in Chapters 5 and 6, a Hall bar of permalloy is deposited on top of the TMD. With regular lithography techniques, a layer of electron beam resist (polymethyl methacrylate (PMMA)) is spin-coated on top of the wafer prior to exposing the Hall bar with electron beam lithography. However, after developing the exposed PMMA regions, some residual polymers remain which contaminate the interface. As the spin-orbit torques in HM/FM bilayers are ascribed to the interaction between the FM and the HM, a pristine interface is of paramount importance to reduce spin relaxation, spin memory loss, or spin-filtering, which would reduce the

SOT strength. To reduce the interface contamination during device fabrication, we developed a fabrication method for spin-orbit torque devices using a polymer-free technique. This process is descibed in detail below, but in general terms it involves the following. First, a PMMA mask with prepatterned Hall bars is fabricated on a separate $Si/SiO_2$ dummy substrate. Subsequently, this PMMA mask is lifted from the dummy substrate and transferred onto an in-house holder, which allows to mechanically align and place the mask on top of the desired flake. In this way, the interface of the flake which will be in contact with the permalloy, will not be in contact with the PMMA, and so, no residual polymers contaminate the HM/FM interface.



Now, knowing the general steps involved, the method is described in more detail below. To start off, the method to prepare the mask is described in steps:

- First, a dummy $Si/SiO_2$ wafer with a size of $18\times35$ mm$^2$ is prepared for the PMMA mask. These dimensions are used such that the PMMA mask will fit nicely onto the holder used to place the mask onto the sample (see Fig. 3.2).
- Next, a water soluble and conductive layer of Electra 92 (All Resist AR-PC 5090.02) is spin-coated on top of the dummy wafer at 1000 rpm for 60 s with 500 rpm/s, and annealed at 90 °C for 40 s, resulting in a 100 nm layer thickness. This layer of Electra 92 allows us to eventually lift the PMMA mask from the $Si/SiO_2$ dummy wafer during a later step. To ensure a homogeneous coverage, wait 2 to 3 minutes after placing the Electra 92 solution onto the wafer before starting the spin-coater. Carefully, check whether the Electra 92 layer is spin-coated homogeneously. From experience, we noticed that the Electra 92 solution degrades with time rather fast, resulting in an inhomogeneous coverage, and should therefore be renewed if no homogeneous layer can be obtained. To reduce the degrading process, the Electra 92 should be stored in a fridge, and personal bottles should be filled from the main bottle in an nitrogen environment, to reduce any condensation from entering the main Electra 92 bottle.
- Subsequently, a layer of PMMA 950K 4 *wt*% (All Resist AR-PC 679.04) is spin-coated at 1000 rpm for 180 s with 500 rpm/s and annealed at 180 °C for 40 s, resulting in a layer thickness of 630 nm.
- Using electron beam lithography (EBL), a matrix of $16\times16$ Hall bars are exposed in the center of the dummy wafer with a 10 kV acceleration voltage and a dose of 220 µC/cm$^2$. Depending on the minimum feature size of the Hall bar, the aperature is chosen accordingly. Generally, if the minimum features size is about 1 µm, an aperture of 30 µm is used. For feature sizes larger than 3 µm, an aperature of 120 µm can be used. A convenient way to expose the matrix, is by using the "Filter" → "Matrix Copy" option in the eline software of the EBL provided by Raith. Note that the dummy wafer is rather large and requires a large sample holder at the e-beam machine.
- The exposed Hall bars are developed in a development solution of methyl isobutyl ketone (MIBK) and isopropyl alcohol (IPA) (MIBK:IPA, 1:3) for 60

s, rinsed in IPA for 30 s to stop the development, and blow dried using Nitrogen gas.

After the PMMA mask is prepared on the dummy wafer and the Hall bars are exposed and developed, the PMMA mask needs to be first transferred onto a home-made aluminum holder, which is used to subsequently transfer the PMMA mask onto the desired flake. This process is illustrated in Fig. 3.2 and is described in steps below:



- A home-made holder is used to transfer the PMMA mask on top of the $Si/SiO_2$ substrate (see Fig. 3.2). To make sure that the PMMA mask will stick well to the holder, the holder is first etched in an reactive ion etcher (RIE) using $O_2$ gas at 40 W RF power for 20 seconds. The oxygen etching makes the holder hydrophilic which causes the PMMA to stick better.
- Before placing the dummy wafer in a water filled petri dish, a scratch is made in the PMMA/Electra layer on the outer rim of the dummy wafer using a sharp tweezers or scalpel, going all around the wafer. This scratch will allow the water to more easily go under the PMMA layer and dissolve the Electra layer when the dummy wafer is placed in the water filled petri dish.
- The dummy wafer with the exposed and developed Hall bars is placed in a petri dish filled with demineralized water. Initially, the dummy wafer will float on top of the water. Using a tweezers, one corner of the substrate is gently pushed under water. This allows the Electra to dissolve at the corner, causing the PMMA to lift from the $Si/SiO_2$ wafer locally. Gradually, more and more Electra will dissolve, which causes more and more PMMA to lift from the wafer. After some time (approximately 10 minutes), the Electra layer is fully dissolved and the $Si/SiO_2$ wafer sinks to the bottom while the PMMA mask floats on top of the water.
- The next step is to take out the PMMA mask using the holder. The holder is placed in the petri dish and the petri dish is carefully tilted such that the water level exceeds the height of the holder, as illustrated in Fig. 3.2. Using a tweezers, the floating PMMA mask is gently aligned with the holder as illustrated in Fig. 3.2. The exposed matrix of Hall bars is visible as small speckles on the PMMA layer and should be aligned with the hole in the holder. By slowly placing the petri dish horizontally again, the water levels lowers and the PMMA mask deposits on the holder. Now, the holder with the deposited PMMA mask can be taken out of the petri dish and dried using a clean room tissue. The part of the PMMA mask that wraps around the sides of the holder should be gently moved upwards such that the PMMA mask is only at the front side of the holder. The PMMA is moved slightly inwards towards the hole such that the PMMA mask is able to form a dome shape when inflated in a later step.
- Next, the holder is placed in a manual transfer stage with the PMMA mask facing towards the substrate on which it needs to be transferred. Here, the gas

inlet of the holder is connected to a nitrogen tank which supplies nitrogen gas to inflate the PMMA mask. A home made glass slide is placed in a dedicated slot of the holder which closes off the cavity of the holder, creating a slight over pressure in the cavity. This over pressure causes the PMMA mask to inflate and form a dome shape as illustrated in Fig. 3.2.

- By changing the focus of the microscope in the transfer stage, the Hall bar which is most closely located to the lowest part of the dome is identified and aligned to the flake of interest. The lowest Hall bar is used here such that the first contact point between the PMMA mask and the substrate is in close proximity to the Hall bar, which reduces misalignment issues.

- The PMMA mask is slowly lowered on to the substrate. As a side note, if there is no proper contact between the PMMA mask and the flake (due to folds in the PMMA for instance), the temperature can be increased to a maximum of 85 °C. This will relax the PMMA mask and might cause better contact. If the mask is placed correctly, however, no additional heating is used.

- Finally, the PMMA layer needs to be removed from the holder, finalizing the transfer on to the final $Si/SiO_2$ substrate. First the flow of nitrogen gas is stopped and the glass slide is removed. Next, the PMMA is pierced around the hole by hand using a sharp needle. Subsequently, the holder is gently lifted, finalizing the transfer of the mask onto the flake. An example of a flake with a deposited mask is shown in Fig. 3.3(b).

- With the Hall bar mask deposited, the permalloy/$Al_2O_3$ layers can be deposited. However, as manually deposited PMMA mask does not always cover the sides of the substrate, these sides need to be masked off. Therefore, an aluminum plate with a 3 mm hole is carefully aligned on to the substrate using an optical microscope, such that the deposited Py/$Al_2O_3$ will only deposit at the Hall bar mask around the flake.

- Next, the sample is loaded in the e-beam evaporator (Temescal FC2000) and pumped to a vacuum below $3 \times 10^{-6}$ mbar. Here, 6 nm of Py and 17 nm of $Al_2O_3$ are deposited, both at a rate of 0.3Å/s.

- The final step is the lift off of the Py/$Al_2O_3$ in acetone at 48 °C for 10 minutes. As the PMMA layer is placed on top mechanically, the lift off should be performed more gently compared to spin-coated layers, not to remove all the Py/$Al_2O_3$.

After following these steps, one should have successfully deposited the Py/$Al_2O_3$ Hall bar on top of the desired flake using the polymer-free technique. In principle, this technique is not limited to Hall bars but can be used for other purposes as well, as the shape of the mask can be designed using electron beam lithography accordingly.

Now that the permalloy Hall bar is deposited, the next step is to contact the Hall bar. This is discussed in the next section.

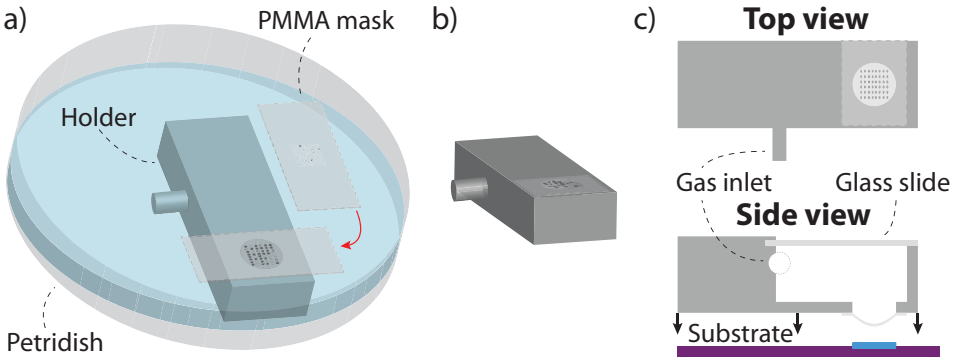


Figure 3.2: A schematic illustrating the polymer-free technique, where a PMMA mask is mechanically deposited on top of a flake. (a) As the Electra is dissolved, the PMMA mask is lifted from the dummy $Si/SiO_2$ wafer in petri dish filled with water. Next the holder is placed in the petri dish and the floating mask is aligned onto the holder. (b) The PMMA mask and holder are taken out of the petri dish and dried. (c) The holder with the PMMA mask is mounted in a manual transfer stage which allows one to align the mask on top of the flake. Using nitrogen gas, an over pressure is created into the cavity of the holder, such that the PMMA mask is inflated and forms a dome. Using the transfer stage, the PMMA mask is slowly lowered and transferred onto the desired flake.

### 3.1.3. Lithography and contact fabrication

In order to apply currents and measure voltages in these devices, the $Py/Al_2O_3$ Hall bar needs to be contacted using conductive contacts. As the interface here is not of major importance, standard lithography techniques can be used to fabricate the titanium/gold contacts. To improve the changes of a proper lift-off in the final steps, a bilayer of PMMA is used which increases the natural undercut of the PMMA. The steps involved with the contact fabrication are described below:

- First, a layer of PMMA 50K 9 $wt\%$ (All Resist AR-P 631.09) is spin-coated at 4000 rpm for 60 s with 500 rpm/s and annealed at 180 °C for 40 s, resulting in a 300 nm layer thickness.
- Next, a layer of PMMA 950K 2 $wt\%$ (All Resist AR-P 679.02) is spin-coated at 4000 rpm for 60 s with 500 rpm/s and annealed at 180 °C for 40 s, resulting in a 70 nm layer thickness.
- Before we can expose the markers, we need to have a rough reference as to where we need to expose the markers on the substrate without risking the exposure of the PMMA close to the sample. This reference is created by making two scratches in the PMMA with the end of a sharp tweezer. By making pictures of the scratches an loading those into the contact design software (LayoutEditor), the scratches can be outlined and positioned in the contact design relative to the sample position. In principle, one scratch is sufficient to expose the markers around the sample using the "origin correction" in the eline software. Here, however, two scratches are used such that a "2-point alignment" can be used, which results in higher accuracy.

- Using EBL with a 10 kV acceleration voltage and a dose of 140 µC/cm$^2$, four small markers, separated by 180 µm, and four large markers, separated by 1900 µm, are exposed in a 2000×2000 µm$^2$ write field. These markers are centered around a specific feature, such as a Hall bar or a flake, and are needed for the alignment of the contacts which will be exposed in a later step.
- Subsequently, the exposed markers are developed for 60 s in a solution of MIBK:IPA (1:3), rinsed with IPA for 30 s, and finally dried by nitrogen gas. The developed markers are clearly visible in the SEM of the EBL machine when using 10 kV acceleration voltage, and allow to accurately position the contacts onto the specific feature (e.g. Hall bar, flake, etc.).
- Next, the contacts are exposed in two steps. First, the small contacts near the center of the design are exposed in a small write field of 200×200 µm$^2$ with a 10, 30, or 60 µm aperture (depending on the minimum feature size), a 10 kV acceleration voltage, and a 140 µC/cm$^2$ dose. Secondly, the larger parts of the contacts are exposed in a larger write field of 2000×2000 µm$^2$ with a 120 µm aperture, 10 kV acceleration voltage, and a dose of 1.5 × 140 µC/cm$^2$.
- After contact exposure, the contacts are developed as described before. A microscope image of a device after contact development is depicted in Fig. 3.3(c).
- For the spin-orbit torque devices with an Py/$Al_2O_3$ Hall bar, before the Ti/Au contacts are deposited, the $Al_2O_3$ capping layer needs to be removed locally to allow for a direct contact between the Ti/Au and the Py layer. The $Al_2O_3$ is chemical etched away in a solution of tetramethylammonium hydroxide (TMAH) 4% (Microposit MF CD-26 Developer) for 40 s at 40 °C. Next, the sample is quickly rinsed to remove the TMAH: first in demineralized water for 5 seconds, subsequently in IPA for another 5 seconds, and finally it is dried using nitrogen gas. As a side note, the chemical etch rate is highly dependent on temperature. By performing an etch test we found that the etch rate is $(2.9 \pm 0.2)$ nm/min at room temperature, and increased to $(46.4 \pm 0.2)$ nm/min at 50°C, and is non-linear.
- After the $Al_2O_3$ capping layer is removed below the contacts, the sample is loaded in an electron beam evaporator (Temescal FC2000) which is pumped down to pressures below $3 \times 10^{-6}$ mbar. While transferring the sample from the wet bench to the Temescal FC2000, the Py layer is exposed to ambient conditions which causes the top layer to oxidize, obstructing good electrical contact to the permalloy layer. Therefore, before the Ti/Au contacts are deposited, in-situ argon etching is performed in the electron beam evaporator (Temescal FC2000) for 20 seconds to remove the oxidized Py layer.
- Immediately after, without breaking the vacuum, the Ti/Au contacts are deposited. First, the layer of 5 nm titanium (Ti) at 0.5 Å/s, and secondly, a 55 nm layer of gold (Au) is evaporated at 0.5 Å/s for the first 10 nm and at 2 Å/s for the remaining 45.

- Next, the evaporated layers of Ti/Au on the PMMA are lifted off by dissolving the PMMA layer in heated acetone (48 °C) for 10 minutes, after which the sample is rinsed with IPA and dried with nitrogen gas. If all goes well, only the Ti/Au that is in direct contact with the $Si/SiO_2$ substrate remains in place, as illustrated in Figs. 3.3(d) and 3.3(e).
- Subsequently, the TMD flake, partially protected by the $Al_2O_3$ capping layer, is etched in a Hall bar by reactive ion etching (RIE). We use $CF_4$ (9.5 sccm) + $O_2$ (0.5 sccm) at 30 W RF power and 5 W ICP which etches approximately 1 nm of $WSe_2$ per 10 s. A microscope image of a finalized device, where the flake is etched into the Hall bar shape, is depicted in Fig. 3.3(f).
- Finally, the sample is wire bonded to a chip carrier and loaded in one of the experimental setups, described in Sec. 3.2.1.

## 3.2. Electrical measurements

After the device fabrication is finished successfully and the device is wire bonded to a chip carrier, the device can be mounted into a setup for electrical or optical

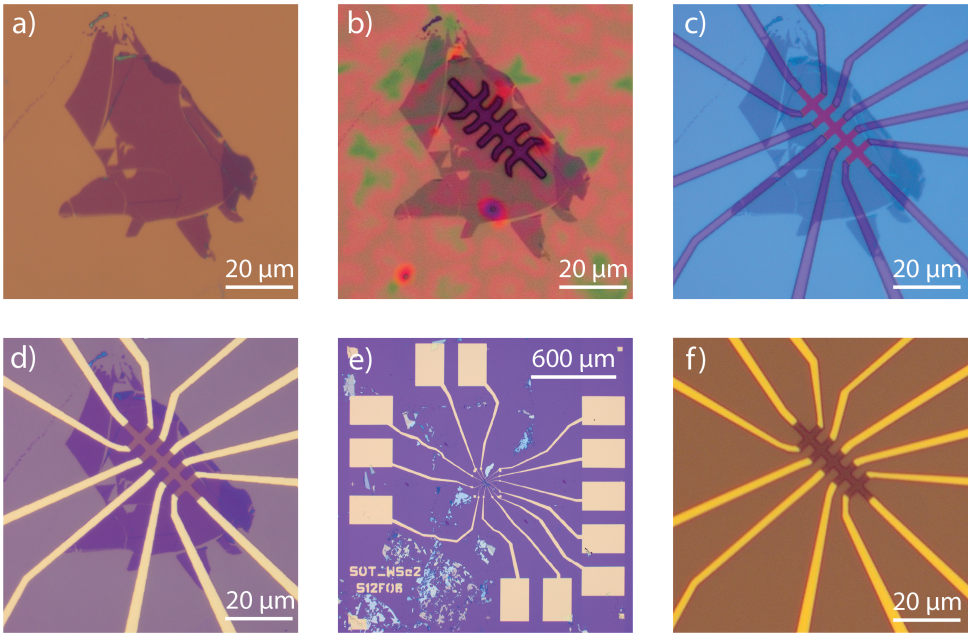


Figure 3.3: A collection of hotographs at different stages of the device fabrication process. (a) A bilayer $WSe_2$ flake on the $Si/SiO_2$ after exfoliation. (b) The Hall bar PMMA mask deposited on top of the $WSe_2$ flake as described above. (c) The $Py/Al_2O_3$ is deposited and a new layer of PMMA is spin-coated. Subsequently, the contacts are exposed using e-beam lithography and developed in MIBK:IPA (1:3). (d) A zoomed in micrograph of the device after Ti/Au deposition. (e) Zoomed out micrograph of the same device as in (d). (f) The final device after etching away the TMD layer not covered by the $Al_2O_3$ capping layer.

measurements. In this section, first, the setup and electrical connections used for the spin-orbit torque measurements will be described, after which the initial electrical characterization of 2-probe, 3-probe, and 4-probe measurements are discussed. For the setups used for photocurrent measurements presented in Chapters 7 and 8, I refer to Sec. 3.4.

### 3.2.1. Setup description

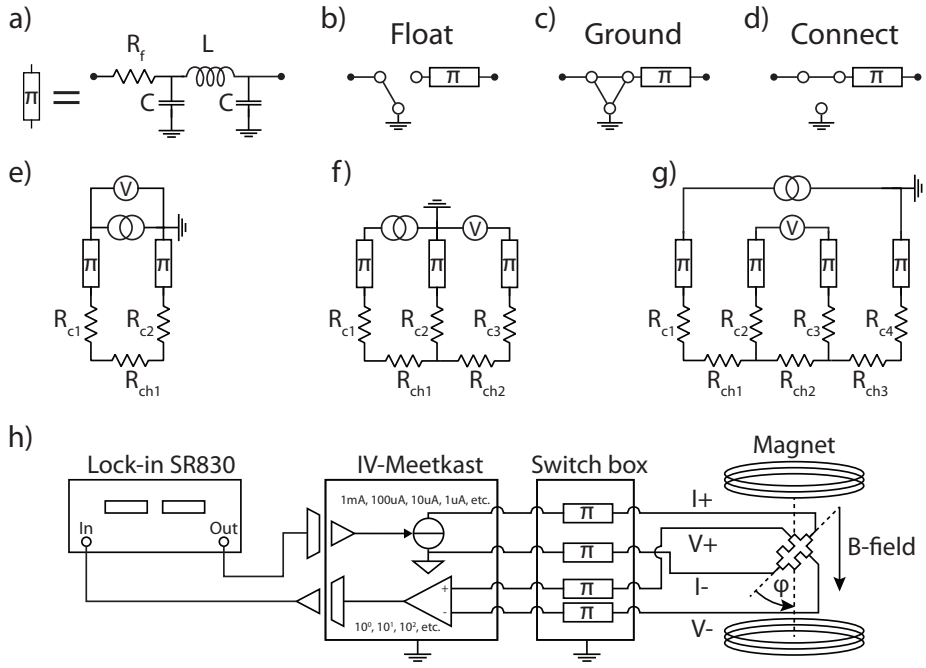


Figure 3.4: (a) A $\pi$-filter used to protect the device against high voltage spikes from electrostatic discharge and electrical fast transients when connections are made of broken. These $\pi$-filters are mounted in a home build switch box which allows one to conveniently use and connect the different contacts of the device. By means of a 3-way toggle switch the contacts of the sample are either (b) floating, (c) grounded, or (d) connected, as illustrated here. Note that the sample is connect to the right side, and all the measurement equipement (e.g. voltage meters, current sources, etc.) are connected to the left of this diagram. (e) 2-Probe configuration where one measures $R_{c1} + R_{ch1} + R_{c2}$. (f) 3-Probe configuration where one measures the contacts resistance $R_{c2}$. (g) 4-Probe measurements where the resistance of the channel, $R_{ch2}$, is measured. (h) Electrical connections of the multiple instruments used for harmonic Hall measurements.

The spin-orbit torque measurements presented in this thesis are performed by means of the harmonic Hall technique. Here, a low-frequency AC charge current is applied through the device, and the first- and second-harmonic Hall voltages are measured while the sample is rotated with respect to an in-plane applied magnetic field. In this subsection, the setup used for these measurements is described. For details on the relation between the second-harmonic Hall voltage and the spin-orbit torques, I refer to Sec. 3.3.

After wire bonding the sample to a 18 pin chip carrier, the chip carrier is loaded into the sample holder of a setup which allows for the harmonic Hall measurements, as depicted in Fig. 3.4(h). The sample holder is positioned in between the poles of a GMW 5403 Electromagnet, which provides the applied magnetic field. By rotating the sample with respect to the magnetic field, the angle between the applied current direction in the sample and the magnetic field can be altered, changing $\phi$, where a positive $\phi$ is defined as depicted in Fig. 3.4(h). All spin-orbit torque measurements are performed at room temperature at ambient pressures.



Using a shielded 18-pin Fischer cable, the sample is connected to a home made switch box. The switch box contains low-pass ($\pi$-)filters to protect the device against high voltage spikes from electrostatic discharge or electrical fast transients when connections are made or broken. These filters consist of 1 k$\Omega$ resistor ($R_f$) in series with a inductor (L) and two 10 nF capacitors (C) in parallel connected to ground, as depicted in Fig. 3.4(a). By means of a 3-way switch, the switch box allows one to conveniently float, ground, or connect the different contacts of the sample to the outer pins of the switch box, which in turn, are connected to current or voltage sources and current or voltage meters using shielded LEMO cables. These different configurations are shown in Figs. 3.4(b), (c), and (d).

All the spin-orbit torque measurements were performed using a current-biased low-frequency lock-in technique. An SR830 lock-in amplifier supplies a sinusoidal AC voltage which is converted into a current using an home-build voltage-to-current converter (ranging from 10 nA/V to 10 mA/V). Via the switch box, the current is supplied through the channel of the sample, where the negative electrode of the current source (L) is always grounded. The transverse and longitudinal voltage from the sample are then measured by connecting the contacts to a home-build voltage pre-amplifier (with a gain ranging from 1 to $10^5$), and finally connected to the input of the lock-in. Using a GBIP cable, the lock-in is connected to a PC which allows to control the different parameters (e.g. frequency, time constant, filters, output voltage etc.), and record its input voltage.

### 3.2.2. Electrical characterization

Before the spin-orbit torque measurements are performed, the sample is first characterized electrically by means of 2-probe, 3-probe, and 4-probe measurements to check whether there is proper contact between the evaporated Ti/Au contacts and the sample. The equivalent circuit diagrams for these measurements are depicted in Figs. 3.4(e), (f), and (g), respectively. In these diagrams, $R_c$ and $R_{ch}$ represent the contact and channel resistances. Note that the $\pi$-filter also contains a 1 k$\Omega$ resistor. These measurements are performed using a current-biased lock-in technique with a 10 nA AC current at 17.77 Hz. As a side note, it is convenient to use a voltage gain of $10^2$, because in this case every measured mV corresponds to a k$\Omega$ of resistance.

A **2-probe measurement** is used as an initial check to see if the contacts are electrically connected to the device. For a 2-probe measurement, depicted in b, a current is passed through contact 1 to contact 2 and the voltage drop over contact 1 and 2 is measured. The resistance measured is therefore a sum of the contact resistances, channel resistances, and filters: $R_{2P} = 1\text{k}\Omega + R_{c1} + R_{ch1} + R_{c2} + 1$

kΩ. As the total resistance is a sum of different contributions, this measurement is only used as an initial check and should be complemented by 3-probe and 4-probe measurements.

Using a **3-probe measurement**, depicted in c, one can determine the contact resistance of a single contact. Here, a current is passed through contact 1 and 2, while the voltage is measured between contact 3 and 2. As no current is flowing through $R_{ch2}$, $R_{c3}$ and the $\pi$-filter of contact 3, there is no voltage drop. The measured resistance is thus $R_{3P} = R_{c2} + 1\text{k}\Omega$. As the resistance of the wiring is usually small compared to the contact resistance, and we know the resistance of the *pi*-filter, 3-probe measurements allow us to determine the contact resistance.



With a **4-probe measurement**, depicted in d, one can determine the channel resistance of the device. Here, a current is passed through contact 1 and 4, while the voltage is measured between contact 2 and 3. Again, assuming that no current is flowing through contact 2 and 3, the measured voltage drop is the voltage drop across $R_{ch2}$. This thus allows us the exclude the wire, filter, and contact resistances, and only measure the channel resistance. A 4-probe configuration is also used for the harmonic Hall measurements. In this case the voltage probes measure the first- and second-harmonic *transverse* voltage $V_{xy}^{\omega/2\omega}$ rather than the *longitudinal* voltage.

## 3.3. Harmonic Hall measurements

Now that the setup is discussed, I will present a more detailed discussion on the relation between the harmonic Hall voltage and the spin-orbit torque strength in this section. Multiple effects related with these harmonic Hall measurements are discussed, such as the planar Hall effect, anomalous Hall effect, and the anomalous Nernst effect, which allow us to determine the spin-orbit torque strength. But first, a general introduction is given.

The spin-orbit torques in our devices exert a torque on the magnetization of the ferromagnetic permalloy, causing the magnetization to deflect from its equilibrium direction. The deflection can be measured electrically by using the fact that the resistance of the ferromagnetic permalloy depends on the direction of its magnetization with respect to the applied current direction. This effect is called the anisotropic magnetoresistance (AMR) [17, 18], which causes the resistance of the permalloy to depend on whether the current is applied parallel or perpendicular to its magnetization. It is a consequence of the spin-orbit coupling of the material, but the exact microscopic mechanism is material specific. Both the longitudinal resistance, $R_{xx}$, and the transverse resistance (or Hall resistance), $R_{xy}$, depend on the magnetization direction. As the spin-orbit torques are measured in a Hall configuration in this thesis, a short description of the relevant effects for the Hall measurements are given in this section.

The deflection of the magnetization direction can be decomposed into an in-plane and out-of-plane deflection. While both type of deflections result in a change in the transverse resistance, the magnitude of this change may differ. The changes in resistance due to an in-plane deflection is referred to as the planar Hall effect (PHE), while a change in resistance due to an out-of-plane deflection is referred to

as the anomalous Hall effect (AHE). Both effect will be discussed below, starting with the planar Hall effect.

### 3.3.1. Planar Hall effect

Generally, a change in resistance when the magnetization direction is deviated with respect to the current direction is referred to as anisotropic magnetoresistance (AMR) [17, 18]. A resistivity can be defined for the cases when the magnetization is parallel ($\rho_{\parallel}$) or perpendicular ($\rho_{\perp}$) with respect to the current direction. In most materials, the resistance is maximum when the magnetization is parallel to the current direction, and minimum when the magnetization is perpendicular. It is therefore common to describe the magnetoresistance empirically as [19]:

$$\vec{E} = \rho_{\perp}\,\vec{j} + \left(\rho_{\perp} - \rho_{\parallel}\right)\hat{m}\left(\hat{m}\cdot\vec{j}\right). \tag{3.1}$$

Here, $\vec{j}$ is the current density, $\hat{m}$ is a unit vector pointing in the direction of the magnetization, and $\vec{E}$ is the electric field. For the harmonic Hall measurements discussed in the thesis, the current is applied in the $\hat{x}$-direction, and the magnetic field is rotated in-plane, i.e. $\theta = 90°$, and $\hat{m} = (\cos(\phi), \sin(\phi), 0)$ is in the $xy$-plane (illustrated in Fig. 3.5(a)). Therefore, Eq. 3.1 can be rewritten as [20]:

$$E_x = \rho_{\perp}\,j_x + \left(\rho_{\perp} - \rho_{\parallel}\right)j_x\cos(\phi)^2, \tag{3.2}$$

$$E_y = \left(\rho_{\perp} - \rho_{\parallel}\right)j_x\sin(\phi)\cos(\phi) = \left(\rho_{\perp} - \rho_{\parallel}\right)\frac{j_x}{2}\sin(2\phi). \tag{3.3}$$

As the spin-orbit torque measurements are measured in a Hall configuration, we are concerned about Eq. 3.3. When rotating the magnetic field in-plane, we expect the first-harmonic Hall voltage $V_{xy}^{\omega}$ thus to be given by:

$$V_{xy}^{\omega} = I_0 R_{PHE}\sin(2\phi), \tag{3.4}$$

where $I_0$ is the applied current and $R_{PHE}$ is the so-called planar Hall resistance. This modulation of the voltage when the magnetization direction is rotated in-plane is referred to as the planar Hall effect (PHE), and is illustrated in Fig. 3.5(c).

In the case that the current-induced SOTs cause a deflection of the magnetization in the *in-plane* direction, one is thus able to sense the deflection using the planar Hall effect. To relate the change in voltage to the torque strength, the planar Hall resistance is extracted from the first-harmonic Hall measurement, as it is needed to quantify the torque strength from the second harmonic Hall measurements (Eq. 3.11).

### 3.3.2. Anomalous Hall effect

In ferromagnetic materials there is another relevant Hall effect, referred to as the anomalous Hall effect (AHE), which was already discovered in 1881 by Edwin Hall [21]. This effect originates from the same three microscopic mechanisms as the spin Hall effect, discussed in Chapter 2, but only occurs in magnetic materials [22, 23].

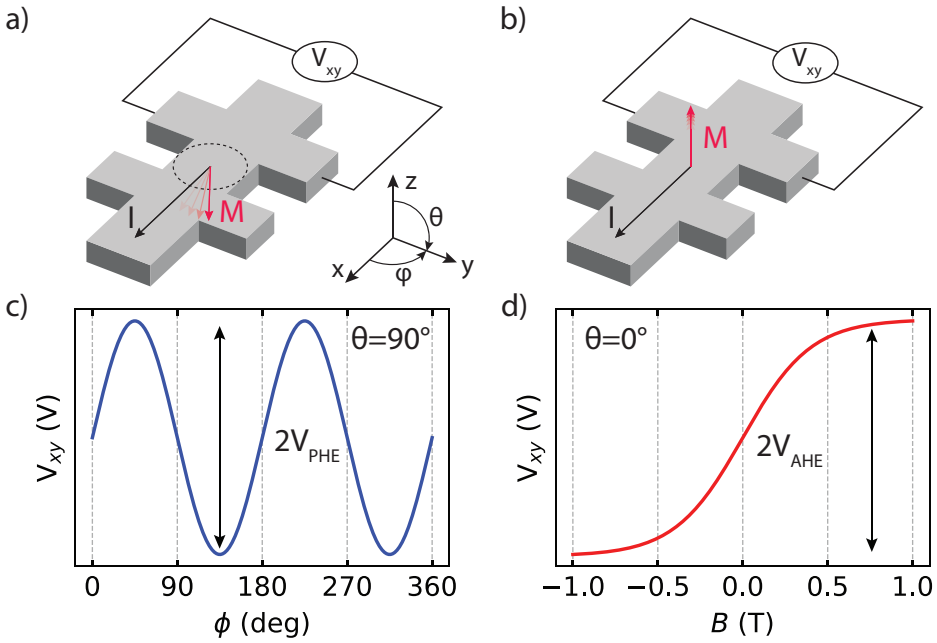


Figure 3.5: A schematic illustration of the (a) planar Hall measurement and (b) anomalous Hall measurement. (a) For the PHE, the magnetization of the magnet is rotated in-plane with respect to the current direction ($I$) and the Hall voltage ($V_{xy}$) is measured. (c) A schematic of the modulation of $V_{xy}$ due to the PHE. (b) For the AHE, an applied magnetic field in the $\hat{z}$-direction pulls the magnetization of the magnet out-of-plane. (d) A schematic of the modulation of $V_{xy}$ due to the AHE.

While the PHE depends on the in-plane direction of the magnetization with respect to the current direction ($\phi$), the AHE depends on the out-of-plane component of the magnetization ($M\cos(\theta)$). The AHE can be described by the empirical relation for the transverse resistivity [23, 24]:

$$\rho_{xy} = R_O B_z + R_s M \cos(\theta), \tag{3.5}$$

where $\rho_{xy}$ is the transverse resistivity, $R_O$ and $R_s$ are the ordinary and anomalous Hall coefficients, respectively, $B_z$ is the out-of-plane component of the external magnetic field, $\theta$ is polar angle of the magnetization ($M$) as shown in Fig. 3.5(a), and $M\cos(\theta)$ is the out-of-plane component of the magnetization of the magnet. Note that the transverse component due to the ordinary Hall effect is linear with $B_z$, while the component from the AHE depends on the out-of-plane component of the magnetization of the magnet ($M_z$). The anomalous Hall effect thus allows one to measure a deviation of the magnetization, for instance due to a SOT, in the *out-of-plane* direction.

For the SOT measurements performed in this thesis, the anomalous Hall resistance ($R_{AHE}$) needs to be determined to extract the spin-orbit torque strength from the harmonic Hall measurements (see Eq. 3.12). This is done by measuring the first-

harmonic Hall voltage while applying an out-of-plane external magnetic field. The external magnetic field pulls the magnetization of the ferromagnet out-of-plane as illustrated in Fig. 3.5(b). While the sample is rotating in-plane for the planar Hall and spin-orbit torque measurement, for the anomalous Hall measurement, the sample needs to be placed in a separate sample holder such that the magnetic field from the electromagnet is aligned to the out-of-plane direction. Subsequently, the Hall resistance is measured, again using a low-frequency current-biased lock-in technique with a current in the order of 10 µA, while sweeping the magnetic field out-of-plane from approximately -1 T to 1 T. It is important to use a strong enough magnetic field to fully pull the magnetization of the permalloy out-of-plane and reach the saturation magnetization (approximately 800 mT for the devices used in this thesis), as schematically depicted in Fig. 3.5(b).



### 3.3.3. Anomalous Nernst effect

Another effect which is relevant for the harmonic Hall measurements is the thermal effect called the anomalous Nernst effect (ANE) [25]. Due to Joule heating, the current applied through the Hall bar in the harmonic Hall measurements generates heat. As the different materials of the Hall bar have different thermal conductivities, a temperature gradient is generated in the out-of-plane direction ($\hat{z}$-direction), which is proportional to the Joule power $I^2R$ [26, 27]. Applying a temperature gradient and a perpendicular magnetic field in a non-magnetic material generates a voltage which is perpendicular to both the temperature gradient and the magnetic field. This effect is referred to as the Nernst effect. In magnetic materials, on the other hand, this effect persists even in the absence of an external magnetic field. Here, a voltage is generated which is perpendicular to both the magnetization $\hat{m}$ and the temperature gradient $\nabla T$ [28]. This effect is known as the anomalous Nernst effect and is analogous to the anomalous Hall effect, but now, the driving force is a temperature gradient rather than a voltage gradient.

The anomalous Nernst effect can be described by [25, 26]:

$$\nabla V_N = -\alpha_N \hat{m} \times \nabla T_z, \tag{3.6}$$

where $\alpha_N$ is the anomalous Nernst coefficient, $\hat{m}$ is the unit vector of the magnetization, and $\nabla T_z$ is the gradient of the temperature in the $\hat{z}$-direction. As the magnetization $\hat{m}$ is in the $xy$ plane for the harmonic Hall measurements, $\nabla V_N$ is also in the $xy$ plane at an angle of $\pi/2 - \phi$. Therefore, $V_{xx}$ and $V_{xy}$ are sinusoidal in $\phi$, with a 90° phase shift:

$$V_{xx} = I_0 R_{ANE} \sin(\phi), \tag{3.7}$$

$$V_{xy} = I_0 R_{ANE} \cos(\phi) = V_{ANE}. \tag{3.8}$$

Note that these equations assume a temperature gradient only in the $\hat{z}$-direction. For any temperature gradient in the $\hat{x}$- or $\hat{y}$-direction, this expression should be expanded. As the thermal conductivity of $SiO_2$ ($\kappa = 1.4$ W m$^{-1}$K$^{-1}$) is much larger

compared to air ($\kappa = 0.024$ W m$^{-1}$K$^{-1}$), we can assume that the heat dissipation takes place mainly via the substrate, generating a positive thermal gradient [26].

For the harmonic Hall measurements, we measure $V_{xy}$ and are therefore mainly interested in Eq. 3.8. As both the measured voltage and the generated anomalous Nernst voltage depend on the current, this thermal effect is measured in the second-harmonic Hall voltage. As $R_{ANE}$ is independent on the applied magnetic field strength, the effect is identified as a constant voltage offset of the B-component (see Eq. 3.12), obtained in the second-harmonic Hall measurements discussed in the next section.



### 3.3.4. Second-harmonic Hall measurements

As discussed in Sec. 3.3.1, when rotating the magnetic field in-plane, the first-harmonic signal corresponds to the planar Hall effect, depicted in Fig. 3.5. For measuring the signal from the current induced torques, on the other hand, we need to measure the second-harmonic Hall voltage. This can be understood hand-wavingly as follows. The measured voltage depends on the current: $V_{xy} = IR$. The resistance $R$, however, depends on the magnetization direction ($R(M)$), which in turn, depends on the current due to the current induced torques: $M(I)$. Therefore, we can denote the resistance as a current independent $R_0$, and a current dependent resistance $R_\tau$, making the total resistance: $R(M(I)) = R_0 + R(\tau)I$. The transverse voltage then becomes:

$$V_{xy} = IR(M(I)) = IR_0 + I^2R(\tau) \tag{3.9}$$

The signal from the torques is thus proportional to $I^2$ and appears in the second-harmonic voltage.

In literature, there are multiple approaches to find the quantitative relation between the second-harmonic Hall voltage and the SOTs [26, 29–31]. Here, we adhere to the method used by Hayashi et al. which is based on minimizing the magnetic energy [30]. A more detailed description of the second-harmonic Hall voltage derivation can be found in the Appendix A.1.3. For convenience, the final equation for the second-harmonic Hall voltage is denoted again here:

$$V_{xy}^{2\omega} = A\cos(2\phi)\cos(\phi) + B\cos(\phi), \tag{3.10}$$

where A and B are:

$$A = \frac{R_{PHE}I_0\tau_\perp/\gamma}{H}, \tag{3.11}$$

$$B = \frac{R_{AHE}I_0\tau_\parallel/\gamma}{H + H_k} + R_{ANE}I_0. \tag{3.12}$$

Here, $R_{PHE}$, $R_{AHE}$, and $R_{ANE}$ are the planar Hall, anomalous Hall, and anomalous Nernst resistances, $I_0$ is the applied current, $\gamma$ is the gyromagnetic ratio, $H$ is the applied field, and $H_k$ is the out-of-plane anisotropy field.

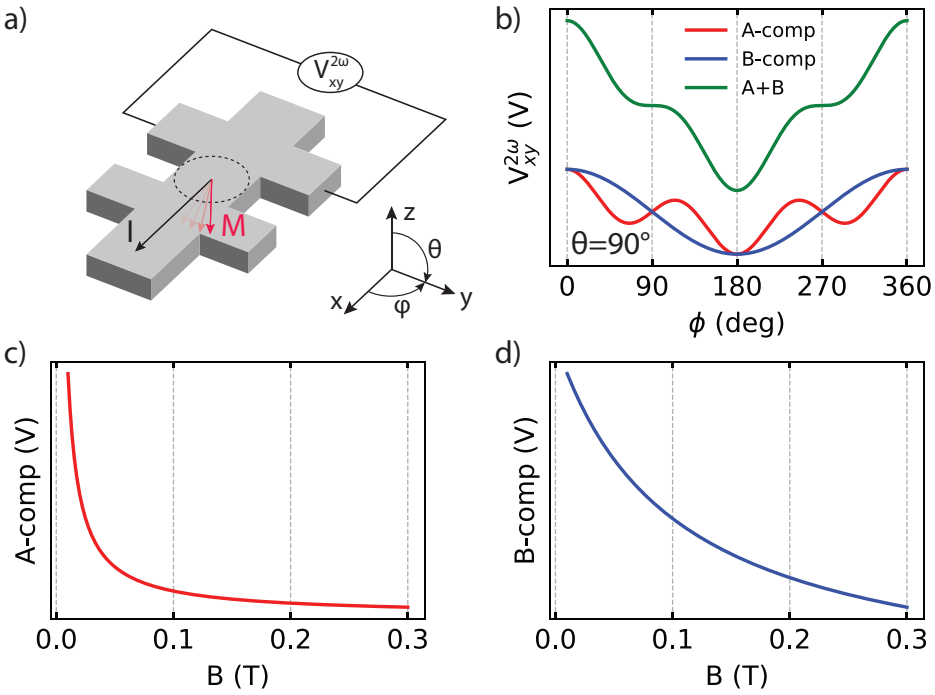


Figure 3.6: (a) A schematic of the harmonic Hall measurement. Similar to the planar Hall measurements, a current is passed through the channel and an applied magnetic field is rotated in-plane. In this case, however, the second-harmonic Hall voltage ($V^{\omega}_{xy}$) is measured as depicted in (b). (b) The $V^{\omega}_{xy}$ is fitted with Eq. 3.10 to extract the amplitude of the A- and B-component. By performing the measurement at different magnetic field strengths, the field dependence of the A- and B-component is obtained as shown in (c) and (d), respectively. By fitting the field dependence of the A- and B-component to Eqs. 3.11 and 3.12, respectively, the out-of-plane and in-plane torque are extracted.

The A- and B-component are related to the out-of-plane and in-plane torque, respectively. Initially, this might be counter intuitive as the A-component is dependent on $R_{PHE}$, which is related to magnetization deviations in the in-plane direction, while the B-component is dependent on the $R_{AHE}$, related to deviations in the out-of-plane direction. However, as mentioned before in Sec. 2.2.3, the measurements in this thesis are performed in a low-frequency quasi-static regime. While the initial deflection of the magnetization will be in the direction of the torque (i.e. $\frac{d\vec{m}}{dt} \sim \gamma \frac{d\vec{L}}{dt}$), given enough time ($\sim$ picoseconds in most materials), the magnetization will precess around the effective field, which is the cross product between the magnetization and the torque direction, and eventually align along the effective field (finding an equilibrium position between all the effective fields acting on the magnetization, e.g. demagnetizing field, anisotropy, SOT effective fields). As we measure in a low-frequency regime, we are sensitive to the effective fields related to the SOTs and not to the intial ultrafast reaction of the magnetization. Therefore, the out-of-plane effective field from $\vec{\tau}_{DL}$ gives rise to a deflection of the magnetiza-

tion in the out-of-plane direction, while the in-plane effective field related to $\vec{\tau}_{FL}$ causes a deflection in the in-plane direction.

By fitting the second-harmonic voltage to Eq. 3.10, the contribution of the A-component (Eq. 3.11) and B-component (Eq. 3.12), depicted in Fig. 3.5, can be extracted. By extracting the A- and B-component for different applied magnetic fields, we can determine their field dependence. From Eqs. 3.11 and 3.12, we expect them to fall of with the applied field as illustrated in Fig. 3.6 ($\propto 1/H$ and $\propto 1/(H + H_k)$, respectively). At high fields, we therefore only expect a $\cos(\phi)$ dependence of $V_{xy}^{2\omega}$ due to the field independent contribution of the anomalous Nernst effect (second part in Eq. 3.12). By fitting the field dependence of the A- and B-component to Eqs. 3.11 and 3.12, knowing the applied current $I_0$, $R_{PHE}$ from the first-harmonic Hall voltage (see Sec. 3.3.1), $R_{AHE}$ from the out-of-plane measurement (see Sec. 3.3.2), $H_k$, and $\gamma$, finally $\tau_\perp$ and $\tau_\parallel$ can be determined.

The second-harmonic Hall measurements were performed in the setup depicted in Fig. 3.4. A low-frequency ($f$ ranging from 27.77 Hz to 377.7 Hz, depending on the device), AC current $I = I_0 \sin(2\pi f t)$ ($I_0$ ranging from 400-800 µA) is applied through the channel of the TMD/Py Hall bar. Next, while rotating the sample in-plane from $-190°$ to $+190°$ inside the constant magnetic field, the first and second-harmonic Hall voltages are measured. These are performed for different magnetic fields ranging from 10 mT to 300 mT.

## 3.4. Optical measurements

Apart from the SOT measurements discussed above, studies on the opto-electronic response of 2D materials are presented. Therefore, the setups used for the Raman spectroscopy, scanning photocurrent, and polarization-dependent photocurent measurements are described and discussed in this section.

### 3.4.1. Raman measurements

Raman spectroscopy was used to characterize the monolayer flake of $MoSe_2$ in Chapter 8, and the different phases of $MoTe_2$ in Chapter 7 [32]. These Raman spectroscopy measurements were performed using a Renishaw Raman microscope with a linearly polarized 532 nm wavelength excitation laser, 50x objective, and a 1800 or 2400 l/mm grating. In Chapter 7, the crystallographic phase of $MoTe_2$ by laser irradiation from the Raman measurement setup. By raster scanning the diffraction limited laser spot over the flake, in steps of 500 nm with 0.1 s of exposure per step, and a laser power of $\geq$3.25 mW, the region of interest is transformed.

### 3.4.2. Scanning photocurrent measurements

To measure the photocurrent response of vdW based phototransistors or -diodes, multiple optical setups can be used. Here, I will discuss the scanning photocurrent measurement used in Chapter 7. As the name suggests, in this type of measurement, the laser spot is scanned across the sample in a raster-like fashion. By measuring the intensity of the reflected light, and subsequently measure the induced photocurrent in the device, one is able to obtain two mappings: one of the reflectivity of the

device, and one of the induced photocurrent. To illustrate this, the results from an example measurement on a $MoTe_2$ photodiode depicted in Fig. 3.7(a), is shown in Fig. 3.7(b) and (c). The reflectivity map in Fig. 3.7(b) shows a map of the device geometry as the Ti/Au contacts, $SiO_2$, and $MoTe_2$ reflect the light differently, providing contrast for these different materials. This allows one to easily distinguish these different regions and thus provides spatial resolution on where exactly the laser spot is relative to the device. By comparing the reflectivity map with the corresponding photocurrent map in Fig. 3.7(c), we can easily pinpoint where in the device the photocurrent is generated (e.g. at the Ti/Au contacts or at the 2D vdW material). This may shed light on the microscopic mechanisms involved in the generation of the photocurrent.



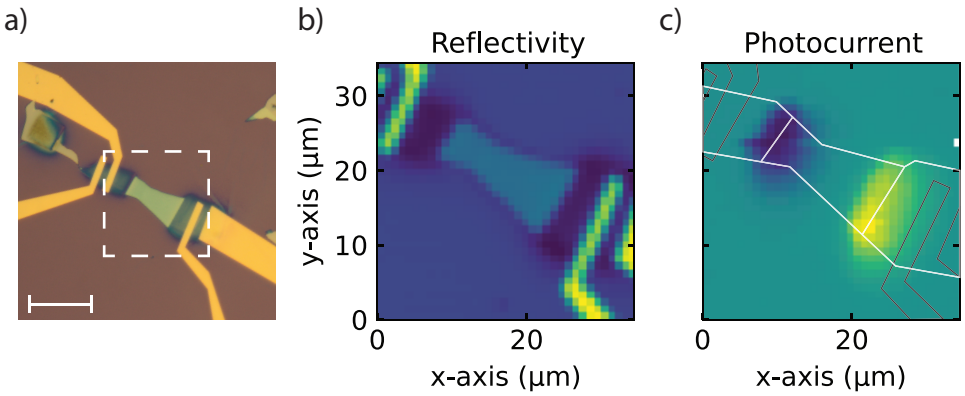


Figure 3.7: (a) An optical microscope image of a $MoTe_2$ device used to measure scanning photocurrents (scale bar is 20 µm). The region indicated with the dashed white square corresponds to the region where the focussed laser spot is scanned in a raster-like fashion, while the (b) reflectivity and (c) induced photocurrent are measured. (b) The different intensities of the reflected light for the different materials provide contrast and allows one to resolve where the laser spot is relative to the device. (c) By comparing the photocurrent map with the reflectivity map, the position where the photocurrent is induced, is retrieved. The white lines indicate the flake and the black lines the Ti/Au contacts and are added to guide the eye.

The setup used for scanning photocurrent measurements is illustrated in Fig. 3.8. A supercontinuum white light laser (NKT Photonics SuperK EXTREME) is used as illumination source in combination with a tunable acusto-optic wavelength filter (SuperK Select) which provides two laser outputs with a spectral range of 450 nm - 680 nm (VIS) and 690 nm - 1100 nm (VIS-NIR), respectively. As only one of these outputs can be used at a time, the flip mirror M2 in Fig. 3.8 allows for convenient switching between the different beam lines. The light of each arm passes through a telescope arrangement of the concave and convex lenses L1 and L2, where L1 and L2 are separated by $\Delta x = f_1 + f_2$ to expand and collimate the laser beam. The beam is expanded to fully fill the back of the final objective (Mitutoyo OBJECTIVE/BF-NIR 20X/FS) with which the laser light is focusses onto the sample. By completely filling the back of this objective, the smallest laser spot size (diffraction limited, ∼µm) is achieved. Next, a chopper is used to modulate the light on and off, which

serves as a reference for the lock-in detection by a Stanford Research Systems SR830 lock-in amplifier. Via mirror M3, the beam is directed to a half-wave plate ($\lambda/2$)

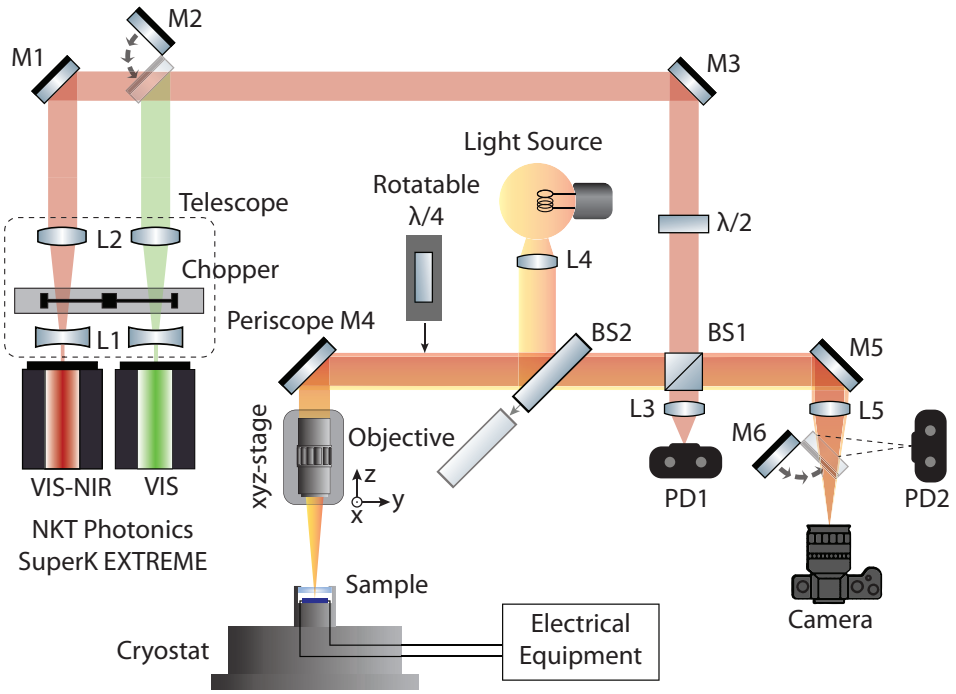


Figure 3.8: A schematic of the setup used in Chapter 7 for scanning photocurrent measurements, consisting of a laser source (NKT photonics SuperK EXTREME) which has two output lines: VIS (450-680 nm) and VIS-NIR (690-1100 nm). The sample is loaded in a cryostat and electrically connected to the electrical equipment discussed in Sec. 3.2. By scanning the objective with the motorized xyz-stage, the laser spot is scanned across the sample while the electrical response is measured. The photodiodes PD1 and PD2 are used to measure the power of the laser and the reflection, respectively.

with which the polarization of the linearly polarized laser can be rotated. Generally the laser light is polarized horizontally (i.e. in the plane of the optical table: s-polarized). Subsequently, the beam is directed to a beam splitter cube (BS1) where a part of the light is reflected to the sample, while the transmitted light is monitored by a silicon photodiode (PD1, Thorlabs PDA36A-EC) which allows to monitor the output power of the laser. The reflected light passes through a beam splitter (BS2), mounted on a flip mount, which is used to direct the light from a white light LED to the sample for illumination. The illumination from the LED is only used to capture the image of the sample on to a camera, which enables us to visually align the laser spot on the sample. When a measurement is initiated, BS2 is flipped out of the beam path to increase the laser power reaching the sample. After the beam splitter, a motorized quarter-wave plate ($\lambda/4$) can be placed in the beam path, with which the polarization can be changed from linear to circular, and thus, allows for

polarization-dependent photocurrent measurements. Next, using a periscope mirror (M4), the light is directed downwards to the objective. The objective is mounted on a motorized xyz-stage with which the objective can be moved in all three directions; by moving in the $\hat{z}$-direction, the sample can be put in focus, while moving in the xy-plane enables one to scan the laser spot over the sample. The sample itself is kept in vacuum inside a LakeShore Janis flow cryostat and is wire bonded to a 24-pin chip carrier which allows for the (opto)electronic measurements.

Next, to monitor the intensity of the reflected light, first, the reflection of the sample is captured using the objective, after which it follows its way back to the beam splitter cube BS1. Here, the reflection is partially transmitted and directed by mirror M5 towards the lens L5, which focuses the image on to the camera. Another flip mirror M6 is also positioned here, which allows us to direct the laser light towards another photodiode (PD2), such that we can measure the intensity of the reflected laser light during an actual measurement.

The scanning photocurrent measurements are performed either by measuring the photocurrent or photovoltage. The photocurrent can be measured either directly with a lock-in amplifier, or by first converting the photocurrent into a voltage using a current-preamplifier. The current pre-amplifier used in this thesis is either a Standford Research Systems SR570 current pre-amplifier, or a home-build current pre-amplifier (IVVI-meetkast), discussed before. Because the IVVI-Meetkast is able to amplify the signal with higher gain, resulting in a higher signal-to-noise ratio compared to the SR570, this instrument is preferred. The output voltage of the current pre-amplifier is subsequently measured with the lock-in. When measuring the photovoltage, the induced photovoltage can either be measured directly using a lock-in, or can first be amplified using the home-build voltage pre-amplifier (IVVI-meetkast). Drain source voltages ($V_{ds}$) and gate voltage ($V_g$) can be applied to the sample by connecting the contacts or gate to a source-meter (Keithley 2400/2450).

### 3.4.3. Polarization-dependent photocurrent measurements

In this section, an overview is provided of the setup used for the polarization-dependent photocurrent measurements discussed in Chapter 8. The setup is depicted in Fig. 3.9. First the optical part of the setup is described, after which the electrical part will be discussed.

A continuous wave (CW) titanium:sapphire laser (M Squared SolsTiS, 700 nm - 1000 nm) is used as illumination source. As this is a high power laser source, the first part of the setup consists of a half-wave plate ($\lambda/2$) and a polarizing beam splitter (BS1) which reduces the laser power by directing part of the laser light to the beam dump. Next, the laser passes through a chopper to modulate the light on and off, which allows us to lock-in on that specific frequency using a Stanford Research SR830 lock-in amplifier, similar as for the setup discussed above. After passing two steering mirrors, M1 and M2, the beam passes through a telescope configuration with a concave lens L1 and convex lens L2, separated by $\Delta x = f_1 + f_2$ to expand and collimate the beam. Contrary to the optical setup depicted in Fig. 3.8, the laser is not focused onto the sample such that the polarization of the light is well defined. In addition, expanding the beam in this setup allows for more homogeneous

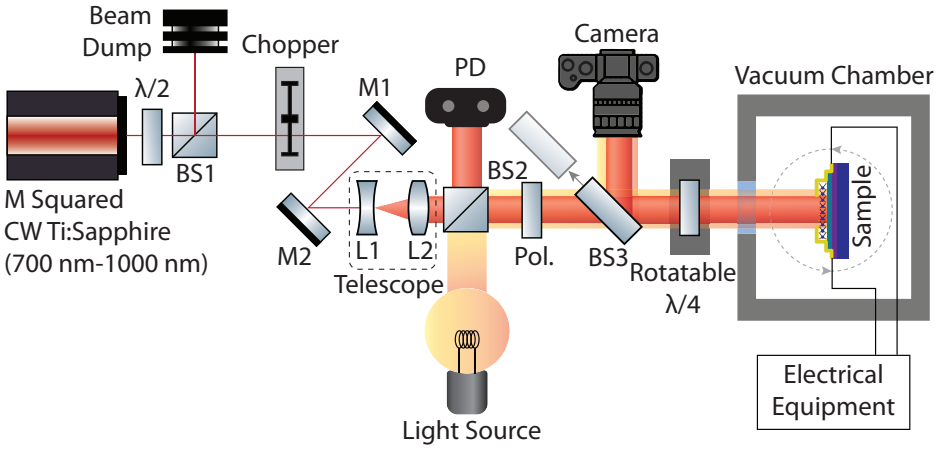


Figure 3.9: A schematic of the setup used in Chapter 8 to perform polarization-dependent photocurrent measurements. Here, the polarization of the laser source (M Squared Ti:sapphire laser (700-1000 nm)) is first set with a polarizer (Pol.), after which a rotatable quarter-wave plate allows one to change the polarization from linear to circular. As the polarization of the light is best defined when the light is fully collimated, no objective is used to focus the light on the sample. To measure the induced photocurrents, the sample is electrically connected to the electrical equipment discussed in Sec. 3.2.

illumination of the entire sample as discussed in Chapter 8. To monitor the intensity of the laser output using a photo diode (PD), and allow for white light illumination of the sample from a light source, a beam splitter (BS2) is placed after the telescope configuration, after which the polarization is set using a polarizer (Pol.). Next, a movable beam splitter (BS3) is positioned in the beam path, to direct the reflection from the sample onto the CMOS sensor of a camera. By connecting the camera to a monitor, it allows us to see the sample and check for proper alignment of the laser on to the sample. Before reaching the sample, the laser passes a quarter-wave plate ($\lambda/4$), mounted in a motorized rotation stage. This $\lambda/4$ plate allows us to change the laser polarization from linear to circular by rotating the optical axis of the $\lambda/4$ plate relative to the linearly polarized light of the laser using the PC. The sample itself is kept at room temperature in a vacuum chamber and is mounted on a rotatable sample holder, which allows one to change the laser incidence angle manually in steps of 10°.

For the electrical connections, again, the Ti/Au contacts of the sample are connected to the rest of the equipment via a switch box containing low-pass ($\pi-$)filters, as discussed in Sec. 3.2.1. The contacts are connected to a current pre-amplifier (CPA, Stanford Research Systems SR570), which converts the detected photocurrent into an amplified voltage, via the $\pi$-filters discussed in Sec. 3.2.1. Next, this voltage is measured by a lock-in amplifier (Stanford Research Systems SR830) which is locked to the chopping frequency of the chopper. By means of a GPIB connection, the data from the lock-in are recorded and stored on the PC. In addition, the sample can be connected to a voltage source (Keithley 2400 or 2450) to apply a $V_{ds}$ or $V_g$.

The measurements are initiated and recorded using a home-written MATLAB code.

# Bibliography


[1] Z. Cai, B. Liu, X. Zou, and H.-M. Cheng, "Chemical Vapor Deposition Growth and Applications of Two-Dimensional Materials and Their Heterostructures", Chemical Reviews **118**, 6091–6133 (2018).

[2] Y. Zhang, Y. Yao, M. G. Sendeku, L. Yin, X. Zhan, F. Wang, Z. Wang, and J. He, "Recent Progress in CVD Growth of 2D Transition Metal Dichalcogenides and Related Heterostructures", Advanced Materials **31**, 1901694 (2019).

[3] A. Ciesielski and P. Samorì, "Grapheneviasonication assisted liquid-phase exfoliation", Chem. Soc. Rev. **43**, 381–398 (2014).

[4] R. J. Young, I. A. Kinloch, L. Gong, and K. S. Novoselov, "The mechanics of graphene nanocomposites: A review", Composites Science and Technology **72**, 1459–1476 (2012).

[5] K. S. Novoselov, V. I. Falko, L. Colombo, P. R. Gellert, M. G. Schwab, and K. Kim, "A roadmap for graphene", Nature **490**, 192–200 (2012).

[6] R. F. Frindt and A. D. Yoffe, "Physical properties of layer structures : optical properties and photoconductivity of thin crystals of molybdenum disulphide", Proceedings of the Royal Society of London. Series A. Mathematical and Physical Sciences **273**, 69–83 (1963).

[7] K. D. Dorfman, "The fluid mechanics of genome mapping", AIChE Journal **59**, 346–354 (2013).

[8] Y. Huang, E. Sutter, N. N. Shi, J. Zheng, T. Yang, D. Englund, H.-J. Gao, and P. Sutter, "Reliable Exfoliation of Large-Area High-Quality Flakes of Graphene and Other Two-Dimensional Materials", ACS Nano **9**, 10612–10620 (2015).

[9] K. Kim, M. Yankowitz, B. Fallahazad, S. Kang, H. C. P. Movva, S. Huang, S. Larentis, C. M. Corbet, T. Taniguchi, K. Watanabe, S. K. Banerjee, B. J. LeRoy, and E. Tutuc, "van der Waals Heterostructures with High Accuracy Rotational Alignment", Nano Letters **16**, 1989–1995 (2016).

[10] D. S. L. Abergel, A. Russell, and V. I. Fal'ko, "Visibility of graphene flakes on a dielectric substrate", Applied Physics Letters **91**, 063125 (2007).

[11] H. Li, J. Wu, X. Huang, G. Lu, J. Yang, X. Lu, Q. Xiong, and H. Zhang, "Rapid and Reliable Thickness Identification of Two-Dimensional Nanosheets Using Optical Microscopy", ACS Nano **7**, 10344–10353 (2013).

[12] P. Blake, E. W. Hill, A. H. Castro Neto, K. S. Novoselov, D. Jiang, R. Yang, T. J. Booth, and A. K. Geim, "Making graphene visible", Applied Physics Letters **91**, 063124 (2007).

[13] I. Jung, M. Pelton, R. Piner, D. A. Dikin, S. Stankovich, S. Watcharotone, M. Hausner, and R. S. Ruoff, "Simple Approach for High-Contrast Optical Imaging and Characterization of Graphene-Based Sheets", Nano Letters **7**, 3569–3575 (2007).

[14] A. Castellanos-Gomez, N. Agraït, and G. Rubio-Bollinger, "Optical identification of atomically thin dichalcogenide crystals", Applied Physics Letters **96**, 213116 (2010).

[15] H. Zhang, J. Huang, Y. Wang, R. Liu, X. Huai, J. Jiang, and C. Anfuso, "Atomic force microscopy for two-dimensional materials: A tutorial review", Optics Communications **406**, 3–17 (2018).

[16] K. S. Novoselov, D. Jiang, F. Schedin, T. J. Booth, V. V. Khotkevich, S. V. Morozov, and A. K. Geim, "Two-dimensional atomic crystals", Proceedings of the National Academy of Sciences **102**, 10451–10453 (2005).

[17] W. Thomson, "XIX. On the electro-dynamic qualities of metals:Effects of magnetization on the electric conductivity of nickel and of iron", Proceedings of the Royal Society of London **8**, 546–550 (1857).

[18] T. McGuire and R. Potter, "Anisotropic magnetoresistance in ferromagnetic 3d alloys", IEEE Transactions on Magnetics **11**, 1018–1038 (1975).

[19] J.-P. Jan, "Galvamomagnetic and Thermomagnetic Effects in Metals", in *Solid state physics - advances in research and applications*, Vol. 5, C (1957), pp. 1–96.

[20] H. X. Tang, R. K. Kawakami, D. D. Awschalom, and M. L. Roukes, "Giant Planar Hall Effect in Epitaxial (Ga,Mn)As Devices", Physical Review Letters **90**, 107201 (2003).

[21] E. Hall, "XVIII. On the Rotational Coefficient in nickel and cobalt", The London, Edinburgh, and Dublin Philosophical Magazine and Journal of Science **12**, 157–172 (1881).

[22] N. A. Sinitsyn, "Semiclassical theories of the anomalous Hall effect", Journal of Physics: Condensed Matter **20**, 023201 (2008).

[23] N. Nagaosa, J. Sinova, S. Onoda, A. H. MacDonald, and N. P. Ong, "Anomalous Hall effect", Reviews of Modern Physics **82**, 1539–1592 (2010).

[24] J. M. D. Coey, "History of Magnetism and Basic Concepts", in *Handbook of magnetism and magnetic materials* (Springer International Publishing, Cham, 2021), pp. 3–51.

[25] S. Y. Huang, W. G. Wang, S. F. Lee, J. Kwo, and C. L. Chien, "Intrinsic Spin-Dependent Thermal Transport", Physical Review Letters **107**, 216604 (2011).

[26] C. O. Avci, K. Garello, M. Gabureac, A. Ghosh, A. Fuhrer, S. F. Alvarado, and P. Gambardella, "Interplay of spin-orbit torque and thermoelectric effects in ferromagnet/normal-metal bilayers", Physical Review B **90**, 224427 (2014).

[27] G. Stiehl, "Crystal Symmetry and Spin-Orbit Torques", PhD thesis (Cornell University, 2018), pp. 1–203.

[28] S. N. Guin, K. Manna, J. Noky, S. J. Watzman, C. Fu, N. Kumar, W. Schnelle, C. Shekhar, Y. Sun, J. Gooth, and C. Felser, "Anomalous Nernst effect beyond the magnetization scaling relation in the ferromagnetic Heusler compound Co2MnGa", NPG Asia Materials **11**, 16 (2019).

[29] K. Garello, I. M. Miron, C. O. Avci, F. Freimuth, Y. Mokrousov, S. Blügel, S. Auffret, O. Boulle, G. Gaudin, and P. Gambardella, "Symmetry and magnitude of spinorbit torques in ferromagnetic heterostructures", Nature Nanotechnology **8**, 587–593 (2013).

[30] M. Hayashi, J. Kim, M. Yamanouchi, and H. Ohno, "Quantitative characterization of the spin-orbit torque using harmonic Hall voltage measurements", Physical Review B **89**, 144425 (2014).

[31] M.-H. Nguyen and C.-F. Pai, "Spinorbit torque characterization in a nutshell", APL Materials **9**, 1–15 (2021).

[32] R. Saito, Y. Tatsumi, S. Huang, X. Ling, and M. S. Dresselhaus, "Raman spectroscopy of transition metal dichalcogenides", Journal of Physics: Condensed Matter **28**, 353002 (2016).

# chapter 4

## Spin-orbit torques in transition metal dichalcogenide/ferromagnet heterostructures

*In recent years, there has been a growing interest in spin-orbit torques (SOTs) for manipulating the magnetization in nonvolatile magnetic memory devices. SOTs rely on the spin-orbit coupling of a nonmagnetic material coupled to a ferromagnetic layer to convert an applied charge current into a torque on the magnetization of the ferromagnet (FM). Transition metal dichalcogenides (TMDs) are promising candidates for generating these torques with both high charge-to-spin conversion ratios, and symmetries and directions which are efficient for magnetization manipulation. Moreover, TMDs offer a wide range of attractive properties, such as large spin-orbit coupling, high crystalline quality and diverse crystalline symmetries. Although numerous studies were published on SOTs using TMD/FM heterostructures, we lack clear understanding of the observed SOT symmetries, directions, and strengths. In order to shine some light on the differences and similarities among the works in literature, in this mini-review we compare the results for various TMD/FM devices, highlighting the experimental techniques used to fabricate the devices and to quantify the SOTs, discussing their potential effect on the interface quality and resulting SOTs. This enables us to both identify the impact of particular fabrication steps on the observed SOT symmetries and directions, and give suggestions for their underlying microscopic mechanisms. Furthermore, we highlight recent progress of the theoretical work on SOTs using TMD heterostructures and propose future research directions.*

Published as: Jan Hidding and Marcos H. D. Guimarães, "*Spin-Orbit Torques in Transition Metal Dichalcogenide/Ferromagnet Heterostructures*," Front. Mater. **7**, 594771 (2020), DOI: 10.3389/fmats.2020.594771 [1].

## 4.1. Introduction

Spin-orbit torques (SOTs) are promising candidates for effective manipulation of magnetization through electric currents with applications in nonvolatile magnetic memory and logic devices. SOTs convert an electric current into a magnetic torque in non-magnetic/ferromagnetic heterostructure, i.e. an electric current through the stack can modulate the direction of the ferromagnets magnetization [2, 3]. Devices showing large SOT efficiencies usually rely on a nonmagnetic material with large spin-orbit coupling in contact with a ferromagnet (FM). Transition metal dichalcogenides (TMDs), with chemical formula $MX_2$, where M is a transition metal (e.g. Mo, and W) and X a chalcogen element (e.g. S and Se), can provide large spin-orbit coupling and pristine surfaces which can result in a more intimate contact between the TMD and the FM layer. Furthermore, this family of materials offers a wide range of electronic and crystalline properties and symmetries. Although numerous articles were published on SOTs in TMD/ferromagnetic heterostructures, a clear understanding of the different mechanisms underlying observed SOTs remain yet to be understood.



In this mini-review, we give an overview of the recent progress on SOTs in TMD/FM heterostructures. Materials with high charge-to-spin conversion efficiencies, such as $WTe_2$ and $TaTe_2$ [4–6], are often considered as good candidates for large SOT efficiencies. However, large charge-to-spin conversion efficiencies are no guarantee for large SOT efficiencies, as SOTs are often an emergent phenomenon, depending on proximity effects (spin-orbit coupling and magnetic exchange), wave function overlap, and interface spin transparency (spin mixing conductance) as well. Indeed, the observed torques in TMD/FM heterostructures cannot always be explained by well-known effects such as the bulk spin Hall effect (SHE) [7–9] or the interfacial Rashba-Edelstein Effect (REE) [10–14] (Fig. 4.1), indicating that other mechanisms involving material specific properties or interfacial effects are into play. This is supported by recent works suggesting that both the type of ferromagnetic layer [15, 16] and the interface properties between the TMD and the ferromagnetic layer [17–21] are of paramount importance for the observed SOTs, allowing for enhanced and unconventional SOTs.

To describe to different torques, we use the notation in terms of odd ($\tau_o^\zeta \propto \hat{m}\times\hat{\zeta}$) or even ($\tau_e^\zeta \propto \hat{m} \times (\hat{\zeta} \times \hat{m})$) with respect to the magnetization direction ($\hat{m}$), with $\zeta = x, y, z$. These torques are also named, respectively, field-like (FL) and damping-like (DL) torques in many papers in literature [3], with directions out-of-plane or in-plane with respect to the TMD/FM plane (Fig. 4.1). For a fair comparison between the results in literature we use the torque conductivities ($\sigma^\zeta_{o(e)}$) to quantify the SOT strength, which expresses the torques per unit area per unit electric field. This figure of merit is adopted rather than the torque efficiency ($\xi^{j_c}_{FL(AD)}$), because the electric field across the device can be more accurately determined when compared to the current density [22].

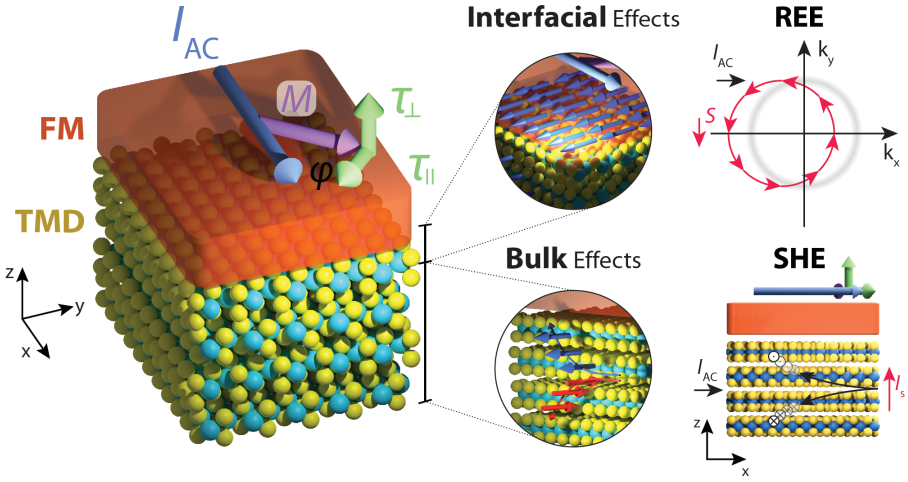


Figure 4.1: Schematics of SOTs in TMD/FM heterostructures. A charge current, usually oscillating at low (RF) frequencies for SHH (ST-FMR) measurements is applied along a device consisting of a TMD layer and a FM. The magnetization of the FM layer, oriented along an external magnetic field, observes a current-induced SOT in-plane ($\tau_{\parallel}$) and out-of-plane ($\tau_{\perp}$), indicated by the green arrows. These torques may arise from multiple microscopic effects arising in the bilayer, which may originate either from the TMD/FM interface (top), e.g. through the Rashba-Edelstein Effect (REE), or the bulk of the material (bottom), as for example through a spin Hall effect (SHE) in the TMD layer.

## 4.2. Discussion on recent progress

The field of SOTs using TMD-based devices has been rapidly developed in the past 5 years. Experimental studies have used different TMD sources (e.g. mechanical exfoliation or chemical vapor deposition, CVD), FM materials, deposition methods (e.g. sputtering or electron-beam evaporation), and measurement techniques, namely second-harmonic Hall (SHH) [23–26] or spin-torque ferromagnetic resonance (ST-FMR) [27–29]. So far, it is unclear how these different techniques and procedures affect the measured SOTs.

In this section, we discuss the results for semiconducting, semi-metallic and metallic TMDs, giving an overview of their fabrication and measurement techniques (Table 4.1). Comparing the TMDs in this way allows us to pinpoint important differences and similarities in the observed torques.

### 4.2.1. Semi-conducting TMDs

Shao et al. were one of the first to examine SOTs in TMD/FM heterostructures [30]. There, SOTs were quantified by the non-resonant SHH measurements on monolayer (1L) $MoS_2$ and $WSe_2$ coupled with CoFeB (3 nm). They observed a temperature independent out-of-plane FL torque $\tau_o^y$ $(\hat{m}\times\hat{y})$ for both devices with a corresponding torque conductivity of $\sigma_o^y = 2.88\times10^3(\hbar/2e)(\Omega\mathrm{m})^{-1}$ and $5.52\times10^3(\hbar/2e)(\Omega\mathrm{m})^{-1}$ for $MoS_2$ and $WSe_2$, respectively. No in-plane DL torque of the form $\tau_e^y(\hat{m}\times(\hat{y}\times\hat{m}))$ was observed in either of their devices. This DL torque is observed in SOT measurements

on Pt/Py bilayers and is often ascribed to the SHE [31]. Since the monolayer TMDs are much less conductive than the FM layer, the SOTs here are interfacial in nature, and the results point to the REE mechanism [32–35].

Interestingly, in a concurrent work, Zhang et al. obtained different results using a high-frequency technique, ST-FMR, on 1L-$MoS_2$/Permalloy ($Ni_{80}Fe_{20}$ Py) 5 nm [36]. There, they identified an in-plane DL $\tau_e^y$ ($\hat{m} \times (\hat{y} \times \hat{m})$) and an out-of-plane FL torque $\tau_o^y$ ($\hat{m} \times \hat{y}$). A torque ratio, $\tau_o^y/\tau_e^y = 0.19 \pm 0.01$ was obtained, indicating that $\tau_e^y$ dominates over $\tau_o^y$, in contrast to the results by Shao and co-workers. This result was repeated using different deposition techniques of the FM layer (sputtering or electron-beam deposition), indicating that the observed torque is independent on the Py deposition technique. The different measurement techniques used by the two groups could explain the discrepancy in the observed torques. However, it has been shown that the SOTs quantified by ST-FMR and SHH techniques agree within the experimental accuracy for several systems [37–39].

The discrepancy between results for $MoS_2$/FM bilayers suggests that not only the spin-orbit material but also the type of ferromagnetic material (CoFeB vs Py) can play a significant role in the observed torques. This is theoretically substantiated in a recent work [15], where calculations on $MoSe_2$/Co, $WSe_2$/Co and $TaSe_2$/Co heterostructures were performed. They find that the hybridization of the Co wavefunctions with those of the TMDs leads to dramatic transmutation of the electronic and spin structure of the Co layers, even within eight layers away from the interface. This suggests that injecting unpolarized spin currents in these spin-orbit-proximitized layers of Co generates non-equilibrium spin densities, which in turn leads to a nonzero local torque on the magnetization. Both the spin polarization direction and magnitude were shown to differ between the different TMDs and complex spin textures were obtained for the spin-orbit-proximitized layers. These results indicate that the FM material can play an active role in the type of SOTs observed. Moreover, recent theoretical works [18] pointed out that different scattering mechanisms lead to different torque symmetries, indicating that the sample quality, symmetry and nature of scatterers also plays a role here. Different FM materials in FM/TMD heterostructures might therefore exhibit different SOTs as was the case for Shao et al. and Zhang et al.

More recently, $WS_2$ was studied by Lv et al. in a 1L-$WS_2$/Py (10 nm) heterostructure [40] using CVD-grown $WS_2$ and electron-beam evaporated Py layer. The authors observe both a DL torque $\tau_e^y$ and a FL torque $\tau_o^y$ in their ST-FMR measurements, which are ascribed to the interfacial REE. Furthermore, they observed a gate-dependent SOT ratio ranging from $\tau_o^y/\tau_e^y = 0.05$ to 0.22 within a range of $V_g = -60$ V to 60 V, absent in their reference sample of Pt/Py. Gate-dependent SOTs were observed in SHH measurements on a topological insulator [41], but not yet reported in TMD/FM heterostructures. The increasing SOT ratio with gate-voltage could be explained by an increased carrier density leading to an enhanced current at the $WS_2$/Py interface. The modulation of SOT strength using a gate voltage is a step towards applications for data storage and processing and more research should be done to improve the gate tunability of SOTs in TMD/FM heterostructures [31, 42–44].

### 4.2.2. Semi-metallic TMDs

In addition to semiconducting TMDs, a variety of semi-metallic TMDs have been studied, with special focus given to low-symmetry crystals. A particularly interesting candidate is $WTe_2$, belonging to space group $Pmn2_1$. In a $WTe_2$/FM heterostructure, however, the symmetries are reduced to a single mirror plane perpendicular to the a-axis and the identity, space group Pm. The low device symmetry allows for unconventional SOTs, such as an out-of-plane DL torque $\tau_e^z$ $(\hat{m} \times (\hat{z} \times \hat{m}))$, which is especially interesting for applications in high-density memory devices since these torques are very effective for magnetization switching of perpendicular magnetic anisotropy materials [31].

MacNeill et al. were the first to examine SOTs using $WTe_2$ [37]. Using ST-FMR, the authors observed $\tau_e^z$, along the conventional SOTs $\tau_o^y$ and $\tau_e^y$, and extracted a torque conductivity of $\sigma_e^z = 3.6 \pm 0.8 \times 10^3 (\hbar/2e)(\Omega\text{m})^{-1}$ with the current driven along the low-symmetry a-axis. The other FL and DL torque conductivities were measured at $\sigma_o^y = 9 \pm 3 \times 10^3 (\hbar/2e)(\Omega\text{m})^{-1}$ and $\sigma_e^y = 8 \pm 2 \times 10^3 (\hbar/2e)(\Omega\text{m})^{-1}$, respectively. The magnitude of $\tau_e^z$ was found to depend on the angle between the electric current and the $WTe_2$ a-axis, showing a gradual decrease of the torque ratio $\tau_e^z/\tau_o^y$ when the projection of the current on the b-axis increases, giving support to its origin being correlated with the crystal symmetry. Even though an initial thickness dependence on the torques revealed little variation, a more thorough study with a wider thickness range ($t = 0.7 - 16$ nm) revealed additional bulk contributions to the SOTs in addition to the interfacial ones [45]. The thickness dependence of $|\tau_o^y|$, shows a strong increase with increasing $WTe_2$ thickness, suggesting it originates from an Oersted field produced by the current in the $WTe_2$ layer. The unusual out-of-plane DL torque $\tau_e^z$ shows a slowly decreasing magnitude with increasing thickness ($t \geq 4$ nm), while thinner layers show significant device-to-device variations. In the same work, the authors indicated that the in-plane DL torque $\tau_e^y$ possesses a similar thickness dependence as $\tau_e^z$. These torques remain large down a $WTe_2$ monolayer, suggesting that their microscopic origin is interfacial with some possible (smaller) additional bulk contribution.

Subsequent studies indicated a strong temperature dependence (2-300 K) on $\tau_o^y$ with the current flowing along the b-axis of $WTe_2$ using ST-FMR measurements [46]. While this temperature dependence was observed for thicker samples (20 nm and 31 nm), thinner samples (5.6 nm and 7.0 nm) only showed a weak temperature dependence. Furthermore, for a current applied along the a-axis (I $\parallel$ a), no temperature dependence is observed. A torque conductivity as high as $\sigma_o^y = 1.3 \times 10^5 (\hbar/2e)(\Omega\text{m})^{-1}$ was reported. Calculations of the Oersted field contribution to $\tau_o^y$ could not explain the large enhancement. The enhanced SOT at low temperatures with I $\parallel$ b-axis was therefore ascribed to a spin accumulation created by spin-momentum locking in Fermi arcs which exist only along the b-axis, experimentally observed for $WTe_2$ nanoribbons with thicknesses in the range of 10 nm to 40 nm [47]. The origin of the relatively high $\tau_o^y$ which remains for thinner devices, is ascribed to the REE.

More recently, $WTe_2$/Py heterostructures have been shown to be very efficient for current-induced in-plane magnetization switching, with switching current den-

sities in the order of $10^5$ A/cm$^2$ [39]. In the same work, the authors also reported a thickness dependence on the spin Hall efficiency in $WTe_2$, with larger values at higher thicknesses. However, the ST-FMR results show a significant frequency dependence and the role of artifacts such as skin-depth effects could not be ruled out. Nevertheless, the low threshold for current-induced magnetization switching indicates a promising direction for TMDs in future applications. Interestingly, these structures have also shown the presence of a Dzyaloshinskii-Moriya interaction, an essential ingredient for chiral magnetism.

The anisotropic in-plane conductivity in low-symmetry crystals can also impact SOTs. Results on $TaTe_2$/Py heterostructures have shown SOTs with Dresselhaus-like symmetries ($\hat{m} \times \hat{x}$) [38]. These torques have been shown to arise from Oersted-fields, generated by in-plane transverse current components due to conductivity anisotropy of $TaTe_2$. A similar, albeit smaller effect has been shown to be present in $WTe_2$/Py bilayers. Apart from the regular Oersted torque and Dresselhaus-like torque in the $TaTe_2$/Py heterostructures, the other torques are small or zero. Cross-sectional high-angle annular dark-field scanning transmission electron microscopy (HAADF-STEM) has indicated intermixing at the $TaTe_2$/Py interface which is likely to affect the effective SOTs due to a change in the local electronic environment and the spin mixing conductance of the interface. Interestingly, a change in the SOTs in topological-insulator/ferromagnet devices due to intermixing at the interface has been recently reported [48]. Here we point out that in addition to the changes in the SOTs arising from the different electronic structures for devices using different FM layers (e.g. Py, Co, CoFeB), the materials intermixing should also be carefully considered and potentially quantified in order to obtain a more in-depth understanding of the microscopic mechanisms involved.

Interestingly, both $TaTe_2$ and $WTe_2$ have shown to induce an in-plane magnetic anisotropy on Py, indicating a strong interaction between the semi-metallic TMDs and the FM layer. The anisotropy induced by $WTe_2$ was shown to be about 10s of mT and one order of magnitude larger than the one induced by $TaTe_2$. Additionally, the two TMDs induced anisotropy in different directions with respect to their crystal orientations, hinting towards the dependence of the induced magnetic anisotropy and the electronic structure of the TMD.

Another interesting semi-metallic TMD is $\beta$-$MoTe_2$ which, different than $WTe_2$ and similar to $TaTe_2$, possess inversion symmetry in its bulk form. Using $\beta$-$MoTe_2$/Py bilayers Stiehl et al. observe the presence of an out-of-plane DL torque $\tau_e^z$ using ST-FMR measurements [49]. This is allowed by the inversion symmetry breaking at the $\beta$-$MoTe_2$/Py interface and indicates that inversion asymmetry in the bulk is not a strict requirement for $\tau_e^z$ to be observed. The authors report a thickness independent torque conductivity of $\sigma_e^z = 1.02 \pm 0.03 \times 10^3(\hbar/2e)(\Omega\text{m})^{-1}$, 1/3 of the value reported for $WTe_2$. The standard in-plane DL torque $\tau_e^y$ was also observed with $\sigma_e^y = 5.8 \pm 0.16 \times 10^3(\hbar/2e)(\Omega\text{m})^{-1}$, and showed no apparent thickness dependence. The lack of a thickness dependent on $\tau_e^z$ and $\tau_e^y$ for both $WTe_2$ and $\beta$-$MoTe_2$, strongly suggests an interfacial origin for these SOTs.

In addition to the out-of-plane DL torque $\tau_e^z$, the low crystal symmetries of $WTe_2$ and $\beta$-$MoTe_2$ also allow for the presence of an in-plane FL torque $\tau_o^z$ (m

Œz ). While this torque was not observed in $WTe_2$, it was present in $\beta$-$MoTe_2$ devices. There, both $\tau_e^z$ and $\tau_o^z$ have shown similar temperature dependences, but different thickness dependences, hinting towards two microscopic mechanisms for $\tau_o^z$: one related and another unrelated to $\tau_e^z$. However, the physical mechanisms that generate these torques are still unknown.

More recently, $PtTe_2$/Py devices [50] have shown a high spin-torque conductivity for the in-plane DL torque $\sigma_e^y = 1.6 \times 10^5 (\hbar/2e)(\Omega\text{m})^{-1}$. This value is one order of magnitude (or larger) than the values encountered in other TMD-based devices and comparable to devices based on heavy-metal or topological-insulators. This large spin-torque conductivity has been ascribed to a combination of the SHE and spin-momentum locking in topological surface states of $PtTe_2$, as previously observed in topological insulators [51–54].



### 4.2.3. Metallic TMDs

Despite offering stronger spin-orbit interaction and higher conductivity, metallic TMDs have received less attention than their semi-metallic and semiconducting counterparts. To date, only two experimental studies have been reported [55, 56].

Thickness dependent ST-FMR measurements on $NbSe_2$ (1 to 10 layers) /Py heterostructures revealed an in-plane DL torque $\tau_e^y$ with a torque conductivity ($\sigma_e^y = 3\times10^3(\hbar/2e)(\Omega\text{m})^{-1}$ comparable to other TMD/Py heterostructures and observable down to a monolayer of $NbSe_2$ [55]. Similar to $\beta$-$MoTe_2$/Py [49], $\tau_e^y$ shows only a weak thickness dependence. An out-of-plane FL torque ($\sigma_o^y = 40\times10^3(\hbar/2e)(\Omega\text{m})^{-1}$ was also observed, and attributed to Oersted fields due to their linear scaling with $NbSe_2$ thickness. However, for thin $NbSe_2$ layers, the estimated Oersted-field contribution overestimates the observed torque magnitude, and, for monolayer $NbSe_2$ a sign change is observed. These observations for $\tau_e^y$ and $\tau_o^y$ indicate a contribution from interfacial torques.

In addition to the SOTs with conventional symmetries, an in-plane FL torque $\tau_o^z$ ($\hat{m} \times \hat{z}$) was observed in some devices. Since the trigonal symmetry of $NbSe_2$ does not allow for their presence, and given the seemly random thickness dependence of $\tau_o^z$, the authors argue that these torques could arise from uncontrollable strain from the fabrication procedure, which reduces the $NbSe_2$ symmetries. Although $\tau_e^z$ is subject to the same symmetry constraints, $\tau_e^z = 0$ for all measured devices, which is in contrast to the torques obtained for $WTe_2$, where $\tau_o^z = 0$, and $\tau_e^z \neq 0$ [37, 45]. This indicates that symmetry analysis alone is not sufficient to predict the observed torques in these systems and that other microscopic factors related to, for example, interface quality [18, 24], Berry curvature [57], or local atomic point-group symmetries [58] could play an important role.

A large spin-torque conductivity of $\sigma_e^y = 2.63 \times 10^5 (\hbar/2e)(\Omega\text{m})^{-1}$ has been recently reported for the metallic monolayer $TaS_2$/Py heterostructures [56] using ST-FMR measurements. This result is attributed to a clean interface which is supported by cross-sectional TEM imaging. Using DFT calculations, the authors observe a considerable redistribution of the band structure which they hold accountable for the prominent DL torque.

Table 4.1: Recent studies on TMD/FM heterostructures with their fabrication techniques and spin torque conductivities.

| Reference | SOT material (thickness) | Fabrication technique | Ferro-magnet | Deposition technique | Measurement technique | Spin torque conductivity [$\times 10^3$ (ħ/2e)(Ωm)$^{-1}$] | Proposed mechanism/ Source |
|---|---|---|---|---|---|---|---|
| | | **Semiconducting** | | | | | |
| (Shao et al., 2016) | $MoS_2$ (1 L) | CVD | CoFeB (3 nm) | Magnetron sputtering | SHH | $\sigma_o^y$ = 2.88 | REE |
| (Shao et al., 2016) | $WeS_2$ (1 L) | CVD | CoFeB (3 nm) | Magnetron sputtering | SHH | $\sigma_o^y$ = 5.52 | REE |
| (Zhang et al., 2016) | $MoS_2$ (1 L) | CVD | Py (5 nm) | Magnetron sputtering | ST-FMR | $\sigma_e^y$ =Observed | Interfacial |
| (Lv et al., 2018) | $WS_2$ (1 L) | CVD | Py (10 nm) | E-beam evaporation | ST-FMR | $\sigma_o^y$ =Observed | REE |
| | | | | | | $\sigma_e^y$ =Observed | REE |
| | | **Semi-metallic** | | | | | |
| (MacNeill et al., 2017a) | $WTe_2$ (1.8 - 15 nm) | Exfoliation | Py (6 nm) | Sputtering | ST-FMR/SHH | $\sigma_o^y = 9 \pm 3$ | Interfacial |
| | | | | | | $\sigma_e^y = 8 \pm 2$ | Interfacial |
| | | | | | | $\sigma_e^z = 3.6 \pm 0.8$ | Interfacial |
| | | | | | | $\sigma_o^z = 0$ | - |
| (MacNeill et al., 2017b) | $WTe_2$ (1 L - 16 nm) | Exfoliation | Py (6 nm) | Sputtering | ST-FMR/SHH | $\sigma_o^y$ =Observed | Oersted |
| | | | | | | $\sigma_e^y$ =Observed | - |
| | | | | | | $\sigma_e^z$ =Observed | - |
| | | | | | | $\sigma_o^z = 0$ | - |
| (Li et al., 2018) | $WTe_2$ (5.6 - 31 nm) | Exfoliation | Py (6 nm) | Sputtering | SHH | $\sigma_o^y = 1.3 \times 10^2$ | Fermi arcs |
| | | | | | | $\sigma_e^y$ =Observed | - |
| (Shi et al., 2019) | $WTe_2$ (5.8 - 122 nm) | Exfoliation | Py (6 nm) | Sputtering | ST-FMR/SHH | $\sigma_e^y = 6 \times 10^1$ (l//b) | |
| | | | | | | $\sigma_e^y$ = 5.95 (l//a) | Bulk |
| | | | | | | $\sigma_e^z$ =Observed (l//a) | |
| (Stiehl et al., 2019b) | $TaTe_2$ (4.5 - 19.7 nm) | Exfoliation | Py (6 nm) | Sputtering | ST-FMR/SHH | $\sigma_e^y$ =Weak | - |
| | | | | | | $\sigma_o^z$ =Sometimes observed | - |
| | | | | | | $\sigma_e^z = 0$ | - |
| | | | | | | $\sigma_o^x$ =Observed (Dresselhaus) | Oersted (resist. anisotropy) |
| (Stiehl et al., 2019a) | $MoTe_2$ (1 L - 14.2 nm) | Exfoliation | Py (6 nm) | Sputtering | ST-FMR/SHH | $\sigma_o^y$ = 15 | Oersted |
| | | | | | | $\sigma_e^y = 5.8 \pm 0.16$ | Interfacial |
| | | | | | | $\sigma_e^z = 1.02 \pm 0.03$ | Interfacial |
| | | | | | | $\sigma_o^z = 0.81 \pm 0.05$(t > 3 nm) | Interfacial |
| (Xu et al., 2020) | $PtTe_2$ (3 - 20 nm) | CVD | Py (2.5, 5.0, 7.5, 10 nm) | Sputtering | ST-FMR | $\sigma_o^y$ =Observed | - |
| | | | | | | $\sigma_e^y = 1.6 \times 10^2$ | SHE + TSS |
| | | **Metallic** | | | | | |
| (Guimarães et al., 2018) | $NbSe_2$ (1 - 10 L) | Exfoliation | Py (6 nm) | Sputtering | ST-FMR | $\sigma_o^y$ = 40 | Oersted |
| | | | | | | $\sigma_e^y$ = 3 | REE |
| | | | | | | $\sigma_e^z$ = 0 | - |
| | | | | | | $\sigma_o^z$ = 1 | Strain |
| (Husain et al., 2020) | 1T-$TaS_2$ (1 L) | Ion-beam sputtering | Py | - | ST-FMR/SHH | $\sigma_o^y$ =Negligible | - |
| | | | | | | $\sigma_e^y = 2.63 \times 10^2$ | Interfacial |

## 4.3. Conclusions

In this review, we have given an overview of the current status of the field of SOTs in TMD/FM heterostructures. A multitude of SOT symmetries, magnitudes and directions were observed, which could not always be explained by well-known effects such as the SHE and REE. Different mechanisms that do not rely on a large spin-orbit coupling, such as anisotropic in-plane conductivity and uniaxial strain, can also play an important role. Additionally, interfacial effects such as spin-orbit filtering, spin-orbit precession and spin-momentum locking in topological surface states may affect the observed torques. In combination with the large torque conductivities obtained at clean interfaces, this suggests that the TMD/FM interface quality is of paramount importance for both the torque magnitude and direction. Lastly, the ferromagnetic layer, often considered to play a passive role, can have a significant effect on the observed SOTs due to changes of the electronic structure and intermixing at the interface. DzyaloshinskiiMoriya interaction (DMI) has been shown to arise at TMD/FM interfaces demonstrating a strong interaction between these materials [21, 39, 59]. The large interfacial DMI in these heterostructures could be explored in future devices combining chiral magnetic structures and SOTs.



Although the crystal symmetry allows for a reasonable prediction of the allowed SOTs, a better understanding of the underlying microscopic mechanisms is key in qualitatively explaining the observed SOTs. In this regard, thickness dependent measurements provide a tool to better differentiate bulk effects from interfacial effects. However, as the contributions of different effects are measured all at once, it remains difficult to distinguish the numerous mechanisms underlying the torques with the current experimental techniques. To clarify the role of the ferromagnetic layer, a variety of devices with different FM materials should be fabricated.

Van der Waals heterostructures composed of TMDs, two-dimensional magnetic materials and graphene should allow for the study of SOTs at the ultimate thickness. Due to their small thickness, in addition to possibly reducing the device footprint, atomically-thin materials are more susceptible to external stimuli, such as gate-voltages, strain and illumination. Along these lines, interesting predictions point to the modulation of SOT and magnetization by gate-voltages in these structures [60, 61]. The exploration of gate-tunable SOTs in TMD/FM heterostructures could serve as a first step towards non-volatile data processing and storage as well as processing-in-memory applications. By giving an overview of the current status of the field, we hope to facilitate progress on elucidating the different underlying physical mechanisms for the SOTs.

# Bibliography


[1] J. Hidding and M. H. D. Guimarães, "Spin-Orbit Torques in Transition Metal Dichalcogenide/Ferromagnet Heterostructures", Frontiers in Materials **7**, 1–8 (2020).

[2] P. Gambardella and I. M. Miron, "Current-induced spinorbit torques", Philosophical Transactions of the Royal Society A: Mathematical, Physical and Engineering Sciences **369**, 3175–3197 (2011).

[3] A. Manchon, J. elezný, I. M. Miron, T. Jungwirth, J. Sinova, A. Thiaville, K. Garello, and P. Gambardella, "Current-induced spin-orbit torques in ferromagnetic and antiferromagnetic systems", Reviews of Modern Physics **91**, 035004 (2019).

[4] B. Zhao, D. Khokhriakov, Y. Zhang, H. Fu, B. Karpiak, A. M. Hoque, X. Xu, Y. Jiang, B. Yan, and S. P. Dash, "Observation of charge to spin conversion in Weyl semimetal WTe2 at room temperature", Physical Review Research **2**, 013286 (2020).

[5] A. M. Hoque, D. Khokhriakov, B. Karpiak, and S. P. Dash, "Charge-spin conversion in layered semimetal TaTe2 and spin injection in van der Waals heterostructures", Physical Review Research **2**, 033204 (2020).

[6] C. K. Safeer, N. Ontoso, J. Ingla-Aynés, F. Herling, V. T. Pham, A. Kurzmann, K. Ensslin, A. Chuvilin, I. Robredo, M. G. Vergniory, F. de Juan, L. E. Hueso, M. R. Calvo, and F. Casanova, "Large Multidirectional Spin-to-Charge Conversion in Low-Symmetry Semimetal MoTe2 at Room Temperature", Nano Letters **19**, 8758–8766 (2019).

[7] M. Dyakonov and V. Perel, "Current-induced spin orientation of electrons in semiconductors", Physics Letters A **35**, 459–460 (1971).

[8] J. E. Hirsch, "Spin Hall Effect", Physical Review Letters **83**, 1834–1837 (1999).

[9] J. Sinova, S. O. Valenzuela, J. Wunderlich, C. H. Back, and T. Jungwirth, "Spin Hall effects", Reviews of Modern Physics **87**, 1213–1260 (2015).

[10] V. Edelstein, "Spin polarization of conduction electrons induced by electric current in two-dimensional asymmetric electron systems", Solid State Communications **73**, 233–235 (1990).

[11] S. D. Ganichev, E. L. Ivchenko, V. V. Bel'kov, S. A. Tarasenko, M. Sollinger, D. Weiss, W. Wegscheider, and W. Prettl, "Spin-galvanic effect", Nature **417**, 153–156 (2002).

[12] Y. K. Kato, R. C. Myers, A. C. Gossard, and D. D. Awschalom, "Current-Induced Spin Polarization in Strained Semiconductors", Physical Review Letters **93**, 176601 (2004).

[13] I. Mihai Miron, G. Gaudin, S. Auffret, B. Rodmacq, A. Schuhl, S. Pizzini, J. Vogel, and P. Gambardella, "Current-driven spin torque induced by the Rashba effect in a ferromagnetic metal layer", Nature Materials **9**, 230–234 (2010).

[14] S. D. Ganichev, M. Trushin, and J. Schliemann, "Spin polarisation by current", Spintronics Handbook: Spin Transport and Magnetism, Second Edition, 269–315 (2016).

[15] K. Dolui and B. K. Nikoli, "Spin-orbit-proximitized ferromagnetic metal by monolayer transition metal dichalcogenide: Atlas of spectral functions, spin textures, and spin-orbit torques in Co/MoSe2, Co/WSe2, and Co/TaSe2 heterostructures", Physical Review Materials **4**, 104007 (2020).

[16] D. Go and H.-W. Lee, "Orbital torque: Torque generation by orbital current injection", Physical Review Research **2**, 013177 (2020).

[17] V. P. Amin, P. M. Haney, and M. D. Stiles, "Interfacial spinorbit torques", Journal of Applied Physics **128**, 151101 (2020).

[18] F. Sousa, G. Tatara, and A. Ferreira, "Skew-scattering-induced giant antidamping spin-orbit torques: Collinear and out-of-plane Edelstein effects at two-dimensional material/ferromagnet interfaces", Physical Review Research **2**, 043401 (2020).

[19] D. Go, F. Freimuth, J.-P. Hanke, F. Xue, O. Gomonay, K.-J. Lee, S. Blügel, P. M. Haney, H.-W. Lee, and Y. Mokrousov, "Theory of current-induced angular momentum transfer dynamics in spin-orbit coupled systems", Physical Review Research **2**, 033401 (2020).

[20] K. R. Sahoo, T. P. Chakravarthy, R. Sharma, S. Bawari, S. Mundlia, S. Sasmal, K. V. Raman, T. N. Narayanan, and N. K. Viswanathan, "Probing ProximityTailored High SpinOrbit Coupling in 2D Materials", Advanced Quantum Technologies **3**, 2000042 (2020).

[21] A. Kumar, A. K. Chaurasiya, N. Chowdhury, A. K. Mondal, R. Bansal, A. Barvat, S. P. Khanna, P. Pal, S. Chaudhary, A. Barman, and P. K. Muduli, "Direct measurement of interfacial DzyaloshinskiiMoriya interaction at the MoS2/Ni80Fe20 interface", Applied Physics Letters **116**, 232405 (2020).

[22] M.-h. Nguyen, D. C. Ralph, and R. A. Buhrman, "Spin Torque Study of the Spin Hall Conductivity and Spin Diffusion Length in Platinum Thin Films with Varying Resistivity", Physical Review Letters **116**, 126601 (2016).

[23] K. Garello, I. M. Miron, C. O. Avci, F. Freimuth, Y. Mokrousov, S. Blügel, S. Auffret, O. Boulle, G. Gaudin, and P. Gambardella, "Symmetry and magnitude of spinorbit torques in ferromagnetic heterostructures", Nature Nanotechnology **8**, 587–593 (2013).

[24] M. Hayashi, J. Kim, M. Yamanouchi, and H. Ohno, "Quantitative characterization of the spin-orbit torque using harmonic Hall voltage measurements", Physical Review B **89**, 144425 (2014).

[25] C. O. Avci, K. Garello, M. Gabureac, A. Ghosh, A. Fuhrer, S. F. Alvarado, and P. Gambardella, "Interplay of spin-orbit torque and thermoelectric effects in ferromagnet/normal-metal bilayers", Physical Review B **90**, 224427 (2014).

[26] A. Ghosh, K. Garello, C. O. Avci, M. Gabureac, and P. Gambardella, "Interface-Enhanced Spin-Orbit Torques and Current-Induced Magnetization Switching of Pd/Co/AlOx Layers", Physical Review Applied **7**, 014004 (2017).

[27] L. Liu, T. Moriyama, D. C. Ralph, and R. A. Buhrman, "Spin-Torque Ferromagnetic Resonance Induced by the Spin Hall Effect", Physical Review Letters **106**, 036601 (2011).

[28] D. Fang, H. Kurebayashi, J. Wunderlich, K. Výborný, L. P. Zârbo, R. P. Campion, A. Casiraghi, B. L. Gallagher, T. Jungwirth, and A. J. Ferguson, "Spinorbit-driven ferromagnetic resonance", Nature Nanotechnology **6**, 413–417 (2011).

[29] A. J. Berger, E. R. J. Edwards, H. T. Nembach, A. D. Karenowska, M. Weiler, and T. J. Silva, "Inductive detection of fieldlike and dampinglike ac inverse spin-orbit torques in ferromagnet/normal-metal bilayers", Physical Review B **97**, 094407 (2018).

[30] Q. Shao, G. Yu, Y.-W. Lan, Y. Shi, M.-Y. Li, C. Zheng, X. Zhu, L.-J. Li, P. K. Amiri, and K. L. Wang, "Strong Rashba-Edelstein Effect-Induced SpinOrbit Torques in Monolayer Transition Metal Dichalcogenide/Ferromagnet Bilayers", Nano Letters **16**, 7514–7520 (2016).

[31] R. Ramaswamy, J. M. Lee, K. Cai, and H. Yang, "Recent advances in spin-orbit torques: Moving towards device applications", Applied Physics Reviews **5**, 031107 (2018).

[32] I. M. Miron, K. Garello, G. Gaudin, P.-J. Zermatten, M. V. Costache, S. Auffret, S. Bandiera, B. Rodmacq, A. Schuhl, and P. Gambardella, "Perpendicular switching of a single ferromagnetic layer induced by in-plane current injection", Nature **476**, 189–193 (2011).

[33] P. M. Haney, H.-W. Lee, K.-J. Lee, A. Manchon, and M. D. Stiles, "Current induced torques and interfacial spin-orbit coupling: Semiclassical modeling", Physical Review B **87**, 174411 (2013).

[34] V. P. Amin and M. D. Stiles, "Spin transport at interfaces with spin-orbit coupling: Formalism", Physical Review B **94**, 104419 (2016).

[35] V. P. Amin and M. D. Stiles, "Spin transport at interfaces with spin-orbit coupling: Phenomenology", Physical Review B **94**, 104420 (2016).

[36] W. Zhang, J. Sklenar, B. Hsu, W. Jiang, M. B. Jungfleisch, J. Xiao, F. Y. Fradin, Y. Liu, J. E. Pearson, J. B. Ketterson, Z. Yang, and A. Hoffmann, "Research Update: Spin transfer torques in permalloy on monolayer MoS2", APL Materials **4**, 1–9 (2016).

[37] D. MacNeill, G. M. Stiehl, M. H. D. Guimaraes, R. A. Buhrman, J. Park, and D. C. Ralph, "Control of spinorbit torques through crystal symmetry in WTe2/ferromagnet bilayers", Nature Physics **13**, 300–305 (2017).

[38] G. M. Stiehl, D. MacNeill, N. Sivadas, I. El Baggari, M. H. D. Guimarães, N. D. Reynolds, L. F. Kourkoutis, C. J. Fennie, R. A. Buhrman, and D. C. Ralph, "Current-Induced Torques with Dresselhaus Symmetry Due to Resistance Anisotropy in 2D Materials", ACS Nano **13**, 2599–2605 (2019).

[39] S. Shi, S. Liang, Z. Zhu, K. Cai, S. D. Pollard, Y. Wang, J. Wang, Q. Wang, P. He, J. Yu, G. Eda, G. Liang, and H. Yang, "All-electric magnetization switching and DzyaloshinskiiMoriya interaction in WTe2/ferromagnet heterostructures", Nature Nanotechnology **14**, 945–949 (2019).

[40] W. Lv, Z. Jia, B. Wang, Y. Lu, X. Luo, B. Zhang, Z. Zeng, and Z. Liu, "Electric-Field Control of SpinOrbit Torques in WS2/Permalloy Bilayers", ACS Applied Materials & Interfaces **10**, 2843–2849 (2018).

[41] Y. Fan, X. Kou, P. Upadhyaya, Q. Shao, L. Pan, M. Lang, X. Che, J. Tang, M. Montazeri, K. Murata, L.-t. Chang, M. Akyol, G. Yu, T. Nie, K. L. Wong, J. Liu, Y. Wang, Y. Tserkovnyak, and K. L. Wang, "Electric-field control of spinorbit torque in a magnetically doped topological insulator", Nature Nanotechnology **11**, 352–359 (2016).

[42] X. Li, J. Casamento, P. Dang, Z. Zhang, O. Afuye, A. B. Mei, A. B. Apsel, D. G. Schlom, D. Jena, D. C. Ralph, and H. G. Xing, "Spinorbit torque field-effect transistor (SOTFET): Proposal for a magnetoelectric memory", Applied Physics Letters **116**, 242405 (2020).

[43] M. Filianina, J.-P. Hanke, K. Lee, D.-S. Han, S. Jaiswal, A. Rajan, G. Jakob, Y. Mokrousov, and M. Kläui, "Electric-Field Control of Spin-Orbit Torques in Perpendicularly Magnetized W/CoFeB/MgO Films", Physical Review Letters **124**, 217701 (2020).

[44] B. Dieny, I. L. Prejbeanu, K. Garello, P. Gambardella, P. Freitas, R. Lehndorff, W. Raberg, U. Ebels, S. O. Demokritov, J. Akerman, A. Deac, P. Pirro, C. Adelmann, A. Anane, A. V. Chumak, A. Hiroata, S. Mangin, M. C. Onbasli, M. d. Aquino, G. Prenat, G. Finocchio, L. L. Diaz, R. Chantrell, O. C. Fesenko, and P. Bortolotti, "Opportunities and challenges for spintronics in the microelectronic industry", arXiv preprint (2019).

[45] D. MacNeill, G. M. Stiehl, M. H. D. Guimarães, N. D. Reynolds, R. A. Buhrman, and D. C. Ralph, "Thickness dependence of spin-orbit torques generated by WTe2", Physical Review B **96**, 054450 (2017).

[46] P. Li, W. Wu, Y. Wen, C. Zhang, J. Zhang, S. Zhang, Z. Yu, S. A. Yang, A. Manchon, and X.-x. Zhang, "Spin-momentum locking and spin-orbit torques in magnetic nano-heterojunctions composed of Weyl semimetal WTe2", Nature Communications **9**, 3990 (2018).

[47] P. Li, Y. Wen, X. He, Q. Zhang, C. Xia, Z.-M. Yu, S. A. Yang, Z. Zhu, H. N. Alshareef, and X.-X. Zhang, "Evidence for topological type-II Weyl semimetal WTe2", Nature Communications **8**, 2150 (2017).

[48] F. Bonell, M. Goto, G. Sauthier, J. F. Sierra, A. I. Figueroa, M. V. Costache, S. Miwa, Y. Suzuki, and S. O. Valenzuela, "Control of SpinOrbit Torques by Interface Engineering in Topological Insulator Heterostructures", Nano Letters **20**, 5893–5899 (2020).

[49] G. M. Stiehl, R. Li, V. Gupta, I. E. Baggari, S. Jiang, H. Xie, L. F. Kourkoutis, K. F. Mak, J. Shan, R. A. Buhrman, and D. C. Ralph, "Layer-dependent spin-orbit torques generated by the centrosymmetric transition metal dichalcogenide $\beta$-MoTe2", Physical Review B **100**, 184402 (2019).

[50] H. Xu, J. Wei, H. Zhou, J. Feng, T. Xu, H. Du, C. He, Y. Huang, J. Zhang, Y. Liu, H.-C. Wu, C. Guo, X. Wang, Y. Guang, H. Wei, Y. Peng, W. Jiang, G. Yu, and X. Han, "High Spin Hall Conductivity in LargeArea TypeII Dirac Semimetal PtTe2", Advanced Materials **32**, 2000513 (2020).

[51] A. R. Mellnik, J. S. Lee, A. Richardella, J. L. Grab, P. J. Mintun, M. H. Fischer, A. Vaezi, A. Manchon, E.-A. Kim, N. Samarth, and D. C. Ralph, "Spin-transfer torque generated by a topological insulator", Nature **511**, 449–451 (2014).

[52] Y. Wang, D. Zhu, Y. Wu, Y. Yang, J. Yu, R. Ramaswamy, R. Mishra, S. Shi, M. Elyasi, K.-L. Teo, Y. Wu, and H. Yang, "Room temperature magnetization switching in topological insulator-ferromagnet heterostructures by spin-orbit torques", Nature Communications **8**, 1364 (2017).

[53] Y. Wang, P. Deorani, K. Banerjee, N. Koirala, M. Brahlek, S. Oh, and H. Yang, "Topological Surface States Originated Spin-Orbit Torques in Bi2Se3", Physical Review Letters **114**, 257202 (2015).

[54] O. J. Clark, M. J. Neat, K. Okawa, L. Bawden, I. Markovi, F. Mazzola, J. Feng, V. Sunko, J. M. Riley, W. Meevasana, J. Fujii, I. Vobornik, T. K. Kim, M. Hoesch, T. Sasagawa, P. Wahl, M. S. Bahramy, and P. D. C. King, "Fermiology and Superconductivity of Topological Surface States in PdTe2", Physical Review Letters **120**, 156401 (2018).

[55] M. H. D. Guimarães, G. M. Stiehl, D. MacNeill, N. D. Reynolds, and D. C. Ralph, "SpinOrbit Torques in NbSe2/Permalloy Bilayers", Nano Letters **18**, 1311–1316 (2018).

[56] S. Husain, X. Chen, R. Gupta, N. Behera, P. Kumar, T. Edvinsson, F. García-Sánchez, R. Brucas, S. Chaudhary, B. Sanyal, P. Svedlindh, and A. Kumar, "Large Damping-Like SpinOrbit Torque in a 2D Conductive 1T-TaS2 Monolayer", Nano Letters **20**, 6372–6380 (2020).

[57] H. Kurebayashi, J. Sinova, D. Fang, A. C. Irvine, T. D. Skinner, J. Wunderlich, V. Novák, R. P. Campion, B. L. Gallagher, E. K. Vehstedt, L. P. Zârbo, K. Výborný, A. J. Ferguson, and T. Jungwirth, "An antidamping spinorbit torque originating from the Berry curvature", Nature Nanotechnology **9**, 211–217 (2014).

[58] X. Zhang, Q. Liu, J.-W. Luo, A. J. Freeman, and A. Zunger, "Hidden spin polarization in inversion-symmetric bulk crystals", Nature Physics **10**, 387–393 (2014).

[59] Y. Wu, S. Zhang, J. Zhang, W. Wang, Y. L. Zhu, J. Hu, G. Yin, K. Wong, C. Fang, C. Wan, X. Han, Q. Shao, T. Taniguchi, K. Watanabe, J. Zang, Z. Mao, X. Zhang, and K. L. Wang, "Néel-type skyrmion in WTe2/Fe3GeTe2 van der Waals heterostructure", Nature Communications **11**, 3860 (2020).

[60] K. Dolui, M. D. Petrovic, K. Zollner, P. Plechac, J. Fabian, and B. K. Nikolic, "First-principles theory of proximity spin-orbit torque on a two-dimensional magnet: Current-driven antiferromagnet-to-ferromagnet reversible transition in bilayer CrI3", arXiv preprint, 1–8 (2019).

[61] K. Zollner, M. D. Petrovi, K. Dolui, P. Plechá, B. K. Nikoli, and J. Fabian, "Scattering-induced and highly tunable by gate damping-like spin-orbit torque in graphene doubly proximitized by two-dimensional magnet Cr2Ge2Te6 and monolayer WS2", Physical Review Research **2**, 043057 (2020).

# chapter 5

## Interfacial spin-orbit torques and magnetic anisotropy in $WSe_2$/permalloy bilayers

*Transition metal dichalcogenides (TMDs) are promising materials for efficient generation of current-induced spin-orbit torques (SOTs) on an adjacent ferromagnetic layer. Numerous effects, both interfacial and bulk, have been put forward to explain the different torques previously observed. Thus far, however, there is no clear consensus on the microscopic origin underlying the SOTs observed in these TMD/ferromagnet bilayers. To shine light on the microscopic mechanisms at play, here we perform thickness dependent SOT measurements on the semiconducting $WSe_2$/permalloy bilayer with various $WSe_2$ layer thickness, down to the monolayer limit. We observe a large out-of-plane field-like torque with spin-torque conductivities up to $1 \times 10^4 \, (\hbar/2e) \, (\Omega m)^{-1}$. For some devices, we also observe an in-plane antidamping-like torque, albeit with a large corresponding error. Both torques show no clear dependence on the $WSe_2$ thickness, as expected for a Rashba system. Unexpectedly, we observe a strong in-plane magnetic anisotropyup to about $6.6 \times 10^4$ erg $cm^{-3}$induced in permalloy by the underlying hexagonal $WSe_2$ crystal. Using scanning transmission electron microscopy, we confirm that the easy axis of the magnetic anisotropy is aligned to the armchair direction of the $WSe_2$. Our results indicate a strong interplay between the ferromagnet and TMD, and unveil the nature of the SOTs in TMD-based devices. These findings open new avenues for possible methods for optimizing the torques and the interaction with interfaced magnets, important for future non-volatile magnetic devices for data processing and storage.*

Published as: Jan Hidding et al., "*Interfacial Spin-Orbit Torques and Magnetic Anisotropy in $WSe_2$/Permalloy Bilayers*," J. Phys. Mater. **4** 04LT01, 289 (2021), DOI:10.1088/2515-7639/ac24ee [1].

## 5.1. Introduction

The electrical manipulation of magnetic layers is extremely appealing for future non-volatile and energy-efficient data processing and memory devices [2–4]. One of the most promising approaches to accomplish this is the use of spin-orbit torques (SOTs), where an electric current through a high spin-orbit material can apply a torque on the magnetization of an interfaced ferromagnetic layer [3]. One of the key components of materials showing large SOTs is the presence of a high spin-orbit coupling. For this reason, heavy-metal layers such as Pt [5–8], and Ta [9], have been used to generate efficient SOTs. These systems were shown to be capable of switching the direction of out-of-plane magnetic layers with relatively small current densities ($5 \times 10^5$ A cm$^2$) [10]. Therefore, heavy-metal-based SOT devices have been in the spotlight for future magnetic random-access memory devices [3].

The application of heavy-metal layers for SOT devices has many advantages, such as the easy integration with CMOS-compatible processes [11], but it suffers from a relatively low SOT efficiency. This is partially due to their relatively weak spin Hall effect - a few 10s of percent - combined with the fact that their spin Hall-generated torques do not possess the optimum symmetry for deterministic magnetization switching of magnetic layers with perpendicular magnetic anisotropy, such as the ones used in high-density memory recording. This has pushed researchers to explore more exotic material systems, such as topological insulators and two-dimensional (2D) materials, for SOT generation. Topological insulators were shown to generate very large SOTs and magnetic switching current densities orders of magnitude lower than conventional heavy-metal devices [12–18]. However, a large portion of the current still flows through the bulk of the material and does not profit from the high spin-orbit coupling at the (topological) surface states, which reduces the SOT efficiency.

The large family of van der Waals materials, such as transition metal dichalcogenides (TMDs), have shown to be a promising material platform for the study of SOTs [19]. Due to their versatile properties, where similar materials can show drastically different values of, e.g. conductivity or spin-orbit coupling, these systems can be used to pinpoint key ingredients for effective SOT generation. The study of SOTs in TMDs with low crystal symmetries illustrates this well [20–24]. There, researchers identified the presence of SOTs with unusual symmetries, not allowed in conventional systems and made possible by the low symmetry of the TMD layers. The particular case of semi-metallic $WTe_2$ is very attractive since it showed a large out-of-plane antidamping-like torque [20, 21], ideal for the switching of layers with perpendicular magnetic anisotropy, in addition to large SOT efficiencies and very small critical current densities for magnetization switching [25]. The antiferromagnetic insulator $NiPS_3$ also demonstrated very large SOT efficiencies, surpassing conventional Pt/ferromagnet systems at low temperatures [26].

Semiconducting TMDs, such as hexagonal $MoS_2$ and $WSe_2$, have also attracted significant attention. These materials have shown more modest SOT efficiencies [27–30] but are more attractive for industrial integration due to their air stability and the more developed methods for wafer-scale growth on CMOS-compatible substrates [31]. Even though SOTs in semiconducting TMD/ferromagnet systems have

been studied before, a clear consensus on the torque symmetries and mechanisms is still lacking [27, 32–34]. Moreover, all studies performed previously used chemical vapor deposition (CVD) grown layers, which, despite providing large scale films, suffer from a lower crystalline and electronic quality compared to their mechanically exfoliated counterparts.

Here, we report current induced SOTs in high-quality single crystal $WSe_2$ interfaced with a ferromagnet, $Ni_{80}Fe_{20}$ (permalloyPy), for multiple $WSe_2$ thicknesses, down to the monolayer limit. We observe a large out-of-plane field-like torque ($\tau_{FL}$), and, for some of our devices, an in-plane antidamping-like torque ($\tau_{DL}$) with no clear dependence on the $WSe_2$ thickness for both $\tau_{FL}$ and $\tau_{DL}$. Our results are consistent with SOTs arising from an interfacial (Rashba) spin-orbit coupling. Furthermore, we observe a large magnetic anisotropy induced on the Py layer for all our devices. Two devices in particular, possessing the largest anisotropy values, allow us to identify that the magnetic anisotropy induced in the Py layer closely follows the armchair crystallographic axis of the $WSe_2$ crystal. Our study shines light on the fundamentals of SOTs in TMD/ferromagnet bilayers, making it possible to narrow down on specific microscopic mechanisms. Moreover, our observation of a large magnetic anisotropy in Py following the crystallographic axis of $WSe_2$ should further enhance the understanding of the interaction between these two materials, essential for optimizing future TMD-based spintronic devices.



## 5.2. Experimental methods

### 5.2.1. Device fabrication

Our samples are fabricated by mechanically exfoliating a bulk $WSe_2$ crystal (HQ Graphene) on $Si/SiO_2$ [35]. Thin $WSe_2$ flakes are selected using optical microscopy and their thickness determined by optical contrast [36] and atomic-force microscopy. Monolayer flakes are further confirmed by their intense photoluminescence [37]. Only flakes with a low RMS roughness ($< 400$ pm) and with no steps are selected to avoid artifacts in our measurements due to the roughness of the ferromagnetic layer. For this study, final devices were fabricated using $WSe_2$ flakes with a thickness ranging from monolayer to four layers. Subsequently, a separately prepared mask with a Hall bar opening, made on poly (methyl methacrylate) (PMMA), is dry-transferred on top the $WSe_2$ flakes to ensure a pristine interface between the $WSe_2$ flake and a 6 nm thick Py layer which is deposited by electron-beam evaporation. The Py is capped with a 17 nm thick $Al_2O_3$ layer to protect it from oxidation. Next, Ti/Au (5/55 nm) contacts are fabricated using standard lithography and thin-film evaporation techniques. An $Al_2O_3$ wet etch with tetramethylammonium hydroxide is performed just before metal deposition. Finally, to create a well-defined device geometry, the $WSe_2$/Py bilayers are patterned in a Hall bar geometry using $CF_4/O_2$ (9.5/0.5 sccm) reactive plasma etching (30 W RF, 5 W ICP), where the $Al_2O_3$ layer serves as a hard mask. For most devices, the channel of our Hall bars, which establish the current direction, is defined along the edge of the flake. This is done to ensure that the current direction is applied at a nearly constant crystallographic direction. An optical image of a device before the last etching step is shown in Fig.

5.1(a).

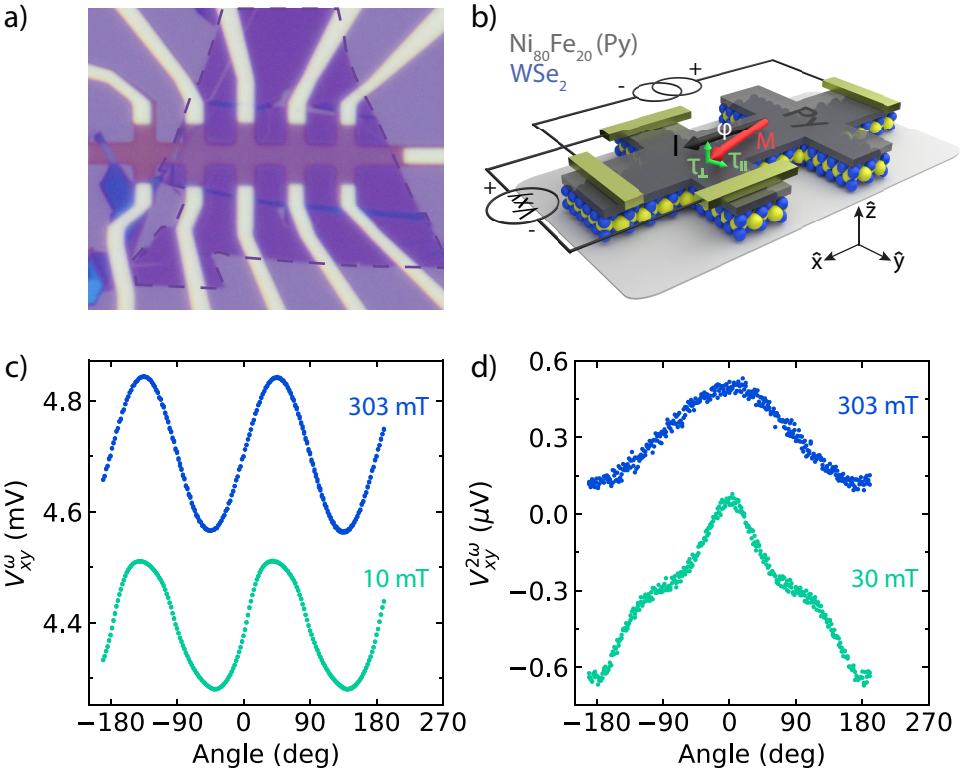


Figure 5.1: (a) Optical micrograph of a typical device ($D_2^B$) before etching the device into the Hall bar geometry. The $WSe_2$ flake is outlined by the dashed line. (b) Schematic of the $WSe_2$/Py device geometry and harmonic Hall measurement configuration. A current is driven along the $\hat{x}$-direction and the external magnetic field is rotated in-plane, while measuring the transverse first and second-harmonic Hall voltages ($V_{xy}^{\omega/2\omega}$) along the $\hat{y}$-direction. (c) and (d) show the first and second-harmonic Hall voltages versus in-plane rotation of the magnetic field, respectively, at low and high external magnetic fields. Note that the signals were offset for clarity.

### 5.2.2. Electrical measurements

The SOTs in our devices are characterized at room temperature using conventional low-frequency harmonic Hall measurements [5, 38, 39] with currents ranging from $I_0 = 400 - 600$ μA and frequencies below 200 Hz. With this technique, a constant magnetic field $\mu_0 H$(10-300 mT) is applied in the sample plane and the sample is rotated, so the field makes an angle $\phi$ with respect to the current. Meanwhile, the first and second-harmonic Hall voltages, $V_{xy}^{\omega}$ and $V_{xy}^{2\omega}$, respectively, are measured, as shown in Fig. 5.1(b). For a small magnetic anisotropy compared to $\mu_0 H$, the magnetization angle is $\phi_M \approx \phi$. The first-harmonic Hall resistance ($R_{xy}^{\omega} = V_{xy}^{\omega}/I_0$) is given by:

$$R_{xy}^{\omega} = R_{PHE}\sin^2(\theta)\sin(2\phi) + R_{AHE}\cos(\theta) \tag{5.1}$$

where $\theta$ is the magnetic fields polar angle ($\theta = 90°$for in-plane magnetic fields), and $R_{PHE(AHE)}$ is the strength of the planar (anomalous) Hall effect resistance. In the presence of out-of-plane field-like and in-plane antidamping-like SOTs ($\tau_{FL}$ and $\tau_{DL}$) and an anomalous Nernst effect voltage ($V_{ANE}$), a second-harmonic Hall voltage is generated and can be described by [5, 38]:

$$V_{xy}^{2\omega}(\phi) = A\cos(2\phi)\cos(\phi) + B\cos(\phi) \tag{5.2}$$

where the $A$- and $B$-component are given by:

$$A = \frac{R_{PHE}I_0\tau_{FL}/\gamma}{H} \tag{5.3}$$

$$B = \frac{R_{AHE}I_0\tau_{DL}/\gamma}{H + H_K} + V_{ANE} \tag{5.4}$$

with $\gamma$ the gyromagnetic ratio, $H$ is the applied magnetic field and $H_K$ the out-of-plane anisotropy field. Due to the hexagonal symmetry of $WSe_2$, in the absence of strain, only torques with conventional symmetries are allowed [22, 40]. Therefore, we expect no unconventional SOTs related to the crystal structure in our devices, which agrees with our experimental results. The SOT terms are assumed to have the conventional symmetry properties with respect to the magnetization direction ($\hat{m}$), i.e. $\tau_{FL} \propto \hat{m}\times\hat{y}$ and $\tau_{DL} \propto \hat{m}\times(\hat{y}\times\hat{m})$, where $\hat{y}$ is the direction perpendicular to the current (see Fig. 5.1(b)).



### 5.2.3. Scanning transmission electron microscopy

We prepared cross-sectional specimen with a Helios G4 CX focused ion-beam (FIB) at 30 kV from Thermo Fisher Scientific, either parallel or perpendicular to the device current direction, using gradually decreasing acceleration voltages of 5 kV and 2 kV for the final polishing. Transmission electron microscopy (TEM) analyses were performed with a double aberration corrected Themis Z from Thermo Fisher Scientific, operated at 300 kV. High-angle annular dark-field scanning TEM (HAADF-STEM) images were recorded with probe currents of about 50 pA, convergence semi-angle 21 mrad or 30 mrad and HAADF collection angles 61 − 200 mrad.

## 5.3. Results

We performed harmonic Hall measurements for six $WSe_2$/Py devices with various $WSe_2$ thicknesses. For convenience, we will refer to the devices as $D_1$, $D_2^{A/B/C}$ and $D_4^{A/B}$for the remainder of the text, where the subscript denotes the number of $WSe_2$ layers and the superscript the device label. We observe a large out-of-plane field-like torque in all but one of our $WSe_2$/Py devices with some of them showing an additional in-plane antidamping-like torque with a correspondingly large error bar.

The device that did not show a measurable SOT ($D_2^C$), however, shows unprecedentedly large magnetic anisotropy. As discussed in the last section, the large

magnetic anisotropy counteracts the SOTs, making it very challenging to properly quantify them by our measurement technique. First, however, we will discuss the harmonic Hall measurements of the SOTs in the other five devices.

### 5.3.1. Interfacial SOTs

Figure 5.2(a) shows the second-harmonic Hall voltage for a two-layer ($\sim$ 1.4 nm thick) $WSe_2$/Py device ($D_2^A$) as a function of $\phi$ for various magnetic field strengths. The data are fitted to extract the $A$ and $B$ amplitudes (Eq. 5.2), which are then plotted versus $1/H$ and $1/(H+H_K)$ (Fig. 5.2(b)). The presence of SOTs is revealed by the linear dependence on $1/H$ and $1/(H+H_K)$, while the anomalous Nernst effect can be differentiated by an offset in $B$. At low fields the assumption that $H \gg H_a$, no longer holds, resulting in a worse fit and thus larger error bars. Especially, the B-component shows a large field-dependence at low fields, which does not fit well to Eq. 5.4 (grey lines in Fig. 5.2(b)). Therefore, we fit Eq. 5.3 and 5.4 only to measurements performed at 40 mT or higher to extract the field-like ($\tau_{FL}$) and antidamping-like ($\tau_{DL}$) torques, respectively (black lines in Fig. 5.2(b)).



To better quantify and compare the SOTs in our devices, we express them in terms of their spin-torque conductivities, commonly used as figure-of-merit in literature [3]. The spin-torque conductivity is defined as the angular momentum absorbed by the ferromagnet per second per applied electric field per interface area. Due to the independence of the spin-torque conductivities with respect to device geometries and resistances, it gives us a meaningful value which allows us to compare our various devices among each other as well as with values reported in literature. The spin-torque conductivities for $\tau_{FL(DL)}$ are calculated by [24, 41]:

$$\sigma_{FL(DL)} = \frac{2e}{\hbar} M_s t_{Py} w \frac{\tau_{FL(DL)}/\gamma}{R_{sq} I_0} \tag{5.5}$$

where $e$ and $\hbar$ are the electron charge and the reduced Plancks constant, respectively, $M_s$ is the saturation magnetization, $t_{Py} = 6$ nm is the Py thickness, $w$ is the device width, and $R_{sq}$ is the square resistance of the $WSe_2$/Py stack. The parameters for all these devices are summarized in Table 5.1.

The field-like spin torque conductivities for all devices versus layer thickness are shown in Fig. 5.2(c). We observe a $\sigma_{FL}$ ranging from $4.9 \pm 0.3 \times 10^3$ to $12.9 \pm 0.3 \times 10^3 \frac{\hbar}{2e} (\Omega \cdot \mathrm{m})^{-1}$ with no clear correlation with the $WSe_2$ layer thickness. These results are consistent with previous reports on CVD grown monolayer $WSe_2$/ferromagnet devices [28]. Nevertheless, to the best of our knowledge, we report both the highest field-like found for semiconducting TMDs. This indicates that our devices possess a highly transparent interface and a large interaction between the TMD and the ferromagnet. The key differences of our process compared to the previous reports are the higher quality of $WSe_2$ crystals with single crystallographic domains obtained by mechanical exfoliation and a milder deposition of the ferromagnetic layer [28–30]. Our devices show pristine interfaces between $WSe_2$ and Py, with no observable intermixing as confirmed by HAADF-STEM cross-sectional imagingsee below. Therefore, we expect a cleaner interface quality to be the main reason for these high field-like torques.

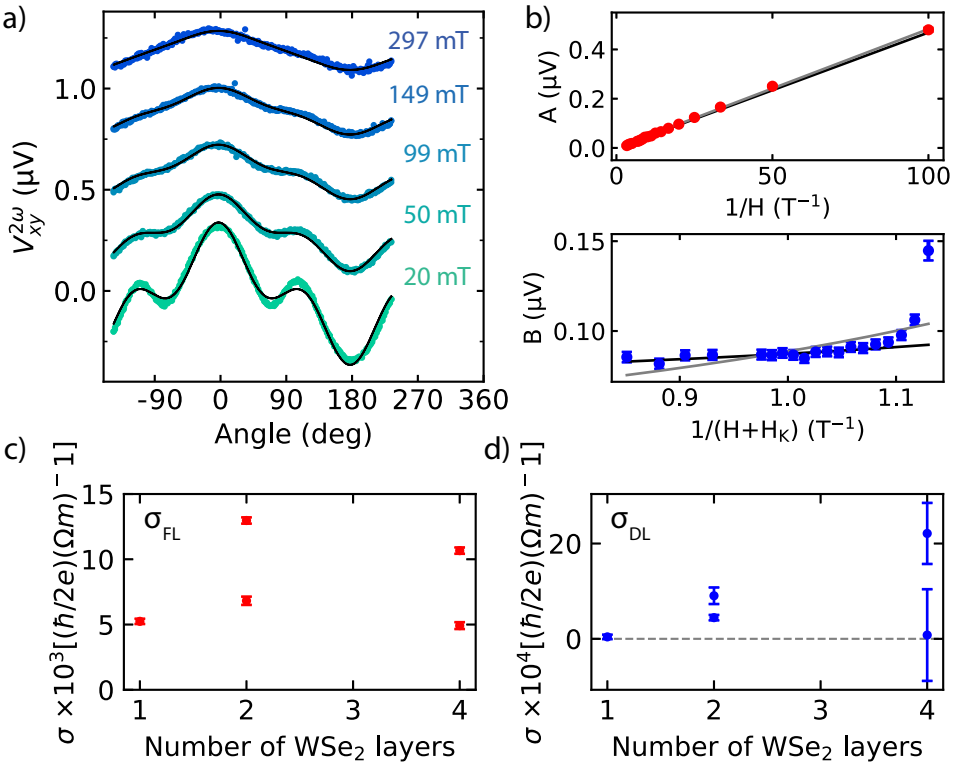


Figure 5.2: (a) Second-harmonic Hall measurements at various magnetic fields for one $WSe_2$/Py device $D_2^A$. The colored circle represent the data while the black line are fits using Eq. 5.2. The measurements for different fields have been offset for clarity. (b) The *A*- and *B*-component extracted from the fit of (a) for various magnetic field strengths. The straight lines corresponds to the fits using Eqs. 5.3 and 5.4. The grey line corresponds to the fit using the data points from all magnetic fields, while the black line corresponds to the fit for fields starting at 40 mT. The error bars are obtained from the standard deviation from the fit. (c, d) The spin-torque conductivities of the (c) field-like and (d) antidamping-like torque, calculated using Eq. 5.5, for devices with various $WSe_2$ thickness.

The B-component shown in Fig. 5.2(d) shows a strong field-dependence at low fields. This behavior is inconsistent with Eq. 5.4 which predicts the B-component to fall of as $1/(H + H_K)$. Previous reports show that the second-harmonic signal might be falsely attributed to a antidamping-like torque $\tau_{DL}$ in cases of significant unidirectional magnetoresistance (UMR) arising from electron-magnon scattering [42]. To verify this, we measured the second-harmonic longitudinal voltage and find a similar second-harmonic signal, with a $\sin(\phi)$ behavior and $1/H$ dependence. A 90°phase shift here is expected since the $V_{xx}^{2\omega}$ is phase shifted relative to $V_{xy}^{2\omega}$ by 90°. Therefore, a contribution from UMR to our second-harmonic signal cannot be ruled out.

By disregarding measurements performed lower than 40 mT, we use Eq. 5.4 to extract an antidamping-like torque and find a $\sigma_{DL}$ ranging from $4 \pm 5 \times 10^3$ to $2.2 \pm 0.7 \times 10^5 \frac{\hbar}{2e}(\Omega \cdot \mathrm{m})^{-1}$ with no clear correlation with the $WSe_2$ layer thickness. In contrast to [30], we do not observe a decreasing $\tau_{DL}$ with increasing $WSe_2$ layer thickness for our devices. Rather, we observe a seemingly increasing $\sigma_{DL}$ with increasing thickness. Moreover, increase scattering at the interface has been predicted to give an increase antidamping-like torque, which could explain the large DL torque observed [29] [30]. However, we note that two devices do not show a significant $\sigma_{DL}$, and the other devices possess a large error bar making these values for the antidamping-like torque unreliable.

As Py is known to show torques even in the absence of other spin-orbit materials [41, 43], we fabricated control $Py/Al_2O_3$ samples to exclude that the strong field-like torque is generated solely in the $Py/Al_2O_3$ layer. Similar to previous reports [30, 43], we observe a non-zero field-like torque, with an average spin-torque conductivity of $\sigma_{FL} = (2.5 \pm 0.1) \times 10^3 \frac{\hbar}{2e}(\Omega \cdot \mathrm{m})^{-1}$. Note that we find a negative spin-torque conductivity, showing that these torques have the opposite direction as the ones we measure in our $WSe_2$ devices. The sign difference indicates that the field-like torque in the $WSe_2$/Py devices reported here are most likely an underestimation of the torques produced at the $WSe_2$/Py interface as they compete with opposite torques produced at the $Py/Al_2O_3$ interface. No significant antidamping-like torque was observed in these $Py/Al_2O_3$ samples (see supplementary information for details).

The absence of a thickness dependence in our devices for the field-like torque indicates that the torque does not originate from current-induced Oersted fields, for which an increasing torque is expected with increasing layer thickness. This is also in agreement with most of the current flowing through the Py layer due to its much higher conductivity when compared to $WSe_2$. A simple estimation suggests that our FL torques could only be explained by an unreasonable large conductivity for $WSe_2$, of $\sigma_{WSe_2} \sim 10^6(\Omega \cdot \mathrm{m})^{-1}$, about 5 orders of magnitude higher than literature values [44]. Moreover, we point out that the sign of the FL torque we obtain is opposite to the one expected from a current flowing through the $WSe_2$ layer. We confirm the sign of the Oersted torques by control Pt/Py devices. We note that we observe no variation of the SOTs with gate voltages ranging up to ±60 V (equivalent to electric fields of ±2.1 MV $\mathrm{cm}^{-1}$) (see supplementary information), similar to previous reports [30], which could be due to a large Schottky barrier [45] or Fermi level pinning at the metal-semiconductor interface [46].

The independence of $\tau_{FL}$ with the $WSe_2$ thickness are consistent with interfacial SOTs [47–49]. In systems with an interfacial Rashba-type spin-orbit coupling, a pure out-of-plane field-like torque is expected. However, it has been theoretically shown that an in-plane antidamping-like torque can arise in the presence of electron scattering [32, 34, 47–49]. Therefore, our data indicate that the SOTs in our devices arise from a Rashba-type spin-orbit coupling at the interface, with possibly, some devices showing a stronger scattering, giving rise to a $\tau_{DL}$. We note, however, that the extracted values for the $\tau_{DL}$ possess a large error bar, making them unreliable. The variation in spin torque conductivities between the devices is ascribed to a difference in $WSe_2$/Py interface quality. Variations in interface quality can affect the spin transparency of the interface, resulting in differences in the torque strength. Furthermore, pristine interfaces are expected to show stronger Rashba-effects. This is in line with our observation that the devices showing a measurable $\tau_{DL}$ also possess the highest $\tau_{FL}$. Lastly, the importance of the interface quality is highlighted by the fact that we observe no measurable SOTs when using standard lithography techniques to fabricate similar devices, where no particular care to maintain a pristine interface was taken (see supplementary information for details).



### 5.3.2. Magnetic anisotropy

One of the most striking differences between our devices, consisting of exfoliated $WSe_2$ crystals, and previous studies based on CVD-grown films is the presence of a strong magnetic anisotropy induced in the Py film. The first-harmonic Hall voltages for our devices are expected to follow a $\sin(2\phi)$ behavior due to the planar Hall effect, Eq. 5.1. However, for all devices, at low external magnetic fields ($< 20$ mT), we observe clear deviations from the planar Hall effect, Fig. 5.1(c) (device $D_2^B$). For device $D_1$, and in particular device $D_2^C$, we observe very strong deviations from the expected $\sin(2\phi)$ behavior even for external magnetic fields up to 100 mT. This demonstrates a very strong induced magnetic anisotropy in the Py layer, as shown in Fig. 5.3(a) for device $D_2^C$, causing the magnetization angle of Py, $\phi_M$, to slightly deviate from the applied magnetic field angle, $\phi$.

To study the magnetic anisotropy in more detail, we modify Eq. 5.1 to account for an in-plane uniaxial anisotropy, with strength $H_A$ much smaller than the applied magnetic field and an easy-axis angle $\phi_E$ with respect to the current [21]:

$$R_\omega = R_{PHE} \sin(2\phi_M) \tag{5.6}$$

with

$$\phi_M = \phi - \frac{H_A}{2H} \sin[2(\phi - \phi_E)] \tag{5.7}$$

For all our devices, apart from $D_1$ and $D_2^C$, we observe $H_A \approx 0.01$ to 0.16 T, and a $\phi_E \approx 0°$or $\pm 30°$, hinting towards a relation between the magnetic anisotropy direction in the Py and the hexagonal crystal structure of the underlying $2_2$. The values we find for $H_A$ for these devices are higher by factors of 2-10 than for those reported in similar systems [20, 21, 23, 24]. Our results for all devices are summarized in the supplementary information.

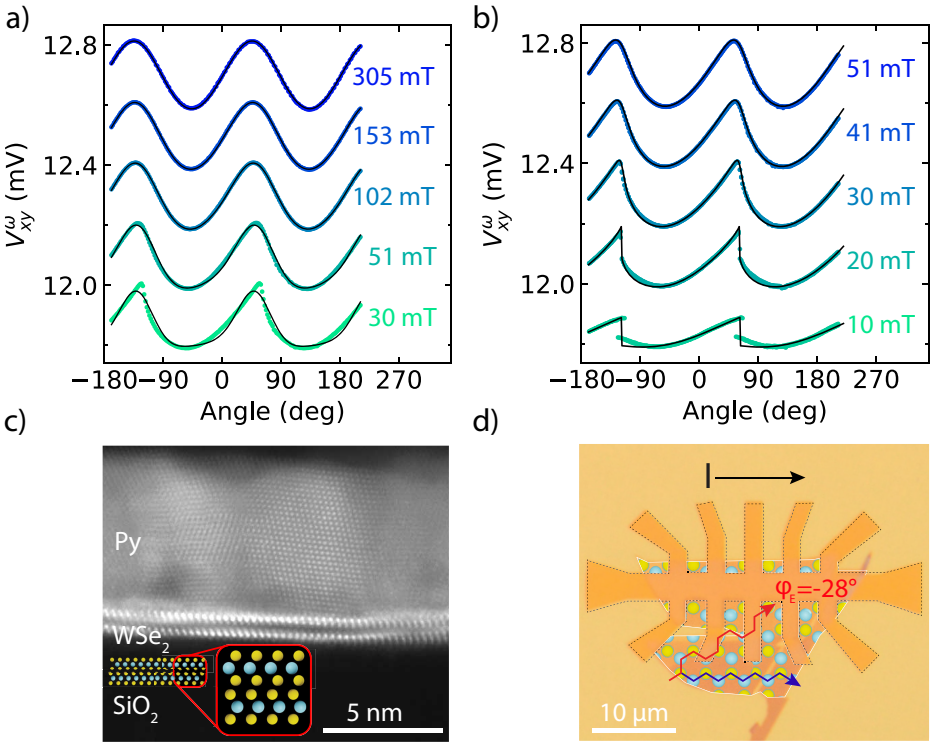


Figure 5.3: (a) First-harmonic Hall voltage for one of the $WSe_2$/Py devices ($D_2^C$), shown in (d). The black line corresponds to the fit using equations (6) and (7) and colored circles to the experimental data. Clear deviations from the planar Hall effect are apparent, indicating an in-plane magnetic anisotropy in the Py layer. (b) First-harmonic Hall voltage for the same device as in (a) for low magnetic fields, fitted with the model discussed in the main text (black line). Note that the plots in (a) and (b) have been given an offset for clarity. (c) Cross sectional HAADF-STEM image of the device shown in (d). The two layers of $WSe_2$ are clearly identified with atomic resolution. The cross section is made perpendicular to the current direction in between the legs of the Hall bar. The crystallographic orientation of the $WSe_2$ layer is apparent from the similarities between the schematic inset, showing the cross section of the armchair direction, and the STEM image, which indicates that the current direction is along the zigzag direction, as shown in (d). (d) Micrograph of the same device in (a) with the hexagonal crystal structure of $WSe_2$ overlayed on the $WSe_2$ crystal (outlined in white). The blue and red arrows indicate the zigzag and armchair direction, respectively. Notice that the channel of the Hall bar (black dashed line) is aligned with one of the cleaving directions of the $WSe_2$ crystal and the current direction is therefore along the flake edge for device $D_2^C$.

For devices $D_1$ and $D_2^C$, showing much stronger anisotropy, we find stronger deviations from the fits using Eqs. 5.6 and 5.7. Due to the stronger anisotropy, the approximation $H_A \ll H$ taken above is no longer valid. Therefore, we use a simple macrospin model to fit the data. First, we find the magnetization angle $\phi_M$ at an applied magnetic field angle $\phi_H$, by minimizing the magnetic energy:

$$E = \left(\frac{K_2}{2}\right)\cos(2\phi_M - 2\phi_E) - h\cos(\phi_M - \phi_H) \tag{5.8}$$

where $K_2$ is the 2-fold anisotropy constant, and $h$ is the Zeeman energy by the applied magnetic field at an angle $\phi_H$. We find that our data agrees with this simple theoretical model with $K_2 = 2\times10^4$erg/cm$^3$ and $6.6\times10^4$erg/cm$^3$ for devices $D_1$ and $D_2^C$, respectively. For devices D1 and DC 2 we find $\phi_E = 60°(D_1)$ and $\phi_E = 28°(D_2^C)$, with respect to the current direction. This suggests that the induced magnetic anisotropy is indeed related to the hexagonal crystal structure of the $WSe_2$.

To confirm the crystallographic direction and the interface quality of our devices, we performed HAADF-STEM cross-sectional imaging in two devices and two additional $WSe_2$ flakes. Figure 5.3(c) shows a cross-sectional HAADF-STEM image of device $D_2^C$. The two layers of the $WSe_2$ are visible with atomic resolution and the STEM image reveals the randomly oriented polycrystalline structure of the Py layer on top. The STEM image shows an atomically sharp interface indicating a clean interface for our fabricated devices. In addition, little to no intermixing is observed demonstrating that the $WSe_2$ layer experiences little to no damage upon evaporation of the Py layer and that the crystalline orientation of the layer remains uniform.

For the crystallographic direction, we find that the edge of all $WSe_2$ flakes studied by STEM follow a zigzag direction. For device $D_2^C$, the Hall bar channel is aligned with the edge of the $WSe_2$ flake, so that the current flows along the zigzag direction (schematically indicated in Fig. 5.3(d)). As we found $\phi_E = 28°$for device $D_2^C$ following our analysis, we conclude that the (uniaxial) magnetic anisotropy observed in the Py layer lies along the armchair direction of the $WSe_2$. For device $D_1$, the Hall bar channel is aligned 30°away from the edge of the $WSe_2$ flake, in which case the current flows along the armchair direction. Correspondingly, we find that $\phi_E = 60°$, which again shows that the (uniaxial) magnetic anisotropy is aligned with the armchair direction of the $WSe_2$.

The correspondence between the magnetic anisotropy direction in Py and the crystallographic directions of the $WSe_2$ indicates a strong interaction between the two materials. Similar results have been found in low-symmetry TMDs, such as $WTe_2$ [20, 21], $MoTe_2$ [24], and $TaTe_2$ [23], with values around $H_A \sim 10$ mT, one order of magnitude lower compared to values observed in our devices (supplementary information Table 5.1). However, systems with higher (hexagonal) symmetries, such as $NbSe_2$ [22] and $NiPS_3$ [26], did not show such effects, even though in the case of $NbSe_2$, the symmetry might have been reduced by strain. We point out that the polycrystallinity of CVD-grown crystals would not allow for such observation, which is supported by the lack of magnetic anisotropy in previous studies [28–30]. Moreover, such large values of the magnetic anisotropy shown by devices $D_1$ and $D_2^C$ are unprecedented in TMD-based devices. We do not fully understand the differences in anisotropy strength between devices $D_1$ and $D_2^C$ and the other devices since all device fabrication steps were identical. Nevertheless, due to the strong dependence of the magnetic anisotropy on the interface quality and the fact that particular care was taken in maintaining a clean interface during fabrication, we

have arguments to believe that our devices have more pristine interfaces, resulting in a stronger interaction between Py and $WSe_2$.

## 5.4. Conclusions

In conclusion, we report large field-like torques in $WSe_2$/permalloy bilayers with no clear dependence on the $WSe_2$ layer thickness. Although we extract an antidamping-like torque in a few devices, due to an unexpectedly strong field-dependence of the B-component at low fields, we are not able to extract a reliable antidamping-like torque. The appearance of a thickness-independent field-like torque in these systems confirms the prediction of recent theoretical work on similar interfacial Rashba systems and accentuates the importance of the heavy metal/ferromagnet interface quality for tailoring towards highly efficient torques. Furthermore, we observe an induced uniaxial magnetic anisotropy in all our devices, with two devices in particular showing very strong anisotropy, aligned with the armchair direction of the $WSe_2$. Although smaller magnetic anisotropy values were observed in low-symmetry TMD-based devices, a microscopic understanding of the mechanisms involved is still lacking. The higher crystal symmetry of $WSe_2$ combined with the larger anisotropy values we observe, are expected to help researchers to develop a more detailed theoretical description of this phenomenon and, eventually, a better understanding of all the effects regarding crystal symmetry involved for SOT devices. The knowledge on the microscopic mechanisms at play, for both SOTs and induced magnetic anisotropy, should shine light on the factors required for the development of more efficient devices for data processing and storage.



## 5.5. Appendices

### 5.5.1. Supplementary note 1: Scanning transmission electron microscopy

We prepared cross-sectional specimen with a Helios G4 CX focused ion-beam (FIB) at 30 kV from Thermo Fisher Scientific, either parallel or perpendicular to the device current direction, using gradually decreasing acceleration voltages of 5 kV and 2 kV for the final polishing. Transmission electron microscopy (TEM) analyses were performed with a double aberration corrected Themis Z from Thermo Fisher Scientific, operated at 300 kV. High-angle annular dark-field scanning TEM (HAADF-STEM) images were recorded with a probe current of about 50 pA, convergence semi-angle 21 mrad or 30 mrad and HAADF collection angles 61-200 mrad. Energy dispersive x-ray (EDX) spectrum imaging was performed with a probe current of about 200 pA, where the spectra were recorded with a Bruker Dual-X system, providing in total 1.76 sr EDX detectors.

We analyzed multiple devices and a bulk $WSe_2$ flake (not covered by permalloy) to confirm that the edge of the flakes indeed corresponds to the zigzag direction. Below (Fig. 5.4), we show the STEM image for device $D_4^A$ and the STEM image for a bulk flake. For both images the cut was made perpendicular to the flake edge. As can be seen from the images, the crystallographic direction corresponds to the armchair direction, similar to the STEM image in the main text, meaning that the flake edge is along the zigzag direction.

We observe that thinner flakes are very susceptible to damage during specimen fabrication by FIB. Thicker flakes, such as the one shown in Fig. 5.4(b), were found to be significantly more robust against damage. These findings are consistent with other reports in literature, such as Ref. [22] and [23].

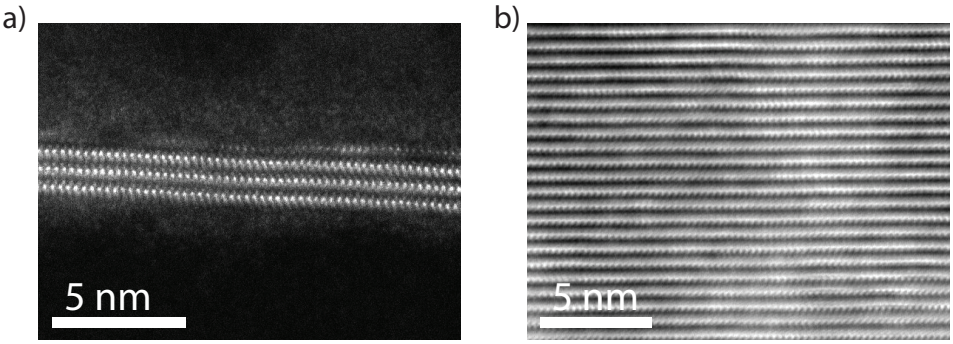


Figure 5.4: Scanning transmission electron microscopy image of (a) device $D_4^A$, and (b) a bulk $WSe_2$ flake. Similar to the STEM image in the main text (Fig. 5.3), the cut is made perpendicular to the edge of the flake. The crystallographic direction observed here (armchair), is similar to the one discussed in the text, indicating that the exfoliated $WSe_2$ flakes preferentially cleave along the zigzag direction.



## 5.5.2. Supplementary note 2: Gate dependence

We also probed the gate dependence of the spin-orbit torques in our devices. For this, we applied a maximum of ±60 V (corresponding to electric fields of ±2.1 MV/cm) to the heavily-doped silicon under of our $SiO_2$ substrate - 285 nm thick. As it can been seen in Fig. 5.5, no clear gate dependence is observed for the A- and B-component (from Eqs. 5.3 and 5.4 in the main text), respectively.

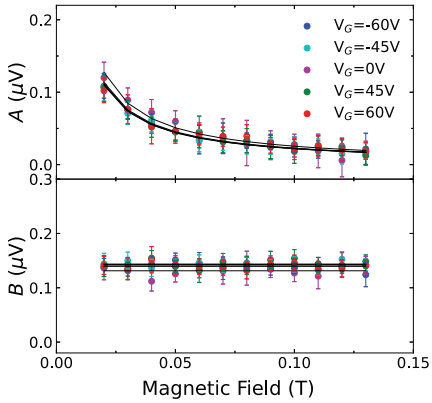


Figure 5.5: The A- and B-component (according to Eqs. 5.3 and 5.4) as a function of magnetic field for different gate voltages for device $D_4^B$.

### 5.5.3. Supplementary note 3: Device fabricated using regular lithography techniques

For the devices discussed in the main text, the permalloy Hall bars on top of the $WSe_2$ were fabricated with a polymer-free technique to ensure a pristine interface between the $WSe_2$ and permalloy. To verify the importance of the interface quality, we also fabricated a device using the regular lithography techniques. Here the polymethyl methacrylate (PMMA) layer was first spun on top of a target $WSe_2$ flake. Next, using e-beam lithography, the Hall bar was patterned and the permalloy was evaporated using electron-beam evaporation. The subsequent fabrication steps were performed as explained in the main text, following the same steps of the other devices.

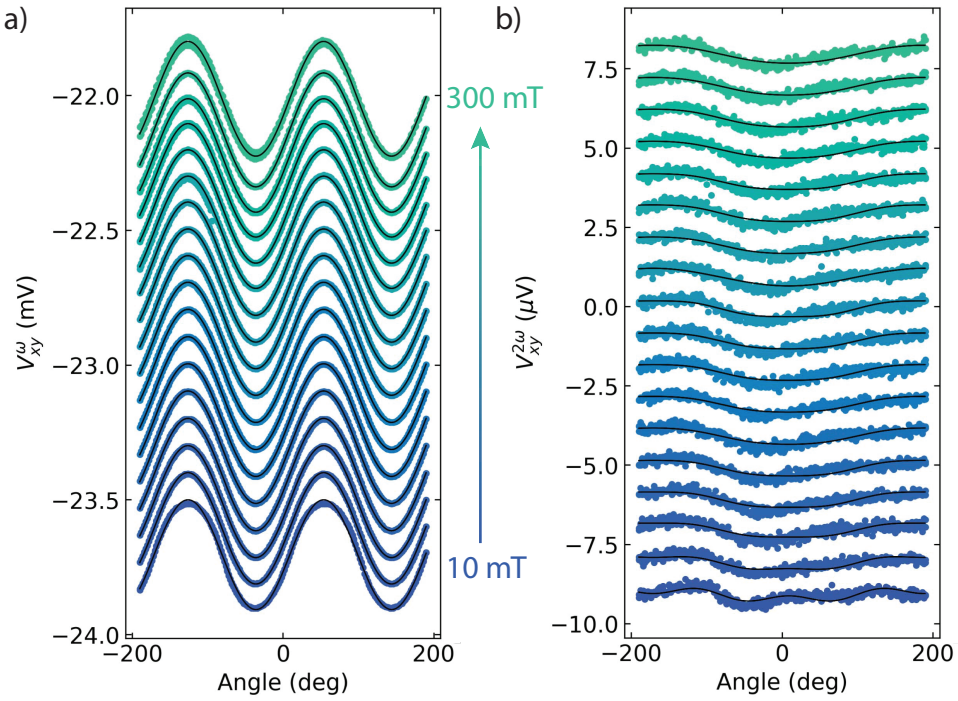


Figure 5.6: (a) First-harmonic and (b) second-harmonic Hall signals obtained for a device fabricated using regular lithography techniques for various magnetic field strengths. For this device, the $WSe_2$ has been in contact with the e-beam resist PMMA prior to the evaporation of permalloy. No significant deviations from the $\sin(2\phi)$ were observed in the first-harmonic Hall signal down to 10 mT fields, indicating little or no magnetic anisotropy. No field dependence was observed for the second-harmonic Hall signal, indicating the absence of measurable spin-orbit torques. The modulation of the second-harmonic Hall voltage is ascribed to the anomalous Nernst effect.

Figure 5.6 shows the first and second-harmonic Hall voltages for this device for different magnetic field strengths. The first-harmonic signal shows no sign of anisotropy even at low fields (10 mT) and follows the regular $\sin(2\phi)$ behavior expected from the planar Hall effect. The second-harmonic signal shows no clear field

dependence, indicating the lack of spin-orbit torques and a significant contribution from Nernst effects. This shows that the polymer-free technique used for the devices discussed in the main text is key in maintaining a pristine interface allowing for large SOTs.

### 5.5.4. Supplementary note 4: Magnetic anisotropy device $D_1$

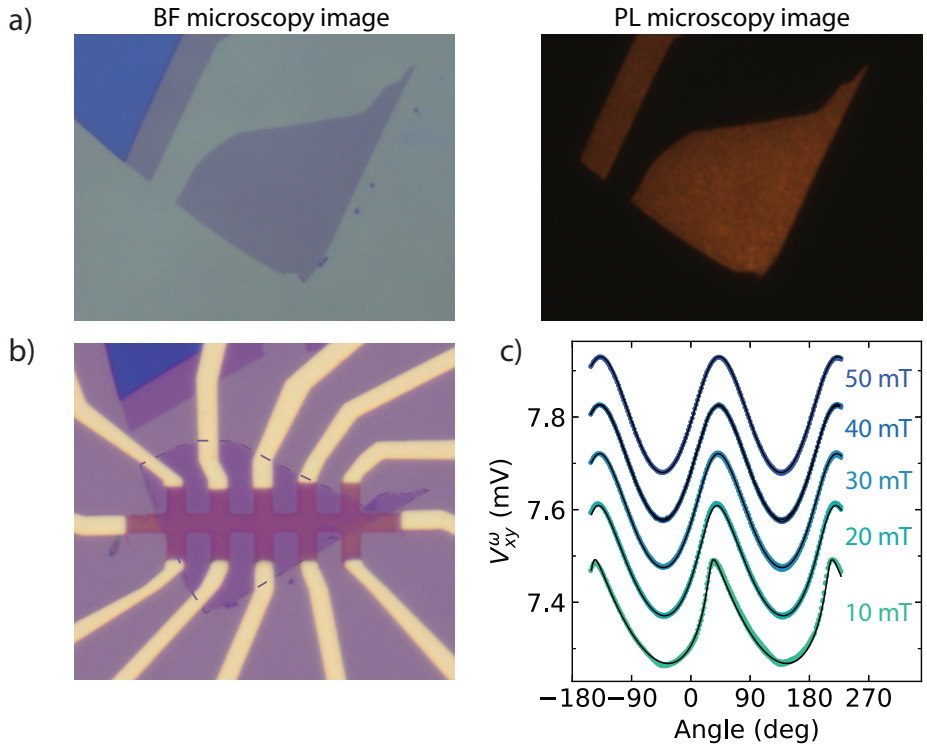


Figure 5.7: (a) Bright field and photoluminescence micrographs of the monolayer $WSe_2$ flake used for device $D_1$. The strong photoluminescence of the flake confirms the monolayer thickness of the TMD flake. (b) Micrograph of device $D_1$, before etching the $WSe_2$ into a Hall bar. Note that the Hall bar channel is aligned 30° away from the flake edge, while the Hall bar channel for device $D_1$, discussed in the main text, was aligned with the flake edge. (c) First-harmonic Hall voltage for the device shown in (b) for low magnetic fields, fitted with the model discussed in the main text (black line). Note that the plots in (c) have been given an offset for clarity.

Like device $D_2^C$ discussed in the main text, device $D_1$ showed a strong in-plane anisotropy (see Fig. 5.7(c)). The monolayer nature of the flake was confirmed by bright field and photoluminescence microscopy images (Fig. 5.7)(a). Note that the Hall bar channel is rotated 30° away from the edge of the flake, see Fig. 5.7(b). The first-harmonic Hall voltage for this device is depicted in Fig. 5.7(c). The easy axis for the magnetic anisotropy for this device was obtained using the same analysis as for $D_2^C$ discussed above. For device $D_1$, we found that the easy axis is aligned

with the current direction. For this device, however, the current direction is along the armchair direction, while the current flows along the zigzag direction in device $D_2^C$, as discussed in the main text. We therefore conclude that, for both devices, the (uniaxial) magnetic anisotropy observed in the Py layer lies along the armchair direction of the $WSe_2$ crystals.

### 5.5.5. Supplementary note 5: Second-harmonic Hall measurements on control Py/$Al_2O_3$ devices

Py is known to show torques even in the absence of spin-orbit materials [30, 43]. To explore the influence of this effect on our measurements we fabricated Py/$Al_2O_3$ devices using the exact same fabrication methods as discussed in the main text. Subsequently, we perform the second-harmonic Hall measurements to extract the torques obtain in these control samples (see Fig. 5.8) We obtain a field-like torque conductivity of $(-2.5 \pm 0.1) \times 10^3 \frac{\hbar}{2e} (\Omega \cdot \mathrm{m})^{-1}$ and $(-2.9 \pm 0.3) \times 10^3 \frac{\hbar}{2e} (\Omega \cdot \mathrm{m})^{-1}$ and a antidamping-like torque of $(-0.2 \pm 0.1) \times 10^3 \frac{\hbar}{2e} (\Omega \cdot \mathrm{m})^{-1}$ and $(-0.3 \pm 0.1) \times 10^3 \frac{\hbar}{2e} (\Omega \cdot \mathrm{m})^{-1}$ for the two samples, respectively.



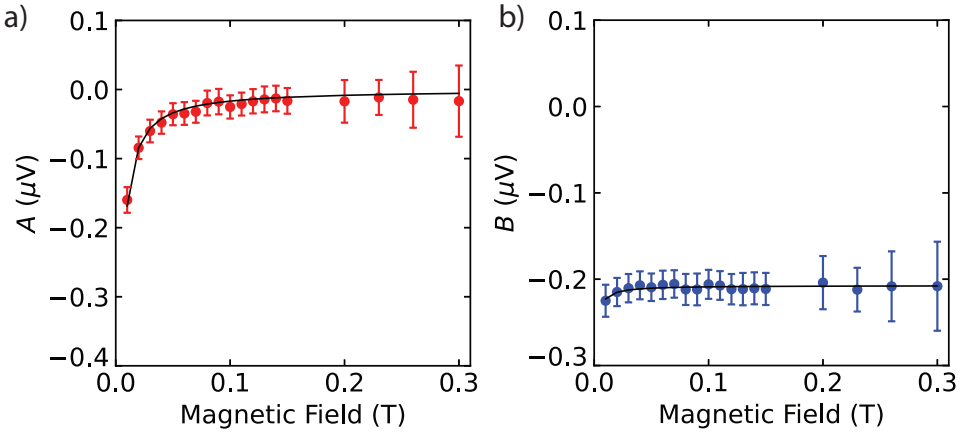


Figure 5.8: The (a) A- and (b) B-components from a control Py/$Al_2O_3$ device. Note that the A-component is negative, while the A-component of the $WSe_2$/Py samples in the main text are positive, indicating that the torques are in opposite directions.

The magnitude of the field-like torque conductivity in these control samples is substantial, but still significantly lower compared to the torques measured in the $WSe_2$-based devices. More importantly, the sign of the field-like torques in these control samples is opposite to the ones obtained in the $WSe_2$/Py devices. This suggests that the torques measured in the $WSe_2$/Py devices are an underestimation of the actual torques produced by the $WSe_2$/Py interface, as they must compete with the torques produced at the Py/$Al_2O_3$ interface. The antidamping-like torque in these control samples are small and therefore cannot explain the DL torques observed in some of the $WSe_2$/Py samples as discussed in the main text.

To compare the torques obtained by us to the ones reported in Ref. [30], we

calculate the spin-torque conductivity for their reported values. The FL torque conductivity in their samples is about $2\times10^3\frac{\hbar}{2e}(\Omega\cdot\mathrm{m})^{-1}$ which is comparable to the FL observed by Shao et al. for CVD-grown $WSe_2$/CoFeB samples, but significantly smaller when compared to our values [28]. We expect that this is due to both a superior interface quality between the $WSe_2$ and Py layer in our samples and a better $WSe_2$ crystal quality obtained from exfoliated flakes. As interfacial torques are expected to mainly give a FL torque, a cleaner interface is expected to give a stronger FL torque. This is in line the fact that they observe a stronger DL torque compared to a FL torque, as a strong DL torque be ascribed to more scattering at the interface [30].

### 5.5.6. Supplementary note 6: Unidirectional magneto-resistance measurements

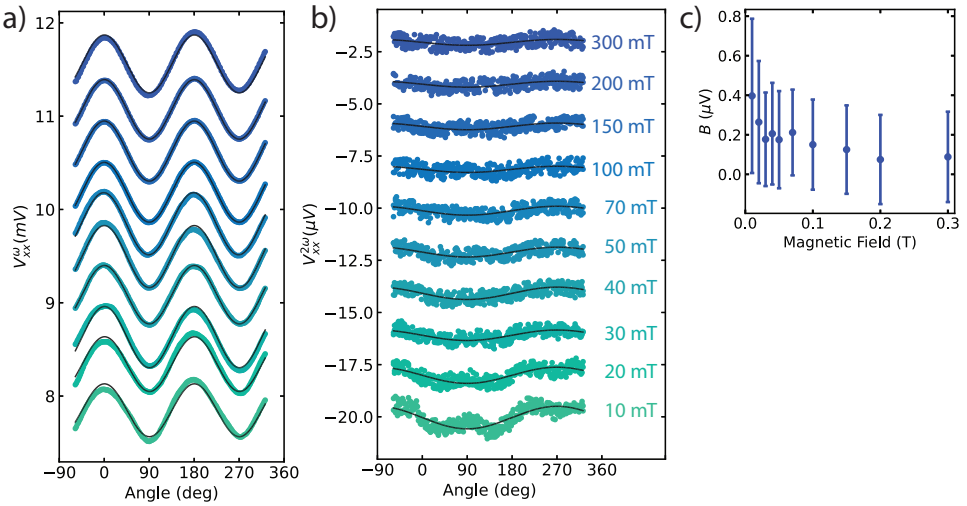


Figure 5.9: The first (a) and the second (b) harmonic longitudinal voltage for various magnetic field strengths for in-plane rotations. (a) A clear AMR signal is observed, as expected for Py. (b) A weak magnetic field dependent modulation is observed which could be ascribed to UMR arising from electron-magnon scattering. To verify whether this signal might leak into our torque measurements, we fit the data with a $\sin(\phi)$ to extract the amplitude and find a decay of the amplitude versus field as shown in (c).

To determine if transverse unidirectional magneto resistance (UMR) due to electron-magnon scattering exists in these samples, we performed control measurements in one of our devices. While rotating the in-plane magnetic field, we measure the first and second-harmonic longitudinal voltage, $V_{xx}^{\omega}$ and $V_{xx}^{2\omega}$, for different magnetic field strengths. The results are shown in Fig. 5.9. Note that we divided the measurements by the number of squares (length/width of the device) to compare the magnitude of the longitudinal and transverse measurements. In the first-harmonic signal we observe a clear anisotropic magnetoresistance (AMR) signal of about 0.3%, as expected for Py. In the second-harmonic measurements, a field-dependent mod-

ulation is observed. We fit the data with a $\sin(\phi)$ and plot the amplitude versus the various magnetic fields as shown in Fig. 5.9c. A decreasing amplitude with increasing field is observed, similar to the B-component of the second-harmonic Hall measurements. Therefore, we cannot rule out the presence of UMR in our harmonic Hall measurements.

### 5.5.7. Supplementary tables

| Device | t | w (μm) | L (μm) | $R_{sq}$ (Ω) | $R_{PHE}$ (Ω) | $R_{AHE}$ (Ω) | $M_s$ (T) | $H_A$ (mT) | φ (deg) |
|---|---|---|---|---|---|---|---|---|---|
| $D_2^A$ | 2L | 2 | 20.5 | 133.4 | 0.430 | 0.44 | 0.9 | 99 ± 2 | -6.4 |
| $D_2^B$ | 2L | 2 | 13 | 219.4 | 0.347 | 0.57 | 0.8 | − 96 ± 2 | 10.4 |
| $D_4^A$ | 4L | 1.5 | 12 | 93.7 | 0.300 | 0.19 | 0.9 | 167 ± 6 | -1.5 |
| $D_4^B$ | 4L | 2 | 14 | 112.4 | 0.305 | 0.20 | 0.8 | − 141 ± 4 | -38.2 |

| Device | t | w (μm) | L (μm) | $R_{sq}$ (Ω) | $R_{PHE}$ (Ω) | $R_{AHE}$ (Ω) | M (T) | $K_2$ (erg/cm$^3$) | φ (deg) |
|---|---|---|---|---|---|---|---|---|---|
| $D_1$ | 1L | 2 | 27.5 | 247 | 0.326 | 0.78 | 0.7 | $2 \times 10^4$ | -60 |
| $D_2^C$ | 2L | 3 | 24 | 206.4 | 0.281 | 0.49 | 0.6 | $6.6 \times 10^4$ | -28 |

Table 5.1: Supplementary Table 1: Device parameters and anisotropy values obtained using Eq. 5.6.

| Device | $\tau_{FL}/\gamma$ (Oe) | $\tau_{DL}/\gamma$ (Oe) | $\sigma_{FL}$ ($10^3$ ħ/2e Ω$^{-1}$m$^{-1}$) | $\sigma_{DL}$ ($10^5$ ħ/2e Ω$^{-1}$m$^{-1}$) |
|---|---|---|---|---|
| $D_1$ | 0.25 ± 0.01 | 0.2 ± 0.3 | 5.2 ± 0.3 | − 0.04 ± 0.05 |
| $D_2^A$ | 0.27 ± 0.01 | 1.8 ± 0.4 | 12.9 ± 0.3 | 0.9 ± 0.2 |
| $D_2^B$ | 0.26 ± 0.02 | 1.7 ± 0.3 | 6.8 ± 0.4 | − 0.44 ± 0.06 |
| $D_2^C$ | - | - | - | - |
| $D_4^A$ | 0.31 ± 0.01 | 6 ± 2 | 10.6 ± 0.3 | 2.2 ± 0.7 |
| $D_4^B$ | 0.14 ± 0.01 | 0.2 ± 2.9 | 4.9 ± 0.3 | 0.07 ± 0.9 |

Table 5.2: Supplementary Table 2: Device torque strengths and spin-torque conductivities.

# Bibliography


[1] J. Hidding, S. H. Tirion, J. Momand, A. Kaverzin, M. Mostovoy, B. J. Van Wees, B. J. Kooi, and M. H. D. Guimarães, "Interfacial spin-orbit torques and magnetic anisotropy in WSe2/permalloy bilayers", Journal of Physics: Materials **4**, 04LT01 (2021).

[2] B. Dieny, I. L. Prejbeanu, K. Garello, P. Gambardella, P. Freitas, R. Lehndorff, W. Raberg, U. Ebels, S. O. Demokritov, J. Akerman, A. Deac, P. Pirro, C. Adelmann, A. Anane, A. V. Chumak, A. Hirohata, S. Mangin, S. O. Valenzuela, M. C. Onbal, M. D'Aquino, G. Prenat, G. Finocchio, L. Lopez-Diaz, R. Chantrell, O. Chubykalo-Fesenko, and P. Bortolotti, "Opportunities and challenges for spintronics in the microelectronics industry", Nature Electronics **3**, 446–459 (2020).

[3] A. Manchon, J. elezný, I. M. Miron, T. Jungwirth, J. Sinova, A. Thiaville, K. Garello, and P. Gambardella, "Current-induced spin-orbit torques in ferromagnetic and antiferromagnetic systems", Reviews of Modern Physics **91**, 035004 (2019).

[4] A. Manchon, H. C. Koo, J. Nitta, S. M. Frolov, and R. A. Duine, "New perspectives for Rashba spinorbit coupling", Nature Materials **14**, 871–882 (2015).

[5] K. Garello, I. M. Miron, C. O. Avci, F. Freimuth, Y. Mokrousov, S. Blügel, S. Auffret, O. Boulle, G. Gaudin, and P. Gambardella, "Symmetry and magnitude of spinorbit torques in ferromagnetic heterostructures", Nature Nanotechnology **8**, 587–593 (2013).

[6] L. Liu, T. Moriyama, D. C. Ralph, and R. A. Buhrman, "Spin-Torque Ferromagnetic Resonance Induced by the Spin Hall Effect", Physical Review Letters **106**, 036601 (2011).

[7] C.-F. Pai, L. Liu, Y. Li, H. W. Tseng, D. C. Ralph, and R. A. Buhrman, "Spin transfer torque devices utilizing the giant spin Hall effect of tungsten", Applied Physics Letters **101**, 122404 (2012).

[8] K.-u. Demasius, T. Phung, W. Zhang, B. P. Hughes, S.-H. Yang, A. Kellock, W. Han, A. Pushp, and S. S. P. Parkin, "Enhanced spinorbit torques by oxygen incorporation in tungsten films", Nature Communications **7**, 10644 (2016).

[9] L. Liu, C.-F. Pai, Y. Li, H. W. Tseng, D. C. Ralph, and R. a. Buhrman, "Spin-Torque Switching with the Giant Spin Hall Effect of Tantalum", Science **336**, 555–558 (2012).

[10] V. Ostwal, T. Shen, and J. Appenzeller, "Efficient SpinOrbit Torque Switching of the Semiconducting Van Der Waals Ferromagnet Cr2Ge2Te6", Advanced Materials **32**, 1906021 (2020).

[11] K. Garello, F. Yasin, H. Hody, S. Couet, L. Souriau, S. H. Sharifi, J. Swerts, R. Carpenter, S. Rao, W. Kim, J. Wu, K. K. V. Sethu, M. Pak, N. Jossart, D. Crotti, A. Furnemont, and G. S. Kar, "Manufacturable 300mm platform solution for Field-Free Switching SOT-MRAM", in 2019 symposium on vlsi circuits, Vol. 2019-June (June 2019), T194–T195.

[12] A. R. Mellnik, J. S. Lee, A. Richardella, J. L. Grab, P. J. Mintun, M. H. Fischer, A. Vaezi, A. Manchon, E.-A. Kim, N. Samarth, and D. C. Ralph, "Spin-transfer torque generated by a topological insulator", Nature **511**, 449–451 (2014).

[13] Y. Wang, P. Deorani, K. Banerjee, N. Koirala, M. Brahlek, S. Oh, and H. Yang, "Topological Surface States Originated Spin-Orbit Torques in Bi2Se3", Physical Review Letters **114**, 257202 (2015).

[14] Y. Wang, D. Zhu, Y. Wu, Y. Yang, J. Yu, R. Ramaswamy, R. Mishra, S. Shi, M. Elyasi, K.-L. Teo, Y. Wu, and H. Yang, "Room temperature magnetization switching in topological insulator-ferromagnet heterostructures by spin-orbit torques", Nature Communications **8**, 1364 (2017).

[15] J. Han, A. Richardella, S. A. Siddiqui, J. Finley, N. Samarth, and L. Liu, "Room-Temperature Spin-Orbit Torque Switching Induced by a Topological Insulator", Physical Review Letters **119**, 077702 (2017).

[16] Y. Fan, P. Upadhyaya, X. Kou, M. Lang, S. Takei, Z. Wang, J. Tang, L. He, L.-t. Chang, M. Montazeri, G. Yu, W. Jiang, T. Nie, R. N. Schwartz, Y. Tserkovnyak, and K. L. Wang, "Magnetization switching through giant spinorbit torque in a magnetically doped topological insulator heterostructure", Nature Materials **13**, 699–704 (2014).

[17] N. H. D. Khang, Y. Ueda, and P. N. Hai, "A conductive topological insulator with large spin Hall effect for ultralow power spinorbit torque switching", Nature Materials **17**, 808–813 (2018).

[18] J. Han and L. Liu, "Topological insulators for efficient spinorbit torques", APL Materials **9**, 1–9 (2021).

[19] J. Hidding and M. H. D. Guimarães, "Spin-Orbit Torques in Transition Metal Dichalcogenide/Ferromagnet Heterostructures", Frontiers in Materials **7**, 1–8 (2020).

[20] D. MacNeill, G. M. Stiehl, M. H. D. Guimaraes, R. A. Buhrman, J. Park, and D. C. Ralph, "Control of spinorbit torques through crystal symmetry in WTe2/ferromagnet bilayers", Nature Physics **13**, 300–305 (2017).

[21] D. MacNeill, G. M. Stiehl, M. H. D. Guimarães, N. D. Reynolds, R. A. Buhrman, and D. C. Ralph, "Thickness dependence of spin-orbit torques generated by WTe2", Physical Review B **96**, 054450 (2017).

[22] M. H. D. Guimarães, G. M. Stiehl, D. MacNeill, N. D. Reynolds, and D. C. Ralph, "SpinOrbit Torques in NbSe2/Permalloy Bilayers", Nano Letters **18**, 1311–1316 (2018).

[23] G. M. Stiehl, D. MacNeill, N. Sivadas, I. El Baggari, M. H. D. Guimarães, N. D. Reynolds, L. F. Kourkoutis, C. J. Fennie, R. A. Buhrman, and D. C. Ralph, "Current-Induced Torques with Dresselhaus Symmetry Due to Resistance Anisotropy in 2D Materials", ACS Nano **13**, 2599–2605 (2019).

[24] G. M. Stiehl, R. Li, V. Gupta, I. E. Baggari, S. Jiang, H. Xie, L. F. Kourkoutis, K. F. Mak, J. Shan, R. A. Buhrman, and D. C. Ralph, "Layer-dependent spin-orbit torques generated by the centrosymmetric transition metal dichalcogenide $\beta$-MoTe2", Physical Review B **100**, 184402 (2019).

[25] S. Shi, S. Liang, Z. Zhu, K. Cai, S. D. Pollard, Y. Wang, J. Wang, Q. Wang, P. He, J. Yu, G. Eda, G. Liang, and H. Yang, "All-electric magnetization switching and DzyaloshinskiiMoriya interaction in WTe2/ferromagnet heterostructures", Nature Nanotechnology **14**, 945–949 (2019).

[26] C. F. Schippers, H. J. M. Swagten, and M. H. D. Guimarães, "Large interfacial spin-orbit torques in layered antiferromagnetic insulator NiPS3/ferromagnet bilayers", Physical Review Materials **4**, 084007 (2020).

[27] K. Dolui and B. K. Nikoli, "Spin-orbit-proximitized ferromagnetic metal by monolayer transition metal dichalcogenide: Atlas of spectral functions, spin textures, and spin-orbit torques in Co/MoSe2, Co/WSe2, and Co/TaSe2 heterostructures", Physical Review Materials **4**, 104007 (2020).

[28] Q. Shao, G. Yu, Y.-W. Lan, Y. Shi, M.-Y. Li, C. Zheng, X. Zhu, L.-J. Li, P. K. Amiri, and K. L. Wang, "Strong Rashba-Edelstein Effect-Induced SpinOrbit Torques in Monolayer Transition Metal Dichalcogenide/Ferromagnet Bilayers", Nano Letters **16**, 7514–7520 (2016).

[29] W. Zhang, J. Sklenar, B. Hsu, W. Jiang, M. B. Jungfleisch, J. Xiao, F. Y. Fradin, Y. Liu, J. E. Pearson, J. B. Ketterson, Z. Yang, and A. Hoffmann, "Research Update: Spin transfer torques in permalloy on monolayer MoS2", APL Materials **4**, 1–9 (2016).

[30] S. Novakov, B. Jariwala, N. M. Vu, A. Kozhakhmetov, J. A. Robinson, and J. T. Heron, "Interface Transparency and Rashba Spin Torque Enhancement in WSe2 Heterostructures", ACS Applied Materials & Interfaces **13**, 13744–13750 (2021).

[31] K. Kang, S. Xie, L. Huang, Y. Han, P. Y. Huang, K. F. Mak, C.-j. Kim, D. Muller, and J. Park, "High-mobility three-atom-thick semiconducting films with wafer-scale homogeneity", Nature **520**, 656–660 (2015).

[32] F. Sousa, G. Tatara, and A. Ferreira, "Skew-scattering-induced giant antidamping spin-orbit torques: Collinear and out-of-plane Edelstein effects at two-dimensional material/ferromagnet interfaces", Physical Review Research **2**, 043401 (2020).

[33] L. Zhu, D. C. Ralph, and R. A. Buhrman, "Spin-Orbit Torques in Heavy-MetalFerromagnet Bilayers with Varying Strengths of Interfacial Spin-Orbit Coupling", Physical Review Letters **122**, 077201 (2019).

[34] K. Zollner, M. D. Petrovi, K. Dolui, P. Plechá, B. K. Nikoli, and J. Fabian, "Scattering-induced and highly tunable by gate damping-like spin-orbit torque in graphene doubly proximitized by two-dimensional magnet Cr2Ge2Te6 and monolayer WS2", Physical Review Research **2**, 043057 (2020).

[35] K. S. Novoselov, D. Jiang, F. Schedin, T. J. Booth, V. V. Khotkevich, S. V. Morozov, and A. K. Geim, "Two-dimensional atomic crystals", Proceedings of the National Academy of Sciences **102**, 10451–10453 (2005).

[36] A. Castellanos-Gomez, N. Agraït, and G. Rubio-Bollinger, "Optical identification of atomically thin dichalcogenide crystals", Applied Physics Letters **96**, 1–3 (2010).

[37] K. F. Mak, C. Lee, J. Hone, J. Shan, and T. F. Heinz, "Atomically Thin MoS2: A New Direct-Gap Semiconductor", Physical Review Letters **105**, 136805 (2010).

[38] M. Hayashi, J. Kim, M. Yamanouchi, and H. Ohno, "Quantitative characterization of the spin-orbit torque using harmonic Hall voltage measurements", Physical Review B **89**, 144425 (2014).

[39] M.-H. Nguyen and C.-F. Pai, "Spinorbit torque characterization in a nutshell", APL Materials **9**, 1–15 (2021).

[40] Y. Liu and Q. Shao, "Two-Dimensional Materials for Energy-Efficient Spin-Orbit Torque Devices", ACS Nano **14**, 9389–9407 (2020).

[41] M.-h. Nguyen, D. C. Ralph, and R. A. Buhrman, "Spin Torque Study of the Spin Hall Conductivity and Spin Diffusion Length in Platinum Thin Films with Varying Resistivity", Physical Review Letters **116**, 126601 (2016).

[42] K. Yasuda, A. Tsukazaki, R. Yoshimi, K. Kondou, K. S. Takahashi, Y. Otani, M. Kawasaki, and Y. Tokura, "Current-Nonlinear Hall Effect and Spin-Orbit Torque Magnetization Switching in a Magnetic Topological Insulator", Physical Review Letters **119**, 137204 (2017).

[43] W. Wang, T. Wang, V. P. Amin, Y. Wang, A. Radhakrishnan, A. Davidson, S. R. Allen, T. J. Silva, H. Ohldag, D. Balzar, B. L. Zink, P. M. Haney, J. Q. Xiao, D. G. Cahill, V. O. Lorenz, and X. Fan, "Anomalous spinorbit torques in magnetic single-layer films", Nature Nanotechnology **14**, 819–824 (2019).

[44] M. K. Agarwal, A. R. Jani, J. D. Kshtriya, M. N. Vashi, and P. K. Garg, "Some transport measurements of WSe2-x single crystals", Crystal Research and Technology **19**, 1575–1582 (1984).

[45] R. T. Tung, "The physics and chemistry of the Schottky barrier height", Applied Physics Reviews **1**, 1–54 (2014).

[46] K. Sotthewes, R. van Bremen, E. Dollekamp, T. Boulogne, K. Nowakowski, D. Kas, H. J. W. Zandvliet, and P. Bampoulis, "Universal Fermi-Level Pinning in Transition-Metal Dichalcogenides", The Journal of Physical Chemistry C **123**, 5411–5420 (2019).

[47] V. P. Amin and M. D. Stiles, "Spin transport at interfaces with spin-orbit coupling: Phenomenology", Physical Review B **94**, 104420 (2016).

[48] V. P. Amin and M. D. Stiles, "Spin transport at interfaces with spin-orbit coupling: Formalism", Physical Review B **94**, 104419 (2016).

[49] V. P. Amin, P. M. Haney, and M. D. Stiles, "Interfacial spinorbit torques", Journal of Applied Physics **128**, 151101 (2020).

# chapter 6

## Role of self-torques in transition metal dichalcogenide/ferromagnet bilayers

*In recent years, transition metal dichalcogenides (TMDs) have been extensively studied for their efficient spin-orbit torque generation in TMD/ferromagnetic bilayers, owing to their large spin-orbit coupling, large variety of crystal symmetries, and pristine interfaces. Although the TMD layer was considered essential for the generation of the observed spin-orbit torques (SOTs), recent reports show the presence of a self-torque in single-layer ferromagnetic devices with magnitudes comparable to TMD/ferromagnetic devices. Here, we perform second-harmonic Hall SOT measurements on metal-organic chemical vapor deposition (MOCVD) grown $MoS_2$/permalloy/$Al_2O_3$ devices and compare them to a single-layer permalloy/$Al_2O_3$ device to accurately disentangle the role of self-torques, arising from the ferromagnetic layer, from contributions from the TMD layer in these bilayers. We report a field-like spin-torque conductivity of $\sigma_{FL} = (-2.8 \pm 0.3) \times 10^3 \frac{\hbar}{2e} (\Omega \cdot \mathrm{m})^{-1}$ in a single-layer permalloy/$Al_2O_3$ device, which is comparable to our $MoS_2$/permalloy/$Al_2O_3$ devices and previous reports on similar TMD/ferromagnetic bilayers, indicating only a minor role of the $MoS_2$ layer. In addition, we observe a comparatively weak damping-like torque in our devices, with a strong device-to-device variation. Finally, we find a linear dependence of the SOT conductivity on the Hall bar arm/channel width ratio of our devices, indicating that the Hall bar dimensions are of significant importance for the reported SOT strength. Our results accentuate the importance of delicate details, like device asymmetry, Hall bar dimensions, and self-torque generation, for the correct disentanglement of the microscopic origins underlying the SOTs, essential for future energy-efficient spintronic applications.*

Submitted to *Phys. Rev. B*: Jan Hidding et al., (2023)

## 6.1. Introduction

Manipulating the magnetization of a magnetic layer by means of a charge current holds an immense promise for more energy-efficient ways of storing and writing information [1–3]. By first converting a charge current into a spin current in materials with large spin-orbit coupling (SOC), the spin current can subsequently exert a torque on the magnetization of an interfaced magnetic material [2]. These current-induced torques, originating from the spin-orbit interaction, are referred to as spin-orbit torques (SOTs). To maximize the SOT strength, an efficient charge-to-spin conversion is advantageous, and thus, materials with large spin-orbit coupling (Pt [4–6], Pd [7–9], W [10, 11], Ta [12–14], Hf [15–17], etc.) have been extensively studied [18]. Two main mechanisms for the charge-to-spin conversion in these materials are the spin-Hall effect (SHE) and the Rashba-Edelstein effect (REE) [2, 19]. For polycrystalline spin Hall metals with inversion symmetry, these effects, however, do not possess the ideal symmetry for field-free switching of the magnetization of magnetic layers with perpendicular magnetic anisotropy (PMA) used in modern high-density memory storage [20, 21]. While epitaxially grown heavy metals have shown an increase in their SOTs compared to their polycrystalline counterparts [22, 23], as long as their inversion symmetry remains intact, no deterministic field-free switching is expected. Multiple methods have been employed to break the inversion symmetry, such as wedged shaped geometries, vertical composition gradients, or interlayer exchange coupling to an additional in-plane exchange-biased magnetic layer, to allow for field-free switching using standard spin-Hall metals [20, 24, 25]. However, the search for the out-of-plane damping-like torque, ideal for switching PMA magnets, lead to the investigation of other, more exotic materials, such as topological insulators and two-dimensional (2D) van der Waals crystals, to search for new materials which allow for energy efficient field-free switching [19, 26–29].



In this regard, the family of 2D van der Waals materials called the transition metal dichalcogenides (TMDs) have gained much interest as spin source material, owing to their large SOC, atomically flat surfaces, and broad range of crystal symmetries [21, 30, 31]. The more conventional and well known semiconducting TMDs, such as $WSe_2$ [32–34], $WS_2$ [35], and $MoS_2$ [33, 36], were studied first, due to their air stability, and developed wafer-scale growth. More recently, however, the low symmetry TMDs have gained much interest since the observation of the out-of-plane damping-like torque in TMD/FM bilayers, which is optimal for switching magnets with PMA [37–43].

Previous reports on SOTs in TMD/ferromagnetic (FM) bilayers often consider the TMD as essential for the generation of the observed SOTs, either through bulk effects, such as the spin-Hall effect, or effects arising from the TMD/Py interface, such as the Rashba-Edelstein effect, spin-orbit filtering, or spin-orbit precession [44, 45]. More recent reports, however, indicate the presence of a self-torque in single-layer ferromagnetic devices without the presence of a spin source material. A recent study performed magneto-optic Kerr effect (MOKE) measurements to probe the SOT at the surface of a single-layer Py device and observe a sizable SOT at the Py interface, which is ascribed to a SHE in the Py [46]. Also, electrical measurements on Py capped with $SiO_2$ or $Al_2O_3$ show the presence of field-like and damping-like

torques in Py devices [47]. And, in metallic bilayers, it was shown that self-induced torques lead to errors in the estimation of the spin-torque strength [48]. These self-torques in ferromagnetic materials make it difficult to accurately determine to what extent the TMD layer is contributing to the SOT [47].

Here, we report second-harmonic Hall measurements on $MoS_2$/Py/$Al_2O_3$ and single-layer Py/$Al_2O_3$ devices to disentangle the contribution of self-torques from the FM layer, and more accurately determine the effect of the $MoS_2$ layer. First, we show that the field-like self-torque in a single-layer Py/$Al_2O_3$ device can be of similar magnitude compared to $MoS_2$/Py/$Al_2O_3$ devices, indicating a minor effect of the TMD. Second, we find strong device-to-device variations on the damping-like torque, showing that interface and device quality can strongly affect our signals and potentially indicating that spurious effects can mimic the behavior of the damping-like torque in these devices. In addition, we study the dependence of the measured spin-orbit torque on the contact/channel width ratio and find a linear dependence of the field-like spin-torque conductivity on the Hall arm/channel width ratio. These results indicate the importance of single-layer reference samples and the device geometry for an accurate determination of the microscopic mechanisms underlying the spin-orbit torques.

## 6.2. Results and Discussion



To compare the SOTs in TMD/Py devices with the self-torques in single-layer Py devices, we fabricate both $MoS_2$/Py/$Al_2O_3$ and Py/$Al_2O_3$ Hall bar devices. Below, we discuss the results from both devices separately. Lastly, we discuss the effect of the Hall bar geometry on the measured SOT using harmonic Hall measurements.

### 6.2.1. $MoS_2$/Py/$Al_2O_3$ devices

We use wafer-scale grown $MoS_2$ obtained by metal-organic chemical vapor deposition (MOCVD) [49]. The MOCVD grown $MoS_2$ layer is characterized using photoluminescence (PL) microscopy and Raman spectroscopy (see Fig. 6.1(b)) before device fabrication. The two characteristic bands of monolayer $MoS_2$ at 385 $cm^{-1}$ and 405 $cm^{-1}$, corresponding to the in-plane ($E^1_{2g}$) and out-of-plane phonon mode ($A_{1g}$), respectively, are clearly observed, as indicated in Fig. 6.1(b) [50]. Furthermore, a strong and homogeneous PL is obtained using PL microscopy shown in the insets of Fig. 6.1(b), indicating the homogeneous coverage of monolayer $MoS_2$ with little strain on the substrate.

Next, multiple $MoS_2$/Py/$Al_2O_3$ Hall bar devices were fabricated to perform the harmonic Hall measurements. An ac current ($I_0$) ranging from 500 to 700 µA is applied, and the first ($V^{\omega}_{xy}$) and second ($V^{2\omega}_{xy}$) harmonic Hall voltage are measured while an applied magnetic field ($H$) is rotated in-plane, making an angle $\phi$ with respect to the current direction (Fig. 6.1(c); the details are described in the Methods section). When assuming a small in-plane magnetic anisotropy compared to $\mu_0 H$, the magnetization is aligned with the external magnetic field and the first-harmonic Hall voltage ($V^{\omega}_{xy}$) is given by [4, 51, 52]:

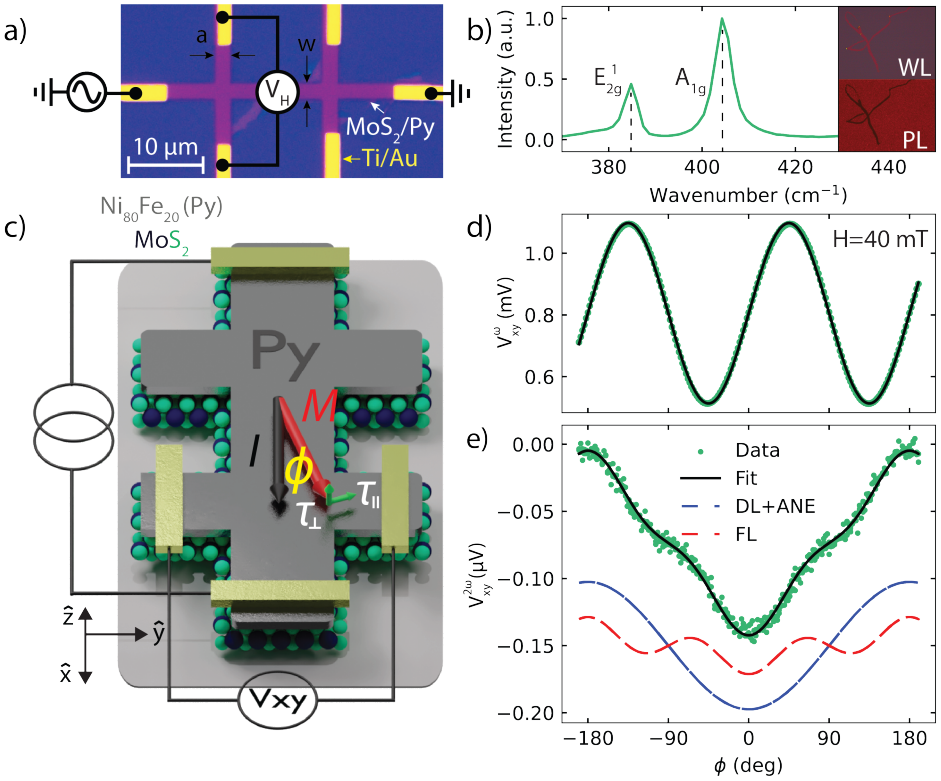


Figure 6.1: (a) Optical micrograph of an actual MOCVD $MoS_2$/Py/$Al_2O_3$ device. (b) A Raman spectrum of the MOCVD grown $MoS_2$ showing the characteristic $E^1_{2g}$ and $A_{1g}$ modes of $MoS_2$. The two insets on the right depict a white light (WL) and photoluminescence (PL) micrograph of a scratch in the MOCVD grown $MoS_2$ layer, indicating a strong PL from the monolayer $MoS_2$. (c) A schematic of a SOT device with the measurement geometry schematically depicted. A low frequency ac current $I$ (black arrow) is applied through the channel and the first and second-harmonic Hall voltage ($V^{\omega(2\omega)}_{xy}$) are simultaneously measured while the magnetization of the permalloy $M$ (red arrow) is rotated in-plane by an external magnetic field. The current induced in-plane (damping-like) and out-of-plane (field-like) SOTs are depicted with the green arrows $\tau_{\parallel}$ and $\tau_{\perp}$, respectively. (d) The measured first-harmonic and (e) second-harmonic Hall voltage versus in-plane angle of the applied magnetic field (40 mT). (d) A clear $\cos(2\phi)$ dependence is observed due to the planar Hall effect of the Py. (e) The second-harmonic Hall voltage (blue points) is fitted (black line) using Eq. (6.2). The dashed blue and red lines indicate the separate $\cos(\phi)\cos(2\phi)$ and $\cos(\phi)$ components from Eq. (6.2), related to the field-like and damping-like torque, respectively.

$$V^{\omega}_{xy}(\phi) = I_0 R_{PHE} \sin(2\phi) + I_0 R_{AHE} \cos(\theta), \tag{6.1}$$

where $\theta$ is the magnetic field's polar angle ($\theta = 90°$ for in-plane measurements) and the $R_{PHE}$ and $R_{AHE}$ are the planar Hall and anomalous Hall effect resistance. The first-harmonic Hall voltage ($V^{\omega}_{xy}$), depicted in Fig. 6.1(d) for a magnetic field of 40 mT, follows a clear $\sin(2\phi)$ behavior due to the planar Hall effect of the Py layer. By

fitting the data to Eq. (6.1) we obtain a planar Hall resistance of $R_{PHE} = 0.40 \pm 0.03$ Ω. In previous reports on exfoliated TMD/FM bilayers, large deviations from the $\sin(2\phi)$ dependence were observed at low magnetic fields, indicating that a strong uniaxial magnetic anisotropy was induced in the Py [32, 37, 40, 41]. In these reports, the induced anisotropy was attributed to a strong interaction between the Py and the crystalline structure of the underlying TMD. As the MOCVD grown TMD in our devices has a grain size of around 1 μm, our Hall bar covers multiple domains [49]. Therefore, no induced magnetic anisotropy in the Py from the TMD crystal structure is expected. This is in line with our observation, as only minor deviations from the $\sin(2\phi)$ fit are observed. For devices with a smaller Hall bar arm width/channel width ratio, these minor deviations disappear completely, indicating that the minor deviations observed for narrow Hall bars are likely due to shape anisotropy of the Hall bar.

To determine the field-like ($\tau_{FL}$) and damping-like torques ($\tau_{DL}$), the second-harmonic Hall (SHH) voltage is measured (Fig. 6.1(e)). The SHH voltage can be described by [4, 51]:

$$V_{xy}^{2\omega}(\phi) = A\cos(2\phi)\cos(\phi) + B\cos(\phi), \tag{6.2}$$

where the A- and B-components are given by:

$$A = \frac{R_{PHE} I_0 \tau_\perp / \gamma}{H} \tag{6.3}$$

$$B = \frac{R_{AHE} I_0 \tau_\parallel / \gamma}{H + H_K} + I_0 R_{ANE}. \tag{6.4}$$

Here, $\gamma$ is the gyromagnetic ratio, $H_K$ is the out-of-plane anisotropy field, and $R_{ANE}$ is the anomalous Nernst resistance. Since our signals are consistent with only the presence of out-of-plane field-like torques and in-plane antidamping torques, we will assume here that $\tau_\perp \equiv \tau_{FL} \propto (\hat{m} \times \hat{y})$ and $\tau_\parallel \equiv \tau_{DL} \propto \hat{m} \times (\hat{y} \times \hat{m})$ The SHH is fitted using Eq. (6.2) to extract the amplitude of the A- and B-components. As can be seen from Fig. 6.1(e), our data is well described by Eq. (6.2). Subsequently, the A- and B-components are determined for different magnetic fields, allowing us to obtain the $\tau_{FL}$, $\tau_{DL}$, and anomalous Nernst resistance ($R_{ANE}$) using Eq. (6.3) and Eq. (6.4). For the $MoS_2$/Py/$Al_2O_3$ devices, we corrected our data for a systematic 15 mT offset in the field due to a residual current in our electromagnet. The $R_{AHE} = 0.15$ Ω is obtained by performing a separate measurement where the first harmonic Hall voltage is measured while sweeping the magnetic field out-of-plane from approximately -1 T to 1 T (see the Methods section, Fig. 6.4).

Figure 6.2 show the field-dependence of the (a) A- and (c) B-component of a MOCVD $MoS_2$/Py/$Al_2O_3$ device. As expected from Eq. (6.3), the A-component shows a linear dependence on the inverse magnetic field, which clearly indicates the presence of a field-like torque $\tau_{FL}$. For the four separate devices, we find a spread in the field-like spin-torque conductivity $\sigma_{FL}$, with a minimum of $(-3.5 \pm 0.2) \times 10^3 \frac{\hbar}{2e} (\Omega \cdot \mathrm{m})^{-1}$ and a maximum of $(-7.5 \pm 0.6) \times 10^3 \frac{\hbar}{2e} (\Omega \cdot \mathrm{m})^{-1}$ for an applied

current density of $0.8\times10^{10}$ A/m$^2$ to $5\times10^{10}$ A/m$^2$ (see the Methods section for the spin-torque conductivity calculation).

This value is comparable to previous reports on chemical vapor deposition (CVD) grown $MoS_2$/CoFeB devices from Shao et al. [33] and slightly lower compared to other semiconducting TMD/Py devices (e.g. $WS_2$, $WSe_2$) [32–35]. Larger field-like torques are reported in semimetallic TMD/Py bilayers, which is explained by the considerable Oersted torque arising from the current flowing through the conducting TMD [37, 39, 40]. Using four-probe measurements, we find a square resistance $R_{sq}$ for the Py layer of 101.4 Ω. The sheet resistance reported for the MOCVD grown $MoS_2$ layer, on the other hand, are much higher than the sheet resistance of Py even for heavily doped layers, ranging from 42 kΩ to 83 kΩ in the transistor on-state [49] at room temperature. Due to the semiconducting character of the $MoS_2$ layer in our devices, no current is expected to flow through the $MoS_2$ and thus no Oersted torque is expected.

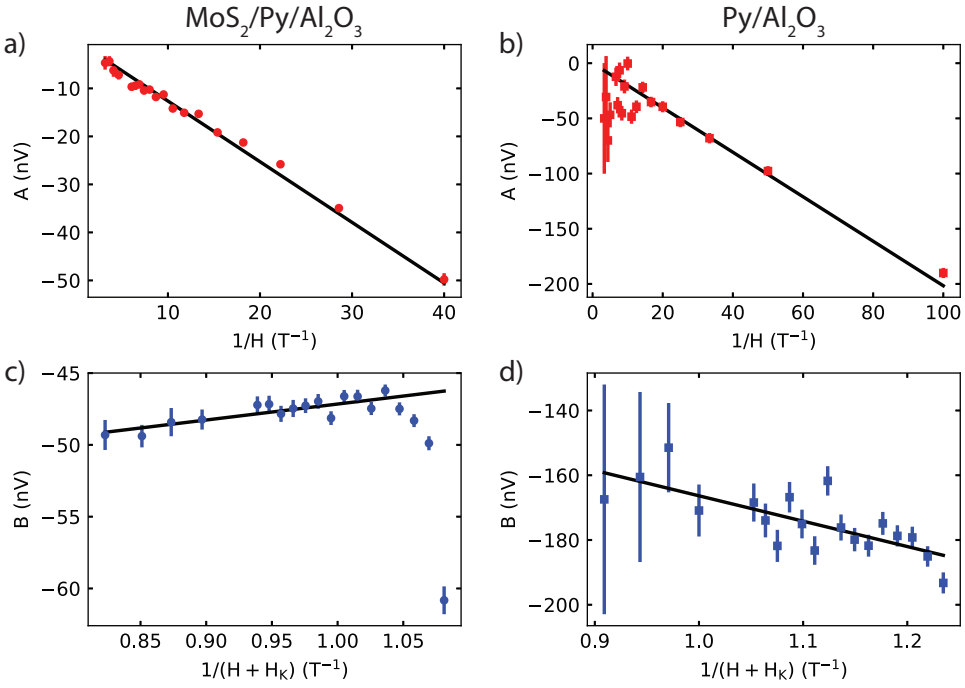


Figure 6.2: A- and B-components from Eq. (6.2) versus the inverse magnetic field for a $MoS_2$/Py/$Al_2O_3$, (a) and (c), and single-layer Py/$Al_2O_3$, (b) and (d), device, respectively. The components were obtained by fitting the second-harmonic Hall voltage (as depicted in Fig. 6.1(e)) to Eq. (6.2) for multiple external magnetic field strengths. A clear linear dependence is observed for the A-component in both devices, and is fitted to Eq. (6.3) to obtain the field-like torque $\tau_{FL}$. Especially for the $MoS_2$/Py/$Al_2O_3$ device, the B-component deviates from the linear trend at low magnetic fields, which could be due to electron-magnon scattering. For the $MoS_2$/Py/$Al_2O_3$ devices, we therefore neglected the fields at low fields (10 mT, 20 mT, and 30 mT) to obtain a better linear fit. Furthermore, we corrected our data for a systematic offset of 15 mT in the applied field.

In the presence of a $\tau_{DL}$, a linear dependence of the B-component is expected versus the inverse field (see Eq. (6.4)). For only one of our four $MoS_2$/Py/$Al_2O_3$ devices, we find a linear dependence of the B-component at high fields, as depicted in Fig. 6.2(c). For the three other devices, we find nonsignificant damping-like spin-torque conductivities ($\sigma_{DL}$) with large errors, with a minimum $\sigma_{DL}$ of $(-4 \pm 32) \times 10^3 \frac{\hbar}{2e}(\Omega \cdot \mathrm{m})^{-1}$ and a maximum $\sigma_{DL}$ of $(3 \pm 3) \times 10^5 \frac{\hbar}{2e}(\Omega \cdot \mathrm{m})^{-1}$. Additionally, we observe large deviations from the linear dependence at low fields in Fig. 6.2(c). This can be explained by the fact that Eq. (6.3) and Eq. (6.4) are derived assuming that $H \gg H_A$, where $H_A$ is the in-plane uniaxial anisotropy field, which does not hold anymore at low magnetic fields [51]. To get a more accurate estimate of the damping-like torque in this device, we therefore neglect the three data points at lowest field when fitting the data to Eq. (6.4). For this single device, we find a damping-like spin-torque conductivity $\sigma_{DL}$ of $(1.2 \pm 0.3) \times 10^5 \frac{\hbar}{2e}(\Omega \cdot \mathrm{m})^{-1}$. This value is comparable to values reported in SOT devices made with Pt, W, and $NiPS_3$, and is significantly higher compared to SOT devices using other TMDs (e.g., $WTe_2$, $MoTe_2$, $WSe_2$, etc.). The presence of both a field-like and damping-like torque in $MoS_2$/Py has been previously reported by Zhang et al. in ST-FMR measurements [36]. There, a torque ratio of $\tau_{FL}/\tau_{DL} = 0.19 \pm 0.01$ is reported, indicating a five times stronger damping-like torque. Similarly, we find a stronger damping-like torque for this one device, showing a damping-like torque a factor of 20 stronger than the field-like torque. On the other hand, Shao et al. report no damping-like torque in their SHH measurements on $MoS_2$/CoFeB bilayers [33], similar to our other devices. These contrasting observations show that there is a significant device-to-device variation for the damping-like torque in these bilayers. This is highlighted by the fact that we observe no significant damping-like torques in three of our four devices. Furthermore, it was shown that the ordinary Nernst effect can contribute to spurious second harmonic Hall voltages in these types of measurements, leading to a linear dependence of the B-component on the external magnetic field [53]. The absence of a clear linear dependence of the B-component on the external magnetic field strength for all $MoS_2$/Py/$Al_2O_3$ and single-layer Py/$Al_2O_3$ devices, indicates that this effect does not play a major role in our devices.



### 6.2.2. Single-layer Py/$Al_2O_3$ device

To determine the contribution of possible self-torques in the Py layer and accurately resolve the effect of the MOCVD grown $MoS_2$ layer on the SOTs, we compare the SOT measurements from the $MoS_2$/Py/$Al_2O_3$ device to a single-layer Py/$Al_2O_3$ reference device. In Figs. 6.2(b) and 6.2(d) the A- and B-components for the single-layer Py/$Al_2O_3$ device are plotted versus the inverse field. Surprisingly, even without the $MoS_2$ layer, we observe a clear linear dependence for the A-component similar to the $MoS_2$/Py/$Al_2O_3$ devices, indicating the presence of a field-like self-torque. Using Eq. (6.3) and Eq. (6.5), we find $\sigma_{FL} = (-2.8 \pm 0.3) \times 10^3 \frac{\hbar}{2e}(\Omega \cdot \mathrm{m})^{-1}$. The $\sigma_{FL}$ has the same sign and its magnitude is only 25% lower compared to the $MoS_2$/Py/$Al_2O_3$ device, which indicates that the presence of the TMD layer does not significantly enhance the field-like SOT conductivity.

For the B-component, however, no large deviations at low fields are observed, as

was the case with the $MoS_2$/Py/$Al_2O_3$ device. Using Eq. (6.3) and Eq. (6.5), we find $\sigma_{DL} = (-2.6 \pm 0.6) \times 10^5 \frac{\hbar}{2e} (\Omega \cdot \mathrm{m})^{-1}$, which is larger and has an opposite sign compared to the single $MoS_2$/Py/$Al_2O_3$ device that did show a significant damping-like torque. For other Py/$Al_2O_3$ samples, however, no clear damping-like torques were observed, suggesting that the damping-like torque is strongly dependent on device (interface) specifics. This indicates that either the origin of the damping-like self-torque stems from different skew-scattering mechanisms which are dependent on interface and material quality, an inhomogeneous current distribution, or that the field-dependence of the B-component is due to spurious effects which mimic the behavior of the damping-like torque, such as unidirectional magnetoresistance due to electron-magnon scattering [54, 55]. The opposite sign could result from the different material interfaces of the Py, which could give rise to different scattering events, resulting in a different damping-like SOT [26, 56]. However, as the magnitude of the damping-like torque is unrealistically high, comparing to the damping-like torque strength observed in Pt/Py samples, we believe that the field-dependence of the B-component is due to spurious effects at low magnetic fields or an inhomogeneous current flow in these devices.

Other reports on single-layer Py devices show both a field-like and a damping-like torque in ST-FMR measurements [47]. Seki et al. observe a field-like torque in all their single-layer Py devices, but only observe a damping-like torque in devices where the structural inversion symmetry was broken due to different interfaces of the Py layer. In our devices, the structural inversion symmetry is broken as well, as the Py is evaporated on $SiO_2$ and capped with $Al_2O_3$, and thus possesses two different interfaces. A difference in electron-scattering from these two interfaces could, in turn, lead to a self-torque. Furthermore, Seki et al. report only damping-like torques for devices where the Py layer is sufficiently thin ($\leq 3$ nm), which could explain why we do not observe a reliable damping-like torque for our Py devices of 6 nm [47]. Also, Schippers et al. report measurements on a similar single-layer Py reference sample with a 6 nm Py thickness, capped with $Al_2O_3$ [57]. At room temperature, they find a $\sigma_{FL}$ which is three times larger, and a $\sigma_{DL}$ which is one order of magnitude smaller. For their samples, however, the layers are deposited using magnetron sputtering, while our samples employed electron beam evaporation, which could lead to different material and interface qualities, and different current distributions in the Py layer.

All these different torque strengths and directions observed for similar $MoS_2$/FM bilayers and single-layer Py devices underline the large device-to-device variation, also observed in our devices. Our observations show that the self-torque, originating solely from the FM layer, can have a significant contribution to the observed SOTs in TMD/FM bilayers.

### 6.2.3. Effect of the Hall bar dimensions

Lastly, we study the effect of the Hall bar arm width/channel width ratio ($a/w$), for the $MoS_2$/Py/$Al_2O_3$ devices by keeping the arm width constant at $a = 2$ μm, while varying the channel width ($w$) from 2 μm to 10 μm. In Fig. 6.3, the raw (a) field-like and (b) damping-like spin-torque conductivities (gray circles) for all devices are

plotted versus $(a/w)$. For comparison, the $\sigma_{FL(DL)}$ from the single-layer $Py/Al_2O_3$ device is included and depicted by the gray unfilled squares. We observe a clear, almost linear, dependence of $\sigma_{FL}$ on the channel width. The $\sigma_{FL}$ for the device with $a/w = 0.2$ is a factor two larger than the device with $a/w = 1$. We stress that the larger error bar for the device with $a/w = 0.2$ is ascribed to a smaller current density compared to the other devices. This observation is in line with recent work from Neumann et al. where the arm width/channel width ratio is shown to affect the estimation of the spin-Hall angle ($\theta_{SH}$) [58]. A significantly decreasing $\theta_{SH}$ is found when the arm width/channel width ratio becomes sufficiently big ($\geq 1$), reporting a value of only 70% at an arm width/channel width ratio of 1. To correct our $\sigma_{FL(DL)}$, we incorporate a factor for each arm width/channel width ratio as reported by Neumann et al. [58], and plot the corrected values in Fig. 6.3 as red (field-like) and blue (damping-like) circles (correction factors can be found in the Methods section).

After the correction, there is no clear monotonic decrease of $\sigma_{FL}$ with the arm width/channel width ratio. However, still some device-to-device variation is found, which could be due to varying interface and material qualities. For $\sigma_{DL}$, the reported values for both the $MoS_2/Py/Al_2O_3$ and the single-layer $Py/Al_2O_3$ devices remain large with correspondingly large error bars as previously discussed. These



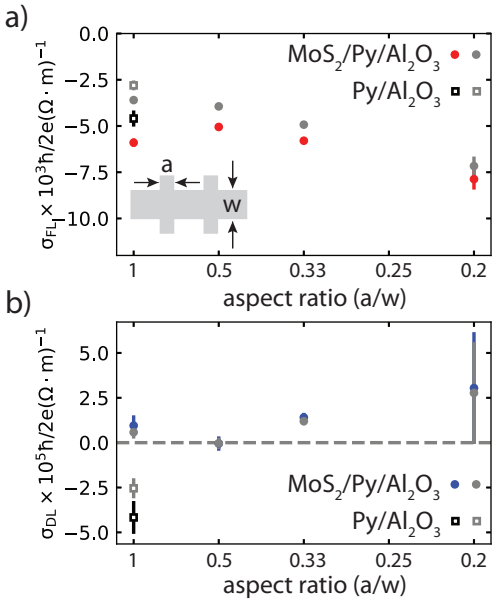


Figure 6.3: (a) Field-like and (b) damping-like spin-torque conductivity for the $MoS_2/Py/Al_2O_3$ devices (circles) and the single-layer $Py/Al_2O_3$ device (squares) versus the arm width/channel width ratio of the Hall bar. The gray points correspond to the raw spin-torque conductivity and the colored points to the corrected spin-torque conductivity, according to Ref. [58]. The inset in (a) shows the voltage arm width ($a$) and the channel width ($w$). For these devices, the arm width is kept constant ($a = 2$ µm), while the channel width is varied.

results emphasize, and function as experimental evidence for, the importance of the geometrical factors of the Hall bar on the obtained SOT values from harmonic Hall measurements in TMD/Py bilayers. Performing similar measurements of the self-torque dependence on the Hall bar dimensions of the single-layer $Py/Al_2O_3$ device could shed light on the reliability of the measured self-torques. Therefore, we suggest these measurements to be performed on single-layer $Py/Al_2O_3$ devices with varying arm width/channel width ratios to better characterize the self-torque in FM layers.

## 6.3. Conclusion

In conclusion, our results indicate that the self-torques, originating from the FM layer, can have significant contributions to the observed SOTs in TMD/FM bilayers. We observe a similar $\tau_{FL}$ in single-layer $Py/Al_2O_3$ devices, indicating that the MOCVD $MoS_2$ layer in our $MoS_2/Py/Al_2O_3$ is of minor importance for the generation of field-like SOTs. This suggests that the FM layer, rather than the TMD, might play a dominant role in the generation of the observed SOTs in TMD/FM bilayers. Previous contrasting SOT observations in similar TMD/FM bilayers could thus be ascribed to differences in the FM layer (e.g., different fabrication techniques, capping layers, interface quality, etc.) rather than different interactions between the TMD and the FM. We therefore recommend that the self-torque in single-layer FM reference samples is also characterized in future studies in order to accurately determine the effect of the TMD layer on the observed SOTs, and that the Hall bar dimensions should be clearly reported. In addition, in HM/FM bilayers, the self-torque in the FM layers could counteract the torque generated by the HM layer, resulting in a reduced net torque. Taking advantage of the self-torques in the FM layer, making them work in conjunction with other SOTs instead, could lead to an increase in the SOT efficiency [48]. Tailoring the FM interfaces to change the self-torque direction and strength, in conjunction with searching for different materials as SOT sources, could be a promising route towards an increase in SOT efficiency. These results pave the way for a more accurate disentanglement of all microscopic mechanisms at play, increasing our understanding of the origins underlying the SOTs, which is essential for more energy efficient magnetic memory devices.

## 6.4. Methods

### 6.4.1. Device fabrication

The $MoS_2$ layer was grown using metal-organic chemical vapor deposition (MOCVD) on a $SiO_2$(285 nm)/Si substrate as described in Ref. [49]. The $MoS_2$ is characterized with a PL microscope using a BrightLine long-pass filter set to check the homogeneity of the monolayer coverage on the $SiO_2$/Si substrate (see Fig. 6.1).

Next, a separately prepared PMMA mask with exposed Hall bars of different widths is deposited on top of the $MoS_2$ covered substrate, which ensures a pristine interface between the permalloy and $MoS_2$ with no polymer contamination. Using electron beam evaporation, 6 nm of permalloy and a capping layer and hard mask of 17 nm of $Al_2O_3$ are deposited. Subsequently, the contacts are defined using standard

e-beam lithography techniques. Then, first an $Al_2O_3$ wet etch with tetramethylammonium is performed for 45 s at 40 °C, after which in-situ Ar-milling is performed prior to the evaporation of the Ti/Au (5/55 nm) contacts. Finally, the remaining $MoS_2$ layer is removed using reactive ion etching ($CF_4$ (9.5 sccm)/$O_2$ (0.5 sccm), 30 W RF, 5W ICP, 30 s).

### 6.4.2. Electrical measurements

The harmonic Hall measurements, illustrated in Fig. 6.1(a) and Fig. 6.1(c), were performed at room temperature using a standard lock-in technique with low frequency (77.77 Hz) ac currents ($I_0$), ranging from 500 μA to 700 μA [4, 51, 52]. Subsequently, the first ($V_{xy}^{\omega}$) and second ($V_{xy}^{2\omega}$) harmonic Hall voltage were measured while an applied magnetic field ($H$), ranging from 10 mT to 300 mT, was rotated in-plane, making an angle $\phi$ with respect to the current (Fig. 6.1(c)). Albeit the different thermal conductivity of $MoS_2$ [59] and $SiO_2$ [13], we find a similar anomalous Nernst voltage for the device width a similar width (2 μm), of -0.13±0.01 mV and -0.13±0.03 mV, respectively.

To better compare the SOTs in our devices to previous reports on SOTs in TMD/FM bilayers, we express the SOT in terms of spin-torque conductivity; the common figure-of-merit in literature due to its independence on geometric factors [6, 40]. The spin-torque conductivity is defined as the total angular momentum absorbed by the ferromagnet per second, per unit interface area, per applied electric field, in units of $\frac{\hbar}{2e}$, and is calculated according to:

$$\begin{aligned}\sigma_{FL(DL)} &= \frac{2e}{\hbar} M_s t_{py} (lw) \frac{\tau_{FL(DL)}/\gamma}{(lw)E} \\ &= \frac{2e}{\hbar} M_s t_{Py} w \frac{\tau_{FL(DL)}/\gamma}{R_{sq} I_0},\end{aligned} \tag{6.5}$$

where $M_s$ is the saturation magnetization, $\hbar$ is the reduced Planks constant, $e$ is the electron charge, $E$ is the electric field, $R_{sq}$ is the square resistance, $I_0$ is the applied current, and $l$, $w$, and $t_{Py}$ are the length, width and Py thickness, respectively.

To correct the magnitude of $\sigma_{FL/DL}$ according to the arm width/channel width ratio of the different devices, we divided the raw values by the correction factors supplied by Neumann et al. [58]. These correspond to 0.91, 0.85, 0.78, 0.61, and 0.61 for arm width/channel width ratio of 0.2, 0.33, 0.5, 1, and 1, respectively.

### 6.4.3. Anomalous Hall measurement

To determine the anomalous Hall resistance, $R_{AHE}$, and the saturation magnetization, $M_s$, needed for determining the damping-like torque $\tau_{DL}$ using Eq. 6.4, we performed anomalous Hall measurements (Fig. 6.4). Using a standard lock-in technique with a low frequency (17.77 Hz) current of 10 μA, the Hall voltage is measured while an out-of-plane magnetic field is swept from ∼-1 T to 1 T, as shown in Fig. 6.4. To reduce errors from any misalignment, the Hall voltage is antisymmetrized. Assuming that the anisotropy of the Py is solely due to shape anisotropy,

the anomalous Hall resistance will saturate when the magnetization is completely saturated in the out-of-plane direction. From the anomalous Hall measurements, we are therefore able to determine that the $H_K$ for our $MoS_2/Py/Al_2O_3$ devices is 0.9 T, and 0.8 T for the single-layer $Py/Al_2O_3$, which is taken to be approximately $\mu_0 M_s$ for strong shape anisotropy. This is in agreement with previously reported values for similar thin Py layers [33, 40, 57].

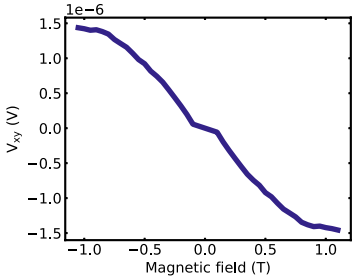


Figure 6.4: Antisymmetrized Hall voltage for the anomalous Hall measurement used to obtain the anomalous Hall resistance, $R_{AHE}$, and the saturation magnetization, $M_s$, needed to determine $\tau_{DL}$ from Eq. (6.4). The data presented here are antisymmetrized to reduce any errors due to sample misalignment.

# Bibliography


[1] A. Manchon, H. C. Koo, J. Nitta, S. M. Frolov, and R. A. Duine, "New perspectives for Rashba spinorbit coupling", Nature Materials **14**, 871–882 (2015).

[2] A. Manchon, J. elezný, I. M. Miron, T. Jungwirth, J. Sinova, A. Thiaville, K. Garello, and P. Gambardella, "Current-induced spin-orbit torques in ferromagnetic and antiferromagnetic systems", Reviews of Modern Physics **91**, 035004 (2019).

[3] B. Dieny, I. L. Prejbeanu, K. Garello, P. Gambardella, P. Freitas, R. Lehndorff, W. Raberg, U. Ebels, S. O. Demokritov, J. Akerman, A. Deac, P. Pirro, C. Adelmann, A. Anane, A. V. Chumak, A. Hirohata, S. Mangin, S. O. Valenzuela, M. C. Onbal, M. D'Aquino, G. Prenat, G. Finocchio, L. Lopez-Diaz, R. Chantrell, O. Chubykalo-Fesenko, and P. Bortolotti, "Opportunities and challenges for spintronics in the microelectronics industry", Nature Electronics **3**, 446–459 (2020).

[4] K. Garello, I. M. Miron, C. O. Avci, F. Freimuth, Y. Mokrousov, S. Blügel, S. Auffret, O. Boulle, G. Gaudin, and P. Gambardella, "Symmetry and magnitude of spinorbit torques in ferromagnetic heterostructures", Nature Nanotechnology **8**, 587–593 (2013).

[5] X. Fan, H. Celik, J. Wu, C. Ni, K.-J. Lee, V. O. Lorenz, and J. Q. Xiao, "Quantifying interface and bulk contributions to spinorbit torque in magnetic bilayers", Nature Communications **5**, 3042 (2014).

[6] M.-h. Nguyen, D. C. Ralph, and R. A. Buhrman, "Spin Torque Study of the Spin Hall Conductivity and Spin Diffusion Length in Platinum Thin Films with Varying Resistivity", Physical Review Letters **116**, 126601 (2016).

[7] M. Jamali, K. Narayanapillai, X. Qiu, L. M. Loong, A. Manchon, and H. Yang, "Spin-Orbit Torques in Co/Pd Multilayer Nanowires", Physical Review Letters **111**, 246602 (2013).

[8] A. Ghosh, K. Garello, C. O. Avci, M. Gabureac, and P. Gambardella, "Interface-Enhanced Spin-Orbit Torques and Current-Induced Magnetization Switching of Pd/Co/AlOx Layers", Physical Review Applied **7**, 014004 (2017).

[9] H.-R. Lee, K. Lee, J. Cho, Y.-H. Choi, C.-Y. You, M.-H. Jung, F. Bonell, Y. Shiota, S. Miwa, and Y. Suzuki, "Spin-orbit torque in a bulk perpendicular magnetic anisotropy Pd/FePd/MgO system", Scientific Reports **4**, 6548 (2014).

[10] C.-F. Pai, L. Liu, Y. Li, H. W. Tseng, D. C. Ralph, and R. A. Buhrman, "Spin transfer torque devices utilizing the giant spin Hall effect of tungsten", Applied Physics Letters **101**, 122404 (2012).

[11] K.-u. Demasius, T. Phung, W. Zhang, B. P. Hughes, S.-H. Yang, A. Kellock, W. Han, A. Pushp, and S. S. P. Parkin, "Enhanced spinorbit torques by oxygen incorporation in tungsten films", Nature Communications **7**, 10644 (2016).

[12] L. Liu, C.-F. Pai, Y. Li, H. W. Tseng, D. C. Ralph, and R. a. Buhrman, "Spin-Torque Switching with the Giant Spin Hall Effect of Tantalum", Science **336**, 555–558 (2012).

[13] C. O. Avci, K. Garello, M. Gabureac, A. Ghosh, A. Fuhrer, S. F. Alvarado, and P. Gambardella, "Interplay of spin-orbit torque and thermoelectric effects in ferromagnet/normal-metal bilayers", Physical Review B **90**, 224427 (2014).

[14] J. Kim, J. Sinha, M. Hayashi, M. Yamanouchi, S. Fukami, T. Suzuki, S. Mitani, and H. Ohno, "Layer thickness dependence of the current-induced effective field vector in Ta|CoFeB|MgO", Nature Materials **12**, 240–245 (2013).

[15] J. Torrejon, J. Kim, J. Sinha, S. Mitani, M. Hayashi, M. Yamanouchi, and H. Ohno, "Interface control of the magnetic chirality in CoFeB/MgO heterostructures with heavy-metal underlayers", Nature Communications **5**, 4655 (2014).

[16] M. Akyol, W. Jiang, G. Yu, Y. Fan, M. Gunes, A. Ekicibil, P. Khalili Amiri, and K. L. Wang, "Effect of heavy metal layer thickness on spin-orbit torque and current-induced switching in Hf|CoFeB|MgO structures", Applied Physics Letters **109**, 022403 (2016).

[17] R. Ramaswamy, X. Qiu, T. Dutta, S. D. Pollard, and H. Yang, "Hf thickness dependence of spin-orbit torques in Hf/CoFeB/MgO heterostructures", Applied Physics Letters **108**, 202406 (2016).

[18] T. Tanaka, H. Kontani, M. Naito, T. Naito, D. S. Hirashima, K. Yamada, and J. Inoue, "Intrinsic spin Hall effect and orbital Hall effect in 4d and 5d transition metals", Physical Review B **77**, 165117 (2008).

[19] Q. Shao, P. Li, L. Liu, H. Yang, S. Fukami, A. Razavi, H. Wu, K. Wang, F. Freimuth, Y. Mokrousov, M. D. Stiles, S. Emori, A. Hoffmann, J. Akerman, K. Roy, J.-P. Wang, S.-H. Yang, K. Garello, and W. Zhang, "Roadmap of SpinOrbit Torques", IEEE Transactions on Magnetics **57**, 1–39 (2021).

[20] G. Yu, P. Upadhyaya, Y. Fan, J. G. Alzate, W. Jiang, K. L. Wong, S. Takei, S. A. Bender, L.-T. Chang, Y. Jiang, M. Lang, J. Tang, Y. Wang, Y. Tserkovnyak, P. K. Amiri, and K. L. Wang, "Switching of perpendicular magnetization by spinorbit torques in the absence of external magnetic fields", Nature Nanotechnology **9**, 548–554 (2014).

[21] Y. Liu and Q. Shao, "Two-Dimensional Materials for Energy-Efficient Spin-Orbit Torque Devices", ACS Nano **14**, 9389–9407 (2020).

[22] A. Kumar, N. Behera, R. Gupta, S. Husain, H. Stopfel, V. Kapaklis, R. Brucas, and P. Svedlindh, "Impact of the crystal orientation on spin-orbit torques in Fe/Pd bilayers", Journal of Physics D: Applied Physics **53**, 355003 (2020).

[23] P. Li, L. J. Riddiford, C. Bi, J. J. Wisser, X.-Q. Sun, A. Vailionis, M. J. Veit, A. Altman, X. Li, M. DC, S. X. Wang, Y. Suzuki, and S. Emori, "Charge-spin interconversion in epitaxial Pt probed by spin-orbit torques in a magnetic insulator", Physical Review Materials **5**, 064404 (2021).

[24] Z. Zheng, Y. Zhang, V. Lopez-Dominguez, L. Sánchez-Tejerina, J. Shi, X. Feng, L. Chen, Z. Wang, Z. Zhang, K. Zhang, B. Hong, Y. Xu, Y. Zhang, M. Carpentieri, A. Fert, G. Finocchio, W. Zhao, and P. Khalili Amiri, "Field-free spin-orbit torque-induced switching of perpendicular magnetization in a ferrimagnetic layer with a vertical composition gradient", Nature Communications **12**, 4555 (2021).

[25] Y.-C. Lau, D. Betto, K. Rode, J. M. D. Coey, and P. Stamenov, "Spinorbit torque switching without an external field using interlayer exchange coupling", Nature Nanotechnology **11**, 758–762 (2016).

[26] F. Sousa, G. Tatara, and A. Ferreira, "Skew-scattering-induced giant antidamping spin-orbit torques: Collinear and out-of-plane Edelstein effects at two-dimensional material/ferromagnet interfaces", Physical Review Research **2**, 043401 (2020).

[27] V. Krizakova, M. Perumkunnil, S. Couet, P. Gambardella, and K. Garello, "Spin-orbit torque switching of magnetic tunnel junctions for memory applications", Journal of Magnetism and Magnetic Materials **562**, 169692 (2022).

[28] H. Yang, S. O. Valenzuela, M. Chshiev, S. Couet, B. Dieny, B. Dlubak, A. Fert, K. Garello, M. Jamet, D.-E. Jeong, K. Lee, T. Lee, M.-B. Martin, G. S. Kar, P. Sénéor, H.-J. Shin, and S. Roche, "Two-dimensional materials prospects for non-volatile spintronic memories", Nature **606**, 663–673 (2022).

[29] H. Kurebayashi, J. H. Garcia, S. Khan, J. Sinova, and S. Roche, "Magnetism, symmetry and spin transport in van der Waals layered systems", Nature Reviews Physics **4**, 150–166 (2022).

[30] J. Hidding and M. H. D. Guimarães, "Spin-Orbit Torques in Transition Metal Dichalcogenide/Ferromagnet Heterostructures", Frontiers in Materials **7**, 1–8 (2020).

[31] S. Husain, R. Gupta, A. Kumar, P. Kumar, N. Behera, R. Brucas, S. Chaudhary, and P. Svedlindh, "Emergence of spinorbit torques in 2D transition metal dichalcogenides: A status update", Applied Physics Reviews **7**, 1–27 (2020).

[32] J. Hidding, S. H. Tirion, J. Momand, A. Kaverzin, M. Mostovoy, B. J. Van Wees, B. J. Kooi, and M. H. D. Guimarães, "Interfacial spin-orbit torques and magnetic anisotropy in WSe2/permalloy bilayers", Journal of Physics: Materials **4**, 04LT01 (2021).

[33] Q. Shao, G. Yu, Y.-W. Lan, Y. Shi, M.-Y. Li, C. Zheng, X. Zhu, L.-J. Li, P. K. Amiri, and K. L. Wang, "Strong Rashba-Edelstein Effect-Induced SpinOrbit Torques in Monolayer Transition Metal Dichalcogenide/Ferromagnet Bilayers", Nano Letters **16**, 7514–7520 (2016).

[34] S. Novakov, B. Jariwala, N. M. Vu, A. Kozhakhmetov, J. A. Robinson, and J. T. Heron, "Interface Transparency and Rashba Spin Torque Enhancement in WSe2 Heterostructures", ACS Applied Materials & Interfaces **13**, 13744–13750 (2021).

[35] W. Lv, Z. Jia, B. Wang, Y. Lu, X. Luo, B. Zhang, Z. Zeng, and Z. Liu, "Electric-Field Control of SpinOrbit Torques in WS2/Permalloy Bilayers", ACS Applied Materials & Interfaces **10**, 2843–2849 (2018).

[36] W. Zhang, J. Sklenar, B. Hsu, W. Jiang, M. B. Jungfleisch, J. Xiao, F. Y. Fradin, Y. Liu, J. E. Pearson, J. B. Ketterson, Z. Yang, and A. Hoffmann, "Research Update: Spin transfer torques in permalloy on monolayer MoS2", APL Materials **4**, 1–9 (2016).

[37] D. MacNeill, G. M. Stiehl, M. H. D. Guimaraes, R. A. Buhrman, J. Park, and D. C. Ralph, "Control of spinorbit torques through crystal symmetry in WTe2/ferromagnet bilayers", Nature Physics **13**, 300–305 (2017).

[38] D. MacNeill, G. M. Stiehl, M. H. D. Guimarães, N. D. Reynolds, R. A. Buhrman, and D. C. Ralph, "Thickness dependence of spin-orbit torques generated by WTe2", Physical Review B **96**, 054450 (2017).

[39] M. H. D. Guimarães, G. M. Stiehl, D. MacNeill, N. D. Reynolds, and D. C. Ralph, "SpinOrbit Torques in NbSe2/Permalloy Bilayers", Nano Letters **18**, 1311–1316 (2018).

[40] G. M. Stiehl, R. Li, V. Gupta, I. E. Baggari, S. Jiang, H. Xie, L. F. Kourkoutis, K. F. Mak, J. Shan, R. A. Buhrman, and D. C. Ralph, "Layer-dependent spin-orbit torques generated by the centrosymmetric transition metal dichalcogenide $\beta$-MoTe2", Physical Review B **100**, 184402 (2019).

[41] G. M. Stiehl, D. MacNeill, N. Sivadas, I. El Baggari, M. H. D. Guimarães, N. D. Reynolds, L. F. Kourkoutis, C. J. Fennie, R. A. Buhrman, and D. C. Ralph, "Current-Induced Torques with Dresselhaus Symmetry Due to Resistance Anisotropy in 2D Materials", ACS Nano **13**, 2599–2605 (2019).

[42] S. Shi, S. Liang, Z. Zhu, K. Cai, S. D. Pollard, Y. Wang, J. Wang, Q. Wang, P. He, J. Yu, G. Eda, G. Liang, and H. Yang, "All-electric magnetization switching and DzyaloshinskiiMoriya interaction in WTe2/ferromagnet heterostructures", Nature Nanotechnology **14**, 945–949 (2019).

[43] I.-H. Kao, R. Muzzio, H. Zhang, M. Zhu, J. Gobbo, S. Yuan, D. Weber, R. Rao, J. Li, J. H. Edgar, J. E. Goldberger, J. Yan, D. G. Mandrus, J. Hwang, R. Cheng, J. Katoch, and S. Singh, "Deterministic switching of a perpendicularly polarized magnet using unconventional spinorbit torques in WTe2", Nature Materials **21**, 1029–1034 (2022).

[44] V. P. Amin, P. M. Haney, and M. D. Stiles, "Interfacial spinorbit torques", Journal of Applied Physics **128**, 151101 (2020).

[45] A. Veneri, D. T. S. Perkins, and A. Ferreira, "Nonperturbative approach to interfacial spin-orbit torques induced by the Rashba effect", Physical Review B **106**, 235419 (2022).

[46] W. Wang, T. Wang, V. P. Amin, Y. Wang, A. Radhakrishnan, A. Davidson, S. R. Allen, T. J. Silva, H. Ohldag, D. Balzar, B. L. Zink, P. M. Haney, J. Q. Xiao, D. G. Cahill, V. O. Lorenz, and X. Fan, "Anomalous spinorbit torques in magnetic single-layer films", Nature Nanotechnology **14**, 819–824 (2019).

[47] T. Seki, Y.-C. Lau, S. Iihama, and K. Takanashi, "Spin-orbit torque in a Ni-Fe single layer", Physical Review B **104**, 094430 (2021).

[48] M. Aoki, E. Shigematsu, R. Ohshima, T. Shinjo, M. Shiraishi, and Y. Ando, "Anomalous sign inversion of spin-orbit torque in ferromagnetic/nonmagnetic bilayer systems due to self-induced spin-orbit torque", Physical Review B **106**, 174418 (2022).

[49] K. Kang, S. Xie, L. Huang, Y. Han, P. Y. Huang, K. F. Mak, C.-j. Kim, D. Muller, and J. Park, "High-mobility three-atom-thick semiconducting films with wafer-scale homogeneity", Nature **520**, 656–660 (2015).

[50] H. Li, Q. Zhang, C. C. R. Yap, B. K. Tay, T. H. T. Edwin, A. Olivier, and D. Baillargeat, "From Bulk to Monolayer MoS2: Evolution of Raman Scattering", Advanced Functional Materials **22**, 1385–1390 (2012).

[51] M. Hayashi, J. Kim, M. Yamanouchi, and H. Ohno, "Quantitative characterization of the spin-orbit torque using harmonic Hall voltage measurements", Physical Review B **89**, 144425 (2014).

[52] M.-H. Nguyen and C.-F. Pai, "Spinorbit torque characterization in a nutshell", APL Materials **9**, 1–15 (2021).

[53] N. Roschewsky, E. S. Walker, P. Gowtham, S. Muschinske, F. Hellman, S. R. Bank, and S. Salahuddin, "Spin-orbit torque and Nernst effect in Bi-Sb/Co heterostructures", Physical Review B **99**, 195103 (2019).

[54] C. O. Avci, J. Mendil, G. S. Beach, and P. Gambardella, "Origins of the Unidirectional Spin Hall Magnetoresistance in Metallic Bilayers", Physical Review Letters **121**, 087207 (2018).

[55] G. Liu, X.-g. Wang, Z. Z. Luan, L. F. Zhou, S. Y. Xia, B. Yang, Y. Z. Tian, G.-h. Guo, J. Du, and D. Wu, "Magnonic Unidirectional Spin Hall Magnetoresistance in a Heavy-MetalFerromagnetic-Insulator Bilayer", Physical Review Letters **127**, 207206 (2021).

[56] K. Zollner, M. D. Petrovi, K. Dolui, P. Plechá, B. K. Nikoli, and J. Fabian, "Scattering-induced and highly tunable by gate damping-like spin-orbit torque in graphene doubly proximitized by two-dimensional magnet Cr2Ge2Te6 and monolayer WS2", Physical Review Research **2**, 043057 (2020).

[57] C. F. Schippers, H. J. M. Swagten, and M. H. D. Guimarães, "Large interfacial spin-orbit torques in layered antiferromagnetic insulator NiPS3/ferromagnet bilayers", Physical Review Materials **4**, 084007 (2020).

[58] L. Neumann and M. Meinert, "Influence of the Hall-bar geometry on harmonic Hall voltage measurements of spin-orbit torques", AIP Advances **8**, 095320 (2018).

[59] R. Yan, J. R. Simpson, S. Bertolazzi, J. Brivio, M. Watson, X. Wu, A. Kis, T. Luo, A. R. Hight Walker, and H. G. Xing, "Thermal Conductivity of Monolayer Molybdenum Disulfide Obtained from Temperature-Dependent Raman Spectroscopy", ACS Nano **8**, 986–993 (2014).

# chapter 7

## Fast Photoresponse in Locally Phase-Engineered $MoTe_2$

*Numerous transition metal dichalcogenides (TMDs) have been extensively studied in recent decades for their potential use in optoelectronic applications, owing to their strong absorption, layer dependent band gap, mechanical strength, and variety of crystal phases. Additionally, new techniques to alter the crystallographic phase of TMDs have recently been discovered, which allow researchers to transform the phase of TMDs locally, creating lateral heterostructures and taking advantage of their different electronic properties. Thus far, only a few reports highlight the potential benefits of phase-transformed TMDs on their optoelectronic properties, and do not clearly disentangle the dominant mechanisms involved in the photocurrent generation. Here, we fabricate a locally phase-transformed $MoTe_2$ device, creating a metal (1T) semiconductor (2H) lateral junction. We perform scanning photocurrent measurements to spatially resolve the areas involved in the photocurrent generation. We find that the photocurrent originates from the 1T'-2H junction, with the photocurrent peak generated at the 2H $MoTe_2$ side of the junction. This observation, together with the non-linear IV-curve, indicates that the underlying mechanisms for the photocurrent is the photovoltaic effect due to a local electric field between the 1T' and 2H $MoTe_2$ regions. Additionally, the 1T'-2H $MoTe_2$ device exhibits a fast optoelectronic response over a wavelength range of 700 nm to 1100 nm, with a rise and fall time of 113 and 110 μs, two orders of magnitude faster when compared to a directly contacted 2H $MoTe_2$ device. These results show the potential of local phase-engineering for the further improvement of TMD based optoelectronic devices.*

## 7.1. Introduction

The large family of 2D materials called the transition metal dichalcogenides (TMDs) have gained much attention in the last two decades due to their versatility, mechanical strength, atomically flat interfaces, and strong absorption at the monolayer limit, making them promising candidates for future (opto)electronic and (opto)spintronic applications [1]. The most commonly studied crystal structure of the TMDs is the most stable hexagonal (2H) phase, for which most TMDs are semiconducting, and possesses a thickness dependent band gap [2, 3]. Apart from the 2H phase, however, TMDs can present a multitude of different crystallographic phases, such as the semiconducting 3R phase, or the semi-metallic 1T, 1T', $1T_d$ phases, which possess different (opto)electronic properties. To benefit from these different properties in a single device, researchers have recently focused on gaining control of the crystallographic phase of TMDs, allowing them to transform the phase of single TMD crystals at will. This new and emerging field is now referred to as the field of phase-engineering.

In literature, multiple methods are used to induce a 2H to 1T' phase transformation for different TMDs, such as crystal deformation [4–7], electrostatic doping [8], chemical doping [9, 10], laser heating [11], etc. In particular, $MoTe_2$ gained much attention as the energy barrier between the 2H and 1T' phase is the smallest ($\sim$40 meV) [12]. It was shown electrically that the Schottky barrier, present when directly contacting the 2H TMD with metallic contacts, is significantly reduced when contacting a 2H TMD via a phase transformed 1T' region [9, 11, 13, 14], with these two-dimensional lateral junctions approaching the quantum limit for the contact resistance [15].



Apart from electrical characterization, only a few reports explored the benefits of local phase transformations on the optoelectronic performance of TMD devices [16, 17]. Lin et al. report an increased reponsivity for 2H $MoTe_2$ devices using 1T' interlayer contacts [17]. However, no scanning photocurrent measurements are performed, which makes it difficult to disentangle the possible microscopic mechanism involved in the photocurrent generation to either the photovoltaic effect (PVE), due to the build in electric field at the Schottky barriers, or the photothermal effect (PTE), due to the different Seebeck coefficients of the 2H and 1T' region [1, 18, 19].

Here, we perform scanning photocurrent measurements on 1T'/2H $MoTe_2$ heterojunction devices, which allow us to spatially resolve the areas involved in the photocurrent generation, giving insights on the underlying mechanisms involved. First, we transform the sides of an exfoliated 2H $MoTe_2$ crystal to a 1T' phase using local heating by laser irradiation, which allows us to contact the 2H $MoTe_2$ via the semi-metallic 1T' regions. We find a clear non-linear behavior for the 1T'-contacted 2H region, indicative of a Schottky barrier between the 1T' and 2H region. Additionally, using the scanning photocurrent measurements, we clearly observe that the photocurrents are generated at the 1T'-2H junction rather than at the Ti/Au electrodes or the 1T' region. More specifically, we find that the peak of the photocurrent is generated at the 2H side of the junction, which suggests that the observed photocurrents in the 1T'-2H junction can be attributed to the PVE rather than the PTE. Lastly, we characterize the optoelectronic performance of the $MoTe_2$ pho-

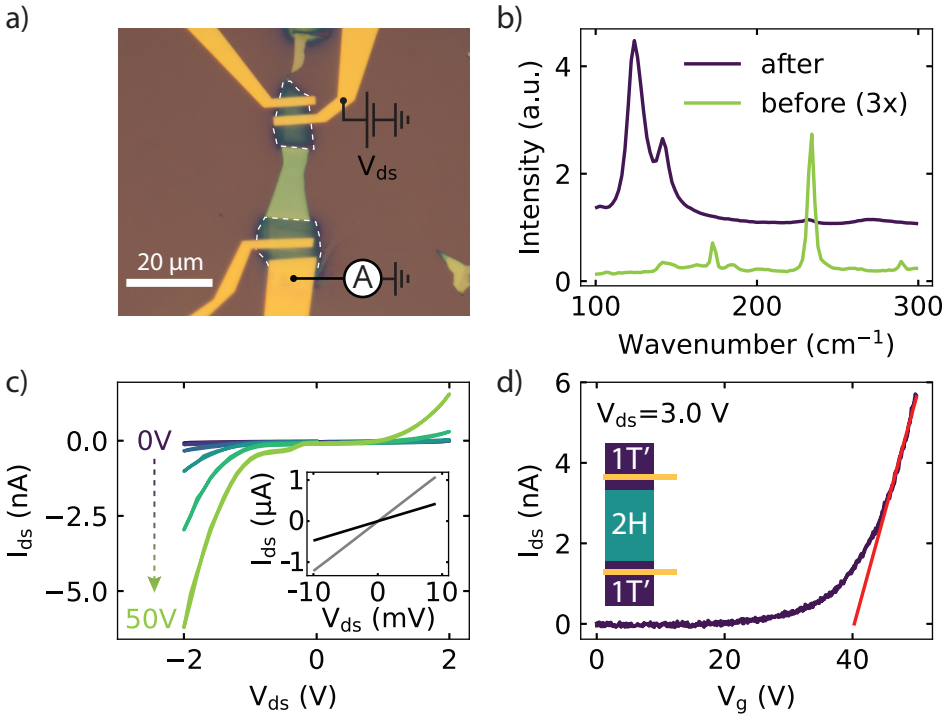


Figure 7.1: (a) Optical micrograph of a phase-changed $MoTe_2$ device, where the phase changed regions are outlined with the white dashed line while the bright green part is the unaltered 2H $MoTe_2$ region. (b) The Raman spectra obtained before (green) and after (dark blue) the phase transformation, which clearly indicate a successful phase transformation. The spectra before is multiplied by 3 for clarity. (c) The $I_{ds} - V_{ds}$-measurements as indicated in (a), with $V_g$ ranging from 0 V to 50 V, taken at 78 K. The non-linear IV characteristics show the Schottky behavior. The IV measurement for the two 1T' regions are depicted in the inset, which clearly show Ohmic behavior. (d) The transfer curve measured with a $V_{ds}$ of 3 V, taken at 78 K, shows clear n-type behavior.



todetector by performing time-resolved, and laser power dependent photocurrent measurements. We find fast rise and fall times of 113 µs and 110 µs, respectively, over a broad spectral range of 700 nm to 1100 nm. By comparing our 1T'-2H $MoTe_2$ photodetector to a 2H $MoTe_2$ diode where the electrodes are directly deposited on the 2H $MoTe_2$ crystal, we are able to show that the temporal response of 1T'-contacted 2H $MoTe_2$ is two orders of magnitude faster. This indicates that phase-engineering can be considered another tool for improving the performance of TMD based optoelectronic devices.

## 7.2. Results and discussion

### 7.2.1. Raman spectroscopy

The device used to perform the optoelectronic measurements is depicted in Fig. 7.1(a). The green region is the untreated 2H $MoTe_2$ while the dark light green regions, indicated by the dashed white line, were irradiated with a laser to initiate the phase transformation from 2H to 1T' (details of the device fabrication can be found in the Methods section). To confirm the phase transformation, we performed Raman spectroscopy measurements as depicted in Fig. 7.1(b). Before laser irradiation, we observe the in-plane $E_{2g}$ mode at 235 $cm^{-1}$ and an out-of-plane $A_g$ mode near 174 $cm^{-1}$, indicative of the 2H $MoTe_2$ phase. After laser irradiation, these peaks disappear, and we observe two new peaks at 124 $cm^{-1}$ and 138 $cm^{-1}$, corresponding to the $A_g$ mode of 1T' $MoTe_2$. This significant change in the Raman spectrum indicates the successful phase transformation of the irradiated regions.

### 7.2.2. Electrical characterization

After fabricating electrical contacts to the phase-changed region, we characterize the structure by sweeping the drain-source voltage ($V_{ds}$) and measuring the drain-source current ($I_{ds}$) for the different regions. In Fig. 7.1(c), the 2-probe $I_{ds}$-$V_{ds}$ measurements are shown for a 2-probe measurement of the 1T'-2H-1T' junction for different gate voltages, ranging from 0 V to 50 V. We observe a clear non-linear behavior for the $I_{ds}$ as function of the $V_{ds}$, indicative of a Schottky barrier present in our device, which could either be between the Ti/Au contact and the 1T' $MoTe_2$, or the 1T'-2H junction. To check this, we performed the $I_{ds}$-$V_{ds}$ measurement on the phase transformed 1T' region only and observe a clear linear behavior showing Ohmic contact between the Ti/Au contacts and 1T' region, depicted in the inset of Fig. 7.1(c). Therefore, we expect the non-linear behavior observed in Fig. 7.1(c) to originate from a Schottky barrier between the 1T'-2H junction. For the 1T' regions, we find a 2-probe resistance of 8 kΩ and 18 kΩ, which again indicate the successful transformation from the semiconducting 2H $MoTe_2$ phase to the semi-metallic 1T' phase.

### 7.2.3. Optoelectrical characterization

To check the optoelectronic response of the 1T'-2H-1T' sample, we perform both scanning photocurrent measurements and time-resolved photocurrent measurements, as described in the methods section. First, the scanning photocurrent measurements are presented, which give more insight on the origin of the photocurrent, after which the time-resolved photocurrent measurements are discussed.

The scanning photocurrent measurements enable us to distinguish spatially where the photocurrent is generated, and thus allows us to check whether the photocurrent originates from the Ti/Au contacts or from the $MoTe_2$ flake itself. When performing the scanning photocurrent measurements, the laser beam is focused and scanned across the sample in a raster like fashion while recording both the reflection and the induced photocurrent. Figure 7.2(a) shows the recorded reflection map with an illumination wavelength of 700 nm, a power of 1 µW, and a full width half maximum

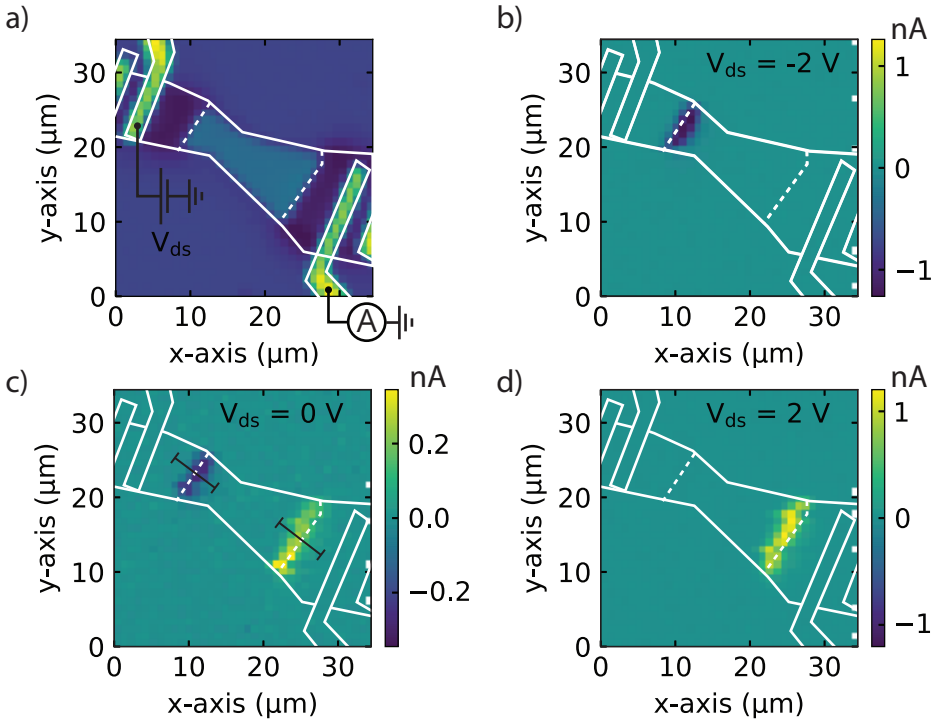


Figure 7.2: (a) Reflectivity map of the scanning photocurrent measurement of the device depicted in Fig. 7.1(a) with the corresponding photocurrent map in (b), (c), and (d), taken at RT. The white outlines indicate the position of the flake and Ti/Au contacts, while the white dashed lines indicates the 1T'-2H junctions for clarity. The photocurrent maps are obtained with $\lambda = 700$ nm, $P = 1$ µW, and a $V_{ds}$ of (b) -2 V, (c) 0 V, and (d) 2 V. From the photocurrent maps, we can clearly see that the induced photocurrent originates from the 1T'-2H junction rather than from the Ti/Au contacts.

(FHWM) spot size of $0.70 \pm 0.02$ µm (see Appendix). The contours of the flake and the Ti/Au contacts are clearly visible and highlighted with the white outlines for clarity. Note that the different phases of the $MoTe_2$ can also be clearly distinguished, and their junctions are highlighted with the white dashed line. The corresponding photocurrent map with a $V_{ds}$ of -2 V, 0 V, and 2 V are depicted in Figs. 7.2(b), (c), and (d), respectively. We clearly observe that the photocurrent originates locally from the 1T'-2H junction, rather than the Ti/Au contacts, which is the case when directly contacting the 2H $MoTe_2$. This, again, confirms a low Schottky barrier between the Ti/Au and 1T' $MoTe_2$, indicating a successful phase transformation.

We observe photocurrents with opposite signs at the two 1T-2H junctions for $V_{ds} = 0$ V. This is in line with the expected behavior for two possible mechanisms: photovoltaic effect (PVE) due to a Schottky barrier at the 1T'-2H junction, or the photo-thermoelectric effect (PTE) due to a different Seebeck coefficient of the two $MoTe_2$ phases. The two mechanisms are schematically depicted in Fig. 7.3. For

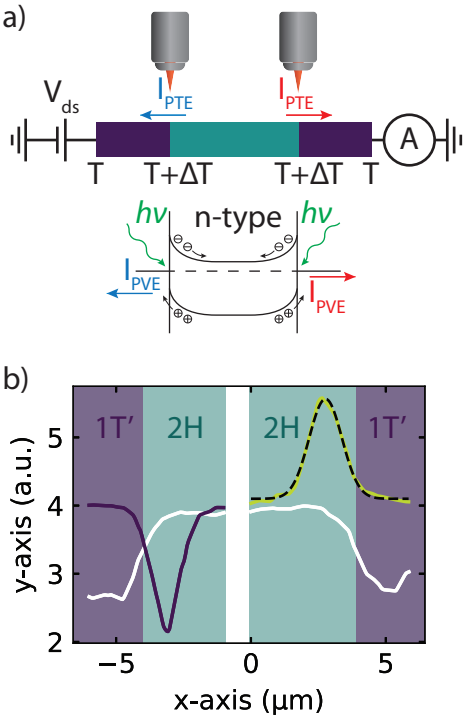


Figure 7.3: (a) A schematic of the photo-thermoelectric (PTE) and photovoltaic effect (PVE). For the PTE, the laser locally heats the device which creates a temperature gradient, which via the Seebeck effect causes a induced photocurrent ($I_{PTE}$). For the PVE, the localized electric field at the Schottky barrier causes a separation of the photo-induced carriers, resulting in $I_{PVE}$. Note that the two effect produce a photocurrent with the same direction, and that the induced photocurrent is opposite on both junctions. (b) A line trace of the photocurrent mapping, indicated in black in Fig. 7.2(c), showing the reflection (white) and negative (dark blue) and positive (green) photocurrent peaks along the line trace. Both the maximum and minimum photocurrent are obtained in the 2H region, as expected for a localized electric field from a Schottky barrier. The phases are indicated by the dark blue (1T') and green (2H) background.



the PTE, local heating due to the laser irradiation causes a temperature gradient ($\Delta T$) which is converted into a voltage difference ($V_{PTE}$) due to a difference in the Seebeck coefficient of the 1T' ($S_{1T'}$) and 2H ($S_{2H}$) phase [1, 20]:

$$V_{PTE} = (S_{1T'} - S_{2H})\Delta T. \tag{7.1}$$

In a short-circuit configuration, this thus leads to an induced photocurrent. The Seebeck coefficient of 2H $MoTe_2$ was shown to be $S_{2H} \sim 230$ μV $K^{-1}$ [21], while 1T' $MoTe_2$ has a lower Seebeck coefficient of $S_{1T'} \sim 30$ μV $K^{-1}$ [21]. As the $V_{PTE}$ generated at the two junctions are opposite, also the expected photocurrent has an opposite sign, as illustrated in Fig. 7.3(a). Assuming that the maximum photocurrent solely originates from the PTE, we can extract the local temperature gradient that is produced by the laser using Eq. 7.1. By considering the photocurrent gen-

erated at the 2H-1T' interfaces in Fig. 7.2(c), and the 2-probe resistance through the channel, together with the values for the Seebeck coefficient mentioned above, we find unrealistically high temperature gradients of between 7490 K and 11952.5 K, which indicates that the PTE would not (solely) explain our observations.

For the PVE driven photocurrent, the localized electric field at the 1T'-2H interface causes the photo-induced electron-hole pairs to separate, resulting in a photocurrent [20]. For our n-type $MoTe_2$, the band alignment is depicted in Fig. 7.3(a). The electric field from the Schottky barrier is positioned in the 2H-region. By taking a line scan of the reflection map and photocurrent map, indicated by the red line in Fig. 7.2(c), we can more accurately determine the position of the photocurrent peak with respect to the 1T'-2H junction. Here, we find that the peak of the photocurrent arises in the 2H region rather than at the 1T'-2H junction, which is in line with the expectation for the PVE [19]. Additionally, assuming a donor density of $N_d$ of $10^{11}$ $cm^2$ [22], a barrier height $\phi_{bi}$ of 60 meV [17], and a relative $\epsilon_r$ of 12, we estimate the depletion width of our Schottky barrier ($W$) using:

$$W = \sqrt{\frac{2\epsilon_0 \epsilon_r \phi_{bi}}{eN_d}}, \tag{7.2}$$

where $e$ is the electron charge, $\epsilon_0$ is the permittivity of free space. We estimate a width in the order of $\sim 2$ µm, which corresponds well to the FWHM of $1.5 \pm 0.2$ µm we find by fitting the positive photocurrent peak with a Gaussian.

Buscema et al. observe a similar photocurrent sign in their scanning photocurrent measurements on an n-type $MoS_2$ photodiode [23]. However, they attribute the induced photocurrent to the PVE, as they observe a clear photocurrent generation in the center of their Ti/Au contacts and see a linear $I_{ds}$-$V_{ds}$ behavior with no indication of a Schottky barrier. In contrast, for our 1T-2H MoTe2 junctions, we observe a clear non-linear IV-curve, indicating that the Schottky barrier plays a more important role in our devices. Furthermore, they see a pronounced photocurrent even when exciting below the band gap of $MoS_2$. Unfortunately, our optoelectronic setup only allows for excitation up to 1100 nm, which is still above the band gap of $MoTe_2$ ($\sim$1.1 eV $\propto$ $\sim$1127 nm for bulk) [24, 25]. Therefore, we suggest further research to be performed on below band gap excitation to determine to what extent the PTE is contributing to the observed photocurrent.

To characterize the optoelectronic performance of our $MoTe_2$ photodetector, we perform time-resolved photocurrent measurements and power dependent photocurrent measurements, depicted in Fig. 7.4. By measuring the induced photocurrent versus time, using a chopper to chop the light on and off (see Fig. 7.4(a)), we are able to extract the rise ($\tau_r$) and fall time ($\tau_f$)) of the device, which are defined as the time required for the photocurrent to increase from 10% to 90%, and decrease from 90% to 10% of the maximum photocurrent, respectively. By performing these measurements over a range of different excitation wavelengths, we find that we get a short rise and fall time of $\sim$113 µs and $\sim$110 µs, respectively, independent of the wavelength as depicted in Fig. 7.4(b). These response times correspond to a 3 dB frequency of $0.35/\tau_r = 3$ kHz [26], which are close to the performance of graphene/$MoTe_2$/graphene photodetectors [27]. In contrast, when directly contact-

ing the 2H $MoTe_2$ with Ti/Au electrodes, we find a much slower response, as shown in Fig. 7.6(c) in the appendix. Here, we find a clear sawtooth behavior, indicative of capacitive behavior, already at 20 Hz. This shows that using the 1T' regions to contact the 2H $MoTe_2$ increases the response of our $MoTe_2$ photodetector by more than two orders of magnitude.

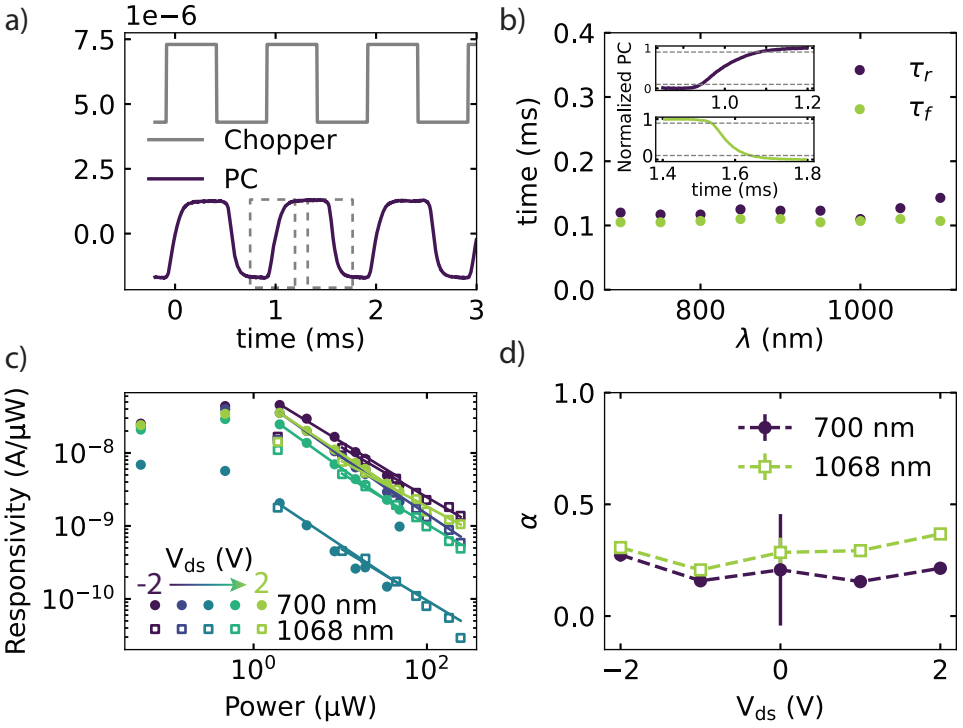


Figure 7.4: (a) Time-resolved photocurrent, taken at RT, where the photocurrent (blue) in the device is plotted together with the chopper signal (grey) versus time show the fast response of our $MoT_2$ photodetector. The dashed grey lines indicate the region used to determine the rise and fall time, as depicted in the inset of (b). (b) The extracted rise (blue) and fall times (green) indicate no wavelength dependence on the fast response for wavelengths ranging from 700 to 1100 nm. The inset shows the rise (blue) and fall (green) curves of the photocurrent from which the rise and fall times are extracted. (c) The power dependent measurements for different $V_{ds}$, ranging from -2 V to 2 V, with a maximum responsivity of $4.5 \times 10^{-}8$ A/μW. Here, the responsivity ($R$) of the device is plotted as function of the laser excitation power ($P$) and fitted at high laser excitation power to a power law: $R \propto P^{\alpha-1}$. The measured $R$ for 700 nm and 1068 nm are indicated by the filled circles and unfilled squared, respectively. (d) The extracted index of the power law ($\alpha$) from the fitting in (c) versus $V_{ds}$ for the wavelengths 700 nm (blue) and 1068 nm (green).

The response dynamics displayed at the 1T'-2H junction are relatively fast compared to other TMD based photodetectors [26, 28] More specifically, compared to other $MoTe_2$ based photodetectors, they are one order of magnitude faster when compared to the report of Huang et al. on 2H $MoTe_2$ [29], and similar to the ones found by Lin et al. in 1T'-contacted 2H $MoTe_2$ [17]. On other TMD-based devices,

a variety of different response dynamics are reported, with the fastest responses reported for deep UV and mid-IR detectors on graphene/$MoTe_2$/black phosphorus devices, which reach bandwidths of 2.1 MHz [30].

Additionally, we characterize the $MoTe_2$ based photodetector by varying the excitation power at a fixed excitation wavelength (700 nm and 1068 nm). From the power dependent measurements, we are able to determine the responsivity: $R = I_{PC}/P$, where $I_{PC}$ is the induced photocurrent and $P$ is the power of the laser [1, 20], and find a maximum $R$ of $4.5 \times 10^{-8}$ A/µW with a wavelength of 700 nm and a 2 V bias. Compared to other reports on TMD based photodetectors, this is relatively low, as the reported responsivities for different TMD based photodetectors range approximately from $7.25 \times 10^{-11}$ A/µW to $1.237 \times 10^{-3}$ A/µW [28]. The low responsivity of our device is not entirely unexpected, as there commonly is a trade-off between fast response and high responsivity in these devices [26]. Additionally, the responsivity of our device is measured with a focused laser spot rather than illuminating the entire device. This could lead to an underestimation of the generated photocurrent as only a small fraction of the photodetector area is used to generate the photocurrent.

Figure 7.4(c) clearly shows a decrease of responsivity with incident excitation power for $P > 1.9$ µW, which is commonly observed in TMD photodetectors [31, 32]. It can be associated with a reduced number of photogenerated carriers available for extraction under high photon flux due to the saturation of recombination/trap states that influence the lifetime of the generated carriers [33]. The responsivity versus laser power can be expressed by a power law $R \propto P_d^{\alpha-1}$ for $P > 1.9$ µW, where $P$ is the laser power, and $\alpha$ is the index of the power law [29, 34]. From the fit, we are able to extract $\alpha$ for the two different wavelengths at different $V_{ds}$ as shown in Fig. 7.4(d). The deviation from the ideal slope of $\alpha = 1$, where the responsivity does not dependent on the laser power, can be attributed to complex processes in the carrier generation, trapping, and electron-hole recombination in the $MoTe_2$ [35, 36]. For the PTE, a value of $\alpha \sim 0.8$ is expected, while we find a value of $\alpha \sim 0.25$, which indicates again that the PTE is not responsible for the photocurrent in our device [18].



## 7.3. Conclusion

In conclusion, our results indicate that contacting the 2H region of $MoTe_2$ via a phase-transformed 1T' region is beneficial for the temporal optoelectronic response of $MoTe_2$ based photodetectors. Our scanning photocurrent measurements and non-linear IV curves, clearly show that the origin of the photocurrent in our device can be ascribed to the Schottky barrier between the 1T'-2H junction, rather than the photo-thermoelectric effect or Schottky barriers at the Ti/Au electrode-TMD interface. Contacting the $MoTe_2$ via the phase-transformed 1T' region, therefore, allows one to study the intrinsic properties of the TMD rather than the electrode-TMD interactions, beneficial for fundamental research. Additionally, an increase of 2 orders of magnitude in the optoelectronic temporal response is observed when contacting the 2H $MoTe_2$ via the 1T' regions. This shows that tailoring the crystallographic phase of TMDs locally, altering their optoelectronic response at will, can

have a profitable effect on the optoelectronic operation. Our results, in combination with the wide variety of phase-engineering techniques and different TMDs available, could lead to a further improved performance of TMD-based optoelectronic devices, leading to more sensitive, faster and flexible photodetectors.

## 7.4. Methods

### 7.4.1. Device fabrication

The 2H $MoTe_2$ flakes are obtained by mechanical exfoliation (bulk crystal supplied by HQ Graphene) and transferred onto a $Si/SiO_2$ (285 nm) substrate in a nitrogen environment. Using an optical microscope, the $MoTe_2$ flakes are selected based on their size, thickness, and homogeneous surface. Next, the Raman spectra are obtained with an inVia Qonto Raman microscope using a linearly polarized laser with an excitation wavelength of $\lambda = 532$ nm and a 2400 l/mm grating and a laser power of $\sim 100$ µW with a diffraction limited laser spot of $\sim 1$ µm. Using the same system, the 2H-1T' phase transformation is performed by selectively illuminating parts of the $MoTe_2$ flake with the 532 nm laser beam in a raster-like fashion, using steps of 500 nm and 0.1 s illumination. We find that a laser power $\geq 3.25$ mW (laser spot size around 500 nm) is needed to initiate the phase transformation. Finally, using standard lithography techniques, the Ti/Au (5 nm/55 nm) contacts are fabricated on top of the flake by means of electron beam lithography and electron beam evaporation.



### 7.4.2. Optoelectronic measurements

The electrical characterization (i.e. IV-sweeps, transfer curves) is performed using a Keithley 2400 and 2450 source measure unit at 78 K. For the optoelectronic measurements, a supercontinuum white light laser (NKT Photonics SuperK EXTREME) is used as illumination source, and the measurements are taken at room temperature. The induced photocurrent is measured in a short circuit configuration using a Stanford Research Systems SR830 lock-in amplifier, which is referenced to the frequency of the optical chopper. The photocurrents are either measured directly by the lock-in amplifier, or converted to a voltage using a home build current pre-amplifier, which is subsequently measured by the lock-in amplifier. The time-resolved photoresponse of the device, depicted in Fig. 7.3(a), is measured using a chopper and an oscilloscope (Keysight DSOX1204A) at room temperature.

## 7.5. Acknowledgements

We would like to acknowledge Prof. M. A. Loi and E. K. Tekelenburg for their help with the Raman measurements and thank J. G. Holstein, H. Adema, H. de Vries, A. Joshua, and F. H. van der Velde for their technical support. Sample fabrication was performed using NanoLabNL facilities. This work was supported by the Dutch Research Council (NWOSTU.019.014), the Zernike Institute for Advanced Materials, and innovation program under grant agreement No. 881603 (Graphene Flagship).

## 7.6. Author contributions

J.H. and C.A.C.S. fabricated the samples, and together with D.V. performed both the electrical and optical measurements under supervision of M.H.D.G. K.R. joined to perform additional measurements on additional samples also under supervision of M.H.D.G. J.H. performed the data analysis and, together with M.H.D.G. wrote the paper with comments from all authors.

## 7.7. Appendices

### 7.7.1. Laser spot determination

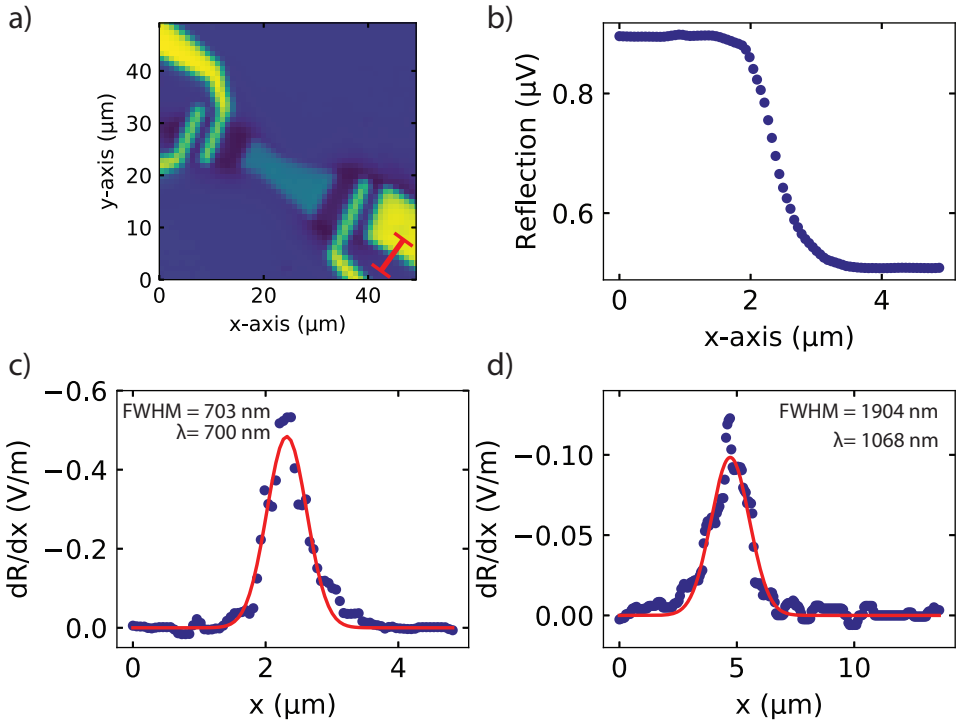


Figure 7.5: (a) Reflection map taken with $\lambda = 700$ nm of the device depicted in Fig. 7.1(a), where the red line indicated the position of the line trace to determine the laser spot size. (b) The data (blue circles) of the line trace in (a), which shows the clear step from the Ti/Au electrode to the $SiO_2$ substrate. (c) By taking the derivative of the data depicted in (b) (blue circles), and fitting it with a Gaussian (red line), the FWHM of the laser spot used to do the scanning is determined. (d) Same as (c) but now for $\lambda = 1068$ nm

.

To determine the spot size of our laser at the wavelengths of 700 nm and 1068 nm, we use the software Gwyddion to take a line trace over a scanning map of the reflectivity. The reflectivity map for 700 nm is depicted in Fig. 7.5(a), where the position of the line trace is indicated with a red line and the line trace itself is

depicted in Fig. 7.5(b). By fitting the derivative of the data in Fig. 7.5(b) with a Gaussian, we are able to determine the FWHM of the laser spot, as show in Figs. 7.5(c) and (d) for 700 nm and 1068 nm, respectively. For a wavelength of 700 nm, we find a diffraction limited FWHM of $0.70 \pm 0.02$ µm, while for the 1068 nm, we find a broader FWHM of $1.91 \pm 0.04$ µm.

### 7.7.2. Mobility

The transfer curve of Fig. 7.1(d), for the device depicted in Fig. 7.1(a), shows clear n-type behavior with a threshold voltage of $V_{th} = 40.3$ V. The mobility $\mu$ of the device is determined by fitting the right part of the transfer curve to:

$$\mu = \left(\frac{dI_{ds}}{dV_g}\right)\left(\frac{l}{wC_gV_{ds}}\right), \tag{7.3}$$

where $(dI_{ds}/V_g)$ is the slope at positive $V_g$, $l$ and $w$ are the length and width of the channel, $C_g$ is the area capacitance of the $SiO_2$ back gate ($1.2 \times 10^{-4}$ F/m$^2$), and $V_{ds}$ is the drain-source voltage (3 V). We find a low mobility of 0.08 cm$^2$/(V · s).

### 7.7.3. Other phase-engineered $MoTe_2$ device

Surprisingly, another fabricated phase transformed $MoTe_2$ device exhibits clear p-type behavior, and shows different mobilities compared to the device depicted in Fig. 7.1(a). When contacting the 2H $MoTe_2$ directly with the Ti/Au contacts, we find a mobility of 1.74 cm$^2$/V · s, while if the 2H region is contacted via the 1T' region, similar to Fig. 7.1(d), we find a mobility of 14.18 cm$^2$/V · s, in agreement with the reports of Bae et al. [14] on electrical measurements on phase changed $MoTe_2$ devices and larger compared to similar measurements reported by Zhang et al. [13]. The 8-fold increase in mobility, here, again indicates that the phase transformation has let to less invasive contacts with lower Schottky barriers compared to the direct contacts.

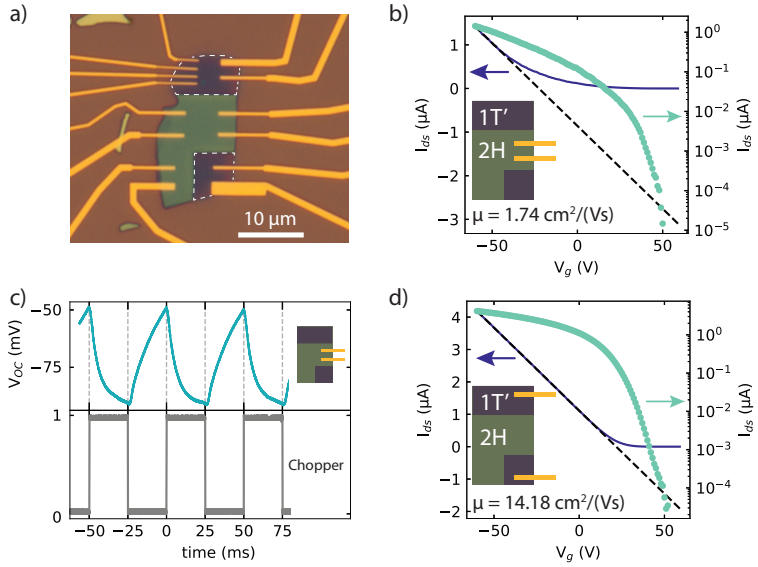


Figure 7.6: (a) Optical micrograph of another phase-engineered $MoTe_2$ device similar to the device depicted in Fig. 7.1(a) in the main text. The white dashed regions indicate the areas where the 2H $MoTe_2$ are transformed to 1T' by laser irradiation. (b) Transfer curve measured with the Ti/Au electrodes directly deposited on the 2H region, which shows clear p-type behavior. (d) The transfer curve measured with the Ti/Au electrodes on the 1T' region. By fitting the curve on negative gate voltages and using Eq. 7.3, we are able to extract a mobility of 1.74 $cm^2/(V \cdot s)$ and 14.2 $cm^2/(V \cdot s)$, respectively. (c) The top panel shows the temporal photovoltage response (green) of the $MoTe_2$ device when the 2H crystal is directly contacted with the Ti/Au electrodes. The bottom panel depicts the signal from the chopper (grey), which chops the light on and off. A much slower optoelectronic response is observed compared to the response of the device discussed in the main text, as shown in Fig. 7.4(a).

# Bibliography


[1] M. Buscema, J. O. Island, D. J. Groenendijk, S. I. Blanter, G. A. Steele, H. S. J. van der Zant, and A. Castellanos-Gomez, "Photocurrent generation with two-dimensional van der Waals semiconductors", Chemical Society Reviews **44**, 3691–3718 (2015).

[2] K. F. Mak, C. Lee, J. Hone, J. Shan, and T. F. Heinz, "Atomically Thin MoS2: A New Direct-Gap Semiconductor", Physical Review Letters **105**, 136805 (2010).

[3] S. Manzeli, D. Ovchinnikov, D. Pasquier, O. V. Yazyev, and A. Kis, "2D transition metal dichalcogenides", Nature Reviews Materials **2**, 17033 (2017).

[4] M. Dave, R. Vaidya, S. G. Patel, and A. R. Jani, "High pressure effect on MoS2 and MoSe2 single crystals grown by CVT method", Bulletin of Materials Science **27**, 213–216 (2004).

[5] S. Song, D. H. Keum, S. Cho, D. Perello, Y. Kim, and Y. H. Lee, "Room Temperature Semiconductor Metal Transition of MoTe2 Thin Films Engineered by Strain", Nano Letters **16**, 188–193 (2016).

[6] Y.-c. Lin, D. O. Dumcenco, Y.-s. Huang, and K. Suenaga, "Atomic mechanism of the semiconducting-to-metallic phase transition in single-layered MoS2", Nature Nanotechnology **9**, 391–396 (2014).

[7] B. Shang, X. Cui, L. Jiao, K. Qi, Y. Wang, J. Fan, Y. Yue, H. Wang, Q. Bao, X. Fan, S. Wei, W. Song, Z. Cheng, S. Guo, and W. Zheng, "Lattice -Mismatch-Induced Ultrastable 1T-Phase MoS2Pd/Au for Plasmon-Enhanced Hydrogen Evolution", Nano Letters **19**, 2758–2764 (2019).

[8] Y. Wang, J. Xiao, H. Zhu, Y. Li, Y. Alsaid, K. Y. Fong, Y. Zhou, S. Wang, W. Shi, Y. Wang, A. Zettl, E. J. Reed, and X. Zhang, "Structural phase transition in monolayer MoTe2 driven by electrostatic doping", Nature **550**, 487–491 (2017).

[9] R. Kappera, D. Voiry, S. E. Yalcin, B. Branch, G. Gupta, A. D. Mohite, and M. Chhowalla, "Phase-engineered low-resistance contacts for ultrathin MoS2 transistors", Nature Materials **13**, 1128–1134 (2014).

[10] Y. Ma, B. Liu, A. Zhang, L. Chen, M. Fathi, C. Shen, A. N. Abbas, M. Ge, M. Mecklenburg, and C. Zhou, "Reversible Semiconducting-to-Metallic Phase Transition in Chemical Vapor Deposition Grown Monolayer WSe2 and Applications for Devices", ACS Nano **9**, 7383–7391 (2015).

[11] S. Cho, S. Kim, J. H. Kim, J. Zhao, J. Seok, D. H. Keum, J. Baik, D.-h. Choe, K. J. Chang, K. Suenaga, S. W. Kim, Y. H. Lee, and H. Yang, "Phase patterning for ohmic homojunction contact in MoTe2", Science **349**, 625–628 (2015).

[12] K.-A. N. Duerloo, Y. Li, and E. J. Reed, "Structural phase transitions in two-dimensional Mo- and W-dichalcogenide monolayers", Nature Communications **5**, 4214 (2014).

[13] X. Zhang, Z. Jin, L. Wang, J. A. Hachtel, E. Villarreal, Z. Wang, T. Ha, Y. Nakanishi, C. S. Tiwary, J. Lai, L. Dong, J. Yang, R. Vajtai, E. Ringe, J. C. Idrobo, B. I. Yakobson, J. Lou, V. Gambin, R. Koltun, and P. M. Ajayan, "Low Contact Barrier in 2H/1T MoTe2 In-Plane Heterostructure Synthesized by Chemical Vapor Deposition", ACS Applied Materials & Interfaces **11**, 12777–12785 (2019).

[14] G. Y. Bae, J. Kim, J. Kim, S. Lee, and E. Lee, "MoTe2 Field-Effect Transistors with Low Contact Resistance through Phase Tuning by Laser Irradiation", Nanomaterials **11**, 2805 (2021).

[15] Y. Wang and M. Chhowalla, "Making clean electrical contacts on 2D transition metal dichalcogenides", Nature Reviews Physics **4**, 101–112 (2021).

[16] H. Yamaguchi, J.-C. Blancon, R. Kappera, S. Lei, S. Najmaei, B. D. Mangum, G. Gupta, P. M. Ajayan, J. Lou, M. Chhowalla, J. J. Crochet, and A. D. Mohite, "Spatially Resolved Photoexcited Charge-Carrier Dynamics in Phase-Engineered Monolayer MoS2", ACS Nano **9**, 840–849 (2015).

[17] D.-y. Lin, H.-p. Hsu, G.-h. Liu, T.-z. Dai, and Y.-t. Shih, "Enhanced Photoresponsivity of 2H-MoTe2 by Inserting 1T-MoTe2 Interlayer Contact for Photodetector Applications", Crystals **11**, 964 (2021).

[18] X. Xu, N. M. Gabor, J. S. Alden, A. M. van der Zande, and P. L. McEuen, "Photo-Thermoelectric Effect at a Graphene Interface Junction", Nano Letters **10**, 562–566 (2010).

[19] Y. Zhang, H. Li, L. Wang, H. Wang, X. Xie, S.-L. Zhang, R. Liu, and Z.-J. Qiu, "Photothermoelectric and photovoltaic effects both present in MoS2", Scientific Reports **5**, 7938 (2015).

[20] N. Huo and G. Konstantatos, "Recent Progress and Future Prospects of 2D-Based Photodetectors", Advanced Materials **30**, 1801164 (2018).

[21] D. H. Keum, S. Cho, J. H. Kim, D.-H. Choe, H.-J. Sung, M. Kan, H. Kang, J.-Y. Hwang, S. W. Kim, H. Yang, K. J. Chang, and Y. H. Lee, "Bandgap opening in few-layered monoclinic MoTe2", Nature Physics **11**, 482–486 (2015).

[22] HQgraphene, *MoTe2 (2H Molybdenum Ditelluride)*, 2023.

[23] M. Buscema, M. Barkelid, V. Zwiller, H. S. J. van der Zant, G. A. Steele, and A. Castellanos-Gomez, "Large and Tunable Photothermoelectric Effect in Single-Layer MoS2", Nano Letters **13**, 358–363 (2013).

[24] C. Ruppert, B. Aslan, and T. F. Heinz, "Optical Properties and Band Gap of Single- and Few-Layer MoTe2 Crystals", Nano Letters **14**, 6231–6236 (2014).

[25] I. G. Lezama, A. Arora, A. Ubaldini, C. Barreteau, E. Giannini, M. Potemski, and A. F. Morpurgo, "Indirect-to-Direct Band Gap Crossover in Few-Layer MoTe2", Nano Letters **15**, 2336–2342 (2015).

[26] Pinki Yadav, S. Dewan, R. Mishra, and S. Das, "Review of recent progress, challenges, and prospects of 2D materials-based short wavelength infrared photodetectors", Journal of Physics D: Applied Physics **55**, 313001 (2022).

[27] K. Zhang, X. Fang, Y. Wang, Y. Wan, Q. Song, W. Zhai, Y. Li, G. Ran, Y. Ye, and L. Dai, "Ultrasensitive Near-Infrared Photodetectors Based on a GrapheneMoTe2Graphene Vertical van der Waals Heterostructure", ACS Applied Materials & Interfaces **9**, 5392–5398 (2017).

[28] H. Xiao, L. Lin, J. Zhu, J. Guo, Y. Ke, L. Mao, T. Gong, H. Cheng, W. Huang, and X. Zhang, "Highly sensitive and broadband photodetectors based on WSe2/MoS2 heterostructures with van der Waals contact electrodes", Applied Physics Letters **121**, 023504 (2022).

[29] H. Huang, J. Wang, W. Hu, L. Liao, P. Wang, X. Wang, F. Gong, Y. Chen, G. Wu, W. Luo, H. Shen, T. Lin, J. Sun, X. Meng, X. Chen, and J. Chu, "Highly sensitive visible to infrared MoTe2 photodetectors enhanced by the photogating effect", Nanotechnology **27**, 445201 (2016).

[30] D. Shen, H. Yang, C. Spudat, T. Patel, S. Zhong, F. Chen, J. Yan, X. Luo, M. Cheng, G. Sciaini, Y. Sun, D. A. Rhodes, T. Timusk, Y. N. Zhou, N. Y. Kim, and A. W. Tsen, "High-Performance Mid-IR to Deep-UV van der Waals Photodetectors Capable of Local Spectroscopy at Room Temperature", Nano Letters **22**, 3425–3432 (2022).

[31] H. S. Lee, S.-W. Min, Y.-G. Chang, M. K. Park, T. Nam, H. Kim, J. H. Kim, S. Ryu, and S. Im, "MoS2 Nanosheet Phototransistors with Thickness-Modulated Optical Energy Gap", Nano Letters **12**, 3695–3700 (2012).

[32] O. Lopez-Sanchez, D. Lembke, M. Kayci, A. Radenovic, and A. Kis, "Ultrasensitive photodetectors based on monolayer MoS2", Nature Nanotechnology **8**, 497–501 (2013).

[33] M. Buscema, D. J. Groenendijk, S. I. Blanter, G. A. Steele, H. S. J. van der Zant, and A. Castellanos-Gomez, "Fast and Broadband Photoresponse of Few-Layer Black Phosphorus Field-Effect Transistors", Nano Letters **14**, 3347–3352 (2014).

[34] X. Zhang, B. Liu, W. Yang, W. Jia, J. Li, C. Jiang, and X. Jiang, "3D-branched hierarchical 3C-SiC/ZnO heterostructures for high-performance photodetectors", Nanoscale **8**, 17573–17580 (2016).

[35] H. Kind, H. Yan, B. Messer, M. Law, and P. Yang, "Nanowire Ultraviolet Photodetectors and Optical Switches", Advanced Materials **14**, 158–160 (2002).

[36] F. Liu, H. Shimotani, H. Shang, T. Kanagasekaran, V. Zólyomi, N. Drummond, V. I. Fal'ko, and K. Tanigaki, "High-Sensitivity Photodetectors Based on Multilayer GaTe Flakes", ACS Nano **8**, 752–760 (2014).

# chapter 8

## The role of device asymmetries and Schottky barriers on the helicity-dependent photoresponse of 2D phototransistors

*Circular photocurrents (CPC), namely circular photogalvanic (CPGE) and photon drag effects, have recently been reported both in monolayer and multilayer transition metal dichalcogenide (TMD) phototransistors. However, the underlying physics for the emergence of these effects are not yet fully understood. In particular, the emergence of CPGE is not compatible with the $D_{3h}$ crystal symmetry of two-dimensional TMDs, and should only be possible if the symmetry of the electronic states is reduced by influences such as an external electric field or mechanical strain. Schottky contacts, nearly ubiquitous in TMD-based transistors, can provide the high electric fields causing a symmetry breaking in the devices. Here, we investigate the effect of these Schottky contacts on the CPC by characterizing the helicity-dependent photoresponse of monolayer $MoSe_2$ devices both with direct metal-$MoSe_2$ Schottky contacts and with hBN tunnel barriers at the contacts. We find that, when Schottky barriers are present in the device, additional contributions to CPC become allowed, resulting in emergence of CPC for illumination at normal incidence.*

Published as: Jorge Quereda, Jan Hidding, et al., "*The role of device asymmetries and Schottky barriers on the helicity-dependent photoresponse of 2D phototransistors*," npj 2D Materials and Applications **5**, 13 (2021)

## 8.1. Introduction

Two-dimensional (2D) transition metal dichalcogenides (TMDs) offer a privileged material platform for the realization of ultra thin and efficient optoelectronics [1] [2]. Their strong optical absorption, fast optoelectronic response, and high power conversion efficiencies, combined with functional properties such as flexibility, transparency, or self-powering make these materials highly promising for the development of optoelectronic devices [3] [4] [5] [6] [7].

A particularly interesting feature of 2D-TMDs is the coupling between their spin and valley degrees of freedom [8]. In these materials, the optical band gap is located at two non-equivalent valleys in the reciprocal space, usually labeled as K and K, presenting different optical selection rules and opposite spinorbit splitting both in the valence band and in the conduction band. In consequence, upon band-edge optical excitation with circularly polarized light, the spin and valley degrees of freedom of the optically excited electrons can be controlled by appropriately selecting the illumination wavelength and helicity [9]. It was recently shown that when a monolayer TMD (1L-TMD) is illuminated at an oblique angle with respect to the crystal plane, a helicity-dependent photocurrent (circular photocurrent, CPC) emerges. This effect has been attributed to circular photogalvanic (CPGE) and photon drag (CPDE) effects [10] [11] [12] and opens exciting possibilities for the realization of 2D self-powered optoelectronic and opto-spintronic devices.

The physical origin of CPCs in 1L-TMDs is still far from understood. In particular, the emergence of CPGE requires a low crystal symmetry not compatible with the $D_{3h}$ symmetry found in pristine 1L-TMDs. Therefore, it requires an external agent such as mechanical strain or a strong external electric field to reduce the crystal symmetry to, at most, a single mirror-plane symmetry [11]. One possible agent that can cause this symmetry breaking is the strong electric field that emerges in Schottky contacts to 1L-TMDs [13] when an external bias is applied. In a recent work [11] we studied CPC in a hexagonal boron nitride (hBN) encapsulated 1L-$MoSe_2$ phototransistor. There, the Schottky barriers were expected to be suppressed, or at least largely reduced, by the presence of bilayer hBN tunnel barriers between the metallic contacts and the 1L-$MoSe_2$ channel [14] [15]. Here, to clarify the role of Schottky barriers we investigate helicity-dependent photocurrents in 1L-$MoSe_2$ devices both with direct metal/$MoSe_2$ contacts and with metal/hBN/$MoSe_2$ tunnel contacts. In both cases, we observe a CPC that is maximized for an illumination wavelength $\lambda = 790$ nm (matching the room-temperature A-exciton resonance of 1L-$MoSe_2$), increases with the gate voltage, and depends nontrivially on the sourcedrain voltage and the light incidence angle. However, for the direct metal contact geometry, a nonzero drainsource voltage applied between the sensing contacts is needed to obtain a measurable photocurrent, while for the device with hBN tunnel barriers a nonzero CPC can be clearly observed even at zero drainsource voltage. We find that for devices with direct metal/$MoSe_2$ contacts where asymmetric Schottky barriers are expected to be present, a nonzero CPC emerges even for light incident normal to the crystal plane. This is contrary to the case of the device with hBN tunnel barriers. Our results thus confirm that the presence of strong, anisotropic electric fields near the direct metal/$MoSe_2$ contacts reduces the symmetry of the $MoSe_2$ channel,

leading to the emergence of additional contributions to the CPC, not present in devices with tunnel hBN contacts.

The contact-dependent contributions to CPC observed here could also be present in earlier reported measurements attributed to the valley-hall effect [16] (VHE) and to a Berry-curvature-induced circular photogalvanic effect [10]. These additional contributions to the observed CPC could be distinguished by their characteristic dependence on the illumination angle. Our results thus demonstrate the crucial importance of angle-resolved measurements for an adequate characterization of helicity-dependent optoelectronic effects in 2D systems.

## 8.2. Results

Device characterization and measurement geometry Fig. 8.1(a) shows a sketch of the device with direct metal/1L-$MoSe_2$ contacts (a microscope image of the actual device can be found in Supplementary Note 1). We first exfoliated and identified 1L-$MoSe_2$ and multilayer hBN flakes by standard micromechanical cleavage, and confirmed their flake thickness by atomic force microscopy (see Supplementary Note 1). Then, we used a dry, adhesive-free pick-up technique [17] to fabricate the 1L-$MoSe_2$/hBN heterostructure on a $SiO_2$ (285 nm)/p-doped Si substrate. Finally, we fabricated Ti (5 nm)/Au (75 nm) electrodes on top of the structure by standard electron-beam lithography and metal evaporation. The contact geometry shown in Fig. 8.1 allows us to measure the optoelectronic response of the device in two perpendicular directions. We use a similar fabrication process and contact geometry for the device with hBN tunnel barriers, as detailed in the Methods section. In that case, the 1L-$MoSe_2$ channel is fully encapsulated between a thick hBN layer and a bilayer hBN, and metallic electrodes are fabricated directly on top of the bilayer hBN.

For all the measurements described below, the devices were kept in vacuum and at room temperature. Figure 8.1(b) shows a two-terminal transfer characteristic of the non-encapsulated device, presenting a clear n-type behavior with a threshold gate voltage $V_g^{th} = 40$ V. The device threshold voltage also presented a slow drift over long periods of time, changing by up to 1015 V over a 24 h period. We attribute this slow drift to charging/discharging of local impurities at the $SiO_2$ substrate.

The IV characteristic (inset in Fig. 8.1(b)) is highly nonlinear, due to the presence of asymmetric Schottky barriers at the metal-$MoSe_2$ contacts. The device with hBN tunnel barriers also presents a nonlinear IV characteristic, as shown in Supplementary Note 2 and discussed in detail in ref. [14].

For characterizing the device photoresponse, we uniformly illuminate the whole sample using a wavelength-tunable continuous wave (CW) laser source and measure the resulting photocurrent. Importantly for our measurements, we use collimated light for optical excitation, as opposed to focusing the light with a high numerical aperture microscope objective. This illumination geometry allows us to control precisely the light incidence angle $\phi$. Figure 8.1(c) shows the registered sourcedrain current $I_{12}$ when the laser source is turned on and off using a chopper for sourcedrain voltage $V_{12} = 10$ V, gate voltage $V_g = 50$ V, illumination wavelength $\lambda = 790$ nm, linear polarization, and light incidence angle $\phi = 30°$. As shown in Fig. 8.1(a), the

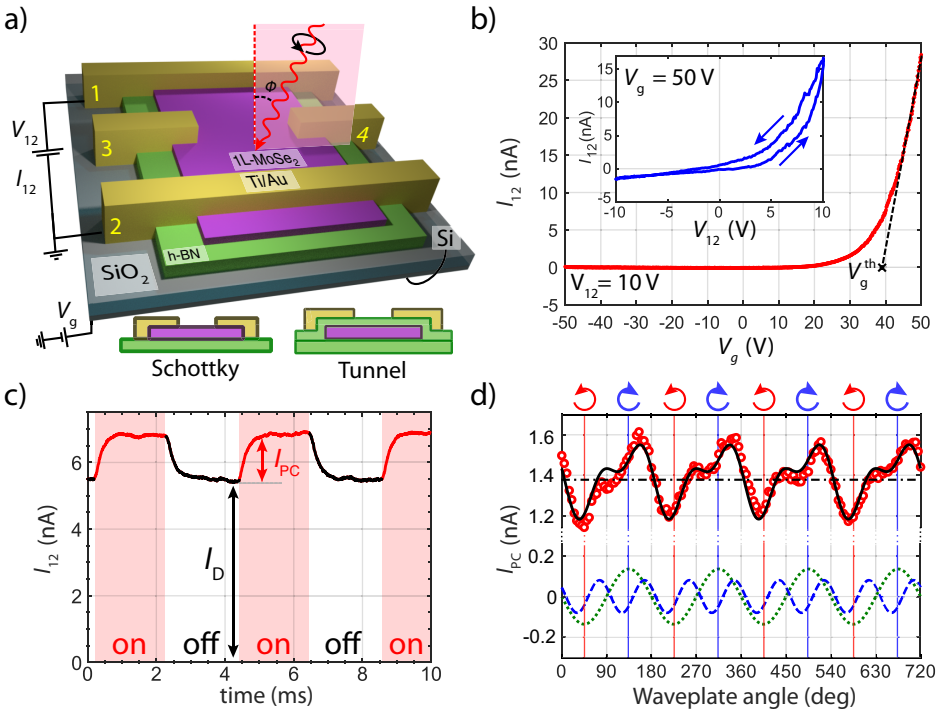


Figure 8.1: Device geometry and optoelectronic response. (a) Schematic of the device with direct metal/1L-$MoSe_2$ contacts and measurement geometry. The optical excitation is achieved by exposing the entire device to a wavelength tuneable laser source, hitting the sample at an oblique angle of incidence $\phi$. The polarization and helicity of the light excitation is selected using a $\lambda/4$ wave plate. The bottom diagrams show a side view of the two possible device geometries, either with Ti/Au Schottky contacts fabricated directly on top of the 1L-$MoSe_2$/hBN structure (left) or with a top bilayer hBN flake acting as tunnel barrier between the 1L-$MoSe_2$ and the contacts (right). (b) Two terminal transfer characteristic of the device for $V_{12} = 10$ V, showing a clear n-type behaviour. The threshold gate voltage is found to be around $V_g^{th} = 40$ V. Inset: IV characteristic measured at $V_g = 50$ V. Arrows indicate scan direction. (c) Total current $I_{12}$ along the device for $V_{12} = 10$ V and $V_g = 50$ V. When the light excitation ($\lambda = 790$ nm) is turned on, the total current along the device increases by $I_{PC} = 1.4$ nA. (d) Photocurrent $I_{PC}$ (red circles) as a function of the wave plate rotary angle $\phi$ and fitting to Eq. 8.1 (black, solid line). The discontinuous lines represent the three separate contributions indicated in Eq. 8.1, $I_0$ (black, dash-dotted line), $L\sin(4\theta + \delta)$ (blue, dashed line) and $C\sin(2\theta)$ (green, dotted line).

illumination plane (highlighted in faint red in the figure) is fixed along the direction between contacts 3 and 4.

When the light is turned on, electrons in the $MoSe_2$ valence band undergo an optical transition to the conduction band, either directly or by formation of excitons, which results in an increase in the conductivity (photoconductivity). Thus, the current flowing through the device increases by $I_{PC}$. In the measurements discussed below, $I_{PC}$ is registered using a lock-in amplifier set at the frequency of the mechanical chopper.

In a 2D-TMD phototransistors, photoconductivity can emerge from two main

coexisting mechanisms [18] [19] [20] [21] [22] [23]: photoconductive effect, where light-induced formation of electronhole pairs leads to an increased charge carrier density; and photovoltaic effect, where light-induced filling or depletion of localized states results in a shift of the Fermi energy. When the characteristic relaxation times for these localized states are very long, photovoltaic effects appear as photodoping, and the Fermi energy shift remains for a long time, or even permanently, after the optical excitation is turned off [24].

To characterize the helicity-dependent photoresponse of our device we tune the polarization of the incident light by a $\lambda/4$ wave plate. Over a 360°wave plate rotation, the light is modulated twice between left and right circular polarization. Figure 8.1(d) shows the helicity-dependent photocurrent $I_{PC}$ as a function of the angle $\theta$ of the fast axis of the wave plate with respect to the polarization axis of the incoming laser. The resulting signal $I_{PC}(\theta)$ can be phenomenologically described as

$$I_{PC}(\theta) = I_0 + C\sin(2\theta) + L\sin(4\theta + \delta) \tag{8.1}$$

Here, $I_0$, $C$, and $L$, respectively, account for the polarizationindependent, helicity-dependent, and linear polarizationdependent components of $I_{PC}$. Note that the helicity-dependent component $C\sin(2\theta)$ must be zero for $\theta = 0$ (wave plate fast axis aligned with incident polarization), which corresponds to the output bean being fully linearly polarized. In contrast, the linear polarization-dependent part $L\sin(4\theta + \delta)$ can in principle be maximal for any arbitrary angle, depending on the relative orientation of the incident light polarization and the device. Thus, a phase $\delta$ must be included in the equation. It is also worth remarking that Eq. 8.1 is purely phenomenological, and no assumption is made regarding the microscopic origin of the linear- and helicity-dependent components. In particular, $C$ can include contributions from several effects, including CPGE and CPDE

### 8.2.1. Spectral behavior of CPC

Figure 8.2 shows the spectral dependence of the polarization independent ($I_0$) and helicity-dependent ($C$) photocurrent components, measured in two-terminal configuration using contacts 1 and 2, with $V_{12} = 10$ V, $V_g = 50$ V, and $\phi = 30°$. Both $I_0$ and $C$ are peaked around $\lambda \approx 790$ nm, matching the wavelength of the 1L-$MoSe_2$ A-exciton resonance [19] [25] [26]. For off-resonance wavelengths shorter than 775 nm, $C$ becomes strongly suppressed, even when $I_0$ still remains large. This result is consistent with our earlier measurements in hBN-encapsulated devices [11] and with recent optical measurements showing that light-induced valley population imbalance under off-resonance excitation is rapidly relaxed by intervalley scattering of high-energy excited carriers [9] [27]. Therefore, resonant exciton absorption is necessary for efficient CPC generation. For excitation wavelengths longer than $\lambda \approx 825$ nm only a small polarization-independent photocurrent is observed.

### 8.2.2. Dependence of CPC on the gate voltage

Next, we investigate the effect of the gate voltage on the photocurrent. We apply gate voltages between $V_g = 50$ V and +50 V while keeping a constant drainsource voltage $V_{12} = 10$ V and illuminating the sample at $\lambda = 790$ nm and $\phi = 30°$. Figure

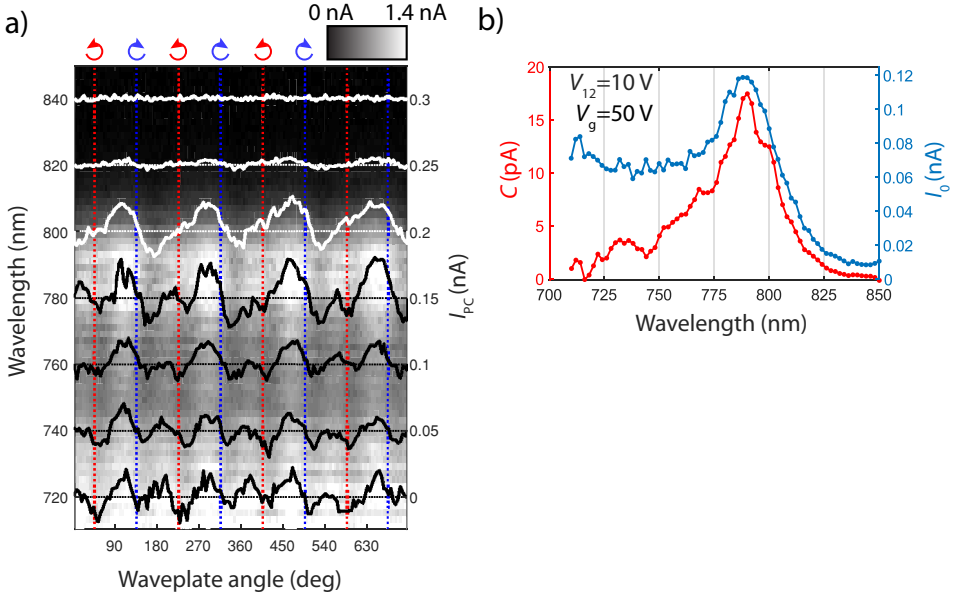


Figure 8.2: Spectral dependence of the $C$ fitting parameter for $\phi = 30°$, $V_{12} = 10$ V and $V_g = 50$ V. (a) Colormap of $I_{PC}$ as a function of the wave plate angle (x-axis) and the excitation wavelength (left axis). The gray scale in the colormap represents $I_{PC}$, and the solid lines (right axis) show individual $I_{PC}$ profiles at equispaced wavelengths between 720 and 840 nm. For clarity, the base level of these profiles has been shifted vertically in steps of 0.5 nA. (b) $I_0$ (blue, right axis) and $C$ (red, left axis) parameters, obtained from least-square fitting of Eq. 8.1 to the data shown in (a), as a function of the excitation wavelength.

8

8.3(a) shows the registered photocurrent for the device with direct metal/$MoSe_2$ contacts as a function of the incident light polarization. $I_0$, $C$, and $L$ can be extracted from fittings to Eq. 8.1 as described above. Figure 8.3(b) shows $I_0$ and $C$ as a function of the gate voltage. Both for $I_0$ and $C$, a nonzero signal can only be observed at gate voltages near to or above Vth. A similar gate dependence of photoconductivity has been earlier observed in TMD phototransistors [18] [28], and indicates that the observed photoconductivity originates mainly from the photovoltaic effect mentioned above. Thus, the effect of the gate voltage is simply to modulate the overall photoresponse of the device, but does not change the ratio between $I0$ and $C$. As shown in Figs. 8.3(b) and (c), the described behavior is observed both for samples with direct metal/$MoSe_2$ contacts and with hBN tunnel barriers. However, for the sample with tunnel contacts, a nonzero $I_0$ and $C$ can be observed even at $V_g < V_{th}$, indicating the presence of an additional contribution to photocurrent. We attribute this new contribution to an enhanced photoconductive effect in hBN-encapsulated samples [18].

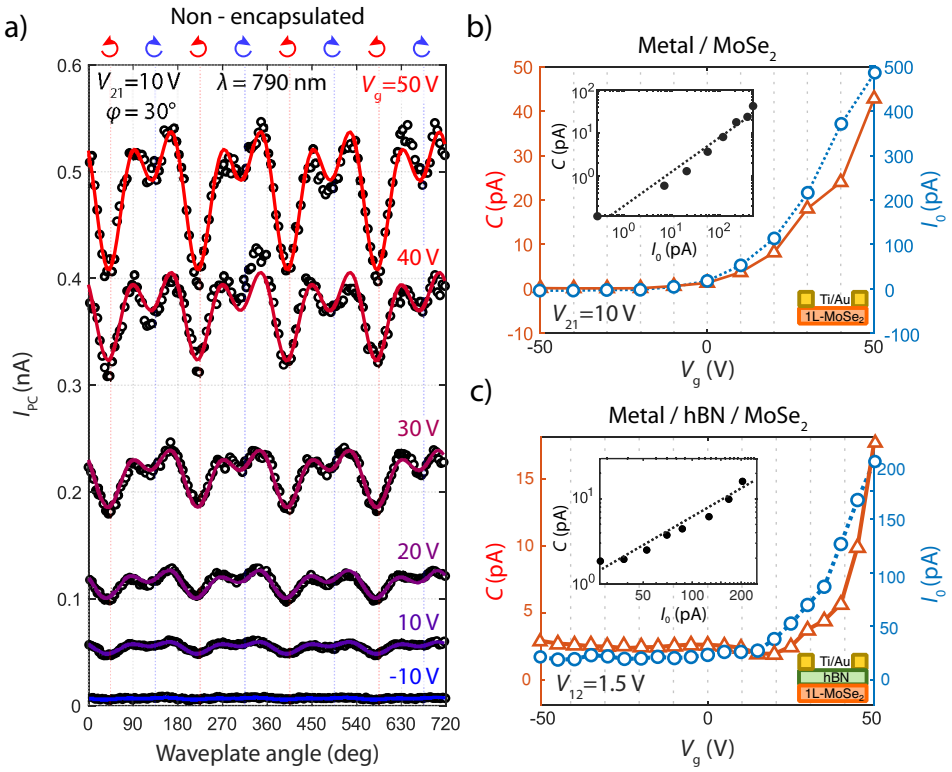


Figure 8.3: Effect of the gate voltage on the helicity-dependent photocurrent. (a) Measured photocurrent $I_{PC}$ in the non-encapsulated device for different gate voltages $V_g$, from -10 V to 50 V, as a function of the $\lambda/4$ wave plate angle. The black solid lines are least square fits of the experimental data to Eq. 8.1. (b-c) $V_g$ dependence of the $I_0$ (blue circles, right axis) and $C$ (orange triangles, left axis) photocurrent components for the non-encapsulated (b) and hBN-encapsulated (c) devices. The insets in pannels (b) and (c) show $C$ as a function of $I_0$ in logarithmic scale.

8

## 8.2.3. CPC and illumination angle of incidence

Figure 8.4(a) shows the measured photocurrent for $\lambda = 790$ nm, $V_{12} = 10$ V, and $V_g = 50$ V as a function of the wave plate angle for different illumination angles. From these measurements we extract the angle dependence of the helicity-dependent photocurrent, $C$, shown in Fig. 8.4(b). The dependence of CPC on the illumination angle allows us to extract information on the underlying physical mechanism.

As we discussed in ref. [11], CPGE cannot occur in a material with $D_{3h}$ symmetry, such as pristine 1L-$MoSe_2$, while CPDE can only give contributions proportional to $\sin(2\phi)$, which are odd upon inversion of the illumination angle $\phi$ and should cancel out for illumination normal to the crystal plane. For the device with direct metal/$MoSe_2$ contacts studied here we find that $C$ does not present even or odd parity upon inversion of the illumination angle. Furthermore, a nonzero helicity-dependent signal is observed even for normal-incidence illumination. This is in strong contrast with our results in hBN encapsulated devices (see Supplemen-

tary Note 2 and ref. [11]). For these devices, a nonzero angle of incidence is needed to generate a measurable CPC. Simple symmetry arguments can be used to show that a nonzero CPC signal at $\phi = 0°$can only appear if the symmetry of the crystal is reduced to at most a single mirror-plane symmetry [11]. Thus, our results establish that the presence of non-equivalent Schottky barriers in the vicinity of the metallic contacts results in a largely reduced symmetry of the electronic states, allowing for additional contributions to the CPC. In fact, as shown in Supplementary Note 3, we observe that the overall strength and angle dependence of the CPC varies from one set of contacts to another, further suggesting that this effect is largely affected by the local geometry near the electrodes.

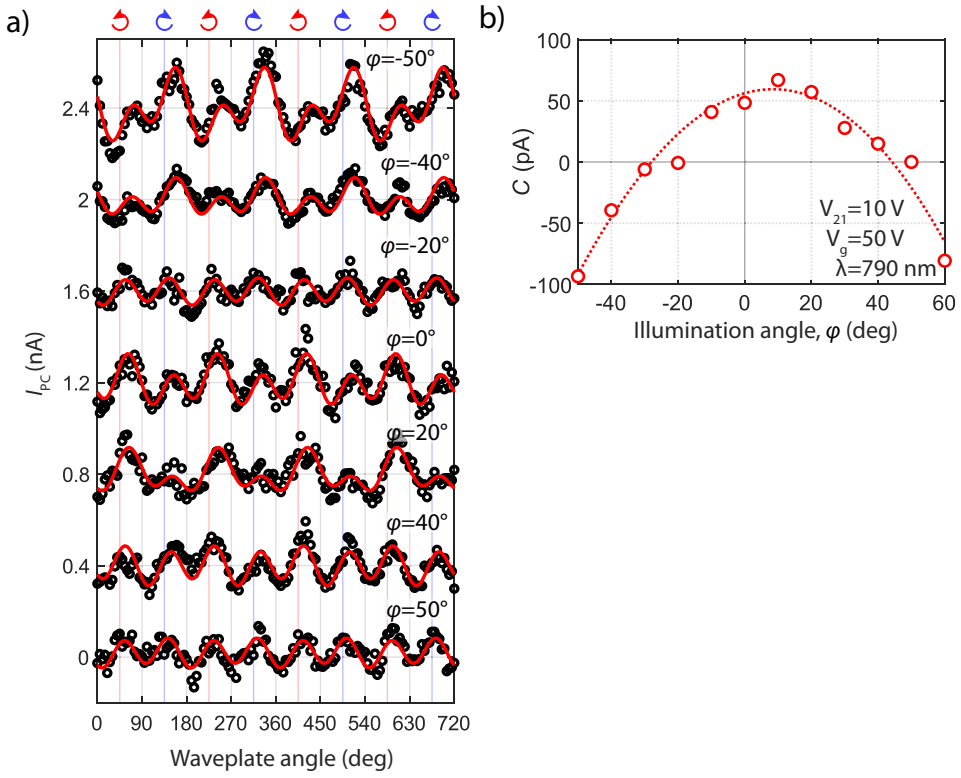


Figure 8.4: Dependence of $C$ on the illumination angle. (a) Photocurrent $I_{PC}$ for $V_{12} = 10$ V and $V_g = 50$ V as a function of the wave plate angle for different illumination angles. Dots indicate experimental data. Solid lines are fittings to Eq. 8.1. (b) Dependence of $C$ on the illumination angle, extracted from the fittings shown in (a). The dotted line is a parabolic fitting of the experimental data, shown as a guide to the eye.

### 8.2.4. Effect of the drain–source voltage on CPC

Finally, we evaluate the dependence of the CPC on the drainsource voltage. As mentioned above, for the sample without hBN tunnel barriers a nonzero bias voltage

needs to be applied in order to observe nonzero $C$ and $L$ photocurrent components. This is again in contrast with our results for hBN encapsulated devices (see Supplementary Note 2 and ref. [11]), where a clear helicity-dependent photocurrent appears even in short-circuit configuration.

When $V_{12}$ is swept, both $C$ and $L$ increase with the absolute value of $V_{ds}$. However, the sign and amplitude of $C$ depend on the angle of incidence in a nontrivial way. We also observe that $C$ and $L$ are largely dependent on the selected set of sourcedrain contacts for a fixed angle of incidence (see Supplementary Note 3). Figure 8.5 shows the dependence of $C$ and $L$ on the drainsource voltage $V_{12}$ for two different angles of incidence ($\phi = +50°$and $\phi = +50°$). For $+50°$a nonzero helicity-dependent photocurrent $C$ is clearly observed for positive drain source voltages $V_{12}$, increasing monotonically with the applied voltage (see Fig. 8.5(c)). For negative voltages a smaller but measurable $C$ is observed. Intriguingly, the sign of $C$ is preserved when changing the sign of the drainsource voltage. However, when the illumination angle is inverted from $50°$to $50°$the sign of $C$ flips from positive to negative, and a large signal is only observed for negative $V_{12}$ (Fig. 8.5(c)). It is worth noting that the behavior described here is only valid for a specific set of contacts in the device and changes in a nontrivial way with the angle of incidence. Vds-dependent measurements for additional contacts and illumination angles can be found in Supplementary Note 3. The fact that $C$ and $L$ modulate differently with the drainsource voltage for different sets of contacts is consistent with our hypothesis, i.e., that the presence of nonhomogeneous Schottky barriers alters the symmetry of electronic states and thus enables additional contributions to the CPC, largely affecting the total measured CPC signal.

## 8.3. Discussion

In a seminal theory work [29], Moore and Orenstein showed that the presence of a nonzero Berry curvature in a 2D system can lead to the emergence of CPGE under illumination normal to the crystal symmetry of this CPC is compatible with contributions from Berry curvature-induced CPGE, the observed signal could also be explained by the emergence of helicity-dependent photovoltaic effects near the metal$MoSe_2$ interfaces.

As discussed in earlier literature [11], a nonzero CPC under normal incidence illumination such as the one shown here is only possible for a device with, at most, a single mirror-plane symmetry. Indeed, we observe that when an hBN tunnel barrier is inserted between the contacts and the 2D channel, the CPC signal upon normal illumination disappears. This indicates that the presence of strong electric fields at the Schottky contacts plays an important role in reducing the symmetry of the $MoSe_2$ channel, enabling additional contributions to CPC. The particularities of the electric field profile in the vicinity of a specific metalsemiconductor contact strongly influence the measured signal, resulting in the observed contact dependent CPC.

Importantly, earlier measurements on helicity-dependent photoresponse carried out in 1L-TMD devices with direct metalsemiconductor contacts could also show contributions caused by a symmetry reduction near the contacts. For example, for the valley-Hall effect [16], N. Ubrig et al. recently showed that the helicity-dependent

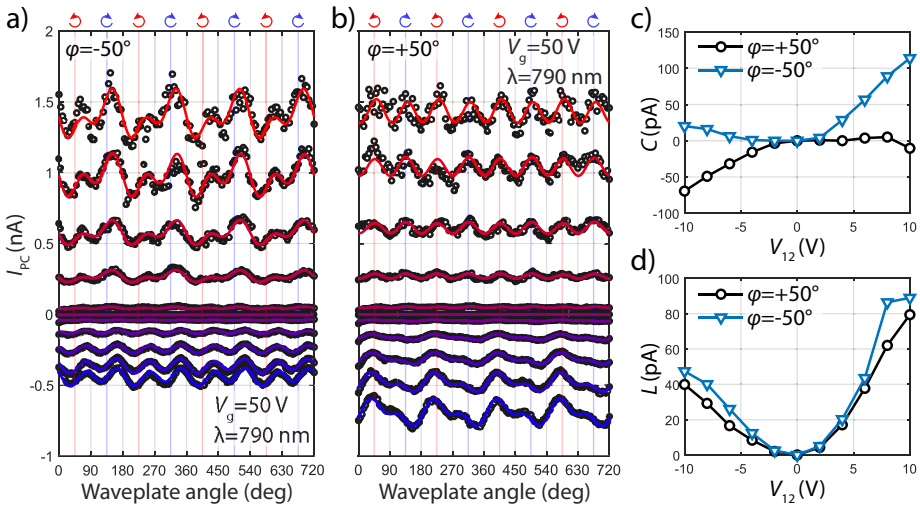


Figure 8.5: Dependence of $C$ and $L$ on the drain source voltage. (a-b) Photocurrent $I_{PC}$ as a function of the wave plate angle for different drain-source voltages $V_{12}$ between -10 V (blue) and +10 V (red), for a light incidence angles $\phi = +50°$ (a) and $\phi = +50°$ (b). Dots indicate experimental data. Solid lines are fittings to Eq. 8.1. (c-d) Dependence of $C$ (c) and $L$ (d) on the drain source voltage, extracted from the fittings shown in (a) and (b).

signal is strongly modified when the vicinity of the electrodes is exposed to light [13], which could be caused by a contact-induced symmetry breaking. In light of our measurements, inserting few-layer hBN as tunnel barrier between the semiconductor channel and the metallic contacts minimizes possible effects of Schottky barriers on the device photoresponse, granting access to the intrinsic properties of a 2D-TMD. In particular, for devices with hBN tunnel barriers the CPGE cancels out for normal incidence, as expected from the crystal symmetry.

Our results also show that CPCs can be very largely and nontrivially modulated by the illumination angle, even for incidence angles as small as 10°. However, most reports on helicity-dependent optoelectronic measurements rely on high numerical aperture objectives to focus the laser beam onto a small area of the sample. While this method has the advantage of granting micrometer spatial resolution, it comes at the price of losing resolution on the illumination angle, as the measured photoresponse will be averaged over a broad range of angles. Thus, in order to obtain a complete microscopic understanding of the helicity-dependent optoelectronic response of 2D-TMD devices, spatially resolved experiments should be used in combination with angle-resolved measurements. We envision that the symmetry-breaking generated by Schottky contacts can also be used for engineering of CPC in 2D-TMD phototransistors, opening up possibilities to tuning the photoresponse for circularly polarized light at particular incident angles for angular-resolved photodetectors.

# 8.4. Appendices

## 8.4.1. Supplementary note 1: Optical and AFM images of the device

In this section we focus on the fabrication of the non-encapsulated device. We address the reader to the methods section in the main text and the supplementary information of Ref. [1] for details on the fabrication of the hBN encapsulated device. Supplementary Figs. 8.6(a) and 8.6(b) show an optical micrograph and an AFM image of the $MoSe_2$/hBN heterostructure prior to contact fabrication. The $MoSe_2$ crystal presents monolayer and a three-layer regions and is cracked into 5 separate regions. The leftmost part of the crystal consists of a uniform monolayer. Supplementary Fig. 8.7(a) shows an optical image of the final device after contact fabrication. Electrodes 1 to 4 are numbered accordingly with Fig. 8.1(a) in the main text.

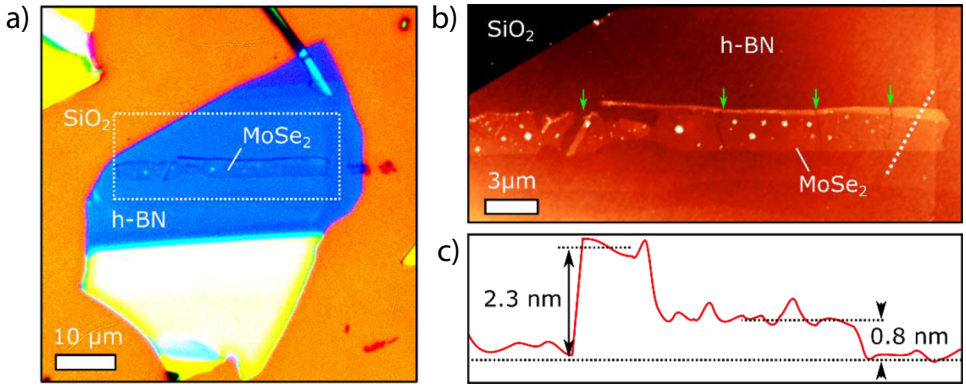


Figure 8.6: (a) Enhanced-contrast optical microscope image of the $MoSe_2$ flake transferred on top of a few nm thick hBN. (b) Tapping-mode AFM image of the region marked in (a). The $MoSe_2$ flake presents a series of cracks that split in in separate regions (indicated by green arrows in the figure). The leftmost region in the figure is a homogeneous monolayer, while the other four regions contain both monolayer and 3-layer $MoSe_2$ (c) Single AFM scan across the dashed white line indicated in (b), showing the monolayer (0.8 nm) and three-layer (2.3 nm) regions.



## 8.4.2. Supplementary note 2: Additional CPC measurements in the hBN encapsulated device

In this section we present additional measurements in the hBN encapsulated monolayer $MoSe_2$ device. Supplementary Fig. 8.7(b) shows a two-terminal IV-characteristic of the device, and Supplementary Figs. 8.8(a) and (c) show the helicity-dependent photocurrent measured in the hBN-encapsulated device with tunnel contacts as a function of the drain-source voltage, for $\lambda = 790$ nm and $\phi = +20°$. Differently from the device with direct metal/$MoSe_2$ contacts shown in the main text, here we observe a nonzero $C$-component at $V_{ds} = 0$ V, even when the polarization-independent component $I_0$ cancels out for this drain-source voltage.

As shown in Supplementary Fig. 8.8(b), the helicity-dependent component of the photocurrent for the encapsulated sample is strongly dependent on the illumination

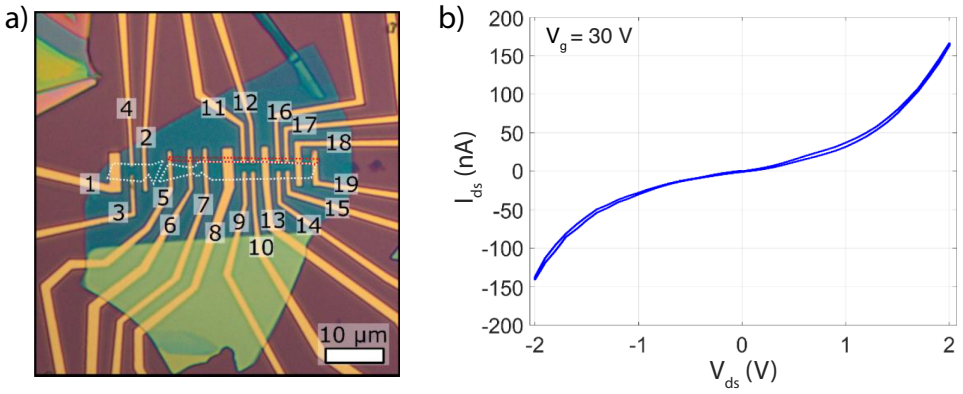


Figure 8.7: (a) Optical image of the non-encapsulated $MoSe_2$ device. The white and red dashed lines indicate the positions of the 1L and 3L-$MoSe_2$ flake regions, respectively. Contacts 1, 2, 3 and 4 are numbered accordingly with the schematic representation of Fig. 8.1(a) in the main text. (b) IV-characteristic of the hBN encapsulated $MoSe_2$ device.

angle $\phi$. In contrast with the non-encapsulated sample, here we observe that at normal incidence ($\phi = 0$) the helicity dependent component cancels out, and only a helicity-independent photocurrent is observed.

### 8.4.3. Supplementary note 3: Additional CPC measurements in the non-encapsulated device

The results shown in the main text are obtained using two specific contacts (number 1 and 2). To examine the role of the contacts in these measurements, similar measurements were performed using another pair of contacts. In this section, the results obtained using contact 14 and 15 (see Supplementary Fig. 8.7) are presented.



#### Spectral measurements in different contacts

As shown in Supplementary Figs. 8.6 and 8.7(a), the device with direct metal-semiconductor contacts is not fully homogeneous, and also contains a three-layer part. Supplementary Fig. 8.9 shows the spectral dependence of the $I_0$, $C$- and $L$-components of $I_{PC}$ when using contacts 16 and 17 (see Supplementary Fig. 8.7(a)) as drain and source. For this situation the device response is mainly dominated by the three-layer region, and the spectral dependence of the $C$ parameter markedly changes with respect to the one shown in the main text.

As shown in Supplementary Fig. 8.9(c) and (d), when we repeat again the spectral measurement using a source contact placed at the three-layer region (contact 16) and a drain contact placed at the single-layer region (contact 14), we recover the spectral behavior described in the main text, i.e. the $C$-component becomes maximal at $\lambda$=790 nm, on resonance with the A exciton transition, and drastically decreases for lower wavelengths, even when $I_0$ and $L$ remain large.

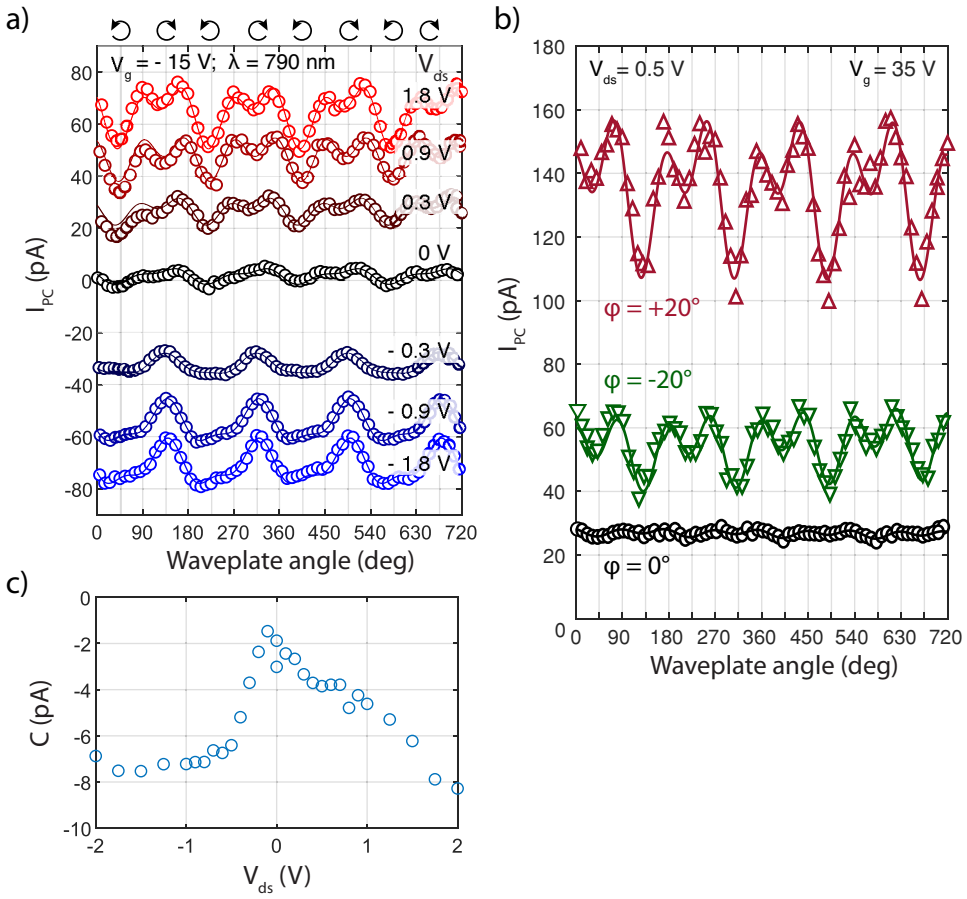


Figure 8.8: (a) Photocurrent $I_{PC}$ as a function of the wave plate angle for different drain source voltages $V_{ds}$ between 1.8 V (blue) and +1.8 V (red), for a light incidence angle $\phi = +20°$ Solid lines are fit s to Eq. 8.1. (c) Dependence of $C$ on the drain-source voltage, extracted from the fittings shown in (a). (c) Photocurrent $I_{PC}$ as a function of the wave plate angle for three different light incidence angles: $\phi = +20°$ (maroon upward triangles), $\phi = 0°$ (black circles) and $\phi = -20°$ (green downward). Solid lines are fits to Eq. 8.1.

### Dependence of CPC on the gate voltage

Similar to section 4 in the main text, gate dependent measurements are performed. We apply gate voltages between $_g$=0 V and 50 V with steps of 5 V while keeping the drain source voltage constant ($V_{ds}$ = 10 V). The sample is illuminated at $\lambda$=790 nm at an incidence angle of $\phi$=50°. The resulting photocurrent is monitored while rotating the quarter-wave plate by two full rotations, as shown in Supplementary Fig. 8.10. This allows us to more accurately remove drift effects. Subsequently, $I_0$, $C$, and $L$ are extracted by fitting the data to Eq. 8.1 in the main text.

In the main text we observe a monotonic increase of the $I_0$, $C$-, and $L$-component with increasing gate voltage, where the ratio of the $L$ and $C$-component stay con-

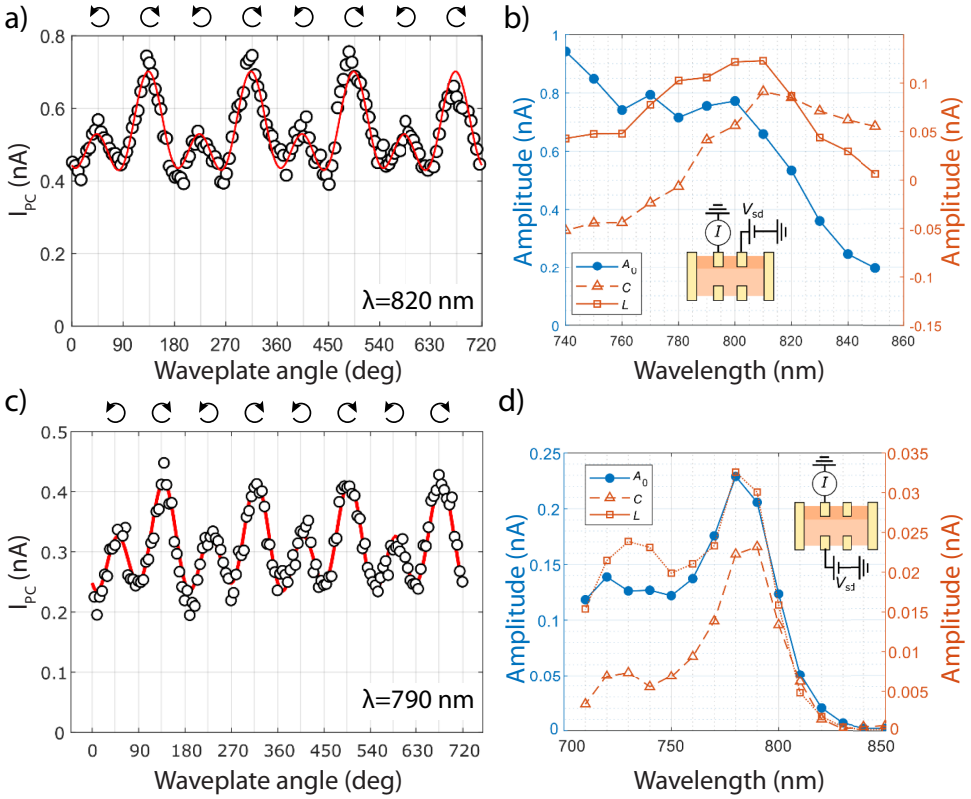


Figure 8.9: Helicity-dependent spectra for contacts 16 and 17: (a) and (b), and contacts 16 and 14: (c) and (d). (a) and (c) depict the photocurrent $I_{PC}$ as a function of the wave plate angle for $\lambda$=820 nm and 790 nm, respectively, and $V_{ds} = 5$ V and $V_g = 50$ V. The red line is a fitting to Eq. 8.1 in the main text. (b) and (d) show the spectral dependence of the $A_0$ (blue filled circles; left axis), $C$ (orange empty squares; right axis) and $L$ (orange empty triangles; right axis) parameters extracted from fittings to Eq. 8.1. The insets in (b) and (d) show a schematic drawing of the device and measurement geometry.



stant. Here we observe a similar gate voltage dependence. Again, the magnitude of all three components increases monotonically with the gate voltage. Note that the sign difference of the components compared to the main text is due to a 180° phase shift during the fitting. These results show that the gate voltage dependence of $C$ is similar for different contacts.

The ratio between the $L$ and $C$-component however, does change upon switching to the different set of contacts. Contrary to the results depicted in the main text, we observe a change in the ratio of the $C$- and $L$-components for different $V_g$ which indicates that the specific ratio of the $C$- and $L$-component is dependent on the set of contacts used.

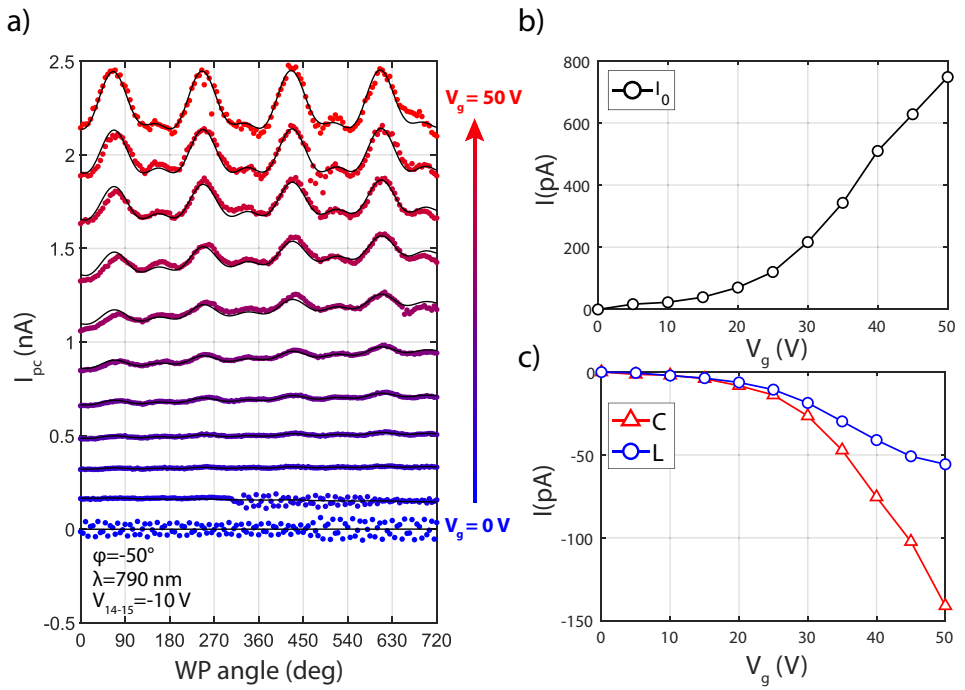


Figure 8.10: Gate dependent photocurrent measurements at an incidence angle of 50° and a $V_{ds}$ of 10 V. The corresponding $I_0$, $C$-, and $L$-component, obtained by fitting to Eq. 8.1, are plotted at the right.

### CPC and illumination angle

Similar to section 5 in the main text, incidence angle dependent measurements were performed, ranging from $\phi = 60°$ to 60°. Both the drain source voltage and the gate voltage are kept constant at $V_{ds}$ = -10 V and 50 V, respectively. As before, the sample is excited by a continuous wave laser with a wavelength of $\lambda$=790 nm. The resulting photocurrent is measured while modulating the polarization of the light using a rotatable quarter-wave plate. Supplementary Fig. 8.11(a) shows the PC measurements obtained for the different incident angles. The extracted $C$-component from these measurements are depicted in Supplementary Fig. 8.11(b). As before, we observe a large dependence of $C$ on the incidence angle with both even and odd components upon reversing the incidence angle.

However, comparing Supplementary Fig. 8.11(b) to Fig. 8.4(b) in the main text, we see distinct differences. In the main text, we observe a maximum $C$-component at and incidence angle of $\phi = 10°$. Here, however, $C$ is maximized at $\phi = 30°$ and shows a larger magnitude compared to the $C$-component at $\phi = 10°$ in the main text. Similar those measurements, a small nonzero $C$-component is obtained at normal incidence ($\phi = 0°$).

The fact that we see distinct differences for different sets of contacts is in line with our assumption that non-homogeneous Schottky barriers in the vicinity of the

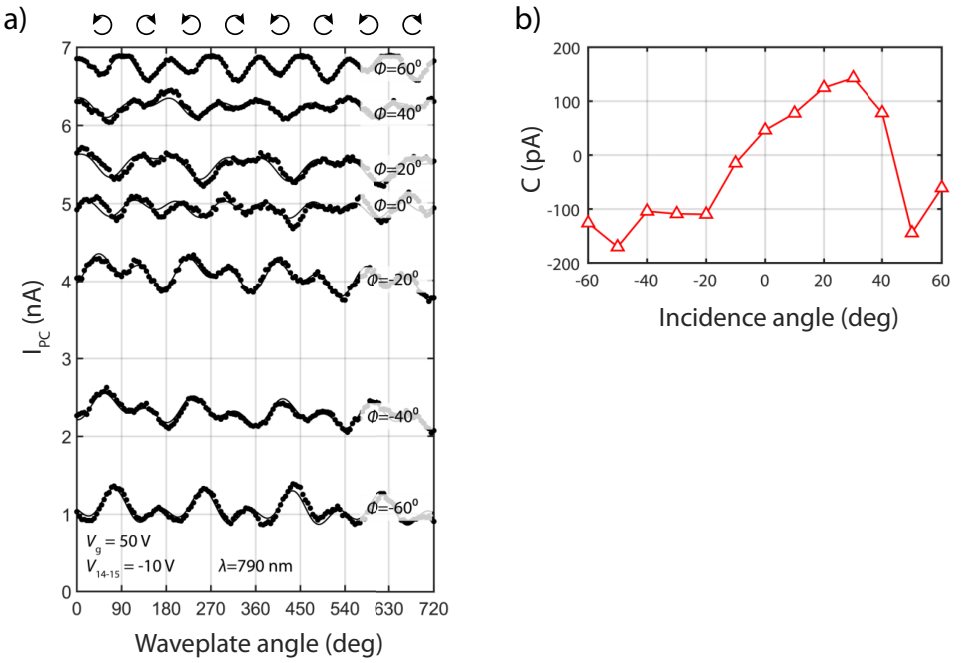


Figure 8.11: Dependence of $C$ on the incidence angle. (a) Photocurrent $I_{PC}$ for $V_{ds}$= 10 V and $V_g$= 50 V as a function of the wave plate angle for different incidence angles. Dots indicate experimental data. Solid lines are fittings to Eq. 8.1. (b) Dependence of $C$ on the incidence angle, extracted from the fittings shown in (a).

metallic contacts play a significant role in these measurements as different contacts are likely to have different Schottky barriers, a different behavior is expected.

8

### Effect of the drain-source voltage on CPC

Next, the drain-source voltage on the CPC is investigated. As before, we illuminate the sample at $\lambda$=790 nm and apply a constant gate voltage of $V_g$= 50 V. We measure the photocurrent while rotating a quarter-wave plate for different drain source voltages (ranging from -10 V to 10 V with steps of 2 V). Two opposite incidence angles of $\phi = 50°$ and 50°, were chosen, as these angles showed a large CPC during the previous incidence-angle dependent measurement (Supplementary Fig. 8.11(b)).

Supplementary Fig. 8.12 shows the dependence of $C$ and $L$ on the drain-source voltage. The $C$-components obtained for $\phi = 50°$ and $\phi = 50°$ are comparable for both negative and positive drain-source voltages. This illustrates once more that a net nonzero $C$-component can be observed when i.e. large N.A. objectives are used to focus down the light. Compared to Fig. 8.5 in the main text, the difference between the $C$-components of the opposite incidence angles is smaller. Furthermore, the $V_{ds}$-dependence on $C$ is significantly different compared to Fig. 8.5 in the main text. There, a large positive $C$-component is obtained at positive $V_{ds}$ at negative incidence angles, while the measurements here show a $C$-component close to zero.

Vice versa, at negative $V_{ds}$, a large and negative $C$-component is obtained here for negative incidence angles, while in the main text it is close to zero. At positive incidence angles, the differences are smaller. For this set of contacts, we observe a monotonic decrease of the $C$-component with decreasing $V_{ds}$ up to -10 V. This is in contrast to the $C$-component at $\phi = 50°$ shown in Fig. 8.5.

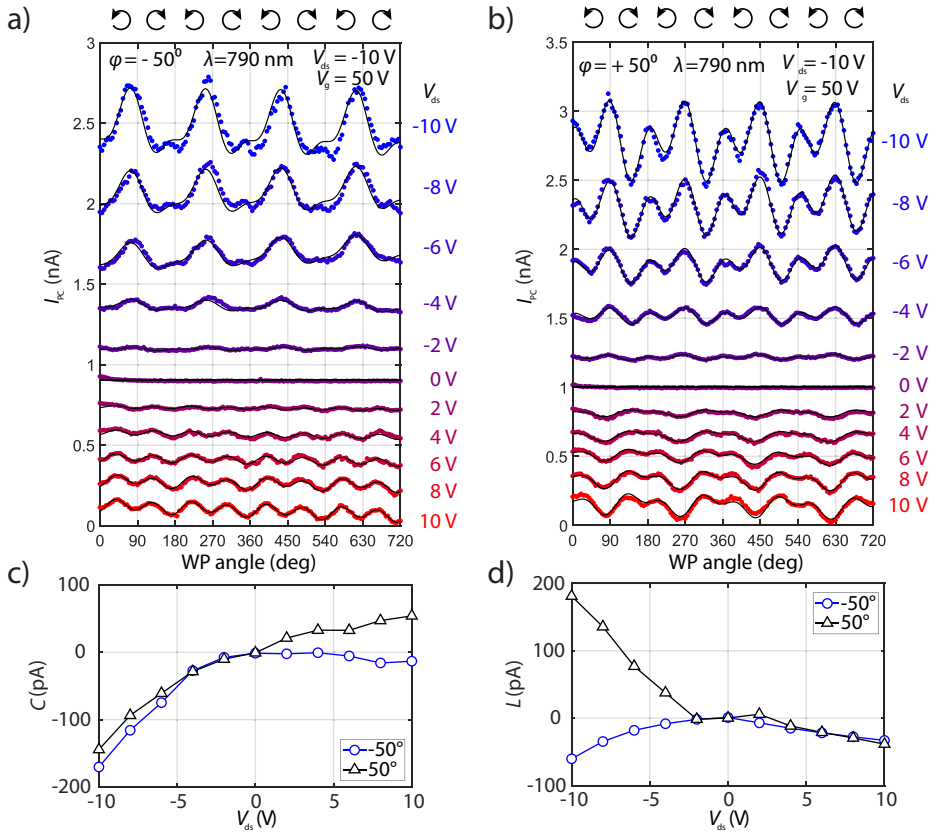


Figure 8.12: Dependence of $C$ and $L$ on the drain source voltage. (a-b) Photocurrent $I_{PC}$ as a function of the wave plate angle for different drain source voltages $V_{ds}$ between 10 V (blue) and +10 V (red), for a light incidence angles (a) $\phi = -50°$ and (b) $\phi = 50°$. Dots indicate experimental data. Solid lines are fittings to Eq. 8.1. (c-d) Dependence of (c) $C$ and (d) $L$ on the drain source voltage, extracted from the fittings shown in (a) and (b).

This shows that, similar to the angle of incidence dependence, the CPC dependence on the $V_{ds}$ is largely influenced by the set of contacts used. Therefore, we conclude that the Schottky barriers at the contacts play an important role in both the magnitude and overall behavior of these signals. The $L$-components obtained for the opposite incidence angles overlap to a larger extent. However, where the $L$-component in the main text shows a symmetric response around $V_{ds}$= 0 V, an asymmetric response is obtained here. At positive $V_{ds}$, the $L$-component increases almost linearly, while at negative $V_{ds}$ a nonlinear decrease is observed for both

incidence angles.

# Bibliography


[1] M. M. Furchi, F. Höller, L. Dobusch, D. K. Polyushkin, S. Schuler, and T. Mueller, "Device physics of van der Waals heterojunction solar cells", npj 2D Materials and Applications **2**, 3 (2018).

[2] F. H. L. Koppens, T. Mueller, P. Avouris, A. C. Ferrari, M. S. Vitiello, and M. Polini, "Photodetectors based on graphene, other two-dimensional materials and hybrid systems", Nature Nanotechnology **9**, 780–793 (2014).

[3] O. Lopez-Sanchez, D. Lembke, M. Kayci, A. Radenovic, and A. Kis, "Ultrasensitive photodetectors based on monolayer MoS2", Nature Nanotechnology **8**, 497–501 (2013).

[4] M. M. Furchi, A. Pospischil, F. Libisch, J. Burgdörfer, and T. Mueller, "Photovoltaic Effect in an Electrically Tunable van der Waals Heterojunction", Nano Letters **14**, 4785–4791 (2014).

[5] D. J. Groenendijk, M. Buscema, G. A. Steele, S. Michaelis de Vasconcellos, R. Bratschitsch, H. S. J. van der Zant, and A. Castellanos-Gomez, "Photovoltaic and Photothermoelectric Effect in a Double-Gated WSe2 Device", Nano Letters **14**, 5846–5852 (2014).

[6] D. Ansell, I. P. Radko, Z. Han, F. J. Rodriguez, S. I. Bozhevolnyi, and A. N. Grigorenko, "Hybrid graphene plasmonic waveguide modulators", Nature Communications **6**, 8846 (2015).

[7] G. Konstantatos and E. H. Sargent, "Nanostructured materials for photon detection", Nature Nanotechnology **5**, 391–400 (2010).

[8] D. Xiao, G.-B. Liu, W. Feng, X. Xu, and W. Yao, "Coupled Spin and Valley Physics in Monolayers of MoS2 and Other Group-VI Dichalcogenides", Physical Review Letters **108**, 196802 (2012).

[9] K. F. Mak, K. He, J. Shan, and T. F. Heinz, "Control of valley polarization in monolayer MoS2 by optical helicity", Nature Nanotechnology **7**, 494–498 (2012).

[10] M. Eginligil, B. Cao, Z. Wang, X. Shen, C. Cong, J. Shang, C. Soci, and T. Yu, "Dichroic spinvalley photocurrent in monolayer molybdenum disulphide", Nature Communications **6**, 7636 (2015).

[11] J. Quereda, T. S. Ghiasi, J.-S. You, J. van den Brink, B. J. van Wees, and C. H. van der Wal, "Symmetry regimes for circular photocurrents in monolayer MoSe2", Nature Communications **9**, 3346 (2018).

[12] H. Yuan, X. Wang, B. Lian, H. Zhang, X. Fang, B. Shen, G. Xu, Y. Xu, S.-C. Zhang, H. Y. Hwang, and Y. Cui, "Generation and electric control of spinvalley-coupled circular photogalvanic current in WSe2", Nature Nanotechnology **9**, 851–857 (2014).

[13] N. Ubrig, S. Jo, M. Philippi, D. Costanzo, H. Berger, A. B. Kuzmenko, and A. F. Morpurgo, "Microscopic Origin of the Valley Hall Effect in Transition Metal Dichalcogenides Revealed by Wavelength-Dependent Mapping", Nano Letters **17**, 5719–5725 (2017).

[14] T. S. Ghiasi, J. Quereda, and B. J. van Wees, "Bilayer h-BN barriers for tunneling contacts in fully-encapsulated monolayer MoSe2 field-effect transistors", 2D Materials **6**, 015002 (2018).

[15] G. Pande, J.-y. Siao, W.-L. Chen, C.-j. Lee, R. Sankar, Y.-M. Chang, C.-d. Chen, W.-h. Chang, F.-c. Chou, and M.-t. Lin, "Ultralow Schottky Barriers in Hexagonal Boron Nitride-Encapsulated Monolayer WSe2 Tunnel Field-Effect Transistors", ACS Applied Materials & Interfaces **12**, 18667–18673 (2020).

[16] K. F. Mak, K. L. McGill, J. Park, and P. L. McEuen, "The valley Hall effect in MoS2 transistors", Science **344**, 1489–1492 (2014).

[17] P. J. Zomer, M. H. D. Guimarães, J. C. Brant, N. Tombros, and B. J. van Wees, "Fast pick up technique for high quality heterostructures of bilayer graphene and hexagonal boron nitride", Applied Physics Letters **105**, 013101 (2014).

[18] M. M. Furchi, D. K. Polyushkin, A. Pospischil, and T. Mueller, "Mechanisms of Photoconductivity in Atomically Thin MoS2", Nano Letters **14**, 6165–6170 (2014).

[19] J. Quereda, T. S. Ghiasi, F. A. van Zwol, C. H. van der Wal, and B. J. van Wees, "Observation of bright and dark exciton transitions in monolayer MoSe2 by photocurrent spectroscopy", 2D Materials **5**, 015004 (2017).

[20] B. Miller, E. Parzinger, A. Vernickel, A. W. Holleitner, and U. Wurstbauer, "Photogating of mono- and few-layer MoS2", Applied Physics Letters **106**, 122103 (2015).

[21] J. O. Island, S. I. Blanter, M. Buscema, H. S. J. van der Zant, and A. Castellanos-Gomez, "Gate Controlled Photocurrent Generation Mechanisms in High-Gain In2Se3 Phototransistors", Nano Letters **15**, 7853–7858 (2015).

[22] H. Fang and W. Hu, "Photogating in Low Dimensional Photodetectors", Advanced Science **4**, 1700323 (2017).

[23] H. Huang, J. Wang, W. Hu, L. Liao, P. Wang, X. Wang, F. Gong, Y. Chen, G. Wu, W. Luo, H. Shen, T. Lin, J. Sun, X. Meng, X. Chen, and J. Chu, "Highly sensitive visible to infrared MoTe2 photodetectors enhanced by the photogating effect", Nanotechnology **27**, 445201 (2016).

[24] J. Quereda, T. S. Ghiasi, C. H. van der Wal, and B. J. van Wees, "Semiconductor channel-mediated photodoping in h-BN encapsulated monolayer MoSe2 phototransistors", 2D Materials **6**, 025040 (2019).

[25] J. S. Ross, S. Wu, H. Yu, N. J. Ghimire, A. M. Jones, G. Aivazian, J. Yan, D. G. Mandrus, D. Xiao, W. Yao, and X. Xu, "Electrical control of neutral and charged excitons in a monolayer semiconductor", Nature Communications **4**, 1474 (2013).

[26] R. Frisenda, Y. Niu, P. Gant, A. J. Molina-Mendoza, R. Schmidt, R. Bratschitsch, J. Liu, L. Fu, D. Dumcenco, A. Kis, D. P. De Lara, and A. Castellanos-Gomez, "Micro-reflectance and transmittance spectroscopy: a versatile and powerful tool to characterize 2D materials", Journal of Physics D: Applied Physics **50**, 074002 (2017).

[27] G. Kioseoglou, A. T. Hanbicki, M. Currie, A. L. Friedman, D. Gunlycke, and B. T. Jonker, "Valley polarization and intervalley scattering in monolayer MoS2", Applied Physics Letters **101**, 221907 (2012).

[28] D. Vaquero, V. Clericò, J. Salvador-Sánchez, A. Martín-Ramos, E. Díaz, F. Domínguez-Adame, Y. M. Meziani, E. Diez, and J. Quereda, "Excitons, trions and Rydberg states in monolayer MoS2 revealed by low-temperature photocurrent spectroscopy", Communications Physics **3**, 194 (2020).

[29] J. E. Moore and J. Orenstein, "Confinement-Induced Berry Phase and Helicity-Dependent Photocurrents", Physical Review Letters **105**, 026805 (2010).

# chapter 9

## Conclusions

*In this final chapter, the conclusions drawn from the research presented in this thesis are highlighted and put in perspective. The chapter ends with an outlook on future research directions worth pursuing to shed light on the most pertinent unanswered questions in the field of spin-orbit torques and photocurrent generation in 2D van der Waals materials.*

## 9.1. Conclusions

This thesis comprised of experimental work on two distinct research areas, namely spin-orbit torques and optoelectronics. While distinct, they both share the same material platform, namely 2D van der Waals materials. Below, I will first conclude the work on spin-orbit torques, and finish with a discussion on the work regarding optoelectronics.

Even after years of intensive research, the main unresolved problem in the field of SOTs still is the understanding of the different microscopic mechanisms underlying the SOTs, and the subsequent control of their magnitude and relative ratios. During the research period of this thesis, the simple picture where the only two relevant effects, the SHE and the REE, resulted in a damping- and field-like torque, respectively, started to dismantle. The review of the field of SOTs in TMD/Py heterostructures presented in Chapter 4 showed that theoretical reports indicate that other mechanisms might be at play, and highlights contradictory observations in experimental work which do not fit this simple picture [1]. To shed more light on the underlying mechanisms, we therefore performed thickness-dependent measurements in Chapter 5, allowing one to distinguish bulk effects from interfacial effects in $WSe_2$/Py bilayers [2]. We observed a strong field-like torque with no clear thickness dependence, suggesting an interfacial origin, and no clear damping-like torque. This observation is inline with theoretical predictions for interfacial effects such as the REE, and matches experimental reports of torques observed in $WSe_2$/CoFeB samples by Shao et al. [3]. The strong field-like torque, together with the atomically sharp interface observed in STEM measurements and the induced magnetic anisotropy in Py aligned with the arm-chair direction of the $WSe_2$, indicate that the clean interface facilitates the strong interactions between the $WSe_2$ and Py in our devices, and therefore, is of paramount importance for efficient SOTs. The field-dependence on the B-component from our second-harmonic Hall measurements could not be explained by the presence of a damping-like torque, and thus indicates that other effect are at play (e.g. unidirectional magnetoresistance from electron-magnon scattering, ordinary Nernst effects, etc.). Therefore, an extension of the theoretical work from Hayashi et al. [4] is needed to incorporate these effects, allowing for a more accurate determination of the damping-like torques using the harmonic Hall technique. An approach to determine which "spurious" effect are at play in these devices, is to perform SOT measurements using different characterization techniques concurrently, such as ST-FMR, MOKE, and harmonic Hall measurements [5].

Additionally, Chapter 6 has shown that the self-torque in the FM layer can be of similar magnitude to the torques reported in TMD/FM bilayers, which are often ascribed to the presence of the TMD layer. Together with recent reports on strong self-torques in 2D van der Waals ferromagnets, this increases the demand for self-torque characterization before the origins of torques in more complicated stacks, made solely from 2D van der Waals materials, can be properly interpreted [6–8]. Gaining more insight on the effect of the FM layer is of crucial importance for an accurate determination of the torque origin. Instead of comparing bilayers with different TMDs having the same FM layer, studies should be performed on bilayers

where the FM is changed rather than the TMD layer. This could shed more light on the exact role of the FM layer in these devices and might enable us to tailor the self-torque in the FM layer to work in conjunction with torques stemming from the TMD layer.

The recently developed phase-engineering techniques for TMDs have mainly been used to show the potential benefit in electrical performance (higher mobility, lower Schottky barrier, high on-off ratio) of TMD-based devices [9]. Only a few reports show the effects on the optoelectrical response, with no reports performing scanning photocurrent measurements [10]. In Chapter 7, we performed a phase-engineering technique based on laser irradiation, allowing us to change the crystallographic phase of a semiconducting 2H $MoTe_2$ flake to the metallic 1T' phase locally, before evaporating the Ti/Au electrodes. Using scanning photocurrent measurements, we are able to clearly show that the optoelectonic response stems from the 2H/1T' junction rather than from the Ti/Au contacts, and was ascribed to a Schottky barrier at this junction. Using the phase-changed region to contact the 2H $MoTe_2$ showed a significant increase in the response time of the device, compared to directly contacting the 2H $MoTe_2$. Other materials, such as black phosphorus or stacks of multiple van der Waals materials, have shown better performance (higher responsivity, faster response times) compared to our device [11, 12]. Nevertheless, we have shown that these phase-engineering techniques might allow for further optimization of these devices, potentially enabling more sensitive and faster photodetectors.

Apart from causing a simple optoelectronic response, we show in Chapter 8 that the Schottky barrier present at the Ti/Au-TMD interface breaks the $D_{3h}$ symmetry of a 2H $MoSe_2$ device, allowing for a helicity-dependent photocurrent to be measured. By comparing the optoelectronic response of $MoSe_2$ devices with and without a hBN tunnel barrier, we show that the presence of a strong E-field from the Schottky barrier gives additional contributions to the helicity-dependent photocurrent, allowing for a non-zero helicity-dependent photocurrent under normal incidence. Inserting a few-layer hBN tunnel barrier between the semiconducting TMD channel and the metallic electrodes minimizes possible effects of Schottky barriers on the device photoresponse. Additionally, performing phase-change techniques to reduce the Schottky barrier between the Ti/Au electrodes and the TMD, as presented in Chapter 7, grants access to the intrinsic properties of the TMD.



## 9.2. Outlook

### 9.2.1. Spin-orbit torques

#### Interfacial damping-like torques

To elucidate the role of impurity induced damping-like SOTs in FM/HM devices [13, 14], and possibly use them in our advantage, Zollner et al. propose the fabrication of a double proximitized graphene device, in $Cr_2Ge_2Te_6$/graphene/$WS_2$ device [14]. In their theoretical work, they show that a damping-like torque can be generated by skew scattering of spin-independent potential barriers or impurities due to proximity induced spin-orbit coupling and an out-of-plane spin texture in graphene. In addition, they predict that the ratio of the damping- and field-like torque can

be controlled via combined top and bottom gates. Experimentally verifying these predictions would shed light on whether spin-independent impurities can generate these interfacial damping-like torques, and might provide new ways to increase the SOT efficiency.

### Crystal symmetry dependence

The observation of a damping-like torque in $WTe_2$/Py samples by MacNeill et al. from 2017 still remains one of the most compelling works on the relation between the crystal symmetry of van der Waals materials and the allowed SOTs [15]. To follow up on this work, local phase-transformations techniques in $MoTe_2$, as discussed in Chapter 7, allow one to reduce the symmetry of half of a $MoTe_2$ crystal, from a highly symmetric 2H phase to a lower symmetry 1T' phase. Similar to MacNeill et al., an out-of-plane damping-like torque is expected for the 1T' phase-changed region, while this torque is expected to be supressed in the 2H phase $MoTe_2$. The experimental verification would strengthen our understanding on the relation between the crystal symmetry and the allowed SOTs and their strenghts. Before these measurements can be performed, however, the local phase-transformation process in $MoTe_2$ by laser irradiation should be optimized to ensure that the phase-transformation occurs homogeneously across the entire desired region.

### Fully 2D SOT devices

While the spin-orbit torque (SOT) devices discussed in Chapters 5 and 6 involve two-dimensional (2D) van der Waals materials, the ferromagnetic material used is a conventional evaporated poly-crystalline layer of permalloy. The recent discovery of (anti)ferromagnetic order in several 2D van der Waals materials opens up opportunities for creating fully 2D stacks for SOT devices [16–20]. While conventional MgO-based MTJ are expected to reach their limit in down-scaling when MTJ sizes reach 30 to 40 nm, having problems with PMA and surface roughness, the development of 2D magnetic-based SOT devices might allow for further down-scaling, owing to their atomically thin and pristine surfaces [21]. Multiple studies have already shown the possibility of field-free switching the 2D van der Waals magnet $Fe_3GeTe_2$ using $WTe_2$, one of the most efficient 2D van der Waals SOT materials [22, 23].

In addition, due to their atomically thin nature, two-dimensional ferromagnetic materials facilitate strong electrostatic gating, which allows for voltage- or light-controlled magnetic properties (magnetoelectronics) [24]. Using ionic-liquid gating, for instance, it was shown that the Curie temperature of thin flakes of the ferromagnetic $Fe_3GeTe_2$ could be elevate above room temperature, showing large modulations of the coercivity [25, 26]. Similarly, doping $Fe_3GeTe_2$ using femtosecond laser pulses, causing a redistribution of the electronic states which favor a stronger exchange interaction, was shown to increase the Curie temperature [27]. Apart from $Fe_3GeTe_2$, also in $Cr_2Ge_2Te_6$ it was found that the Curie temperature could be increased by gating, and in addition, the out-of-plane easy-axis could be tuned to an in-plane direction [28]. Lastly, in the antiferromagnetic semiconductor $CrI_3$, it was shown that the magnet can be switched from antiferromagnetic to ferromagnetic under the influence of an electric field [29]. All these magnetoelectric effects in 2D

van der Waals magnets enable one to tailor the magnetic properties at will using electric fields, which could be used in conjunction with SOTs to facilitate field-free magnetization switching using low energy current pulses.

#### Optical magnetization switching

Another promising research direction is to investigate how light could be used to alter, or facilitate, SOT switching using the strong spin-photon coupling of TMDs. By exciting a monolayer TMD with circularly polarized light, with a wavelength tuned to the excitonic transition, one excites spin-polarized electrons in the out-of-plane direction in the TMD (either spin-up or spin-down, depending on the helicity of the light). It was demonstrated in $MoS_2$/graphene and $WSe_2$/graphene bilayers that the optically excited spins in the TMD are subsequently allowed to diffuse through the graphene, showing anti-symmetric Hanle spin-precession curves when an in-plane magnetic field is applied. As spins in the out-of-plane direction are ideal for the generation of an out-of-plane damping-like torque, monolayer TMD/FM bilayers might be promising for optically generated spin-orbit torques allowing for field-free switching.

Additionally, all-optical switching was reported in $CrI_3$ where the switching was controlled with the helicity of the light without the need of a additional TMD layer [30]. Without the interplay of electrons, here, the angular momentum of the photons is directly transferred to the magnetization. Optical means enable operation at higher frequencies (∼THz) compared to electronics at the time of writing (∼GHz), with unprecedented energy efficiency. Therefore, gaining optical control of magnetization states would be beneficial for fast and energy efficient memory applications. With a diffraction limited spot size, however, high density magnetic memory, achievable with electronic MTJs, is unachievable with light. Newly developed techniques, such as near-field optical techniques [31], where the laser light is directed to an AFM-like tip, allow for strong light-matter interaction on the order of several tens of nanometers, greatly increasing the spatial resolution [31].

### 9.2.2. Optoelectronics

While the technique of photocurrent spectroscopy has already been used since the start of the field of van der Waals materials, it is still considered a promising tool today to obtain a better understanding of light-matter interaction in new and emerging van der Waals materials, ranging from topological insulators, magnetic materials, Moiré materials, etc. Here, I outline a few ways in which photocurrent measurements might shed light on these exotic materials.

#### Moiré materials

While monolayer graphene possesses a broad absorption spectrum due to its gapless band structure, twisted bilayer graphene (tBLG), on the other hand, exhibits surprisingly different properties. Due to the hybridization of the states at the band-crossings, tBLG exhibits a twist-angle dependent band gap. Taking advantage of the twist-angle to tailor the material properties of van der Waals materials was

recently termed the new research field of band structure engineering. From an application point of view, this is a very appealing property, as only one material would allow for optoelectronic sensors, sensitive to a specific and controllable wavelength. Experimentally confirming these properties with photocurrent spectroscopy will enable a better understanding on the interaction of these hybridized states in Moiré materials with light and might confirm the changes in the band structure predicted by theoretical models.

#### 2D van der Waals ferromagnets

The 2D ferromagnetic materials, mentioned before in the SOT section, are also promising for research on opto-spintronics. Recently, it was shown that $Fe_3GeTe_2$ can be used to inject spins into monolayer $WSe_2$ via hBN tunneling contacts, creating a population imbalance between the K- and K'-valleys resulting in a helicity-dependent electroluminescence from the $WSe_2$ [32]. By applying a magnetic field, the magnetization of the $Fe_3GeTe_2$, and correspondingly, the helicity of the electroluminescence could be switched. Likewise, the helicity-dependent electroluminescence possessed hysteresis with an applied out-of-plane magnetic field. Future research could perform the opposite measurements on the same stack of materials: exciting the $WSe_2$ with circularly polarized light and measuring the induced photocurrent, while switching the $Fe_3GeTe_2$ with an external magnetic field. In this case, the imbalance of the population of the K- and K'-valley is created optically, resulting in an out-of-plane spin-polarization. By switching either the helicity or the magnetization of the FGT layer, the photocurrent would increase or decrease, depending on whether the spin-polarization and magnetization are parallel or anti-parallel, respectively. This could enable ultra-thin, helicity-dependent photodetectors or optically controlled spin-valves.

#### Near-field scanning photocurrent measurements

Chapter 7 is only one example of the advantage of scanning photocurrent measurements to obtain a better insight on the underlying photocurrent generation mechanisms [33–37]. The spatial resolution here is limited to the diffraction limited spot size of the laser (∼1 µm). Newly developed techniques on the other hand, such as near-field photocurrent scanning techniques, where the laser light is directed to an AFM-like tip, allow for strong light-matter interaction on the order of several tens of nanometers, greatly increasing the spatial resolution. This allows one to distinguish photocurrent generation mechanisms arising at previously unattainable length scales, for example at magnetic domains [38], topological edge states [39], grain boundaries in CVD-grown van der Waals materials [40], and Moiré heterostructures [41, 42]. All in all, it will increasing our understanding on the role of exchange interaction, topology, and crystal symmetry on the light-matter interaction in solid-state materials.

### 9.2.3. Afterword

Ever since the start in 2004, the research field of 2D van der Waals materials had to life up to high expectations. Almost 20 years later, it is safe to say that the number

of possible applications of these materials has only increased, due to the ever increasing list of different 2D vdW materials, their possible stacking combinations, relative twist angles, etc. On the one hand, the endless number of combinations allow for a wide range of different fundamental physics to be explored, bridging gaps between various, previously disconnected, research areas. On the other hand, effective ways of selecting which combinations of materials are worth pursuing becomes more challenging. In this regard, strong collaboration between theoretical and experimental researchers is key for effective guidance through these unexplored areas. All in all, while there might be plenty of room at the bottom, we surely haven't reached the bottom yet.

# Bibliography


[1] J. Hidding and M. H. D. Guimarães, "Spin-Orbit Torques in Transition Metal Dichalcogenide/Ferromagnet Heterostructures", Frontiers in Materials **7**, 1–8 (2020).

[2] J. Hidding, S. H. Tirion, J. Momand, A. Kaverzin, M. Mostovoy, B. J. Van Wees, B. J. Kooi, and M. H. D. Guimarães, "Interfacial spin-orbit torques and magnetic anisotropy in WSe2/permalloy bilayers", Journal of Physics: Materials **4**, 04LT01 (2021).

[3] Q. Shao, G. Yu, Y.-W. Lan, Y. Shi, M.-Y. Li, C. Zheng, X. Zhu, L.-J. Li, P. K. Amiri, and K. L. Wang, "Strong Rashba-Edelstein Effect-Induced SpinOrbit Torques in Monolayer Transition Metal Dichalcogenide/Ferromagnet Bilayers", Nano Letters **16**, 7514–7520 (2016).

[4] M. Hayashi, J. Kim, M. Yamanouchi, and H. Ohno, "Quantitative characterization of the spin-orbit torque using harmonic Hall voltage measurements", Physical Review B **89**, 144425 (2014).

[5] M.-H. Nguyen and C.-F. Pai, "Spinorbit torque characterization in a nutshell", APL Materials **9**, 1–15 (2021).

[6] Ø. Johansen, V. Risinggård, A. Sudbø, J. Linder, and A. Brataas, "Current Control of Magnetism in Two-Dimensional Fe3GeTe2", Physical Review Letters **122**, 217203 (2019).

[7] T. G. Saunderson, D. Go, S. Blügel, M. Kläui, and Y. Mokrousov, "Hidden interplay of current-induced spin and orbital torques in bulk Fe3GeTe2", Physical Review Research **4**, L042022 (2022).

[8] F. Martin, K. Lee, M. Schmitt, A. Liedtke, A. Shahee, H. T. Simensen, T. Scholz, T. G. Saunderson, D. Go, M. Gradhand, Y. Mokrousov, T. Denneulin, A. Kovács, B. Lotsch, A. Brataas, and M. Kläui, "Strong bulk spinorbit torques quantified in the van der Waals ferromagnet Fe3GeTe2", Materials Research Letters **11**, 84–89 (2023).

[9] X. Yin, C. S. Tang, Y. Zheng, J. Gao, J. Wu, H. Zhang, M. Chhowalla, W. Chen, and A. T. S. Wee, "Recent developments in 2D transition metal dichalcogenides: phase transition and applications of the (quasi-)metallic phases", Chemical Society Reviews **50**, 10087–10115 (2021).

[10] D.-y. Lin, H.-p. Hsu, G.-h. Liu, T.-z. Dai, and Y.-t. Shih, "Enhanced Photoresponsivity of 2H-MoTe2 by Inserting 1T-MoTe2 Interlayer Contact for Photodetector Applications", Crystals **11**, 964 (2021).

[11] M. Buscema, J. O. Island, D. J. Groenendijk, S. I. Blanter, G. A. Steele, H. S. J. van der Zant, and A. Castellanos-Gomez, "Photocurrent generation with two-dimensional van der Waals semiconductors", Chemical Society Reviews **44**, 3691–3718 (2015).

[12] J. Cheng, C. Wang, X. Zou, and L. Liao, "Recent Advances in Optoelectronic Devices Based on 2D Materials and Their Heterostructures", Advanced Optical Materials **7**, 1800441 (2019).

[13] F. Sousa, G. Tatara, and A. Ferreira, "Skew-scattering-induced giant antidamping spin-orbit torques: Collinear and out-of-plane Edelstein effects at two-dimensional material/ferromagnet interfaces", Physical Review Research **2**, 043401 (2020).

[14] K. Zollner, M. D. Petrovi, K. Dolui, P. Plechá, B. K. Nikoli, and J. Fabian, "Scattering-induced and highly tunable by gate damping-like spin-orbit torque in graphene doubly proximitized by two-dimensional magnet Cr2Ge2Te6 and monolayer WS2", Physical Review Research **2**, 043057 (2020).

[15] D. MacNeill, G. M. Stiehl, M. H. D. Guimaraes, R. A. Buhrman, J. Park, and D. C. Ralph, "Control of spinorbit torques through crystal symmetry in WTe2/ferromagnet bilayers", Nature Physics **13**, 300–305 (2017).

[16] B. Huang, G. Clark, E. Navarro-Moratalla, D. R. Klein, R. Cheng, K. L. Seyler, D. Zhong, E. Schmidgall, M. A. McGuire, D. H. Cobden, W. Yao, D. Xiao, P. Jarillo-Herrero, and X. Xu, "Layer-dependent ferromagnetism in a van der Waals crystal down to the monolayer limit", Nature **546**, 270–273 (2017).

[17] C. Gong, L. Li, Z. Li, H. Ji, A. Stern, Y. Xia, T. Cao, W. Bao, C. Wang, Y. Wang, Z. Q. Qiu, R. J. Cava, S. G. Louie, J. Xia, and X. Zhang, "Discovery of intrinsic ferromagnetism in two-dimensional van der Waals crystals", Nature **546**, 265–269 (2017).

[18] Z. Fei, B. Huang, P. Malinowski, W. Wang, T. Song, J. Sanchez, W. Yao, D. Xiao, X. Zhu, A. F. May, W. Wu, D. H. Cobden, J.-H. Chu, and X. Xu, "Two-dimensional itinerant ferromagnetism in atomically thin Fe3GeTe2", Nature Materials **17**, 778–782 (2018).

[19] M. Alghamdi, M. Lohmann, J. Li, P. R. Jothi, Q. Shao, M. Aldosary, T. Su, B. P. T. Fokwa, and J. Shi, "Highly Efficient SpinOrbit Torque and Switching of Layered Ferromagnet Fe3GeTe2", Nano Letters **19**, 4400–4405 (2019).

[20] B. Huang, M. A. McGuire, A. F. May, D. Xiao, P. Jarillo-Herrero, and X. Xu, "Emergent phenomena and proximity effects in two-dimensional magnets and heterostructures", Nature Materials **19**, 1276–1289 (2020).

[21] H. Yang, S. O. Valenzuela, M. Chshiev, S. Couet, B. Dieny, B. Dlubak, A. Fert, K. Garello, M. Jamet, D.-E. Jeong, K. Lee, T. Lee, M.-B. Martin, G. S. Kar, P. Sénéor, H.-J. Shin, and S. Roche, "Two-dimensional materials prospects for non-volatile spintronic memories", Nature **606**, 663–673 (2022).

[22] I.-H. Kao, R. Muzzio, H. Zhang, M. Zhu, J. Gobbo, S. Yuan, D. Weber, R. Rao, J. Li, J. H. Edgar, J. E. Goldberger, J. Yan, D. G. Mandrus, J. Hwang, R. Cheng, J. Katoch, and S. Singh, "Deterministic switching of a perpendicularly polarized magnet using unconventional spinorbit torques in WTe2", Nature Materials **21**, 1029–1034 (2022).

[23] I. Shin, W. J. Cho, E.-S. An, S. Park, H.-W. Jeong, S. Jang, W. J. Baek, S. Y. Park, D.-H. Yang, J. H. Seo, G.-Y. Kim, M. N. Ali, S.-Y. Choi, H.-W. Lee, J. S. Kim, S. D. Kim, and G.-H. Lee, "SpinOrbit Torque Switching in an AllVan der Waals Heterostructure", Advanced Materials **34**, 2101730 (2022).

[24] J. F. Sierra, J. Fabian, R. K. Kawakami, S. Roche, and S. O. Valenzuela, "Van der Waals heterostructures for spintronics and opto-spintronics", Nature Nanotechnology **16**, 856–868 (2021).

[25] Y. Deng, Y. Yu, Y. Song, J. Zhang, N. Z. Wang, Z. Sun, Y. Yi, Y. Z. Wu, S. Wu, J. Zhu, J. Wang, X. H. Chen, and Y. Zhang, "Gate-tunable room-temperature ferromagnetism in two-dimensional Fe3GeTe2", Nature **563**, 94–99 (2018).

[26] S. Y. Park, D. S. Kim, Y. Liu, J. Hwang, Y. Kim, W. Kim, J.-Y. Kim, C. Petrovic, C. Hwang, S.-K. Mo, H.-j. Kim, B.-C. Min, H. C. Koo, J. Chang, C. Jang, J. W. Choi, and H. Ryu, "Controlling the Magnetic Anisotropy of the van der Waals Ferromagnet Fe3GeTe2 through Hole Doping", Nano Letters **20**, 95–100 (2020).

[27] B. Liu, S. Liu, L. Yang, Z. Chen, E. Zhang, Z. Li, J. Wu, X. Ruan, F. Xiu, W. Liu, L. He, R. Zhang, and Y. Xu, "Light-Tunable Ferromagnetism in Atomically Thin Fe3GeTe2 Driven by Femtosecond Laser Pulse", Physical Review Letters **125**, 267205 (2020).

[28] W. Zhuo, B. Lei, S. Wu, F. Yu, C. Zhu, J. Cui, Z. Sun, D. Ma, M. Shi, H. Wang, W. Wang, T. Wu, J. Ying, S. Wu, Z. Wang, and X. Chen, "Manipulating Ferromagnetism in FewLayered Cr2Ge2Te6", Advanced Materials **33**, 2008586 (2021).

[29] S. Jiang, J. Shan, and K. F. Mak, "Electric-field switching of two-dimensional van der Waals magnets", Nature Materials **17**, 406–410 (2018).

[30] P. Zhang, T.-F. Chung, Q. Li, S. Wang, Q. Wang, W. L. B. Huey, S. Yang, J. E. Goldberger, J. Yao, and X. Zhang, "All-optical switching of magnetization in atomically thin CrI3", Nature Materials **21**, 1373–1378 (2022).

[31] Q. Ma, R. Krishna Kumar, S.-Y. Xu, F. H. L. Koppens, and J. C. W. Song, "Photocurrent as a multiphysics diagnostic of quantum materials", Nature Reviews Physics **5**, 170–184 (2023).

[32] J.-X. Li, W.-Q. Li, S.-H. Hung, P.-L. Chen, Y.-C. Yang, T.-Y. Chang, P.-W. Chiu, H.-T. Jeng, and C.-H. Liu, "Electric control of valley polarization in monolayer WSe2 using a van der Waals magnet", Nature Nanotechnology **17**, 721–728 (2022).

[33] J. Park, Y. H. Ahn, and C. Ruiz-Vargas, "Imaging of Photocurrent Generation and Collection in Single-Layer Graphene", Nano Letters **9**, 1742–1746 (2009).

[34] T. Mueller, F. Xia, M. Freitag, J. Tsang, and P. Avouris, "Role of contacts in graphene transistors: A scanning photocurrent study", Physical Review B **79**, 245430 (2009).

[35] X. Xu, N. M. Gabor, J. S. Alden, A. M. van der Zande, and P. L. McEuen, "Photo-Thermoelectric Effect at a Graphene Interface Junction", Nano Letters **10**, 562–566 (2010).

[36] Q. Ma, C. H. Lui, J. C. W. Song, Y. Lin, J. F. Kong, Y. Cao, T. H. Dinh, N. L. Nair, W. Fang, K. Watanabe, T. Taniguchi, S.-Y. Xu, J. Kong, T. Palacios, N. Gedik, N. M. Gabor, and P. Jarillo-Herrero, "Giant intrinsic photoresponse in pristine graphene", Nature Nanotechnology **14**, 145–150 (2019).

[37] Q. Wang, J. Zheng, Y. He, J. Cao, X. Liu, M. Wang, J. Ma, J. Lai, H. Lu, S. Jia, D. Yan, Y. Shi, J. Duan, J. Han, W. Xiao, J.-H. Chen, K. Sun, Y. Yao, and D. Sun, "Robust edge photocurrent response on layered type II Weyl semimetal WTe2", Nature Communications **10**, 5736 (2019).

[38] H. Wang and X. Qian, "Electrically and magnetically switchable nonlinear photocurrent in -symmetric magnetic topological quantum materials", npj Computational Materials **6**, 199 (2020).

[39] Y. Shao, R. Jing, S. H. Chae, C. Wang, Z. Sun, E. Emmanouilidou, S. Xu, D. Halbertal, B. Li, A. Rajendran, F. L. Ruta, L. Xiong, Y. Dong, A. S. McLeod, S. S. Sunku, J. C. Hone, J. Moore, J. Orenstein, J. G. Analytis, A. J. Millis, N. Ni, D. Xiao, and D. N. Basov, "Nonlinear nanoelectrodynamics of a Weyl metal", Proceedings of the National Academy of Sciences **118**, 1–6 (2021).

[40] A. Woessner, P. Alonso-González, M. B. Lundeberg, Y. Gao, J. E. Barrios-Vargas, G. Navickaite, Q. Ma, D. Janner, K. Watanabe, A. W. Cummings, T. Taniguchi, V. Pruneri, S. Roche, P. Jarillo-Herrero, J. Hone, R. Hillenbrand, and F. H. L. Koppens, "Near-field photocurrent nanoscopy on bare and encapsulated graphene", Nature Communications **7**, 10783 (2016).

[41] S. S. Sunku, D. Halbertal, T. Stauber, S. Chen, A. S. McLeod, A. Rikhter, M. E. Berkowitz, C. F. B. Lo, D. E. Gonzalez-Acevedo, J. C. Hone, C. R. Dean, M. M. Fogler, and D. N. Basov, "Hyperbolic enhancement of photocurrent patterns in minimally twisted bilayer graphene", Nature Communications **12**, 1641 (2021).

[42] N. C. H. Hesp, I. Torre, D. Barcons-Ruiz, H. Herzig Sheinfux, K. Watanabe, T. Taniguchi, R. Krishna Kumar, and F. H. L. Koppens, "Nano-imaging photoresponse in a Moiré unit cell of minimally twisted bilayer graphene", Nature Communications **12**, 1640 (2021).

# chapter A

# Appendix

## A.1. Derivation of the second-harmonic Hall signals for spin-orbit torque quantification

This section is highly based on the theoretical work of Hayashi et al. [1], and summarizes the relevant findings, used in this thesis.

In this section, the equation for the first- and second-harmonic Hall voltages used in Sec. 3.3.4 are derived starting from the expression for the magnetic energy of a system. First, by minimizing the magnetic energy of a system in an external magnetic field, the equilibrium direction of the magnetization is found. Next, an expression is found for the deviation of the magnetization from this equilibrium position, due to the current-induced effective fields (or SOTs). Finally, using an empirical equation for the Hall voltage, we are able to find the full expression on how the second harmonic Hall voltage depends on the in-plane and out-of-plane SOTs.

### A.1.1. Equilibrium position of the magnetization

The magnetic energy of a system with a magnetization $\vec{M}$ in an external magnetic field $\vec{H}$ is expressed as:

$$E = -K_{eff}\cos^2(\theta) - K_i \sin^2(\phi)\sin^2(\theta) - \vec{M}\cdot\vec{H} \tag{A.1}$$

Here, $\theta$ and $\phi$ are the polar and azimuthal angles of the magnetization $\vec{M}$, respectively, as illustrated in Fig. 3.5. The first part of right hand side corresponds to the out-of-plane anisotropy energy where $K_{eff}$ is the out-of-plane anisotorpy energy and $K_i$ is the in-plane easy axis anisotropy energy. $\vec{M}$ is defined as:

$$\vec{M} = M_s\hat{m} = M_s(\sin(\theta)\cos(\phi), \sin(\theta)\sin(\phi), \cos(\theta)), \tag{A.2}$$

and similarly, the applied field is described by:

$$\vec{H} = H(\sin(\theta_H)\cos(\phi_H), \sin(\theta_H)\sin(\phi_H), \cos(\theta_H)). \tag{A.3}$$

First, the equilibrium position of the magnetization can be calculated by setting the derivative of Eq. A.1 with respect to the angles to zero, which gives:

A

$$\left(\frac{\partial E}{\partial \theta}\right)\Big|_{\theta=\theta_0,\phi=\phi_0} = 0 \tag{A.4}$$
$$= \sin(2\theta_0)\left(K_{eff} - K_i \sin^2(\phi_0)\right)$$
$$- M_s H\Big[\cos(\theta_0)\sin(\theta_H)\Big(\cos(\phi_0)\cos(\phi_H)$$
$$+ \sin(\phi_0)\sin(\phi_H)\Big) - \sin(\theta_0)\cos(\theta_H)\Big]$$
$$\left(\frac{\partial E}{\partial \phi}\right)\Big|_{\theta=\theta_0,\phi=\phi_0} = 0 \tag{A.5}$$
$$= - K_i \sin^2(\theta_0)\sin(2\phi_0)$$
$$- M_s H \sin(\theta_0)\sin(\theta_H)\sin(\phi_H - \phi_0)$$

Here, the trigonometric identities: $\sin(2\theta) = 2\cos(\theta)\sin(\theta)$, and $\sin(\phi_H - \phi_0) = \sin(\phi_H)\cos(\phi_0) - \cos(\phi_H)\sin(\phi_0)$ are used. Finally, solving Eqs. A.4 and A.5 gives the equilibrium positions of the magnetization $\theta_0$ and $\phi_0$.

### A.1.2. Current-induced deviations of the magnetization

In the presence of current-induced spin-orbit torques (SOTs) or an Oersted field, the magnetization will cant away from its equilibrium position by $\Delta\theta$ and $\Delta\phi$. The SOTs which drive this deviation can be described as an effective magnetic field ($\Delta\vec{H} = \Delta H_x, \Delta H_y, \Delta H_z$). The change in direction of the magnetization ($\Delta\theta$ and $\Delta\phi$) due to the effective field, are then given by:

$$\Delta\theta = \frac{\partial\theta}{\partial H_x}\Delta H_x + \frac{\partial\theta}{\partial H_y}\Delta H_y + \frac{\partial\theta}{\partial H_z}\Delta H_z \tag{A.6}$$

$$\Delta\phi = \frac{\partial\phi}{\partial H_x}\Delta H_x + \frac{\partial\phi}{\partial H_y}\Delta H_y + \frac{\partial\phi}{\partial H_z}\Delta H_z, \tag{A.7}$$

where $\frac{\partial\theta}{\partial H_i}$ and $\frac{\partial\phi}{\partial H_i}$ represent the change of the angles when $\Delta H_i$ is applied. To find $\Delta\theta$ and $\Delta\phi$ we thus first need to find $\frac{\partial\theta}{\partial H_i}$ and $\frac{\partial\phi}{\partial H_i}$, which is done using the following relations:

$$\frac{\partial}{\partial H_i}\left(\frac{\partial E}{\partial \theta}\right) = 0 = \frac{\partial}{\partial \theta}\left(\frac{\partial E}{\partial \theta}\right)\frac{\partial\theta}{\partial H_i} + \frac{\partial}{\partial \phi}\left(\frac{\partial E}{\partial \theta}\right)\frac{\partial\phi}{\partial H_i} + \frac{\partial}{\partial \vec{H}}\left(\frac{\partial E}{\partial \theta}\right)\frac{\partial\vec{H}}{\partial H_i} \tag{A.8}$$

$$\frac{\partial}{\partial H_i}\left(\frac{\partial E}{\partial \phi}\right) = 0 = \frac{\partial}{\partial \theta}\left(\frac{\partial E}{\partial \phi}\right)\frac{\partial\theta}{\partial H_i} + \frac{\partial}{\partial \phi}\left(\frac{\partial E}{\partial \phi}\right)\frac{\partial\phi}{\partial H_i} + \frac{\partial}{\partial \vec{H}}\left(\frac{\partial E}{\partial \phi}\right)\frac{\partial\vec{H}}{\partial H_i}. \tag{A.9}$$

Here, the chain rule is applied (i.e. $\frac{\partial f(x(t),y(t),z(t))}{\partial t} = \frac{\partial f}{\partial x}\frac{\partial x}{\partial t} + \frac{\partial f}{\partial y}\frac{\partial y}{\partial t} + \frac{\partial f}{\partial z}\frac{\partial z}{\partial t}$). Working out Eqs. A.8 and A.8 using Eqs. A.4 and A.5 gives:

$$
\begin{aligned}
&\frac{\partial}{\partial H_i}\left(\frac{\partial E}{\partial \theta}\right) = 0 \\
&= \left[\left(K_{EFF} - K_I \sin^2(\varphi_0)\right) 2\cos(2\theta_0) - M_s \begin{bmatrix} -\sin(\theta_0)\cos(\varphi_0) \\ -\sin(\theta_0)\sin(\varphi_0) \\ -\cos(\theta_0) \end{bmatrix} \cdot \begin{bmatrix} \Delta H_x \\ \Delta H_y \\ \Delta H_z \end{bmatrix}\right] \frac{\partial \theta}{H_i} \\
&+ \left[-K_I \sin(2\theta_0)\sin(2\varphi_0) - M_s \begin{bmatrix} -\cos(\theta_0)\sin(\varphi_0) \\ \cos(\theta_0)\cos(\varphi_0) \\ 0 \end{bmatrix} \cdot \begin{bmatrix} \Delta H_x \\ \Delta H_y \\ \Delta H_z \end{bmatrix}\right] \frac{\partial \varphi}{H_i} \\
&- \left[M_s \begin{bmatrix} \cos(\theta)\cos(\varphi) \\ \cos(\theta)\sin(\varphi) \\ -\sin(\theta) \end{bmatrix} \cdot \begin{bmatrix} 1 & 0 & 0 \\ 0 & 1 & 0 \\ 0 & 0 & 1 \end{bmatrix}\right] \cdot \boldsymbol{e_i},
\end{aligned}
\tag{A.10}
$$

$$
\begin{aligned}
\frac{\partial}{\partial H_i}\left(\frac{\partial E}{\partial \varphi}\right) = 0 = &\left[-K_I \sin(2\theta_0)\sin(2\varphi) - M_s \begin{bmatrix} -\cos(\theta_0)\sin(\varphi_0) \\ \cos(\theta_0)\cos(\varphi_0) \\ 0 \end{bmatrix} \cdot \begin{bmatrix} \Delta H_x \\ \Delta H_y \\ \Delta H_z \end{bmatrix}\right] \frac{\partial \theta}{H_i} \\
&+ \left[-2K_I \sin^2(\theta_0)\cos(2\varphi_0) - M_s \begin{bmatrix} -\sin(\theta_0)\cos(\varphi_0) \\ -\sin(\theta_0)\sin(\varphi_0) \\ 0 \end{bmatrix} \cdot \begin{bmatrix} \Delta H_x \\ \Delta H_y \\ \Delta H_z \end{bmatrix}\right] \frac{\partial \varphi}{H_i} \\
&- \left[M_s \begin{bmatrix} -\sin(\theta)\sin(\varphi) \\ \sin(\theta)\cos(\varphi) \\ 0 \end{bmatrix} \cdot \begin{bmatrix} 1 & 0 & 0 \\ 0 & 1 & 0 \\ 0 & 0 & 1 \end{bmatrix}\right] \cdot \boldsymbol{e_i}.
\end{aligned}
\tag{A.11}
$$

where $e_i$ is a Jacobian Matrix. Together, Eqs. A.10 and A.11 form a set of linear equations which can be solved to obtain $\frac{\partial \theta}{\partial H_i}$ and $\frac{\partial \phi}{\partial H_i}$. First, to shorten these expressions, we can rewrite the last terms of Eqs. A.10 and A.11 as:

$$
\vec{f} = \begin{bmatrix} \cos(\theta)\cos(\varphi) \\ \cos(\theta)\sin(\varphi) \\ -\sin(\theta) \end{bmatrix}, \qquad \vec{g} = \begin{bmatrix} -\sin(\theta)\sin(\varphi) \\ \sin(\theta)\cos(\varphi) \\ 0 \end{bmatrix}. \tag{A.12}
$$

Additionally, we rewrite the out-of-plane and in-plane anisotropy energy as fields:

$$
H_K = H_{ani} - H_{dem} = \frac{2K_{eff}}{M_s}, \qquad H_A = \frac{2K_i}{M_s}, \tag{A.13}
$$

where $H_{ani}$ and $H_{dem}$ are the perpendicular anisotropy and demagnetizing field [2, 3]. Next, the set of linear equations (Eqs. A.10 and A.11) can be solved to obtain:

$$
\frac{\partial \theta}{\partial H_i} = \frac{1}{F_1}(f_i - C g_i), \tag{A.14}
$$

A

$$\frac{\partial\varphi}{\partial H_i} = \frac{1}{F_1 F_2}\Bigg( f_i \left[\frac{1}{2} H_A \sin(2\theta_0)\sin(2\varphi_0) - \cos(\theta_o)(H_x \sin(\varphi_0) - H_y \cos(\varphi_0))\right] - g_i \left[(H_K - H_A \sin^2(\varphi_0))\cos(2\theta_0) + \vec{H}\cdot\hat{m}\right]\Bigg), \tag{A.15}$$

where,

$$F_1 \equiv (H_K - H_A \sin^2(\varphi_0)\cos(2\theta_0)) + \vec{H}\cdot\hat{m} - C\left[\frac{1}{2} H_A \sin(2\theta_0)\sin(2\varphi_0) - \cos(\theta_0)\left(H_x \sin(\varphi_0) - H_y \cos(\varphi_0)\right)\right], \tag{A.16a}$$

$$F_2 \equiv -H_A \sin^2(\theta_0)\cos(2\varphi_0) + \sin(\theta_0)\left(H_x \sin(\varphi_0) - H_y \cos(\varphi_0)\right), \tag{A.16b}$$

$$C \equiv \frac{1}{F_2}\left[\frac{1}{2} H_A \sin(2\theta_0)\sin(2\varphi_0) - \cos(\theta_0)\left(H_x \sin(\varphi_0) - H_y \cos(\varphi_0)\right)\right]. \tag{A.16c}$$

At last, $\Delta\theta$ and $\Delta\phi$ are obtained by substituting Eqs. A.14 and A.15 into Eqs. A.6 and A.7:

$$\Delta\theta = \frac{1}{F_1}\Big[ \left(\cos(\theta_0)\cos(\varphi_0) - C\sin(\theta_0)\sin(\varphi_0)\right)\Delta H_x + \left(\cos(\theta_0)\sin(\varphi_0) + C\sin(\theta_0)\cos(\varphi_0)\right)\Delta H_y - \sin(\theta_0)\Delta H_z\Big], \tag{A.17}$$

$$\begin{aligned}\Delta\varphi = {} & \frac{\Delta H_x \sin(\theta_0)\sin(\varphi_0)}{F_1 F_2}\Big[H_A\left(2\cos^2(\theta_0)\cos^2(\varphi_0) + \cos(2\theta_0)\sin^2(\varphi_0)\right) \\ & - H_K\cos(2\theta_0) - \vec{H}\cdot\hat{m} - \left(H_x\sin(\varphi_0) - H_y\cos(\varphi_0)\right)\frac{\cos^2(\theta_0)\cos(\varphi_0)}{\sin(\theta_0)\sin(\varphi_0)}\Big] \\ & + \frac{\Delta H_y \sin(\theta_0)\cos(\varphi_0)}{F_1 F_2}\Big[H_A\left(2\cos^2(\theta_0)\sin^2(\varphi_0) - \cos(2\theta_0)\sin^2(\varphi_0)\right) \\ & + H_K\cos(2\theta_0) + \vec{H}\cdot\hat{m} - \left(H_x\sin(\varphi_0) - H_y\cos(\varphi_0)\right)\frac{\cos^2(\theta_0)\sin(\varphi_0)}{\sin(\theta_0)\cos(\varphi_0)}\Big] \\ & + \frac{\Delta H_z \sin(\theta_0)}{F_1 F_2}\Big[-\frac{1}{2}H_A\sin(2\theta_0)\sin(2\varphi_0) + \cos(\theta_0)\left(H_x\sin(\varphi_0 - H_y\cos(\varphi_0)\right)\Big].\end{aligned} \tag{A.18}$$

Next, these huge expressions can be simplified by making a few assumptions which apply to the work performed in this thesis. First, we assume the in-plane magnetic anisotropy field to be much smaller compared to the applied magnetic

field: i.e. $|H_A| \ll |H\sin(\theta_H)|$. Therefore, we can assume the magnetization to follow the external magnetic field when the field is rotated in-plane, and thus set $\phi_0 \approx \phi_H$. This simplifies Eqs. A.17 and A.18 to:

$$\Delta\theta = \left[\frac{\begin{array}{c}\cos(\theta_0)\left(\Delta H_x\cos(\varphi_H)+\Delta H_y\cos(\varphi_H)\right)\\ +\sin(\theta_0)\left[C\left(-\Delta H_x\sin(\varphi_H+\Delta H_y\cos(\varphi_H)\right)-\Delta H_z\right]\end{array}}{\left(H_K - H_A\sin^2(\varphi_H)\right)\cos(2\theta_0)+H\cos(\theta_H-\theta_0)-\frac{1}{2}CH_A\sin(2\theta_0\sin(2\varphi_H))}\right], \tag{A.19}$$

$$\begin{aligned}\Delta\varphi = &\frac{1}{-H_A\sin(\theta_0)\cos(2\varphi_H)+H\sin(\theta_H)}\\ &\left[\frac{\left[\left(H_K - H_A\sin^2(\varphi_H)\right)\cos(2\theta_0)+H\cos(\theta_H-\theta_0)\right]\left(-\Delta H_x\sin(\varphi_H)+\Delta H_y\cos(\varphi_H)\right)}{\left(H_K - H_A\sin^2(\varphi_H)\right)\cos(2\theta_0)+H\cos(\theta_H-\theta_0)-\frac{1}{2}CH_A\sin(2\theta_0)\sin(2\varphi_H)}\right.\\ &\left.+\frac{H_A\sin(2\varphi_H)\left[\cos^2(\theta_0)\left(\Delta H_x\cos(\varphi_H+\Delta H_y\sin(\varphi_H)\right)-\frac{1}{2}\sin(2\theta_0)\Delta H_z\right]}{\left(H_K - H_A\sin^2(\varphi_H)\right)\cos(2\theta_0)+H\cos(\theta_H-\theta_0)-\frac{1}{2}CH_A\sin(2\theta_0)\sin(2\varphi_H)}\right],\end{aligned} \tag{A.20}$$

where,

$$C \equiv \frac{H_A\cos(\theta_0)\sin(2\varphi_H)}{-H_A\sin(\theta_0)\cos(2\varphi_H)+H\sin(\theta_H)}. \tag{A.21}$$

These expressions can be simplified further by realizing that the assumption $|H_A| \ll |H\sin(\theta_H)|$ causes $C$ (Eq. A.21) to become zero. Therefore, Eqs. A.19 and A.20 are simplified to their final expression:

$$\Delta\theta = \frac{\cos(\theta_0)\left(\Delta H_x\cos(\varphi_H)+\Delta H_y\sin(\varphi_H)\right)-\Delta H_z\sin(\theta_0)}{\left(H_K - H_A\sin^2(\varphi_H)\right)\cos(2\theta_0)+H\cos(\theta_H-\theta_0)}, \tag{A.22}$$

$$\Delta\varphi = \frac{-\Delta H_x\sin(\varphi_H)+\Delta H_y\cos(\varphi_H)}{-H_A\sin(\theta_0)\cos(2\varphi_H)+H\sin(\theta_H)}. \tag{A.23}$$

Finally, we have reached the expressions for the deviations of polar and azimuthal angle of the magnetization due to the current-induced effective fields. These expressions are used in the next subsection to reach the final expression for the second harmonic Hall voltage.

### A.1.3. Second-harmonic Hall voltage

The transverse Hall voltage ($V_{xy}$) is composed of multiple effects, such as the ordinary Hall effect (neglected here), the planar Hall effect (PHE) (see Sec. 3.4) and the anomalous Hall (AHE) (see Sec. 3.3.2). In the presence of an oscillating magnetization due to SOTs, these latter two effects produce a second-harmonic transverse voltage which is dependent on the exerted torques, and thus allow one to characterize them.

A

Empirically, $V_{xy}$ can be described as [4]:

$$V_{xy} = I\left[R_{PHE}\sin(\theta)^2\sin(2\phi) + R_{AHE}\cos(\theta)\right], \tag{A.24}$$

where $R_{PHE}$ and $R_{AHE}$ are the planar Hall and anomalous Hall resistance, respectively, and $I$ is the applied current. In the presence of SOTs, the magnetization will deflect from its equilibrium direction: $\theta = \theta_0 + \Delta\theta$ and $\phi = \phi_0 + \Delta\phi$. Here, we assume the deflections to be small: $\Delta\theta \ll 1$ and $\Delta\phi \ll 1$. By substituting these angles in Eq. A.24 and performing a Taylor expansion around ($\theta_0$, $\phi_0$) to second order, one obtains:

$$\begin{aligned} V_{xy} \approx & I\Big[R_{PHE}\left(\sin^2(\theta_0) + \Delta\theta\sin(2\theta_0)\right)\left(\sin(2\varphi_0) + 2\Delta\varphi\cos(2\varphi_0)\right) \\ & + R_{AHE}\left(\cos(\theta_0) - \Delta\theta\sin(\theta_0)\right)\Big]. \end{aligned} \tag{A.25}$$

Next, when a low-frequency AC-current ($I = I_0\sin(\omega t)$) is applied, the current-induced SOTs will cause the magnetization to oscillate around its equilibrium direction. Additionally, as the frequency of the applied AC-current is low (10s to 100s of Hz), we can assume the magnetization to be in-phase with the current, and thus describe $\Delta\theta$ and $\Delta\phi$ as $\Delta\theta\sin(\omega t)$ and $\Delta\phi\sin(\omega t)$, respectively. Filling in these expressions for the current and magnetization angles gives:

$$\begin{aligned} V_{xy} = & I_0 R_{PHE}\Big[\sin^2(\theta_0)\sin(2\varphi_0)\sin(\omega t) + 2\Delta\varphi\sin^2(\theta_0)\cos(2\varphi_0)\sin^2(\omega t) \\ & + \Delta\theta\sin(2\theta_0)\sin(2\varphi_0)\sin^2(\omega t) + 2\Delta\theta\Delta\varphi\sin(2\theta_0)\cos(2\varphi_0)\sin^3(\omega t)\Big] \\ & + I_0 R_{AHE}\Big[\cos(\theta_0)\sin(\omega t) - 2\Delta\theta\sin(\theta_0)\sin^2(\omega t)\Big]. \end{aligned} \tag{A.26}$$

This transverse voltage can be expressed as a combination of zeroth ($V_{xy}^0$), first ($V_{xy}^\omega$), and second ($V_{xy}^{2\omega}$). Using the identity $\sin^2(\omega t) = \frac{1}{2} + \frac{1}{2}\cos(2\omega t)$) and keeping all terms up to the second harmonic gives:

$$V_{xy} = V_{xy}^0 + V_{xy}^\omega\sin(\omega t) + V_{xy}^{2\omega}\cos(2\omega t), \tag{A.27a}$$

$$V_{xy}^0 = \frac{1}{2}\left(B_\theta + B_\varphi\right)I_0, \tag{A.27b}$$

$$V_{xy}^\omega = AI_0, \tag{A.27c}$$

$$V_{xy}^{2\omega} = -\frac{1}{2}\left(B_\theta + B_\varphi\right)I_0, \tag{A.27d}$$

where:

$$A = R_{PHE}\sin^2(\theta_0)\sin(2\varphi_0) + R_{AHE}\cos(\theta_0), \tag{A.28a}$$

$$B_\theta = \frac{1}{2}\left[R_{PHE}\sin(2\theta_0)\sin(2\varphi_0) - R_{AHE}\sin(\theta_0)\right]\Delta\theta, \tag{A.28b}$$

$$B_\varphi = R_{PHE}\sin^2(\theta_0)\cos(2\varphi_0)\Delta\varphi. \tag{A.28c}$$

The measurements in this thesis are performed by rotating the magnetization in-plane: i.e. $\theta_0 = 90°$. Furthermore, the in-plane magnetic anisotropy is assumed to be much smaller than the applied external field, $H_A \ll H$, and therefore, we can set $\phi_0 \approx \phi_H$. After using these assumptions and substituting Eqs. A.22 and A.23, the $V_{xy}^{\omega}$ and $V_{xy}^{2\omega}$ become:

$$V_{xy}^{\omega} = I_0 R_{PHE}\sin(2\phi_H), \tag{A.29a}$$

$$V_{xy}^{2\omega} = A\cos(2\phi)\cos(\phi) + B\cos(\phi), \tag{A.29b}$$

where:

$$A = \frac{R_{PHE}I_0\tau_\perp/\gamma}{H} \tag{A.30a}$$

$$B = \frac{R_{AHE}I_0\tau_\parallel/\gamma}{H - H_K}. \tag{A.30b}$$

Following Eq. A.13, $H_K$ is defined as $(H_{ani} - H_{dem})$, which is negative for in-plane magnetized systems, such as the ones used in Chapters 5 and 6. In this thesis, the found values for $H_K$ are reported as positive values. Therefore, the sign before $H_K$ in Eq. is changed to positive. Lastly, the contribution from the anomalous Nernst effect needs to be added (Sec. 3.3.3). Finally, we end up with the final equations reported in Sec. 3.3.4:

$$V_{xy}^{\omega} = I_0 R_{PHE}\sin(2\phi_H), \tag{A.31a}$$

$$V_{xy}^{2\omega} = A\cos(2\phi)\cos(\phi) + B\cos(\phi), \tag{A.31b}$$

where:

$$A = \frac{R_{PHE}I_0\tau_\perp/\gamma}{H} \tag{A.32a}$$

$$B = \frac{R_{AHE}I_0\tau_\parallel/\gamma}{H + H_K} + R_{ANE}I_0. \tag{A.32b}$$

# Bibliography


[1] M. Hayashi, J. Kim, M. Yamanouchi, and H. Ohno, "Quantitative characterization of the spin-orbit torque using harmonic Hall voltage measurements", Physical Review B **89**, 144425 (2014).

[2] C. O. Avci, K. Garello, M. Gabureac, A. Ghosh, A. Fuhrer, S. F. Alvarado, and P. Gambardella, "Interplay of spin-orbit torque and thermoelectric effects in ferromagnet/normal-metal bilayers", Physical Review B **90**, 224427 (2014).

[3] L. Neumann and M. Meinert, "Influence of the Hall-bar geometry on harmonic Hall voltage measurements of spin-orbit torques", AIP Advances **8**, 095320 (2018).

[4] K. Garello, I. M. Miron, C. O. Avci, F. Freimuth, Y. Mokrousov, S. Blügel, S. Auffret, O. Boulle, G. Gaudin, and P. Gambardella, "Symmetry and magnitude of spinorbit torques in ferromagnetic heterostructures", Nature Nanotechnology **8**, 587–593 (2013).

# Summary

While basic logic operations could already be performed by machines before, using bulky and power-hungry vacuum tubes, the invention of the solid-state transistor in 1947 is often coined as the invention that launched us into the information age. Since its invention, the solid-state transistor has undergone an unprecedented miniaturization process, made possible by multiple smaller breakthroughs, such as the invention of integrated circuits (ICs) in 1958 and the complementary metal oxide semiconductor (CMOS) in the early 1990s. While closely following the famous miniaturization trend predicted by Gordon Moore in 1965, better known now as Moore's law, the transistor became progressively smaller, faster, and cheaper. This allowed the technology to become available to the masses, resulting in the smartphones we have in our pockets today, and current state-of-the-art computer chips possessing an astounding number of 114 billion transistors. Naturally, this mind-boggling number begs the question: *"When do we reach the limit?"*. The answer you get depends on who you ask, as there is no clear consensus on when this will happen exactly. However, as the gate electrodes are currently separated by only 200 silicon atoms, reaching a physical limit soon seems inevitable. Additionally, while Moore's law is currently kept alive using clever chip designs rather than relying purely on downscaling of the transistor size, other figures-of-merit, such as the clock frequency and energy consumption per transistor, have already started to stagnate due to increased leakage currents that occur at these small transistor sizes. With the physical limits of conventional CMOS chips approaching, the quest for finding new methods and techniques, to further increase computing speed, capacity, and efficiency, intensifies. This has inspired researchers to explore new fields of physics to reinvent information processing and storage technologies.

One of these new fields of research is called *spintronics*. Here, rather than using the *charge* of the electron, another intrinsic property, called its *spin*, is used to encode, transport, and manipulate information. This quantum mechanical property is a measure of the intrinsic angular momentum and magnetic dipole moment of the electron and has already been successfully exploited in several computer technologies. A prime example is the use of the spintronic effect referred to as giant magnetoresistance (GMR) (awarded with a Nobel prize in 1988) in the read heads of storage hard drive disks (HDDs). With GMR, the resistance between two ferromagnetic materials, spaced with a normal metal, depends on the relative alignment of the magnetization of the two ferromagnetic layers (e.g. parallel or anti-parallel). The low- (parallel) and high-resistive state (anti-parallel) can be assigned to a "1" and "0", respectively, to represent one bit of information. Although HDDs are capable of high-density storage, it is currently considered a slow and energy-consuming storage medium, unsuitable for computer memory that relies on fast and energy-efficient operations. Therefore, other spintronic effects and new ways to implement them are now explored to further optimize information storage devices.

While spintronics might be ideal for energy efficient information storage, trans-

mitting information by electrical means possess some major challenges. Although electronics has allowed us the sophisticated logic devices we have today, the main unresolved issue for electronic devices is Joule heating. The electrical currents in our chips dissipate a significant part of their energy as heat, requiring the chips to be constantly cooled by large heat sinks, making their operations energy inefficient. In this respect, transferring information by optical means, using lasers and optical fibers or wave guides (i.e. the field of photonics), has tremendous potential for high-speed, low-energy data transfer. Gaining mutual control of the electron spin via electrical and optical means, and being able to inter convert the electrical/spin information to optical information and vice versa, could therefore revolutionize information storage and communication technologies in terms of speed and efficiency, combining best of both worlds.

One specific set of semiconducting materials, referred to as two-dimensional (2D) van der Waals materials, is particularly interesting to do exactly this: combining optics with spintronics, also referred to as optospintronics. Especially, the family of 2D van der Waals materials called the transition metal dichacogenides (TMDs) has received much attention, owing to their direct band gap (for atomically thin layers), the possibility to excite specific spins using circularly polarized light, their high mobility, and their matured wafer-scale production. Additionally, their atomically thin nature is highly promising for further downscaling information technologies to the atomic limit. Likewise, they play a central role in this thesis. However, before spintronics and optics can be combined using these materials, a better understanding on the spintronic mechanisms and light-matter interactions in TMD-devices is needed. Hence, this thesis first presents work on a spintronic effect referred to as spin-orbit torques (Chapters 4, 5, and 6), and subsequently continues with work on the light-matter interactions in TMD-devices (Chapters 7 and 8).

The spintronic work entails one particular spintronic effect, namely the spin-orbit torque (SOT). Here, a charge current or charge accumulation where all spins are polarized in the same direction, referred to as a *spin-polarized current* or a *spin-accumulation*, respectively, is used to interact with the magnetization of a magnetic layer. This enables one to switch the magnetization, e.g. from parallel to anti-parallel or vice versa, purely electrically in a fast and energy efficient manner. The spin-current or spin-accumulation can be obtained by multiple charge-to-spin conversion effects present in heavy metals possessing large spin-orbit coupling. By interfacing the heavy metal with a ferromagnet, we can study the interaction between the spin-current or spin-accumulation and the magnetization of the neighboring ferromagnet. The SOT devices considered in this thesis thus consist of a two layered structure: a TMD, possessing high spin-orbit coupling, interfaced with a ferromagnetic material. Here, TMDs are used as high spin-orbit coupling material, as they are considered as an excellent material playground, due to their wide variety of material properties, such as different atomic composition, interface quality, spin-obit coupling strengths, crystal structure symmetries, etc. While the most well known charge-to-spin conversion effects, the spin-Hall effect (SHE) and the Rashba-Edelstein effect (REE), were considered as main contributors to the generated SOTs, recent theoretical studies and contradicting experimental reports indicate the pres-

ence of other mechanisms that might play a role in the SOT generation. To gain more insight in the underlying SOT mechanisms, this thesis present additional experimental work on SOTs in TMD/Py bilayers in Chapters 5 and 6 to shed more light on all mechanisms at play in these devices, as discussed below.

Firstly, to equip the reader with the relevant framework for the experimental work on SOTs discussed in Chapters 5 and 6, firstly, Chapter 4 presents a concise literature review on SOTs in TMD/permalloy heterostructures. We compare the results reported for various TMD/ferromagnetic devices, and highlight the differences and similarities. Additionally, we present an overview of the experimental techniques used to both fabricate and measure the SOT devices, and discusses the ascribed mechanisms underlying the observed SOTs. This enables us to both identify the impact of particular fabrication steps on the observed SOTs, and give suggestions for their underlying microscopic mechanisms.

After the scene is set in Chapter 4, Chapter 5 presents experimental work on SOTs in the TMD $WSe_2$ and permalloy bilayers. Using the harmonic Hall technique, we measure the SOTs in different $WSe_2$/permalloy devices with different $WSe_2$ layer thicknesses, which allows us to elucidate the contribution from interfacial and bulk effects on the observed SOTs. We find a strong field-like torque compared to the damping-like torque in our $WSe_2$/permalloy bilayers, with no clear thickness dependence. Inline with previous theoretical predictions, this indicates that the dominant field-like torque in our devices arises from interfacial effects, such as the REE. Surprisingly, we also observe a strong induced uniaxial magnetic anisotropy in the planar Hall measurements, aligned to a specific crystallographic direction of the underlying $WSe_2$. Together with the strong field-like torque, this serves as an indication that the polymer-free technique used during our device fabrication, facilitates a strong interaction between the $WSe_2$ and permalloy layer, enabling more efficient SOT generation.

Due to multiple reports on the presence of SOTs in devices consisting of only a single ferromagnetic layer, referred to as *self-torques*, we study the role of self-torques in these TMD/permalloy devices in Chapter 6. We show that the field-like torque measured in a single layer permalloy device has a significant magnitude compared to the torques measured in wafer-scale $MoS_2$/permalloy bilayers. This indicates that the self-torque of the ferromagnetic layer can play a dominant role in SOT measurements on TMD/ferromagnet bilayers. Previous contrasting reports on the spin-orbit torques observed in similar TMD/ferromagnet bilayers can thus be ascribed to differences in the material quality or deposition method of the ferromagnetic layer. Additionally, we perform measurements on the different dimensions of the Hall bar, and find that a linear dependence on the extracted field-like torque strength on the Hall bar (channel width)/(arm width) ratio. This finding emphasizes the importance of intricate details, such as device dimensions, on the reported SOT strengths obtained with harmonic Hall measurements, and show that device dimensions should be clearly reported in future SOT studies.

As discussed before, apart from electrical control of the electron spin, the beauty of 2D van der Waals materials is that they also allow for gaining control of the electron spin using light. However, before these materials can fully flourish in op-

tospintronic applications, a better understanding of the light-matter interaction in TMD-devices is needed.

The photocurrent response in the most well studied TMDs ($MoS_2$, $MoSe_2$, $WS_2$, $WSe_2$, etc.), which reside in the semiconducting 2H crystallographic phase, often originates from the Schottky barrier at the interface between the TMD and the metallic electrodes, obscuring the optoelectronic properties of the TMD itself. Therefore, in Chapter 7, we fabricate local crystal phase-transformed $MoTe_2$ devices to reduce the contribution from the Schottky barrier at the TMD/metallic electrode interface and obtain a more intrinsic response of the TMD itself. Using scanning photocurrent measurements to spatially resolve the areas involved in the photocurrent generation, we find that that the photocurrent originates from the junction between the two different phases, the semiconducting hexagonal phase 2H and the semimetallic phase 1T', rather than from the bulky metallic electrodes. This observation, together with the non-linear IV-curve, indicates that the underlying mechanisms for the photocurrent is the photovoltaic effect due to a local electric field between the 1T and 2H-$MoTe_2$ region. Furthermore, we find that the optoelectronic response is two orders of magnitudes faster when using the phase-transformed regions to contact the TMD compared to directly contacting the TMD with the metallic electrodes. This indicates the potential of using phase-transformations in TMDs to further improve the optoelectronic performance of TMD based photodetectors through fully two-dimensional circuitry.

In Chapter 8, we study the polarization-dependence on photocurrents in $MoSe_2$ devices. Here, we show the effect of Schottky contacts on the polarization-dependent photocurrents by characterizing the helicity-dependent photoresponse of a monolayer $MoSe_2$ photodiode with and without hBN tunnel barriers at the contacts. We find that the device with Schottky barrier contacts has additional contributions to the polarization-dependent photocurrent. Additionally, even at normal incidence, the polarization-dependent photocurrent is observed which should not be allowed by symmetry arguments. The non-trivial modulation of the polarization-dependent photocurrents for devices with Schottky barrier contacts indicates that spatially resolved experiments should be used in combination with angle-resolved measurements to obtain a complete microscopic understanding of the helicity-dependent optoelectronic response of 2D-TMD devices. The work shown here thus provides additional steps towards obtaining a full understanding of the polarization-dependent photocurrents in TMDs, which are necessary to intertwine optics and spintronics for TMD-based optospintronic devices.

# Samenvatting

Ondanks dat machines met energieslurpende elektronenbuizen al logische bewerkingen konden uitvoeren, wordt de uitvinding van de transistor in 1947 vaak beschouwd als de gebeurtenis die het huidige informatietijdperk heeft ingeluid. Sinds zijn uitvinding heeft de transistor een ongekende verkleining ondergaan, mede mogelijk gemaakt door verschillende doorbraken zoals de uitvinding van de geïntegreerde schakeling (*integrated circuit*, IC) in 1958 en de complementaire metaaloxide-halfgeleider (*complementary metal oxide semiconductor*, CMOS) in de vroege jaren 90. Dit verkleiningsproces volgde nauwgezet de trend die Gordon Moore in 1965 voorspelde, nu bekend als de wet van Moore, wat resulteerde in steeds kleinere, snellere en goedkopere transistors. De technologie werd beschikbaar voor de massa wat heeft geleid tot de smartphones in onze broekzakken en state-of-the-art computerchips met een verbazingwekkende 114 miljard transistors. Deze duizelingwekkende getallen leiden al snel tot de vraag: *"Wanneer bereiken we ons limiet?"*. Het antwoord dat je krijgt varieert afhankelijk van wie je het vraagt, aangezien er geen consensus is over de exacte einddatum. Desalniettemin, met de huidige minitieuze scheiding van gate elektrodes van maar 200 silicium atomen, lijkt een fysisch limiet nabij. Terwijl de verkleiningstrend van Moore's law in leven wordt gehouden door slimmere chipontwerpen, zijn andere prestatiegetallen zoals de klokfrequentie en het energieverbruik per transistor al gestagneerd door verhoogde lekstromen die optreden bij kleinere transistors. Met de fysieke limieten voor conventionele CMOS-technologie in zicht, is de zoektocht naar nieuwe baanbrekende technologieën geïntensiveerd om de rekenkracht, opslagcapaciteit en efficiëntie verder te vergroten. Dit heeft onderzoekers geïnspireerd om nieuwe onderzoeksgebieden binnen de natuurkunde te verkennen voor een heruitvinding van informatie- en opslagtechnologieën.

Eén van deze onderzoeksvelden staat bekend als *spintronica*. In plaats van gebruik te maken van de *lading* van het elektron, zoals bij conventionele elektronica, maakt spintronica gebruik van een andere intrinsieke eigenschap van het elektron, genaamd *spin*, om informatie te coderen, transporteren en manipuleren. Deze kwantummechanische eigenschap, die een maatstaf is van het intrinsieke impulsmoment en het magnetisch dipoolmoment van het elektron, is al succesvol toegepast in diverse computertechnologieën. Het voornaamste voorbeeld hiervan is het gebruik van het spintronische effect genaamd giant magnetoresistance (GMR), bekroond met de Nobel prijs in 1988, in de leeskoppen van harde schijven (HDDs). Met GMR hangt de elektrische weerstand door twee ferromagnetische lagen die zijn gescheiden door een dunne laag van een normaal metaal af van de relatieve uitlijning van de magnetisatie van deze twee lagen (e.g. parallel of anti-parallel). De tweeledige staten van lage (parallelle uitlijning) en hoge weerstand (anti-parallelle uitlijning) kunnen worden gebruikt als representatie van een "0" of "1", oftewel één bit aan informatie. Hoewel harde schijven een hoge opslagdichtheid hebben, worden ze beschouwd als een traag opslagmedium die veel energie verbruiken, waardoor ze ongeschikt zijn voor toepassingen die snelle en energiezuinige opslag vereisen. Daarom worden an-

dere spintronische effecten en nieuwe manieren om ze te implementeren onderzocht voor de verdere optimalisatie van informatietechnologieën.

Hoewel spintronica ideaal is voor energie-efficiënte dataopslag, zijn er nog uitdagingen met betrekking tot het transport van informatie via elektriciteit. Ondanks dat elektronica de geavanceerde apparaten van vandaag mogelijk maakt, is er een onopgelost probleem voor elektronische apparaten: Joule heating (het joule-effect). De elektrische stromen in chips dissiperen een significant deel van hun energie als hitte, wat constante koeling door grote koelplaten noodzakelijk maakt. Een mogelijk alternatief is het transport van informatie via licht. Laserlicht, optische vezels en golfpijpen (waveguides) bieden een enorm potentieel voor hoogfrequent en energiezuinig datatransport (oftewel fotonica). Zowel optische en elektrische controle krijgen over de spin van het elektron, als een gecontroleerde conversie tussen deze informatiedragers, kunnen daarom technieken voor dataopslag ingrijpend veranderen en leiden tot snellere en meer energiezuinige apparaten.

Eén specifieke groep halfgeleidende materialen, genaamd twee-dimensionele (2D) van der Waals materialen, is bijzonder interessant voor het combineren van optiek en spintronica, ook wel optospintronica genoemd. Met name de familie van 2D van der Waals materialen bekend als de transitiemetaal-dichalcogenides (*transition metal dichalcogenides*, TMDs) heeft hiervoor veel aandacht gekregen. Dit vanwege hun directe band gap bij een dikte van één enkele atoomlaag, de mogelijkheid om specifieke spins te exciteren met circulair gepolariseerd licht en hun gevorderde productie op waferschaal. Bovendien biedt hun atomair dunne karakter de mogelijkheid om informatietechnologieën verder te verkleinen tot de atomaire limiet. Ze spelen daarom ook in dit proefschrift een centrale rol. Echter, voordat spintronica en optica kunnen worden gecombineerd met behulp van deze materialen, is een beter begrip nodig van de spintronische mechanismen en de interacties tussen licht en TMDs in TMD-apparaatjes. Daarom presenteert dit proefschrift eerst experimentele studies naar het spintronische effect genaamd spin-baan krachtmoment (*spin-orbit torques*, SOTs) (hoofdstuk 4, 5 en 6), gevolgd door experimenteel werk over de interacties tussen licht en materie in TMD-apparaatjes (hoofdstuk 7 en 8).

Het eerste spintronische gedeelte behandelt een specifiek spintronisch effect, namelijk de spin-baan krachtmoment. Hierbij wordt een spingepolarizeerde elektronenstroom (i.e. spinstroom) of een spingepolariseerde elektronenaccumulatie (i.e. spin-accumulatie), waarbij alle spins in dezefde richting zijn gepolariseerd, gebruikt om te interageren met de magnetisatie van een magnetisch materiaal. In een speciaal apparaatje, bestaande uit twee magnetische materialen gescheiden door een dunne isolerende laag (een zogehete magnetic tunnel junction (MTJ)) kan deze interactie gebruikt worden om de magnetisatie van één laag elektrisch te schakelen, e.g. van parallel naar anti-parallel en vice versa, op een snelle en energie-efficiënte wijze. De spinstroom of de spin-accumulatie kan worden verkregen met behulp van verschillende lading-naar-spin-conversie-effecten die optreden in zware metalen met een hoge spin-baan koppeling. Door een zwaar metaal in contact te brengen met een ferromagneet, kunnen we de interactie tussen een spinstroom of -accumulatie en de magnetisatie van de naburige ferromagneet onderzoeken. De SOT-apparaatjes in dit proefschrift bestaan dus uit een bilaag: een TMD met een hoge spin-baan kop-

peling, met aangrenzend een ferromagnetisch materiaal. Hier is de keuze gevallen op TMDs als zwaar metaal vanwege hun diversiteit aan materiaaleigenschappen, zoals atomaire compositie, interfacekwaliteit, spin-baan koppeling sterkte, symmetrie van het kristalstructuur, enzovoort. Hoewel de meest bekende lading-naar-spin-conversie-effecten, het spin-Hall effect (SHE) en Rashba-Edelstein effect (REE), werden beschouwd als de voornaamste mechanismen voor de SOTs, tonen recente theoretische studies en contradicties in experimenteel werk de aanwezigheid van andere mechanismen. Om meer inzicht te verkrijgen in de onderliggende SOT-mechanismen presenteert dit proefschrift aanvullend experimenteel onderzoek naar SOTs in TMD/permalloy bilagen in hoofdstuk 5 en 6, zoals beneden beschreven.

Om de lezer uit te rusten met de relevante achtergrond en huidige stand van zaken, presenteert hoofdstuk 4 een beknopt review van SOTs in TMD/permalloy heterostructuren. Hier vergelijken we de resultaten van verscheidene TMD/ferromagnetic apparaatjes en belichten we de verschillen en overeenkomsten. Hierna geven we een overzicht van de experimentele technieken die worden gebruikt om de apparaatjes te fabriceren en te meten, en bespreken we de mechanismen die worden toegeschreven aan de observeerde SOTs. Dit stelt ons in staat om de invloed van bepaalde fabricatiestappen op de SOTs te bepalen en suggesties te doen voor hun onderliggende microscopische mechanismen.

Nadat de toon is gezet in hoofdstuk 4, presenteert hoofdstuk 5 experimenteel werk over SOTs in TMD $WSe_2$ en permalloy bilagen. Met behulp van de harmonische Hall techniek meten we de SOTs in verschillende $WSe_2$/permalloy apparaatjes met verschillende $WSe_2$ laagdiktes. Dit stelt ons in staat om de contributie van lading-naar-spin-conversie-effecten die voortkomen uit het bulk te onderscheiden van de effecten die afkomstig zijn van het $WSe_2$/permalloy raakvlak. We vinden een sterke field-like torque vergeleken met de damping-like torque in onze $WSe_2$/permalloy bilagen, zonder duidelijke afhankelijkheid van de $WSe_2$ dikte. Deze observatie is in lijn met theoretische voorspellingen voor systemen waarbij de effecten van het raakvlak, zoals het REE, domineren. Verrassend genoeg zien we ook een sterke geïnduceerde magnetische anisotropie in de planar Hall-metingen, die uitgelijnd is met een specifieke kristallografische richting van de onderliggende $WSe_2$. Deze observatie, samen met de sterke field-like torque in onze apparaatjes, duidt erop dat de polymeer-vrije fabricatiemethode die is gebruikt voor onze apparaatjes, een sterke interactie tussen de $WSe_2$ en permalloy faciliteert, wat meer efficiënte SOT-opwekking mogelijk maakt.

Door verschillende studies op de aanwezigheid van SOTs in apparaatjes bestaande uit een enkele ferromagnetische laag, ook wel *self-torques* genoemd, bestuderen we in hoofdstuk 6 de rol van self-torques in deze TMD/permalloy apparaatjes. We laten zien dat de field-like torque gemeten in een apparaatje van een enkele laag permalloy een significante groote heeft vergeleken met de SOTs gemeten in waferschaal-geproduceerde $MoS_2$/permalloy bilagen. Dit wijst er op dat de self-torques van de ferromagnetische laag een dominante rol kunnen spelen in SOT metingen in TMD/ferromagnetische bilagen. Contrasterende observaties van SOTs in vergelijkbare TMD/ferromagnetische apparaatjes kunnen dus worden toegeschreven aan een verschil in depositiemethode van de ferromagnetische laag of

een kwaliteit van het materiaal. Daarnaast presenteren we SOT metingen op apparaatjes met verschillende afmetingen van de Hall bar en vinden dat de field-like torque sterkte linear afhankelijk is van de Hall bar (kanaalbreedte)/(armbreedte) ratio. Deze observatie benadrukt het belang van gedetailleerde aspecten en laat zien dat de afmetingen van de gemeten apparaatjes duidelijk gerapporteerd dienen te worden in toekomstig onderzoek naar SOTs.

Zoals eerder besproken ligt de schoonheid van 2D van der Waals materialen in het vermogen om zowel elektrische als optische controle van het elektron spin mogelijk te maken. Echter, voordat deze materialen zich volledig kunnen ontplooien in optospintronische toepassingen, is er een beter begrip nodig van het effect van licht op TMD-apparaatjes.

De fotostroomresponse in de meest bestudeerde TMDs ($MoS_2$, $MoSe_2$, $WS_2$, $WSe_2$, etc.), die zich bevinden in de halfgeleidende 2H kristalgrafische fase, komt vaak voort uit een Schottky-barrière in het raakvlak tussen het metallisch contact en de TMD. Hierdoor zijn de optoelektronische eigenschappen van de TMD zelf vaak in nevelen gehuld. Daarom fabriceren we in hoofdstuk 7 $MoTe_2$-apparaatjes waarbij we lokaal de kristallografische fase van het TMD veranderen op de locatie van de metallisch contacten, om het effect van de Schottky-barrières te verminderen en het intrinsieke optoelektronische response van de TMD te meten. Met scanning-fotostroommetingen vinden we dat de fotostroom ontstaat bij de junctie tussen de twee verschillende fases, de halfgeleidende hexagonale fase 2H en de semimetallischae fase 1T', in plaats van bij de metallische elektrodes. Deze observatie, samen met de non-lineare IV-curve, wijzen er op dat het onderliggende mechanisme voor de fotostroom het fotovoltaisch effect is door een lokaal elektrisch veld tussen de 1T'- en de 2H-$MoTe_2$ regio's. Daarnaast zien we dat, met de fase-getransformeerde contacten, het optoelektronische response twee ordes van grootte sneller is dan met de normale metallische contacten. Dit wijst op het potentieel van lokale fasetransformaties van TMDs voor het verder verbeteren van de optoelektronische prestatie van fotodetectoren gebaseerd op TMDs en volledige 2D schakelingen.

In hoofdstuk 8 bestuderen we de polarisatieafhankelijkheid van fotostromen in $MoSe_2$-apparaatjes. Hier laten we het effect zien van een Schottky-barrière bij de contacten (i.e. Schottky-contacten) op de polarisatieafhankelijke fotostromen in een monolaag $MoSe_2$. Dit doen we door apparaatjes te maken met en zonder hBN-tunnelbarrière bij de contacten. We zien dat fotostroom in het apparaatje met Schottky-contacten extra afhankelijkheden heeft van de polarisatie. Daarnaast observeren we een polarisatieafhankelijke fotostromen bij belichting met een loodrechte invalshoek die, gezien de symmetrie van het kristal, niet mogelijk zouden moeten zijn. De modulatie van de polarisatieafhankelijke fotostromen voor apparaatjes met Schottky-contacten wijzen er op dat zowel locatie- als hoekafhankelijke metingen nodig zijn om een compleet beeld te krijgen van de polarisatieafhankelijkheid van de optoelektronische response van 2D-TMD apparaatjes. Dit werk levert dus extra stappen naar een compleet begrip van de polarisatieafhankelijke fotostromen in TMDs die uiteindelijk nodig is om optica en spintronica te verweven in TMD-gebaseerde optospintronische apparaatjes.

# Acknowledgements

Embarking on the journey to pursue a PhD was a difficult decision to make. I had always admired PhD students, yet never envisioned myself among them. Dedicating four years to a single topic felt like quite a commitment. However, I am immensely grateful for having had this opportunity and for having the courage to see it through. The freedom to delve into my own project, working with fascinating and cutting-edge machinery to advance our scientific understanding and pursue your curiosity, has been a truly enriching experience. Though the path has been challenging at times, this chapter in my life is one I will hold dear. I am indebted to numerous individuals who have supported me on this journey, and I would like to seize this moment to express my sincere gratitude to a few of them.

First and foremost, I want to express my gratitude to the person I am most indebted to, my supervisor **Marcos Guimarães**. It does not seem like five years ago when you came into my office for the first time, telling me that we would likely collaborate, and started explaining me this weird but intriguing concept of spin-orbit torques. As a PhD student that started only a few months before in a new field, I was not entirely sure what this Brazilian man was talking about, but I liked your enthusiasm. Reflecting on the past five years, I am honored to have had the privilege of having you as a mentor. As a first member of the optospintronics group, witnessing the group develop with astounding pace from mere two members to more than ten has been an invaluable experience. As a calm and at times insecure PhD student myself, it was inspiring to see how you sometimes had to fight to earn your place in this competitive academic world. Your tremendous drive and unwavering perseverance to contribute to science are truly admirable. We have certainly shared some good moments, from the first laser delivery to the first working devices to the first results. Over the years, I have learned a lot from you, and not only about spintronics and optics. You also took the time to show me how science works behind the scenes. You involved me in meetings with visiting professors and reviewing papers, and while I sometimes get lost in detail, you taught me a more pragmatic approach to science. I will hold all the lessons learned from you close to heart. Thank you for everything and my best wishes to you and your group!

Mijn oprechte dank gaat ook uit naar mijn tweede begeleider, bij wie ik mijn promotietraject begon, **Bart van Wees**. Ik bewonder jouw kritische en scherpe blik op wetenschappelijk werk waarmee je altijd door mooie praatjes heen weet te prikken en je vinger op de zere plek weet te leggen. Ook waardeer ik, in deze academische wereld waar diplomatie een grotere rol speelt dan ik van tevoren had verwacht, je houding simpelweg jezelf te zijn. Ook jouw korte kantoorbezoekjes met intermezzo's over het driedeurenprobleem, het gevangenendilemma en verhalen van weleer werden gewaardeerd. Bedankt voor alles!

I would like to thank professors **Pietro Gambardella**, **Rembert Duine** en **Jan Anton Koster** for being in my reading committee, and **Beatriz Noheda** and **George Palasantzas** for being in my defense committee. Also thanks to

professors **Maria Loi** and **Wesley Brown** for letting me use their Raman systems, and thanks to **Bart Kooi** for allow us to use his transmission electron microscope setup. **Tamalika**, we did not talk much during my PhD project but I appreciate the few heartwarming talks we had. And thanks for convincing me to do the top master nanoscience which enabled me to do the PhD in the first place!

To make all these devices we need a lot of different and complicated machinery, so I would also like to express my gratitude to the technicians and secretary in the FND for all their support. **Johan**, bedankt voor alle hulp in goede en in slechte tijden. Ik heb het altijd erg gewaardeerd hoe betrokken je bent bij de FND en de gehele faculteit, en niet alleen op technisch vlak. Al zijn we uit ander hout gesneden heb ik altijd met veel ontzag gekeken naar hoe jij je mannetje weet te staan. Daar kan ik nog veel van leren. Ik houd in ieder geval je YouTube-kanaal in de gaten. **Hans**, bedankt voor alle trainingen! Ik heb goede herinneringen aan onze samenwerking aan de BJD opdamper en de TFC om het argon milling weer aan de praat te krijgen, en de nachtelijke duik op Vlieland. **Arjun**, thanks for all the help with the EBL and our little chats once in a while. **Frits** en **Herman**, ook jullie bedankt voor alle technische ondersteuning. En succes Frits met het afmaken van je huis. **Marleen**, bedankt voor alle hulp en het tig keer verlengen van mijn RUG-account.

When deciding to do a PhD, I specifically chose the FND for its compelling topic, but the large size of the group proved to be a valuable bonus, allowing me to connect with so many different people. **Frank**, uiteraard wil ik jou als mijn paranimf en kantoorgenoot voor meer dan 4 jaar hartelijk bedanken. Ook ik heb het samen organiseren van de groepsuitjes altijd met veel plezier gedaan. Jouw pragmatische houding; niet bij de pakken neer zitten, maar aanpakken en door, heb ik altijd bewonderd. Ook de nachtelijke duiken in de Noordzee tijdens de Vlieland meetings en het rijden op de trekker van je vader zal ik niet snel vergeten! Veel plezier in Utrecht met je nieuwe baan. **Aaron**, mi amigo! I am incredibly happy you joined the group and became a part of the latter journey of my PhD. I do not know how you do it, but somehow you manage to always be there when something exciting happens. An extremely useful skill of which I am a little jealous, because apparently I always seem to be absent during these moments. Fortunately for me, you could tell me all about it during our wonderful talks in the office, clean room, and at the coffee machine, and of course the Guitar Hero sessions at your place! Rock on my friend! And, of course, thanks for being my paranymph. **Cedric**, cabron! Que onda? I've mentioned this many times before, but I truly enjoyed the last part of my PhD the most, and having you in the group, first as a master student and later as PhD student, played a significant role in that. Your relaxed attitude, humor, and tequi**l**a (not tequi**lj**a!) helped me through some tough times. Grateful I got to know you. We didn't manage to publish the ten nature papers we planned for at the start, but I am sure you'll manage on your own. Good luck with your PhD. I hope we stay in touch! **Sytze**, ik ben ontzettend blij dat je ervoor gekozen hebt een masterproject te doen in de groep, waarbij ik je dagelijkse begeleider mocht zijn. Het hele spin-orbit torqueproject stond nog in de kinderschoenen en zonder jouw hulp was het misschien wel niet van de grond gekomen. Waar menig perfectionist

zich verliest in details (ik spreek uit ervaring), lijk jij een goede balans te hebben gevonden. Je gaat de diepte in zonder het grote plaatje uit het oog te verliezen. Bewonderingswaardig! Bedankt voor alles en veel succes met het afmaken van je PhD. Ik ben benieuwd wat de toekomst voor jou in petto heeft. **Freddie**, helaas heeft de thymemachine het niet overleefd waardoor ik nu al ben aangekomen bij het einde van m'n PhD. Ik heb altijd met veel plezier met jou samengewerkt in het lab. Jouw nuchtere Groningse houding, je leuke woordgrappen en onze gesprekken over onze problemen hebben me zeker goed gedaan. Lange tijd zaten we een beetje in hetzelfde schuitje, en het was verademend om iemand te hebben die hetzelfde doormaakte. Veel plezier met je nieuwe baan bij Lambert Instruments. **Job**, ik heb altijd enorm genoten van jouw gevoel voor humor tijdens de lunch, koffiepauze of een van de Call-of-Duty en Risk avonden. En natuurlijk was jouw bruiloft een absoluut hoogtepunt. Ik ben erg benieuwd naar wat jouw volgende stappen zullen zijn. Veel succes met de laatste loodjes! **Stella**, malakas! I really enjoyed our talks about SOTs and the funny moments we had with Aaron and Cedric. Good luck with your new job in France. I hope you like the weather better there, spin-orbit torque girl! **Tamas**, thanks for being part of the SOT project. Unfortunately, it was not as fruitful as we wanted, but I still enjoyed our talks and your mathematical riddles. Good luck with finishing your PhD. **Feitze**, jij ook bedankt voor alle leuke gesprekken over ESPs, arduinos, home-automation, HQgraphene, je huis in Lewenborg en je geruststellingen van tijd tot tijd! **Jorge**, thanks for helping me get started in the first few months of my PhD which eventually led to a nice publication. I learned a lot from you and wish you all the best with your scientific career and new family. Also, I am grateful for all the students that have chosen to pursue a research project with me as their daily supervisor: **Sytze**, **Pieter**, **Klaiv**, **Cedric**, and to some extent **Stella** and **Vishesh**. It has been an extremely joyful experience with all of you. I hope you learned at least as much from me as I learned from you guys. Your enlightening questions often made me doubt my own understanding, eventually leading to a better comprehension of all the different topics. You do not really understand a topic unless you are able to explain it to others. I wish you all the best for your future. **Anna**, although we did not work much together, I admired your hard work and attention to detail. Good luck with finishing your PhD! **Talieh**, I enjoyed our time in the office together and admired your unfailing drive! Good luck with your academic career in the US, although you will not need it as you make your own! **Alexey**, thanks for all the help in the clean room. I really learned a lot from your amazing clean room skills and your indestructible calmness. And your initiation of the nightly dives at Vlieland were highly appreciated. **Tian**, you are the reason that the ball started rolling on me getting a PhD position in the FND. Thanks, and good luck with everything in Munich! Lastly, thanks to all the other members of the FND and a few other for making my time as PhD student such a wonderful experience: **Christian**, **Julian**, **Tom**, **Xu**, **Carmem**, **Obed**, **Crystal**, **Ping**, **Arjan**, **Adam**, **Dennis**, **Joop**, **Xiangyang**, **Rafael**, **Anouk**, **Azminul**, **Perihan**, **Maxem**, **Boxuan**, **Geert**, **Feng**, **Harshan**, **Rixt**, **Konstatinos**, **Zohaib**, **Rick**, **Krishna**, **Ioannis**, **Benedito**.

En nu wil ik mijn oprechte dank uitspreken aan de personen die mij nog het

meest dierbaar zijn.

Beste **Martijn**, **Thomas** en **Willem**, ik prijs mezelf gelukkig met zulke goede vrienden en koester onze hechte vriendschap die al sinds de middelbare school bestaat. Onze Århus sessions en andere uitstapjes en (soms wilde) avonturen waren waardevolle momenten om even stoom af te blazen. Het zijn nu enkele op een lange lijst van gedeelde dierbare herinneringen en ik hoop er nog veel nieuwe met jullie aan toe te kunnen voegen. Ik ben erg benieuwd waar onze paden naar zullen leiden.

Lieve **Jet, Albert, Bert, Ellen, Jetske, Brecht, Annegeerte**, en **Nicolaas** bedankt voor al jullie onvoorwaardelijke steun. Al onze leuke uitjes en tradities samen: Sinterklaas, kerst, paaseieren schilderen, concerten bezoeken, muziek maken, spelletjes spelen en ga maar door, waren een fijne afleiding van soms hectische dagen. Ik ben ontzettend blij om zo'n stevige en vertrouwde basis te hebben waarop ik kan bouwen. Op de goede momenten hielpen jullie me herinneren dat dingen in twijfeltrekken inherent is aan het menselijk bestaan.

Lieve **Josien**, alle verantwoordelijkheden die bij een promotie komen kijken, brengen stress met zich mee. Die stress maakte mij niet altijd even vrolijk of energiek. Toch stond jij altijd klaar om mijn beklag aan te horen, me te ondersteunen of op te beuren wanneer het nodig was, en me mijn gang te laten gaan zonder oordeel of verwachting. Ik had me geen fijnere plek kunnen wensen om thuis te komen na een dag vol tegenslagen. Een thuis dankzij jou.

Ten slotte wil ik **Soep**, **Miep**, **Trui**, en in mindere mate **Drop**, **Pip** en **Joppe** bedanken voor het helpen herinneren waar het leven uiteindelijk echt om draait.

Jan Hidding
Groningen, December 2023

# Curriculum Vitæ

## Jan Hidding

20-08-1994 Born in Groningen, The Netherlands.

## Education

2018–2023 Ph.D. research in the Zernike Institude for Advanced Materials
University of Groningen, The Netherlands
*Thesis:* Spin-orbit torques and photocurrents in 2D materials
*Supervisors:* prof. dr. M. H. D. Guimarães and prof. dr. ir. B. J. van Wees

2016–2018 Master of Science, Top master Nanoscience
University of Groningen, The Netherlands
*Thesis:* Excitation energy transport in self-assembled molecular nanotubes
*Supervisor:* prof. dr. M. S. Pshenichnikov

2013–2016 Bachelor of Science, Physics
University of Groningen, The Netherlands
*Thesis:* Anomalous Hall measurements on proximity induced ferromagnetic graphene/YIG heterostructures
*Supervisor:* prof. dr. ir. B. J. van Wees

# List of Publications

1. **J. Hidding**, C. A. Cordero-Silis, D. Vaquero, K. P. Rompotis, J. Quereda, M. H. D. Guimarães, *Photocurrents in Phase Engineered 2H-1T' $MoTe_2$ Phototransistors*, in preparation.

2. T. Liu, A. Roy, **J. Hidding**, H. Jafari, D. K. de Wal, J. Slawinska, M. H. D. Guimarães, B. J. van Wees, *Crystallographic-dependent bilinear magnetoelectric resistance in a thin $WTe_2$ layer*, Phys. Rev. B. **108**, 165407 (2023).

3. **J. Hidding**, K. Mertiri, F. Mujid, J. Park, M. H. D. Guimarães, *Spin-orbit torques in MOCVD grown $MoS_2$/permalloy bilayers*, Phys. Rev. B. **108**, 064419 (2023).

4. **J. Hidding**, S. H. Tirion, J. Momand, A. Kaverzin, M. Mostovoy, B. J. van Wees, B. J. Kooi, and M. H. D. Guimarães, *Interfacial spin-orbit torques and magnetic anisotropy in $WSe_2$/permalloy bilayers*, J. Phys. Mater. **4** 04LT01 (2021).

5. J. Quereda, **J. Hidding**, T. S. Ghiasi, B. J. van Wees, C. H. van der Wal, and M. H. D. Guimarães *npj 2D Materials and Applications*, npj 2D Materials and Applications **5**, 13 (2021).

6. **J. Hidding** and M. H. D. Guimarães, *Spin-orbit torques in transition metal dichalcogenide/ferromagnet heterostructures*, Front. Mater., **7**, 594771 (2020).